**THE DISSERTATION COMMITTEE FOR HANDE GERKUS
CERTIFIES THAT THIS IS THE APPROVED VERSION OF
THE FOLLOWING DISSERTATION:**

Model Experiments to Measure Yield Thresholds and Trajectories for

Plate Anchors and Develop a New Anchor Concept

Committee:

Robert B. Gilbert, Supervisor

Aaron S. Bradshaw

Spyridon A. Kinnas

Ellen Rathje

Brady Cox

Model Experiments to Measure Yield Thresholds and Trajectories for Plate Anchors and Develop a New Anchor Concept

by

Hande Gerkus, B.Sc.; M.E.

DISSERTATION

Presented to the Faculty of the Graduate School of

The University of Texas at Austin

in Partial Fulfillment

of the Requirements

for the Degree of

DOCTOR OF PHILOSOPHY

THE UNIVERSITY OF TEXAS AT AUSTIN

AUGUST 2016

Dedication

To Semra Gerkus and Talat Gerkus

Acknowledgements

First of all, I would like to express my heartfelt gratitude to my supervising professor, Dr. Robert B. Gilbert, for his encouragement, guidance and trust. He introduced me to the Offshore Geotechnical Engineering, broadened my perspective by involving me in various research projects and provided me the opportunity to work with and learn from amazing people from all around the world. I will always appreciate the opportunity to work with him. I am grateful to Dr. Aaron S. Bradshaw for his guidance and help throughout every step of this research project. I would like to extend my thanks to Dr. Spyros Kinnas for his highly valuable guidance on hydrodynamics. I would like to thank Dr. Ellen Rathje and Dr. Brady Cox for their valuable support and comments to improve this research.

I would also give my sincerest thanks to other geotechnical engineering faculty members, Dr. Kenneth Stokoe, II, Dr. Jorge Zornberg, and Dr. Chadi El-Mohtar for their endless efforts in teaching and research.

I would like to thank the National Science Foundation for funding this research project. I would like to thank our project collaborators Dr. Kenneth Gavin, Dr. Paul Doherty Dr. Vinayagamoothy Sivakumar, Joe Giampa, Soroosh Jalilvand and Joe Fanning for their valuable contributions and collaborations.

Working with an amazing research team was the best part of my Ph.D. life. I would like to express my special thanks to Asitha Senanayake, Ying Lai, Dr. Eugenio Iturriaga Flores, Yunhan Huang, Dr. Ching-Hsiang Cheng, Matteo Sottile, Dr. Ali Helwa, Dr. Jinbo Chen, Dr. Matt Gore and Ian McMillan for their friendship, support and for being great colleagues. I learned a lot while working with each one of them but most importantly their friendship made everything better. I would like to thank all my classmates and UT

Model Experiments to Measure Yield Thresholds and Trajectories for Plate Anchors and Develop a New Anchor Concept

Hande Gerkus, Ph.D.

The University of Texas at Austin, 2016

Supervisor: Robert B. Gilbert

The motivation of this research was to experimentally measure yield thresholds and dive trajectories of model plate anchors and develop a new anchor concept: The Flying Wing Anchor®. The objectives of this study were to (1) develop the understanding of pure loading yield thresholds of simple shaped bearing plates in clay under undrained loading, investigate how the undrained shear strength, sensitivity and plasticity of soil affects the pure loading yield thresholds and compare experimental measurements with theoretical predictions (2) asses the initiation of post-yield movement and dive trajectory of bearing plates, (3) optimize the design of the Flying Wing Anchor® concept based on pure loading yield thresholds, initiation of post-yield movement and dive trajectory in clay, (4) develop a simplified plasticity model to predict the initiation of post yield behavior, dive trajectory and the ultimate holding capacity of the new anchor concept in clay and compare theoretical predictions with experimental measurements.

The methodology focuses on experimental testing of model plates and Flying Wing Anchor® concepts in undrained clay. The theoretical calculations are compared with experimental measurements.

The pure loading yield thresholds of the bearing plates in clay under undrained loading were measured. The post-yield movement analysis showed an anchor vertically embedded into soil should initially rotate from vertical to dive deeper with drag loading. The initial Flying Wing Anchor® concept is the one-wing Diamond anchor and further optimization resulted in bi-wing concepts of Paloma and the final concept of Speedy anchors. The new anchor concept dives deeper into soil when loaded in tension. At the ultimate embedment depth, the holding capacity is maximized. The lower shear resistance enables deeper penetration into soil. The holding capacity is maximized over the full anchor surface in bearing due to high resistance in normal loading. Anchor can be pulled out of soil in pure shear and reused. Scaled model tests show the new anchor is a promising sustainable and efficient foundation solution for deep-water offshore wind turbines due to efficient installation method, sustained high capacity and horizontal trajectory during failure that prevents anchor to slide out of soil.

Table of Contents

x

List of Tables

List of Figures

xxiii

xxvii

Chapter 1: Introduction

1.1 MOTIVATION

Renewable energy systems are a major area of research both in the United States and in Europe as the energy demand increases significantly all around the world. The wind energy is considered as one of the main green energy resources. The future of wind energy is in deep-water where offshore wind turbines can produce significant amount of renewable energy without harmful emissions (Musial and Ram, 2010).

The public pressure to locate wind turbines away from the coastal line and the space requirements on onshore increase the demand of offshore wind turbines (Matha, 2009). In the United States, the offshore wind energy has the potential to be a major energy resource especially in the highly populated areas where onshore energy is not available. The winds increase rapidly with increasing distance from the coastal area while getting faster and steadier. This enables offshore wind sites to be reasonably located from the major urban areas. The main challenges of constructing offshore wind turbines are the efforts and high costs of foundations, installations, operation and maintenance (Musial and Butterfield, 2006). Those challenges associated with offshore wind turbine facilities can be reduced significantly by sustainable and efficient foundation concepts that reduce the construction and maintenance costs; and the harmful effects on the marine environment.

The initial criterion for choosing the type of foundation for offshore wind turbines is the water depth and extreme loads (Bradshaw, 2012). In shallow water, foundations such as monopiles, gravity bases, and suction buckets are used to extend the foundation system to sea floor. In transitional water depths, foundations such as multi-piles and jacket substructures are used to extend the foundation system into sea floor. For the deep water wind turbines, floating platforms provide a more feasible solution. The representative

design option for each water depth category is presented in Figure 1.1 (Musial and Ram, 2010).
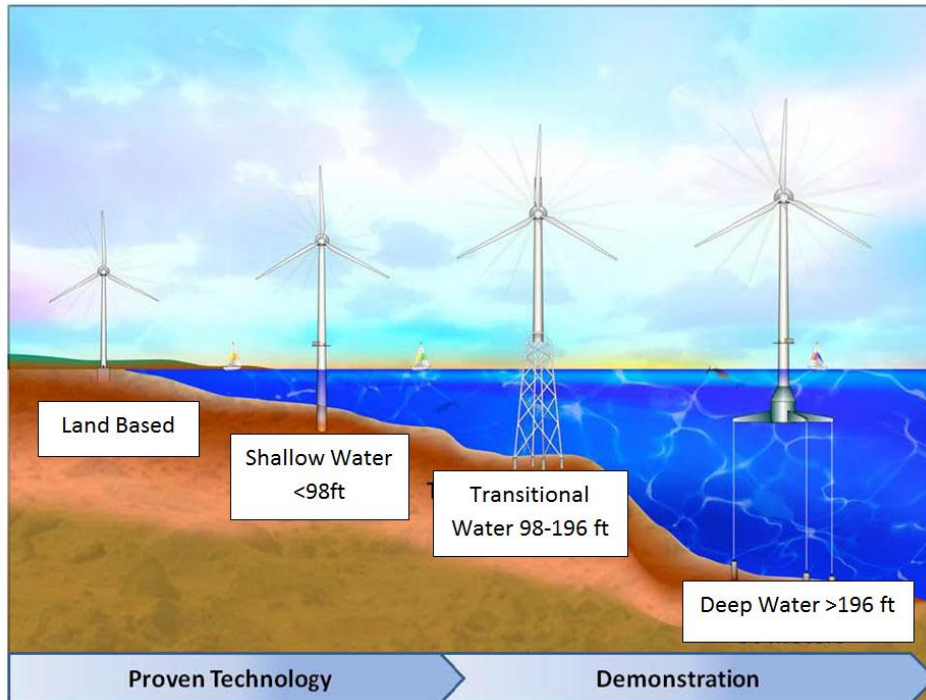
Figure 1.1: Status of Offshore Wind Energy Technology (Musial and Ram, 2010)

The types of floating offshore platforms developed for offshore wind turbines are presented in Figure 1.2 (www.energy.gov, 2014). Floating platforms are secured to seafloor by anchors attached to the platform via mooring systems. The offshore anchors are developed to support floating platforms by providing uplift resistance against the environmental loads that act on the platforms (Mark and Gourvenec, 2010). For offshore wind turbines in deep-water, plate anchors provide an efficient solution for vertical and inclined anchoring. The resistance mobilized over the bearing surface of the anchor is more efficient than frictional resistance of a vertically loaded pile anchor (Bradshaw et al., 2015).

Figure 1.2: Floating Platforms for Offshore Wind Turbines (www.energy.gov)

The motivation of this research is to experimentally measure yield thresholds and dive trajectories of model plate anchors and develop a new anchor concept. This new sustainable anchor concept developed for deep-water offshore wind turbines is the Flying Wing Anchor®. This research focuses on the development of this new anchor concept based on the yield thresholds and dive trajectories of plate anchors and experimental testing of the developed Flying Wing Anchor® concepts.

1.2 OBJECTIVES

The main objectives of this research are:

1. Develop the understanding of pure loading yield thresholds of simple shaped bearing plates that are symmetrical along the longitudinal axis in clay under undrained loading. Study how pure loading yield thresholds change for different geometries. Investigate how the undrained shear strength, sensitivity and plasticity of soil and the loading rod diameter and the rotational loading rates affect the pure

loading yield thresholds of bearing plates. Evaluate how experimental measurements compare with theoretical predictions.

2. Asses the initiation of post-yield movement and dive trajectory of simple shaped bearing plates that are symmetrical along the longitudinal axis in clay under undrained loading conditions.

3. Optimize the design of the Flying Wing Anchor® concept based on pure loading yield thresholds, initiation of post-yield movement and dive trajectory in clay under undrained conditions.

4. Develop a simplified plasticity model that calculates the interactions between the anchor, the loading line, and the soil around the line and the anchor to predict the initiation of post yield behavior, dive trajectory and the ultimate holding capacity of the new anchor concept in clay. Evaluate how theoretical predictions compare with experimental measurements.

1.3 METHODOLOGY

The methodology used for this research is based on experimental testing of scaled anchor models and comparing experimental results by theoretical predictions. The experimental testing setup, testing methods and calculations along with results are summarized in this section. The tasks planned for this research are listed below.

1. Experimentally test models under pure normal, in-plane shear, out-of-plane shear, pitch, roll and yaw loading to measure the pure loading yield thresholds in each of the six-degree-of-freedom under undrained loading conditions in clay. Compare experimental measurements with theoretical calculations.

    a) Experimentally test simple shaped bearing plates that are symmetrical along the longitudinal axis in:

4

       i.   Different undrained shear strength profiles.

      ii.   Different soil sensitivities,

    iii.   Kaolinite and Gulf of Mexico marine clay.

b) Compare measurements with theoretical calculations.

2. Asses the initiation of post-yield movement and dive trajectory of simple shaped bearing plates under combined loading during drag embedment.

    a) Analyze the forces that initiate anchor diving for drag embedment anchors and vertically loaded anchors. Conduct experimental tests and theoretically calculate the forces acting on the scaled anchor models to have a better understanding of plate anchor dive initiation and the effect of shank orientation on the initiation of dive penetration.

    b) Conduct preliminary drag embedment tests using simple shaped bearing plates to observe anchor movement. Theoretically calculate utilization ratios. Determine how the dive penetration of a bearing plate near vertically embedded into soil can be initiated without pulling the bearing plate out of soil.

3. Asses the pure loading yield thresholds and post-yield movement of the Flying Wing Anchor® concepts in clay under undrained loading and optimize the Flying Wing Anchor® concepts based on experimental testing results and theoretical calculations.

    a) Measure the pure loading yield thresholds of one-wing and bi-wing Flying Wing Anchor® concepts in undrained clay.

    b) Conduct tests to analyze the dive trajectory and mobilization of the ultimate holding capacity by studying:

       i.   Anchor pitch rotation from vertical after the free-fall embedment,

      ii.   Fluke-Shank coupling mechanism, shank release angle,

iii.   Anchor dive trajectory under in-plane and out-plane drag loading,

iv.   Effect of different initial embedment depths,

v.   Effect of different initial pitch angles,

vi.   Effect of fluke-shank attachment location.

4.   Develop a simplified plasticity model calibrated with experimental measurements that predicts anchor dive penetration. Compare experimental measurements with prediction model results.

1.4 STRUCTURE OF THE DISSERTATION

This dissertation has 8 chapters. The Appendix section has detailed test results. Contents of each chapter are summarized below.

- Chapter 1: Introduction includes motivation, objectives, methodology and structure of this thesis.

- Chapter 2: Literature Review presents information about offshore structures, mooring systems, offshore anchors, design principles and scaling relationships for plate anchors.

- Chapter 3: Experimental Testing Facility describes the testing facility and instrumentations used for testing the scaled anchor models.

- Chapter 4: Pure Loading Yield Thresholds presents the experimentally measured and theoretically calculated non-dimensional yield thresholds of simple shaped bearing plates that are symmetrical along the longitudinal axis, under pure loading conditions. The details of the scaled anchor models, testing setup and calculation procedures are explained. The experimentally measured and theoretically calculated yield thresholds are compared with the yield thresholds calculated by other researchers.

- Chapter 5: Post-Yield Movement of Bearing Plates presents the research on the initiation of the post-yield movement and the post-yield movement of simple shaped bearing plates. The scaled drag embedment anchor and vertically loaded anchor models were tested and the force mechanics were theoretically calculated to understand the initiation of dive mechanism. The post-yield movement of simple shaped bearing plates were measured experimentally and failure modes were observed.

- Chapter 6: The Experimental Testing of the Flying Wing Anchor® Concepts introduces the developed Flying Wing Anchor® concepts and presents the experimental measurements and theoretical calculations of pure loading yield thresholds and post-yield measurements of the Flying Wing Anchor® concepts. The main components of the anchor concepts, the concepts of free-fall behavior and anchor-post yield behavior are explained. The dive trajectory of scaled one-wing and bi-wing Flying Wing Anchor® concepts were measured and the factors affecting the dive performance of the anchor are discussed.

- Chapter 7: Simplified Plasticity Model to Predict Anchor Dive Trajectory presents the model developed to predict the dive trajectory of the Flying Wing Anchor® concepts. The model assumptions and calculation steps are described. The model predictions are compared with experimental measurements.

- Chapter 8: Conclusions and Recommended Future Work summarizes the important outcomes of this study and proposes how this research can be expanded with further study.

Chapter 2: Literature Review

2.1 INTRODUCTION AND OBJECTIVES

This chapter presents background information about offshore structures, mooring systems, offshore anchors, design principles and scaling information. The focus is to provide information about the offshore environment and the conventional anchors to develop the understanding of how the Flying Wing Anchor® concept has been evolved. The offshore structures initially developed for oil and gas production are also used for offshore wind turbines. The deep-water offshore wind turbines will be constructed on floating platforms that are connected to offshore anchors by mooring lines. Offshore anchors, with emphasis on the plate anchors and dynamically installed anchors, and their design procedures are described in this chapter. Scaling relationships for plate anchors are described to provide insight into how scaled model test results can be used to predict prototype anchors performance.

2.2 OFFSHORE STRUCTURES

Different types of offshore structures are developed for oil and gas production depending on the operating considerations, economic considerations, location of infrastructure and operator's interests. Graphical representations of different offshore structures are presented in Figure 2.1. Fixed platforms are extended to the soil by piles driven into the seafloor. The height of the platform depends on the water depth in the platform location. Fixed platforms are considered economical at water depths less than 2,000 ft (610 m). Compliant towers are combined of a narrow tower with piled foundation systems. Compliant towers have higher flexibility than fixed structures. They are considered for water depths of 1,000 to 2,000 ft (305-610 m). Tension-leg platforms are moored vertically and tension in the mooring system is provided by the buoyant

components. They are used in water depths of 1,000-5,000 ft (305- 1,524 m). Spar is a circular vessel sitting vertically on water that is supported by buoyancy chambers at the top, flooded mid-section and a stabilizing keel at the bottom. Mooring systems are used to provide dynamic stability to Spars. Submersible production platforms are permanently moored floating systems with drilling capabilities. Floating production units (FPU) are ship-shape production facilities without storage. The floating production, storage and offloading (FPSO) facilities are ship-shape production facilities with storage and offloading capabilities. FPU and FPSO can be either moored or dynamically positioned. Spars, semisubmersible production units, disconnectable floating production units (FPU's) and floating production, storage and offloading facilities (FPSO's) can be used in water depths greater than 10,000 ft (3,048 m) (Richardson et al., 2008).
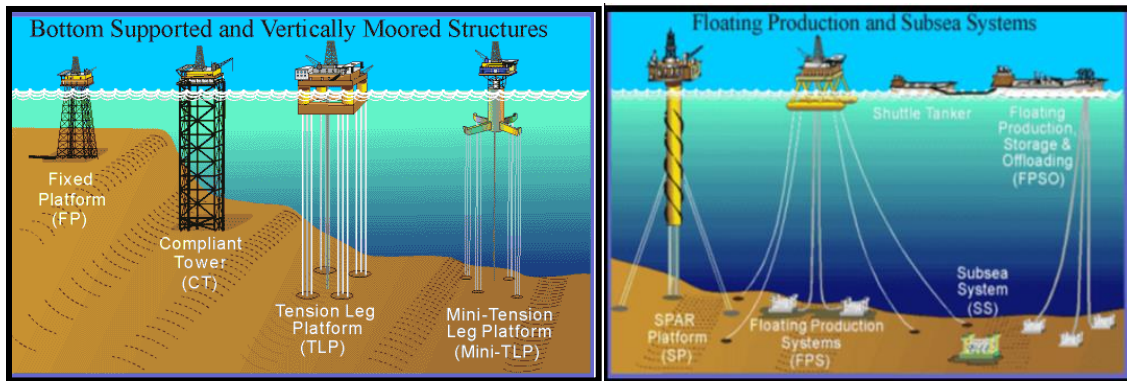
Figure 2.1: Offshore structures (Richardson et al., 2008)

2.3 MOORING SYSTEMS

Mooring systems connect floating platforms to the foundations. Permanent mooring systems are preferred for exploration and production facilities while vessels are usually moored by temporary mooring systems. Semi-submersible drilling rigs are moored with eight point mooring with two mooring lines attach to each column. CALM buoys are

moored with four or more mooring lines at equally spaced angles. Spread moorings are directly connected to FPSOs and FSOs in milder environments. For harsh environments, the turret mooring is preferred for FPSOs and FSOs as it enables the FPSO or FSO to rotate around the turret. Tendon mooring is the Tension Leg Platform on suction or driven piles, used in extreme deep water for semi-permanent production units (Vryhof B.V., 2015).

Catenary mooring systems arrive at the seabed horizontally and resist horizontal loads. Taut leg mooring systems arrive the seabed at an angle and resist both horizontal and vertical loads. The geometry of catenary and taut leg mooring lines are presented in Figure 2.2. Chains, wire ropes or synthetic fiber ropes are used as mooring lines. Chains with different diameters and grades are most common mooring lines. Wire ropes and synthetic fiber ropes have the advantage of having lower weight and higher elasticity. Different types of connectors, such as shackles, links, swivels, and clamps are used to connect components of the mooring lines or connect mooring lines to structures (Vryhof B.V., 2015).
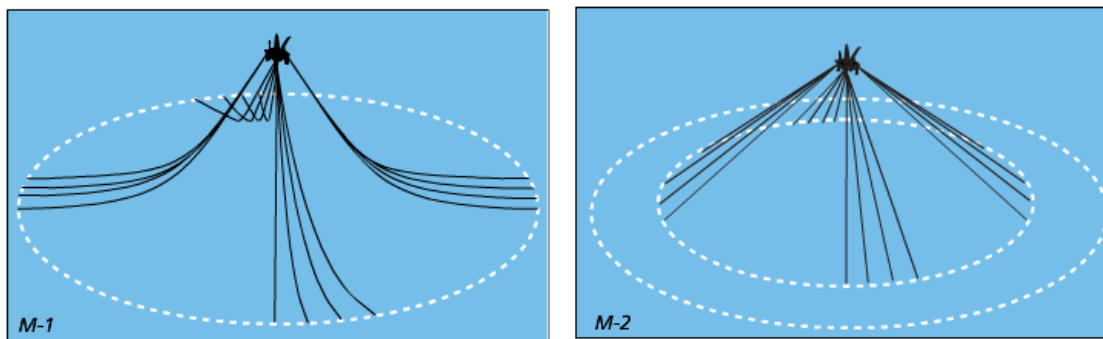
Figure 2.2: Catenary (M-1) and taut leg (M-2) mooring lines (Vryhof B.V., 2015)

Catenary mooring lines have the shape of a catenary curve between the floating platform and the mudline. The catenary systems resist most of the load by the weight of

the mooring line. Mooring lines have 8-16 separate lines connecting from the floating platform to anchors. In deep and ultra-deep water, the taut line moorings with synthetic ropes are preferred over heavy weight chains with catenary systems. The taut line mobilizes most of the restoring forces through elasticity of the line. Taut mooring lines have an angle of 30-45 degrees from the horizontal at the mudline. Taut lines improve the efficiency of the system providing better load sharing between adjacent components, improved control over offsets under steady conditions and smaller variations in tension compared to catenary mooring systems. Tension-leg platforms are moored via vertical mooring lines. Those mooring lines are tensioned taut steel cables attached to the seabed template on one side and the floating platform on the other side (Mark and Gourvenec, 2011). The main components on a mooring line are presented by Bozorgmehrian et al. (2013) on the drawing prepared by Vryhof B. V. (2015).

Components in a typical mooring line

1. wire rope
2. wire rope socket
3. swivel
4. pearlink
5. shackle
6. H-link
7. polyester rope
8. H-link
9. shackle
10. pearlink
11. swivel
12. pearlink
13. chain
14. shackle
15. anchor point

Courtesy: Vryhof Anchor
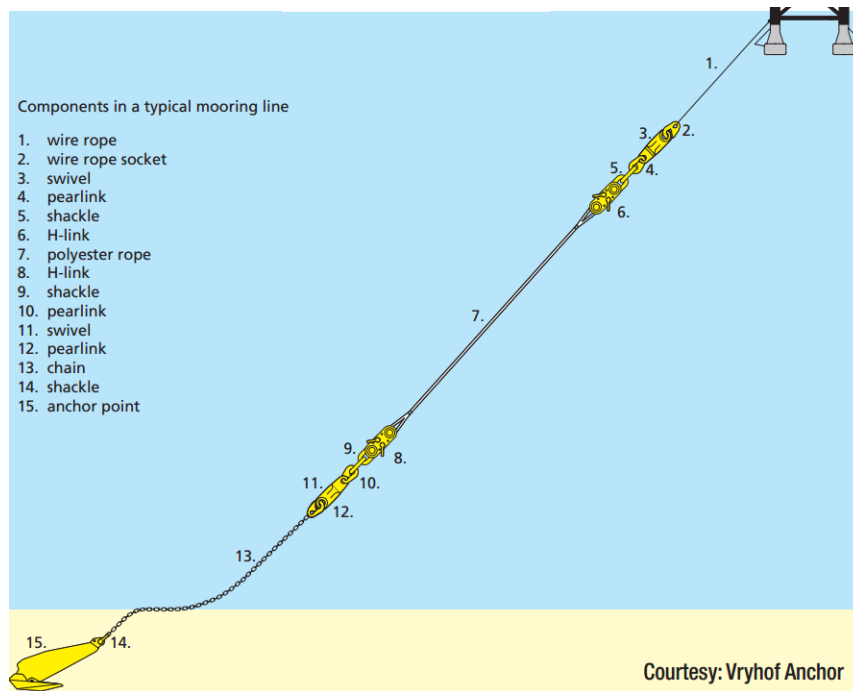
Figure 2.3: Components of a mooring line (Bozorgmehrian et al., 2013)

The design of mooring lines is important since it highly affects the anchor performance. The interaction of the mooring line with the soil determines the angle of loading on the anchor. The horizontal tensioning causes anchor line to cut and slide through soil and cause high shear forces along the line. Since some of the environmental loads transferred from the floating platform are resisted with the chain friction, this enables optimization of anchor size. The angle of the chain at the pad-eye has a significant effect on the anchor performance such that high angles at the pad-eye result in uplift forces acting on the anchor (Mark and Gourvenec, 2011).

Mooring system failures caused 17 mobile offshore drilling units (MODU's) to drift during hurricanes Ivan (2004), Katrina (2005) and Rita (2005). The anchors are designed to primarily resist loads that act within the plane of major axis (in-plane direction) of the anchor. Failure of one or more mooring lines cause remaining anchor to be loaded in out-of-plane loading directions (Gilbert et al., 2009).

2.4 OFFSHORE ANCHORS

Floating platforms are secured to seafloor by anchors attached to the platform via mooring systems. The offshore anchors are developed to support floating platforms by providing uplift resistance against the environmental loads that act on the platforms. Figure 2.4 shows a graphical illustration of the most common offshore anchor types: anchor piles, suction caissons, drag anchors, suction embedded plate anchors and dynamically penetrating anchors (Mark and Gourvenec, 2011). Plate anchors (DEA, VLA, SEPLA) and dynamically penetrating anchors are explained in this section.
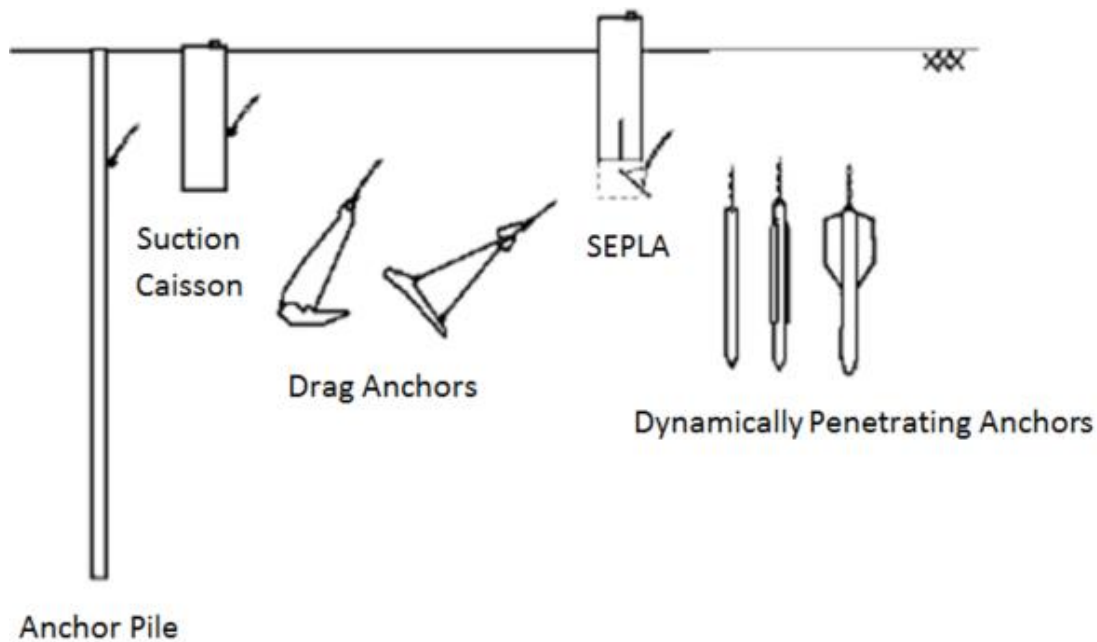
Figure 2.4: Types of embedded anchors (Mark and Gourvenec, 2011)

2.4.1 PLATE ANCHORS

Drag Embedment Anchors (DEA)

Drag embedment anchors are embedded into soil when pulled horizontally and the holding capacity is mobilized by the shear strength of the soil resisting the pullout force. The reliability, integrity and safety of the floating systems highly dependent on the performance of the drag embedment anchors (Sincock and Sondhi, 1993). The main components of a DEA are presented in Figure 2.5 (Vryhof B.V., 2015).
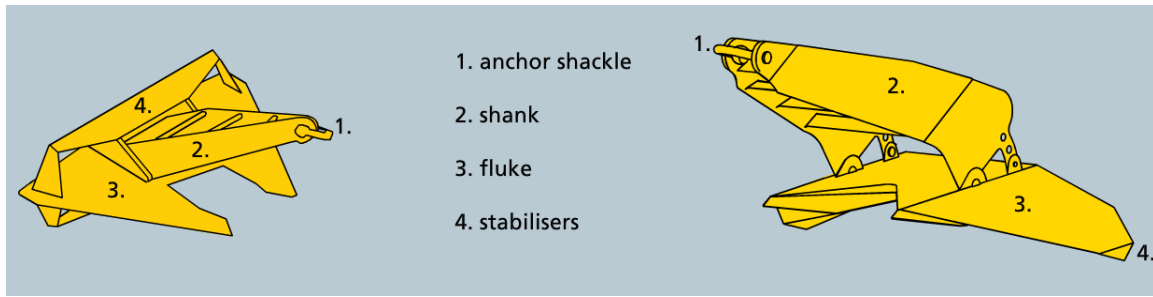
Figure 2.5: Main components of a DEA (Vryhof B.V., 2015)

Fluke is the bearing plate that provides most of the anchor capacity. Shank provides the connection between the anchor fluke and themooring line. Shank's main role is to provide drag embedment installation and it contributes to the anchor holding capacity mostly through friction around the shank surface. Mooring line is attached to the anchor shackle through pad-eye. Stabilizers are used in some anchor types for better anchor performance. DEA's can resist both horizontal and vertical loads. The angle between fluke and shank is in the range of 30-50 degrees, the lower angles are used for sand and stiff clay, the higher angles are used for soft normally consolidated clays. Using higher fluke-shank angles in normally consolidated clay provides deeper anchor embedment. Anchor dive trajectory and ultimate holding capacity are affected by the type of mooring line (DNV, 2002). The Stevpris Mk6 by Vryhof B. V., a commercially available DEA presented in Figure 2.6, has different scales with weights changing from 1.5 tons to 30 tons.

Figure 2.6: Stevpris Mk6 anchor by Vryhof B.V. (www.vryhof.com, 2016)

Vertically Loaded Anchors (VLA)

Vertically loaded anchor are plate anchors that mobilize most of its capacity by the bearing resistance of the fluke. The load is applied through a rigid shank or bridle. The anchor is initially placed on the seafloor and starts to embed into soil parallel to its fluke when loaded. As the anchor dives deeper, an activation mechanism aligns the shank or bridle arrangement so that the fluke rotates and becomes perpendicular to the loading line. This way the ultimate holding capacity of the anchor is maximized over the full fluke surface (Murff, et al., 2005). The VLA's are some of the smallest anchors used for temporary moorings. The number of anchor-handling vessel (AHV) trips can be minimized but the vessel should have additional components to apply the bollard pull required for anchor drag embedment (Zimmerman, et al., 2009). VLA's are preferred in location with water depth up to 1500 m and can be applied for ultra-deep water mooring up to 3000 m of water depth (Colliat, 2002). An example VLA anchor, Stevmanta by Vryhof B. V., is presented in Figure 2.7. The Stevmanta VLA anchor has different fluke sizes between 5-20 m^2. Another VLA anchor, Dennla with 14 m^2 fluke area by Bruce Anchor, is presented in Figure 2.8.

Figure 2.7: Stevmanta anchor by Vryhof B. V. (www.vryhof.com, 2016)

Figure 2.8: Dennla anchor by Bruce Anchors (www.bruceanchor.co.uk, 2016)

Suction Embedded Plate Anchors

Suction embedded plate anchors (SEPLAs) are used for temporary mooring of floating offshore structures in deep and ultra-deep waters. SEPLAs are able resist high loads and can be installed at a precise location (Wong, et al., 2012). SEPLAs are embedded through a suction caisson rather than drag embedment like VLAs and DEAs. Initially a suction caisson with a plate anchor is embedded under self-weight into soil until the frictional and bearing resistance of the soil is equal to the weight of the system. When the embedment stops, the vent valve on the top of caisson is turned off. The water inside the caisson is pumped out to provide deeper caisson embedment by pressure difference on top of the caisson. The plate anchor is released and the caisson is pulled up by pumping water back into the caisson. The anchor line is tensioned to rotate the anchor and the anchor reaches its ultimate orientation (Yang, et al., 2011). SEPLA by Intermoor is presented in Figure 2.9. The SEPLA installation procedure is presented in Figure 2.10.

Figure 2.9: SEPLA by Intermoor (www.intermoor.com, 2016)
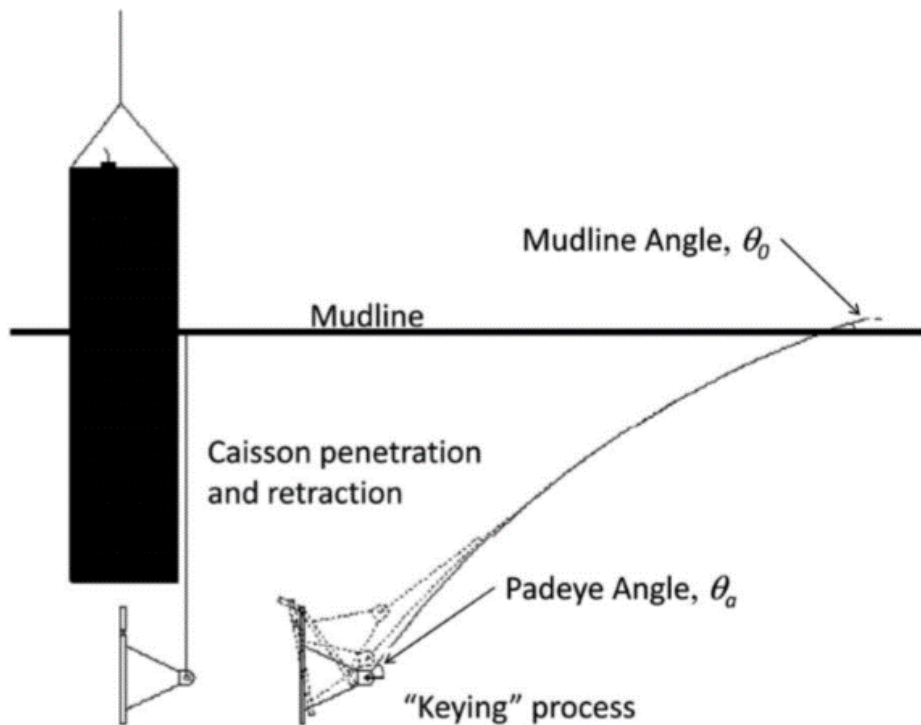
Figure 2.10: SEPLA installation (Yang et al., 2011)

2.4.2 DYNAMICALLY INSTALLED ANCHORS

Dynamically installed anchors are rocket or torpedo shaped anchors such as torpedo anchors and deep penetrating anchors (Figure 2.11). They are released from a certain height from the seafloor and penetrate into soil by the kinetic energy gained during free-fall under self-weight. The expected penetration depths are 2-3 fluke lengths and the holding capacity is 3-5 times the dry weight of the anchor in normally consolidated clay. The anchor capacity is provided by the friction along the soil-structure surface (O'Loughlin et al., 2004). Torpedo piles embed into soil easier and faster than vertically loaded plate anchors (Bonfirm de Santos et al., 2004). Torpedo anchors are developed to achieve penetration velocities between 25-35 m/s (82-115 ft/s) at the seabed. Main advantages of the dynamically installed anchors are: simple and economical fabrication, easy installation,

17

accurate positioning without any specific orientation requirements (Mark and Gourvenec, 2011). The installation procedure of dynamically penetrating anchors is presented in Figure 2.12.

Figure 2.11: Deep penetrating anchor (a) (www.deepseaanchors.com, 2016) and torpedo anchor (b) (Araujo et al., 2004)
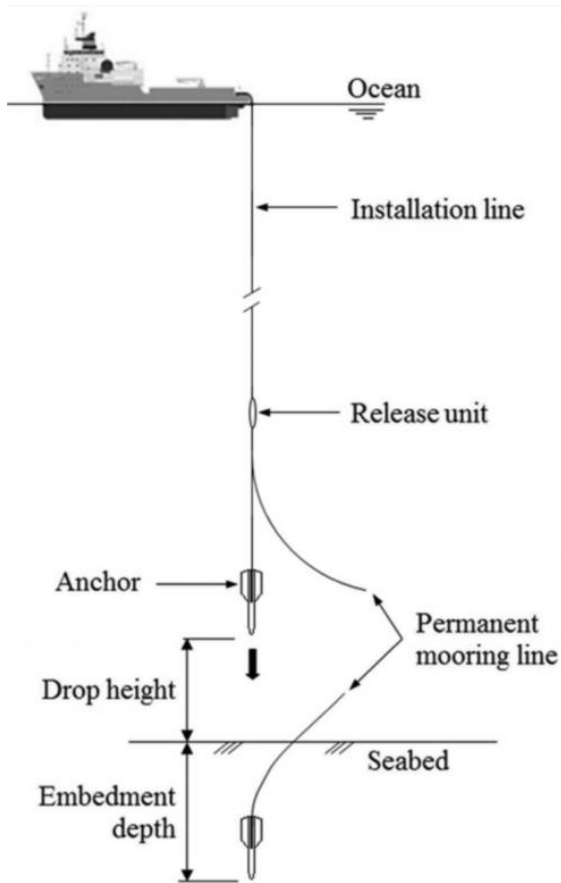
Figure 2.12: Installation procedure of dynamically installed anchors (O'Beirne et al., 2015)

The OMNI-Max anchor (Figure 2.13) is a multi-directional, self-inserting, gravity installed anchor by Delmar Systems, Inc.. The length is 32 ft (9.7 m), width is 10 ft (3 m) and weight is 84,000 lbs (38 tons) in air with fins. The OMNI-Max anchor is released from a certain height above seafloor and penetrates into soil under self-weight after free-fall. The release mechanism is controlled acoustically from the AHV. In a typical Gulf of Mexico marine clay area, the drop height of 150 ft (45 m) above the seafloor results in initial tip penetration up to 75 ft (23 m) (Shelton, 2007).

Figure 2.13: OMNI-Max anchor by Delmar Systems, Inc. (Shelton, 2007)

2.5 DESIGN PRINCIPLES OF PLATE ANCHORS

Plate anchors mobilize their ultimate holding capacity by embedding into deeper soil layers with higher strength. Design principles focus on maximizing the ultimate holding capacity. Prediction of the ultimate holding capacity highly depends on accurately predicting the anchor location and orientation. This section describes the design principles, prediction models and theoretical calculation of the anchor dive penetration and the mobilization of capacity.

2.5.1 DESIGN PRINCIPLES

The ultimate holding capacity of a plate anchor highly depends on the final embedment depth since it is a function of the soil strength around the anchor. The challenge in predicting the anchor capacity is related to the difficulties in predicting anchor installation and final penetration depth. The dive trajectory of the anchor depends on:

- Soil conditions,

- Type and size of the anchor,

- Fluke-shank angle,

- Type and size of the anchor line,

- Line angle at the mudline (Mark and Gourvenec, 2011).

Increasing the anchor fluke area or the penetration depth increases the ultimate holding capacity of the anchor. Streamlining the anchor fluke area decreases the resistance to penetrating deeper. Also preventing soil plug between shank arms reduces the anchor resistance to dive. Using a wire rope compared to chain results in deeper penetration since lateral resistance to penetration along the wire is lower than chains (Vryhof B.V., 2015). The installation behavior of drag embedded plate anchors with chains or wires is schematically presented in Figure 2.14.
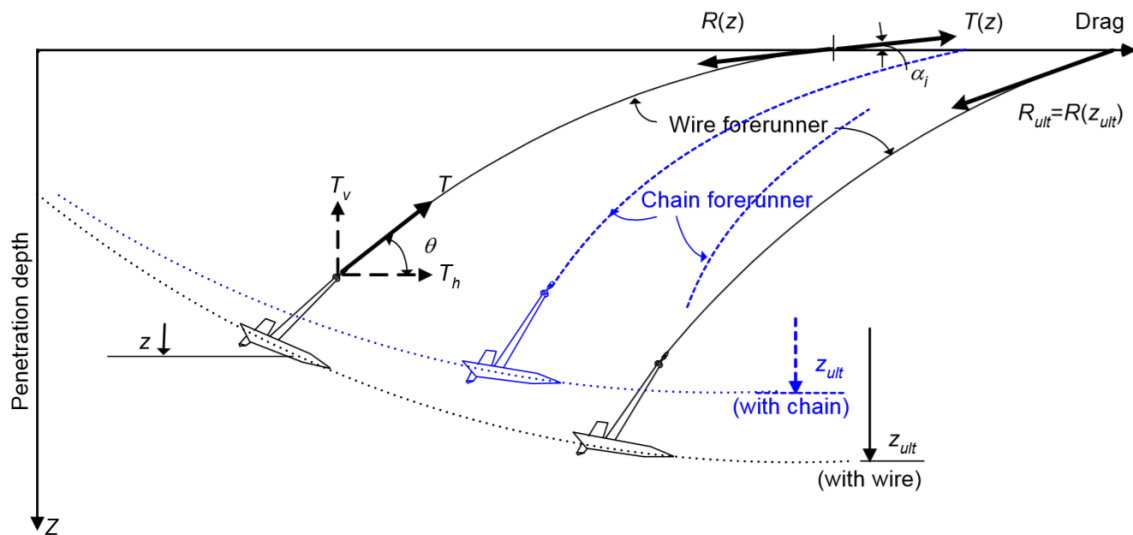
Figure 2.14: Installation of drag embedded plate anchors (DNV, 2002)

2.5.2 TYPES OF PREDICTION MODELS

The anchor trajectory and the holding capacity can be predicted by; empirical methods, limit equilibrium methods, plastic limit analysis and advanced numerical methods (Murff et al., 2005). This section describes the prediction models.

Traditional Model

Traditional approach for predicting anchor holding capacity is using empirically delivered design charts. According to the anchor manual (Vryhof B.V., 2015), the holding capacity of the anchor is described as a combination of:

- Anchor weight: A on Figure 2.15

- Weight of failure wedge: B on Figure 2.15

- Friction acting on the failure wedge along facture lines: C on Figure 2.15

- Friction between fluke surface and soil: D on Figure 2.15

- Bearing capacity of shank and mooring line: E on Figure 2.15

- Friction of the mooring line in and on the soil: E on Figure 2.15
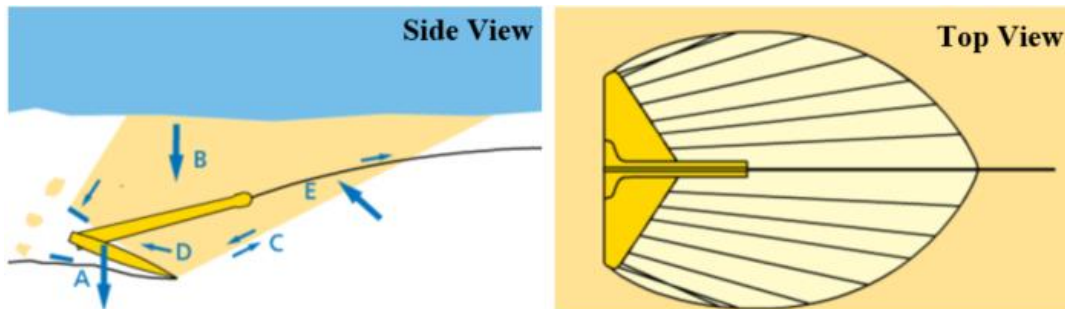
Figure 2.15: Resistances acting on an anchor system (Vryhof B.V., 2015)

An example design chart for Stevpris Mk6 (Figure 2.6) anchor by Vryhof B.V. is presented in Figure 2.16. The ultimate holding capacity of the anchor is presented with

respect to drag, penetration depth , soil type and anchor weight. Based on the test data gathered by Vryhof B. V., the ultimate holding capacity (UHC) of conventional drag embedment anchors can be calculated with respect to its weight (W) by:

$$UHC = A.W^B \ (kN) \tag{2.1}$$

The A and B coefficients for Stevin Mk3 and Stevpris Mk5 drag embedment anchors by Vryhof B. V. are presented in Table 2.1. The UHC of the anchors are generally expressed in terms of efficiency which is calculated by dividing the UHC by the anchor weight. In very soft clay, the efficiencies of 1 t and 10 t Stevpris Mk5 anchor are theoretically 40 and 33. Conventional drag embedment anchors can resist uplift loads when they are penetrated deeply into soil. In hard clays and sands, this resistance to uplift load may be small since the anchor penetrations are shallower than soft clays. Stevpris drag embedment anchors with a weight of 15 t can embed to 15-25 meters in very soft clay (Ruinen and Degenkamp, 2001).

Conventional drag embedment anchors and drag embedded vertically loaded anchors are similar in terms the mechanics of drag embedment (Murff et al., 2005). The failure mechanisms defined for vertically loaded plate anchors are shallow and deep failure. The shallow failure occurs when the anchor is embedded less than 3 fluke lengths. In this kind of failure, anchor is pulled out of soil with the soil column on it. Deep failure occurs when the anchor is embedded more than 3 fluke lengths into soil and the failure mechanism is defined as the flow of soil from the top of fluke to the bottom of fluke as the plastic failure of the soil (Ruinen and Degenkamp, 2001). An example case data for Stevmanta VLA are presented in Table 2.2.
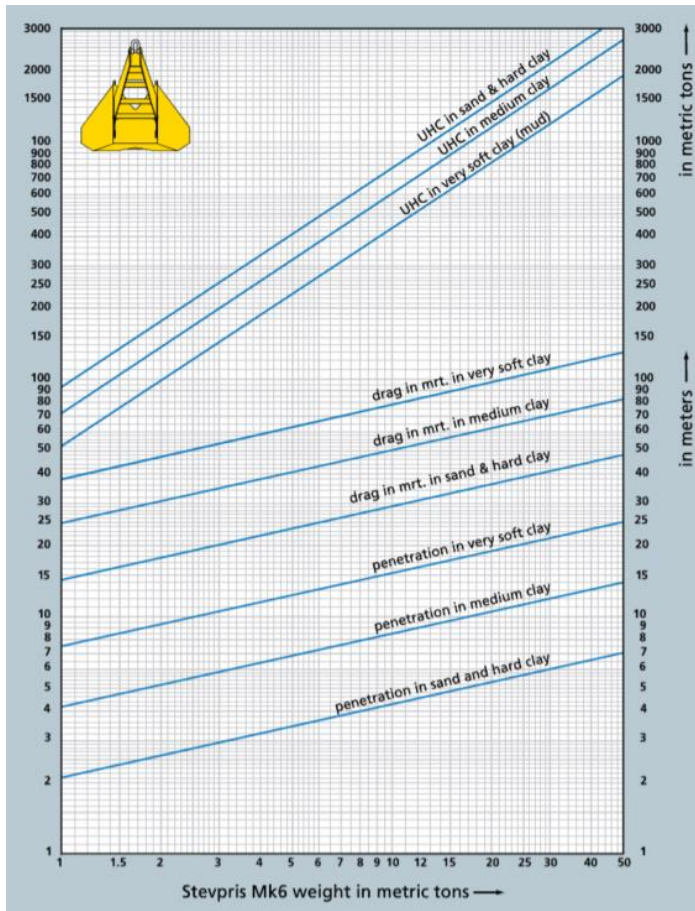
Figure 2.16: Stevpris Mk6 anchor design chart (Vryhof B.V., 2015)

Soil description	Forerunner	A for Stevin Mk3 anchor (kN^{1-B})	A for Stevpris Mk5 anchor (kN^{1-B})	B
very soft clay	chain	20	48	0.92
very soft clay	wire	20	66.3	0.92
medium clay	both	28	67	0.92
hard clay and sand	both	37	86	0.92

Table 2.1: Coefficients for calculating the UHC (Ruinen and Degenkamp, 2001)

Property	Measured Value
Required ultimate pull-out capacity	6852 kN
Anchor	11m^2 Stevmanta VLA
Installation Load	2805 kN
Penetration Depth	23.5 m
Drag Length	45 m

Table 2.2: Example VLA installation data

Limit Equilibrium Methods

Limit equilibrium methods are also used to design plate anchors. The distribution of soil forces on the anchor at failure, coupled with anchor line mechanics, are calculated incrementally. Limit equilibrium models use anchor and soil properties as calculation input (Murff et al., 2005). Neubecker and Randolph (1995) used limit equilibrium methods to calculate the forces acting on the anchor chain for incremental lengths of the chain. This model predicts the changes in chain geometry and chain angle at the attachment point with the increasing chain tension. Dahlberg (1998) used limit equilibrium models to develop a design procedure for plate anchors that takes into account the measured installation resistance, predicted contributions of the anchor line, consolidation and cyclic loading effects. Liu et al. (2012) used limit equilibrium methods to predict the movement direction of anchors with rectangular and wedge shaped flukes in cohesive and non-cohesive soils.

Plasticity Models

Plastic limit analysis are used in anchor design to minimize the failure load with respect to the geometric definition of the failure mechanism that is assumed (Murff et al., 2005). Plastic yield locus that expresses the combination of vertical, horizontal and

moment loads that result in foundation failure are used to characterize fluke failure states (Bransby and O'Neill, 1999; O'Neill et al., 2003; Murff, 1994; Martin, 1994). There are also plasticity based models that couple anchor line models with the anchor models. Aubeny and Chi (2010) developed a plasticity based model that predicts drag embedment anchor behavior in soft soils. Aubeny and Chi (2014) improved this model for vertically loaded anchors which the anchor drag embedment is achieved with a free shank.

Advanced Numerical Methods

The advanced numerical methods such as finite element methods can provide detailed solution to different aspects of anchor performance (Murff et al., 2005). Gilbert et al. (2009) used a commercial program, ABAQUS (2006) to conduct finite element analysis to model out-of-plane loading of plate anchors. Wu et al. (2016) also used finite element modeling to analyze anchor behavior under combined loading both for shallow and deep penetration depths.

The most commonly used commercially available analytical design tool for anchors is the DIGIN developed by DNV. It is calibrated with full-scale field tests, guidelines, anchor line and soil information from field tests. It is used to design drag embedded plate anchors by taking anchor-loading line- soil interactions into account (DNV, 2002).

2.5.3 CALCULATION STEPS

Anchor-Line Interactions

The Neubecker and Randolph (1995) method is an analytical solution to calculate the profile and frictional capacity of the anchor chains. For an anchor chain with inverse catenary profile attached to the anchor at a soil depth of D, tension of T_a and the line angle

of θ_a at the pad-eye (Figure 2.17) the forces acting on the chain are calculated. The tension at the mudline is T_0 and the line angle at the mudline is θ_0.
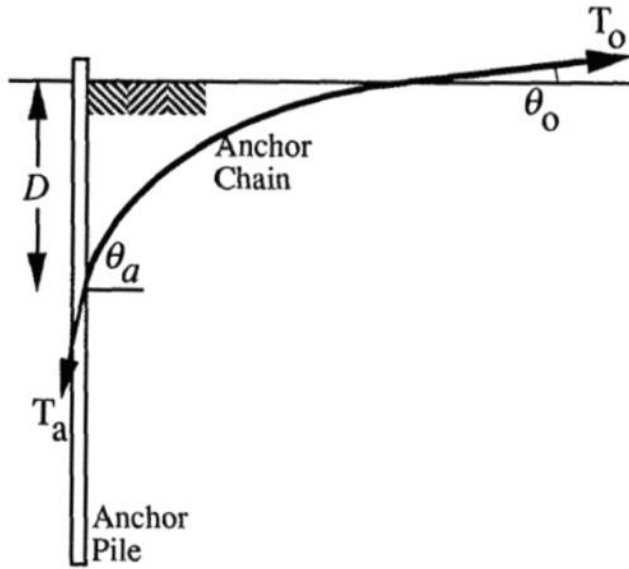
Figure 2.17: Inverse catenary shape of chain (Neubecker and Randolph, 1995)

The Neubecker and Randolph (1995) method focuses on the forces acting on a chain element presented in Figure 2.18. The forces acting on the chain element are the Q bearing resistance normal to the chain per unit length and the F friction force parallel to the chain per unit length. Q and F are calculated as:

$$Q = bN_cs_u \tag{2.2}$$

$$F = \mu Q \tag{2.3}$$

where

μ: friction coefficient (between 0.4-0.6)

27

b: effective chain width (b=2.5 d_b where d_b is the chain diameter, (Degenkamp and Dutta, 1989)

N_c: Equals to 5.1 at the mudline and increases to 7.6 at a depth of z=2.4b

s_u: the local undrained shear strength of the soil
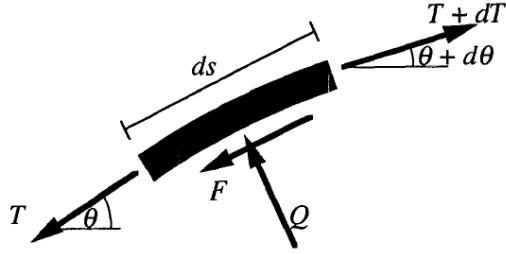
Figure 2.18: Force equilibrium of chain element (Neubecker and Randolph, 1995)

Assuming θ_0 equals to zero, the anchor chain angle at the pad-eye (θ_a) and the tension at the pad-eye (T_a) can be calculated by:

$$\theta_a = \sqrt{\frac{2D\overline{Q}}{T_a}} \tag{2.4}$$

$$\frac{T_0}{T_a} = e^{\mu\theta_a} \tag{2.5}$$

Where $\overline{Q}$ is the average bearing resistance over the depth range $0 \leq z \leq D$. The chain profile is defined in terms of normalized depth z*=z/D and normalized horizontal distance from the anchor x*=x/D. Assuming a constant soil strength profile, the chain profile is calculated by Equation 2.6 and for linearly increasing soil strength profile, the chain profile is calculated by Equation 2.7. The normalized chain tension (T*) is calculated as T*=T_a/D$\overline{Q}$.

$$z^* = \left(1 - \frac{x^*}{\sqrt{2T^*}}\right)$$ (2.6)

$$z^* = e^{-x^*\theta_a}$$ (2.7)

This solution method ignores the anchor chain weight. The effective bearing resistance Q_{eff} can be calculated by subtracting the chain weight, W, from Q to account for chain weight in the calculations (Neubecker and Randolph, 1995). Aubeny and Chi (2014) improved the model developed by Neubecker and Randolph (1995) to account for the normally consolidated soil deposits with nonzero mudline strength (s_{u0}) with the strength gradient of k, for the anchor system and undrained shear strength profile presented in Figure 2.19.

Figure 2.19: Definition sketch for the Aubeny and Chi (2014) model

By using the Aubeny and Chi (2014) model, the normalized horizontal coordinate (x*) of the loading line for a given tension of T_a at the pad-eye and an angle of θ_0 at the mudline, is calculated by:

$$x^* = \sqrt{\frac{1}{2Q_2}} \ln\left[\frac{Q_2 + \frac{Q_1}{2} + \sqrt{Q_2^2 + Q_1 Q_2 + \frac{Q_2 \theta_0^2}{2}}}{Q_2 z^2 + \frac{Q_1}{2} + \sqrt{Q_2^2 (z^*)^2 + Q_1 Q_2 z^* + \frac{Q_2 \theta_0^2}{2}}}\right] \tag{2.8}$$

where:

x^*: normalized horizontal coordinate (x/z_a)

z^*: normalized vertical coordinate (z/z_a)

z_a: depth of pad-eye below mudline

x, z: horizontal, vertical coordinates

Q_1: normalized soil resistance due to mudline strength $(Q_1 = E_n N_c s_{u0} z_a / T_a)$

Q_2: normalized soil resistance due to soil strength gradient $(Q_2 = E_n N_c b k z_a^2 / 2T_a)$

E_n: chain multiplier

N_c: bearing capacity factor for the anchor line

b: anchor line diameter

s_{u0}: soil strength at the mudline

k: soil strength gradient

T_a: anchor line tension at the pad-eye

θ_0: loading line angle from horizontal at the mudline

Equilibrium of Forces acting on the Anchor during Dive Penetration

The assumption of anchor movement is parallel to its fluke during dive penetration is accepted by many researchers (Dunnavant and Kwan 1993; Neubecker and Randolph

30

1996, Yang et al. 2010, Liu et al. 2012, etc.). The bearing and shear forces acting on the anchor during dive penetration are calculated by calculating the soil pressures acting on different elements of the anchor using bearing capacity equations. The mechanical model developed by Neubecker and Randolph (1996) calculates the geotechnical resisting force of the anchor parallel to the direction of movement by:

$$T_p = fA_PN_cs_u \tag{2.9}$$

where A_p is the projected area, N_c is the bearing capacity factor, s_u is the undrained shear strength of the local soil and f is the form factor of the anchor (Neubecker and Randolph, 1996).

The mechanical model developed by Liu et al. (2012) is based on the Neubecker and Randolph (1996) model, and calculates the equilibrium forces acting on the anchor. The equilibrium forces acting on the drag anchor are presented in Figure 2.20. T_a is the drag force at the pad-eye, T_m and T_n are the components parallel to movement direction and normal to movement direction. W is the submerged weight of the anchor with the components of W_m parallel to movement direction and W_n normal to movement direction. F_{bs} and F_{bf} are the bearing resistances of shank and fluke. F_{ss} and F_{sf} are the shearing resistances of shank and fluke. The angles measured from the top surface of the fluke are: θ_a is the angle of the loading line at the pad-eye, θ_s is the shank angle and θ_m is the angle of movement direction. The force equilibrium in the movement direction is achieved by:

$$F_b = F_{bs} + F_{bf} \tag{2.10}$$

$$F_s = F_{ss} + F_{sf} \tag{2.11}$$

31

$$T_m + W_m = F_b + F_s \tag{2.12}$$

$$F_b = N_c s_u A_b \tag{2.13}$$

$$F_s = \alpha s_u A_s \tag{2.14}$$

Where N_c is the bearing capacity factor, A_b is the effective bearing area, α is the adhesion factor, A_s is the effective shearing area and s_u is the undrained shear strength of the soil. The drag force at the pad-eye is calculated by:

$$T_a = \frac{1}{\cos(\theta_a - \theta_m)}[F_b + F_s - W\sin(\theta_0 - \theta_m)] \tag{2.15}$$
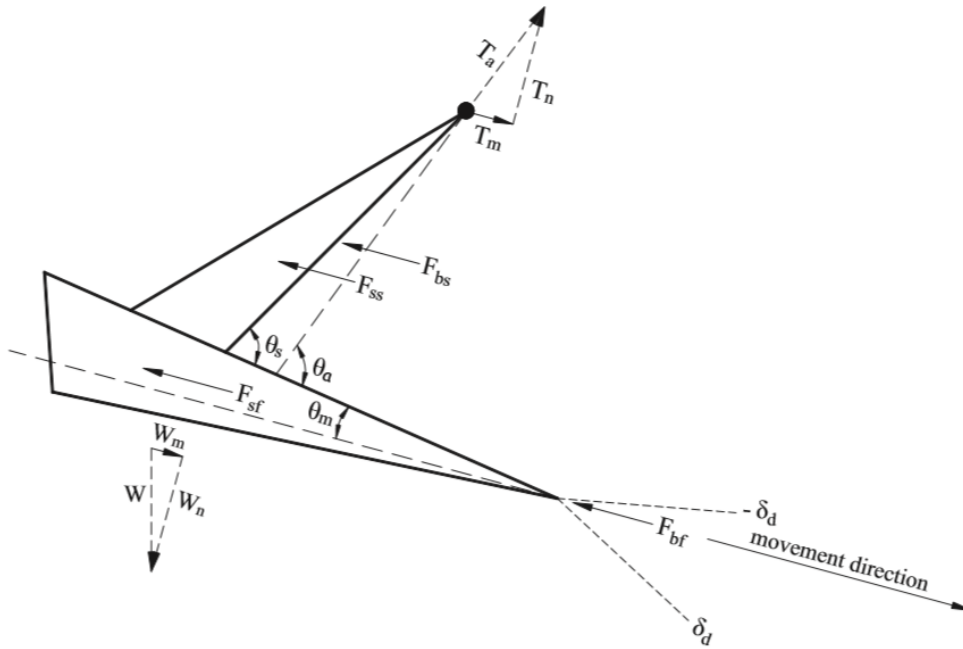
Figure 2.20: Mechanical model of a drag anchor by Liu et al. (2012)

Yield Locus

Plasticity models are used to calculate anchor-soil interactions under combined loading. The plasticity model developed by O'Neill et al., (2003) focuses on the drag embedment anchor-undrained soil interactions during failure. The resulting associated plastic failure locus for combined loading is used to calculate relative plastic displacements during failure. The plastic yield surface of a foundation shows the combination of normal, shear and moment loads that causes foundation failure. The yield locus is mathematically described by $f (V, M, H) = 0$ for the combination of V vertical, M moment and H shear load. The limit-analysis relationship originally developed by Murff (1994) for shallow foundations was adapted to plate anchors by a number of researches. This relationship for the yield locus is:

$$f = (N_n/N_{n,max})^q + [(N_m/N_{m,max})^m + (N_s/N_{s,max})^n]^{(1/p)} - 1 = 0 \qquad (2.16)$$

where $N_{n,max}$, $N_{s,max}$ and $N_{m,max}$ are the bearing capacity factors under conditions of pure loading; and N_n, N_s and N_m are the bearing factors under the particular condition of combined loading; n, m, p, q are the interaction coefficients. The interaction coefficients derived from finite element studies for plane strain analysis are presented in Table 2.3.

Parameter	Bransby and O'Neill (1999)	Elkhatib and Randolph (2005)	Murff, et al. (2005)	Gilbert, et al., (2009)	Yang, et al. (2010)	Wu, et al., 2016
$N_{n,max}$	11.87	11.93		12.0	11.98	12.1
$N_{s,max}$	4.29	4.65		2.25+2(7.5)(t/L) (t: thickness, L: length)	4.39	4.65
$N_{m,max}$	1.49	1.63		1.56	1.645	1.67
m	1.26	2.58	1.56	1.56	1.56	1.35
n	3.72	3.74	4.19	4.19	4.19	3.11
p	1.09	1.09	1.57	1.57	1.57	1.38
q	3.16	1.74	4.43	4.43	4.43	4.3

Table 2.3: Interaction coefficients for strip footing

One of the major differences in VLA and DEA performance during drag embedment is the shank behavior. While DEAs have fixed shank, the VLA shank gets free to rotate at a certain stage during embedment. The plasticity solution proposed by Aubeny and Chi (2014) focuses on the VLA dive trajectory assuming the shank is fixed like a DEA during the initial dive trajectory and becomes free to rotate after a certain embedment. This model is an extension of the model proposed for drag embedment anchors by Aubeny and Chi (2010).

The equivalent non-dimensional yield capacity during dive penetration (N_e) and the non-dimensional yield capacities in normal, tangential and moment under combined

loading were normalized by the fluke area and the undrained shear strength of the soil (Aubeny and Chi, 2014). By writing N_n, N_s and N_m in terms of N_e:

$$N_e = \frac{T_a}{s_u A_f} \tag{2.17}$$

$$N_n = \frac{T_a}{s_u A_f} \sin \theta_a = N_e c_1 \tag{2.18}$$

$$N_s = \frac{T_a}{s_u A_f} \cos \theta_a = N_e c_2 \tag{2.19}$$

$$N_m = \frac{M}{s_u A_f L_f} [e_t \sin\theta_a - e_n \cos\theta_a] = N_e c_3 \tag{2.20}$$

where:

T_a: load acting on the anchor pad-eye

M: moment loading

e: eccentricity of the line load

s_u: undrained shear strength

A_f: fluke area

L_f: fluke length

The coefficients c_1, c_2 and c_3 are functions of N_e and the angle of line force relative to the orientation of the shank for a drag embedment anchor. The interaction between normal, shear and moment loading can be expressed by rewriting Equation 2.16 by using Equations 2.17-2.20 as:

$$f = \left(\frac{|c_1|N_e}{N_{n,max}}\right)^q + \left[\left(\frac{|c_3|N_e}{N_{m,max}}\right)^m + \left(\frac{|c_2|N_e}{N_{t,max}}\right)^n\right]^{1/p} - 1 \qquad (2.21)$$

Fluke Movement

The relative plastic displacements in vertical (δv), horizontal (δh) and rotational ($\delta \beta$) directions can be calculated from the plastic yield locus for foundation failure (O'Neill, et al., 2003). Chen (1975) showed that if the soil surrounding an element is following the condition of normality (associated flow: plastic flow with no change in volume), then the normality is applicable to overall foundation yield locus. Due to assumption of associated flow, O'Neill et al. (2003) stated that for the undrained failure conditions which soil remains attached to the foundation, the ratio of plastic displacements at failure is defined by the gradient of the yield locus. It is assumed that the anchor is deeply embedded thus soil failure is fully constrained and the local to the anchor fluke. It shows that the failure loads will be independent of the anchor orientation The yield locus presented in Figure 2.21(a) shows how the relative magnitudes of horizontal and vertical plastic displacements are calculated for the embedded footing presented in Figure 2.21(b) (O'Neill et al., 2003).

(a) H-V yield locus, M = 0   (b) Embedded footing
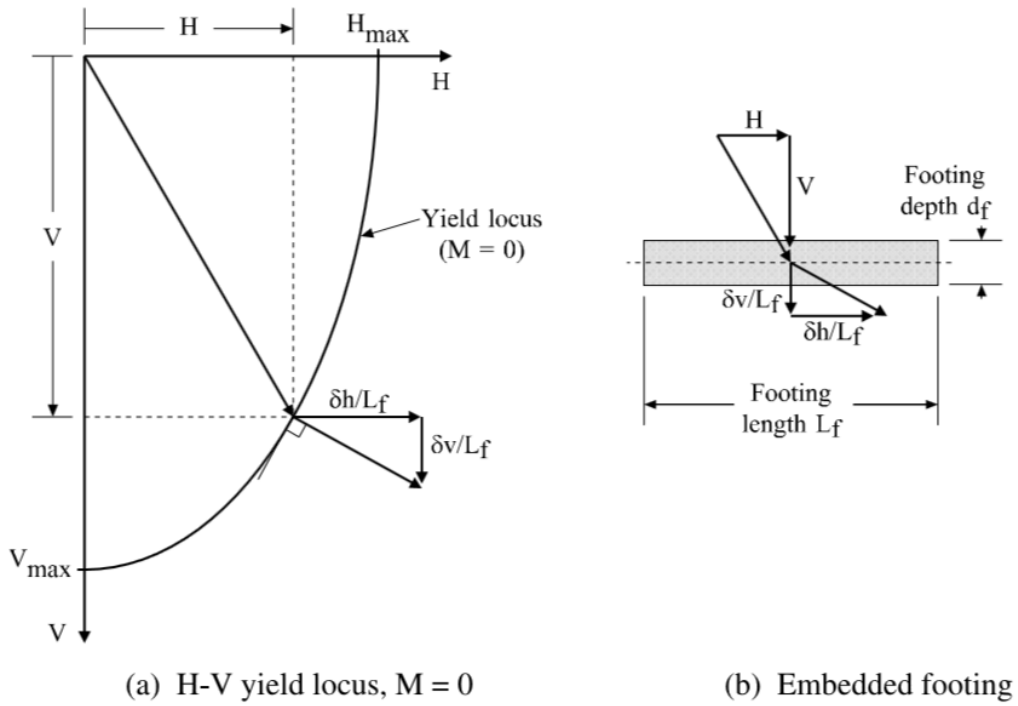
Figure 2.21: The yield locus and plastic potential function, by O'Neill et al. (2003)

For a weightless anchor presented in Figure 2.22, direction of fluke displacement at failure can be predicted from the yield locus. Shank forces do not affect anchor kinematics and elastic displacements are negligible (O'Neill et al., 2003).
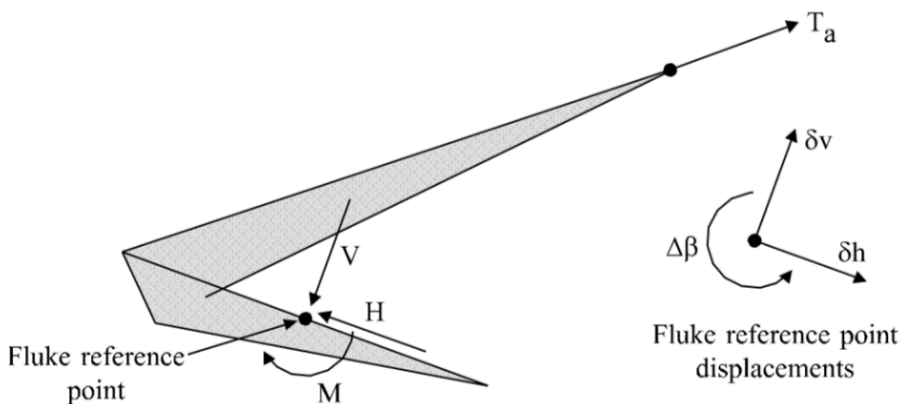
Figure 2.22: Loads and displacements at failure (O'Neill et al., 2003)

Due to assumption of associated flow, the direction of the fluke movement is normal to the plastic yield locus at a given load condition (normal, shear and moment). For an anchor fluke with the fluke length of L_f, the equilibrium solutions by O'Neill, et al. (2003) are:

$$\frac{\delta v}{\delta h} = \frac{\delta f}{\delta V} \Big/ \frac{\delta f}{\delta H} \tag{2.22}$$

$$\frac{\delta \beta}{\delta h / L_f} = \frac{\delta f}{\delta (M/L_f)} \Big/ \frac{\delta f}{\delta H} \tag{2.23}$$

Assuming the fluke incremental displacement in the direction parallel to fluke face is Δh, O'Neill et al. (2003) model calculates the incremental displacement perpendicular to the fluke face (Δv) and fluke rotation about the reference point $\Delta \beta$ by:

$$\Delta v = \left(\frac{\delta f}{\delta V} \Big/ \frac{\delta f}{\delta H} \right) \Delta h \tag{2.24}$$

$$\Delta \beta = \left[\frac{\delta f}{\delta (M/L_f)} \Big/ \frac{\delta f}{\delta H} \right] \frac{\Delta h}{L_f} \tag{2.25}$$

The Aubeny and Chi (2014) model calculates the ratio of rotation to tangential translation (R_{rt}) and the ratio of normal to tangential motion (R_{nt}) for a VLA anchor by:

$$R_{rt} = \frac{c_3}{|c_3|} \frac{m}{n} \frac{N_{t,max}}{N_{n,max}} \frac{\left(|N_m| / N_{m,max} \right)^{m-1}}{\left(|N_s| / N_{s,max} \right)^{n-1}} \tag{2.26}$$

$$R_{nt} = \frac{\left(\frac{N_{t,max}}{N_{n,max}} \right) \left(\frac{pq}{n} \right)}{\left[\left(\left| \frac{N_m}{N_{m,max}} \right| \right)^m + \left(\left| \frac{N_t}{N_{m,max}} \right| \right)^m \right]^{\left(\frac{1}{p} \right)-1}} \frac{\left(\left| \frac{N_n}{N_{n,max}} \right| \right)^{q-1}}{\left(\left| \frac{N_t}{N_{t,max}} \right| \right)^{n-1}} \tag{2.27}$$

An example calculation of R_{nt} with the fluke-line angle for the DEA and VLA anchors are presented in Figure 2.23.
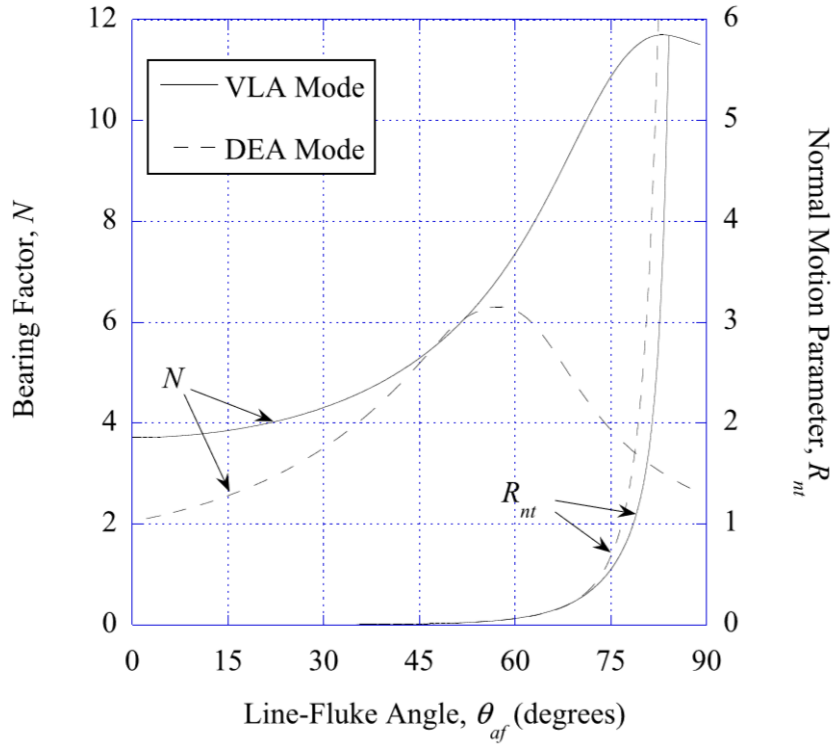
Figure 2.23: R_{nt} calculation (Aubeny and Chi, 2014)

The Aubeny and Chi (2014) model predicts the VLA penetration with a free-shank by assuming a fluke displacement of Δs in the direction of fluke plane, fluke angle of θ_f from horizontal; and calculating the horizontal (Δx) and vertical (Δz) displacements by:

$$\Delta x = \Delta s \left(\cos \theta_f + R_{nt} \sin \theta_f \right)$$

(2.28)

$$\Delta z = \Delta s \left(\sin \theta_f - R_{nt} \cos \theta_f \right)$$

(2.29)

By calculating Δx and Δz, the horizontal and vertical coordinates of the anchor dive trajectory can be calculated. If anchor penetration depth is predicted accurately, the ultimate holding capacity can be calculated using the undrained soil strength of the soil around the anchor at the final embedment depth.

2.6 DESIGN PRINCIPLES OF DYNAMICALLY INSTALLED ANCHORS

The main criteria for designing the dynamically installed anchor is to predict anchor embedment depth accurately. The penetration resistance is highly dependent on the drag resistance during free-fall through water and the viscous-enhanced shear resistance as the anchor penetration into soil starts. Experimental testing and analytical modeling methods are used by researchers to develop relationships between impact velocities, penetration depths and holding capacities (Mark and Gourvenec, 2011).

Audibert et al. (2006) performed laboratory model experiments to calibrate the penetration prediction model. The details of this laboratory model experiments with 1:30 scale torpedo anchor model is presented in Gilbert et al. (2008). The numerical modeling methods are also used to predict the resisting forces on the anchor. The analytical model developed by True (1976) to simulate penetration of vertical projectiles into seafloor under undrained conditions (Equation 2.1). The Morrison's equation (Morrison et al., 1950) is used to calculate the drag force acting on the anchor through free-fall in water. The Morrison's equation (Morrison et al., 1950) is used to calculate the drag force acting on the anchor (Equation 2.4).

$$m \frac{d^2 z}{dt^2} = W_s - F_{drag} - F_{friction} - F_{bearing} \tag{2.30}$$

$$F_{friction} = \alpha s_{u,remolded} A_{shear} \tag{2.31}$$

$$F_{bearing} = N_c s_{u,undisturbed} A_{bearing} \tag{2.32}$$

$$F_{drag} = \frac{1}{2} c_d \rho_{fluid} A_{end} v^2 \tag{2.33}$$

where m is the anchor mass, z is the penetration depth, t is time, W_s is the submerged anchor weight, α is the side shear factor, $s_{u,remolded}$ and $s_{u,undisturbed}$ are the remolded and undisturbed undrained shear strengths of soil respectively, A_{shear} is the anchor area acting in shear and $A_{bearing}$ is the anchor area acting in bearing, c_d is the coefficient of drag, ρ_{fluid} is the density of the salty water, A_{end} is the anchor projected area that the drag force is applied to and v is the anchor velocity at that particular time. The predictions were +/- 10 % of the measured test results (Gilbert et al., 2008).

O'Loughlin et al. (2004) performed centrifuge model tests to evaluate dynamically installed anchor performance. Anchor models with a scale of 1:200 were tested in kaolinite test bed. Installation and holding capacity tests were performed at 200 g. Seabed velocities up to 30 m/s and tip penetrations of 3 anchor lengths were measured in the model tests.

Raie and Tassoulas (2009) developed a computational fluid dynamics (CFD) model to predict resisting forces, embedment depth, pressure and shear distributions on the soil-torpedo anchor interface and in the soil. The commercially available software, FLUENT, was used to analyze moving objects in multiphase domain using the finite-volume method. The soil is modeled as a viscous fluid. The results of the CFD procedure were comparable to laboratory scale and field scale torpedo anchor embedment depths.

After the initial embedment, anchor set-up increases the holding capacity as the shear strength of the soil is recovered with consolidation (Mark ad Gourvenec, 2011).

2.7 SCALING RELATIONSHIPS

It is expensive and difficult to run field tests using prototype anchors. The experimental results obtained by scaled model laboratory tests should be considered in the context of scaling relationships to develop an accurate understanding of prototype anchor performance based on the scaled model test results.

According to the principles of similarity, if anchors with constant shape and form are tested in the same soil with consistent properties, the results obtained from both tests can be related with a simple relationship. If two anchors have the ratio of x between their characteristic lengths such as $L_1/L_2=x$, weight varies with x^3, area varies with x^2 and stresses due to anchor weight vary by x. Assuming a constant unit weight of soil, the similarity applies if the soil strength also increases in the same way. This indicates that the similarity applies in cohesionless soils having a constant drained friction angle or cohesive soils having an undrained shear strength proportional to depth.

Anchor efficiency is defined as the ratio to the anchor weight in air. Design charts consider the overall system capacity as the holding capacity, accounting for the contribution of mooring line resistance as well. If the mooring line/chain is not scaled linearly with the scale of the anchor, assessing the anchor efficiency by scaling becomes questionable. Studies show that the chain and anchors are not in strict similarity (Craig, 1994).

Neubecker and Randolph (1995) analyzed the scaling relationships for drag anchors considering the effects of anchor chain. Anchor design charts are usually prepared by extrapolating from the holding capacity of small anchors by:

$$T_{ult} = T_1 \left(\frac{W}{W_1}\right)^n \tag{2.34}$$

The n value represents the reduction in anchor efficiency with increasing anchor size or weight (Craig, 1994). The n value is between 2/3 to 1. The n value proposed by the U.S. Naval Civil Engineering Laboratory is 0.92 for most of the anchors in soft soil (NCEL, 1987). Neubecker and Randolph (1995) applied scaling relationship to anchor-chain systems. For theoretical derivation of n, the s_u for a soil profile that increases with depth can be written assuming a reference depth of z_0 as:

$$s_u = s \left(\frac{z}{z_0}\right)^{\alpha} \tag{2.35}$$

When the undrained shear strength of the soil is proportional to depth α is 1 and n is 0.83. When the undrained shear strength of the soil is constant with depth, α is 0 and n is 0.67. Fluke area is proportional to the square of anchor dimensions and it is proportional to $W^{2/3}$. At a known depth D, the anchor capacity is proportional to the depth and 2/3rd of the anchor weight as:

$$T_a \propto D^{\alpha} W^{2/3} \tag{2.36}$$

When anchor line is considered, the ultimate capacity of the anchor is proportional to the average bearing resistance of the chain over a depth of $0 \le z \le D$. Assuming an effective chain width of b:

$$T_a \propto D^{\alpha} \bar{Q} \propto b D^{1+\alpha} \tag{2.37}$$

The theoretical value of the n is derived as:

$$n = \frac{4(1+\alpha)}{3(2+\alpha)}$$ (2.38)

Neubecker and Randolph (1995) showed that for any type of given soil, the anchor holding capacity varies with anchor size. The effect of anchor chain size is important when extrapolating results from small anchors.

Anchor manufacturers also present scale influence. For an anchor with characteristic length of L, the scaling influence table prepared by Vryhof B.V. for geometrically proportional anchors is presented in Table 2.4.

Property	Model	Prototype	Related to Weight
Length	L	n	$W^{1/3}$
Fluke area	A	n^2	$W^{2/3}$
Weight	W	n^3	W
Penetration	P	n	$W^{1/3}$
Moment	M	n^4	$W^{4/3}$
Moment of Inertia	I	n^4	$W^{4/3}$
Section Modulus	S	n^3	W
Bending Stress	M/S	$n^4/n^3=n$	$W^{1/3}$
Shear Strength	F/A	$n^3/n^2=n$	$W^{1/3}$

Table 2.4: Scale influence (Vryhof B.V., 2015)

2.8 CONCLUSIONS

This chapter presented information about the offshore structures. The deep-water offshore wind turbines will be constructed on floating platforms moored to foundation system by the chains, wire ropes or synthetic fiber ropes. The catenary mooring lines resist horizontal loads while taut mooring lines resist both horizontal and vertical loads thus increase the efficiency of the system.

The floating platforms are moored to foundation systems known as offshore anchors. Main anchor types are anchor piles, suction caissons, drag anchors, suction embedded plate anchors and dynamically installed anchors. The plate anchors and dynamically installed anchors are explained in details since the new offshore concept attributes to the best aspects of both systems. The plate anchors mobilize most of the holding capacity through bearing of the plate while dynamically installed anchors mobilize most of the holding capacity through friction along the anchor surface. The dynamically installed anchors are installed by free-fall penetration while plate anchors are installed with drag embedment (DEA, VLA) or through a suction caisson (SEPLA).

Design principles of offshore anchors are based on maximizing the ultimate holding capacity. Predicting the ultimate holding capacity of plate anchors highly depend on accurately predicting anchor location and orientation. Prediction models developed for plate anchors are: traditional models, limit equilibrium models, plasticity models and advanced numerical methods. The coupled anchor-loading line-soil analysis and calculations steps are explained in details. The ultimate holding capacity predictions for the dynamically installed anchors highly depend on predicting the anchor embedment depth. Drag forces during free-fall penetration and soil resistance during penetration into soil are calculated to estimate anchor depth after free-fall. Scaled model laboratory and

field tests, centrifuge tests, computational fluid dynamic analysis are used to predict the ultimate holding capacity of dynamically installed anchors.

The scaling relationships are presented to give insight about how scaled testing model results can be used to predict prototype anchor performance. If anchors with constant shape and form are tested in same soil with consistent properties, the results obtained from both tests can be related with a simple relationship. The anchor capacity is presented in terms of anchor efficiency. Both anchor holding capacity and the mooring line holding capacity contribute to the efficiency of the anchor. However, the mooring lines and anchors are not strict in similarity. The theoretical calculations and design charts are developed to account for difference in scaling of the anchor and the mooring line to predict prototype anchor capacity using the scaled model testing.

Chapter 3: Experimental Testing Facility

3.1 INTRODUCTION AND OBJECTIVES

The objective of this chapter is to present information about the experimental testing facility, testing equipment and setups. The experimental testing facility used for the scaled model anchor testing is located in J. J. Pickle Research Campus of The University of Texas at Austin. This facility (Figure 3.1) was previously described by El-Sherbiny (2005), Chen (2013), and Huang (2015).

Figure 3.1: Experimental Testing Facility

3.2 SOIL TEST BEDS

Soil test beds of kaolinite and Gulf of Mexico marine clay were used in this study. Two steel tanks with dimensions of 8 ft in length, 4 ft in width and 6 ft in height, thermoplastic tanks with dimensions of 12 ft in length, 4 ft in width and 3 ft in height and 4 ft in length, 2 ft in width and 2 ft in height (100-gal volume) were used to store and prepare soil test beds. The steel tanks contain normally consolidated kaolinite (Tank 1, Figure 3.2) and over consolidated kaolinite (Tank 2, Figure 3.2). The kaolinite soil test beds were prepared by mixing the dry kaolinite with fresh water. The kaolinite soil test bed

was prepared by mixing the white pulverized kaolinite from Dry Branch Kaolin Company with a mean particle size of 0.7 μm, specific gravity of 2.58, liquid limit ranging between 54-58 % and the plasticity index ranging between 20-26 % with fresh water (El-Sherbiny, 2005). The kaolinite was used for experimental testing due to its high coefficient of consolidation, low compressibility and its workability (Chen C.-H. , 2013). The normally consolidated kaolinite test bed was previously prepared by El-Sherbiny (2005) by mixing the kaolinite at different water contents and placing in layers that forms a linearly increasing soil strength profile. The water content and undrained shear strength relationships obtained from a normally consolidated kaolinite soil test bed (Figure 3.3) prepared by the consolidation of slurry under its own weight (Lee, 2008) was used to estimate target water contents.

Figure 3.2: Kaolinite Test Beds (El-Sherbiny, 2005)
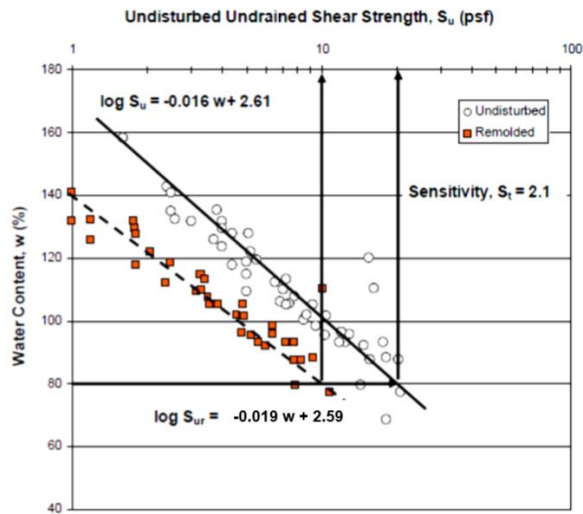
Figure 3.3: Water Content versus Undrained Shear Strength of the Kaolinite (Lee, 2008)

The thermoplastic tanks shown in Figure 3.4 were prepared by mixing Gulf of Mexico marine clay with 35 g/lt water that represents the saltine level of ocean water in Gulf of Mexico (Horan, 2012). The Gulf of Mexico marine clay soil test bed was prepared by mixing Gulf of Mexico marine clay samples obtained from different locations in Gulf of Mexico. The specific gravity of the Gulf of Mexico marine clay is measured as 2.75, the liquid limit as 105 % and the plasticity index as 62 %. A soil barrel with dimensions of 1.6 ft in diameter and 2.6 ft in height was used to remold the soil and prepare remolded soil test beds.

Figure 3.4: Gulf of Mexico Marine Clay Test Beds

The undrained shear strength of the soil profile was measured before testing by an in-situ t-bar test (El-Sherbiny, 2005). The t-bar testing device consists of an acrylic rod with 1 inch in diameter and 4 inch in length, inserted into a loading rod (Figure 3.5). The t-bar is inserted into the soil by pushing the rod at a constant rate of 0.8 in/sec (20 mm/sec) with the help of weights attached on top of the insertion rod. The load cell attached on the other side of the insertion rod records the insertion resistance (Figure 3.6).
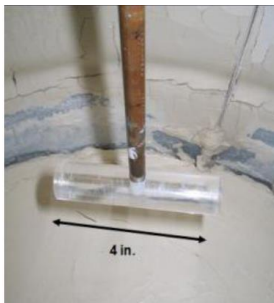
Figure 3.5: Acrylic t-bar and insertion rod (Gilbert et al. 2012)
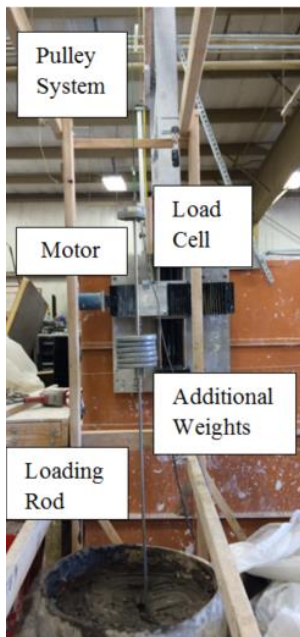
Figure 3.6: T-Bar test in progress

A separate insertion test is conducted by removing the acrylic rod and only measuring the friction and bearing resistance of the insertion rod. The soil resistance acting on the insertion rod is subtracted from the t-bar measurement to calculate the soil resistance acting on the acrylic rod. The undrained shear strength, s_u, was calculated by (Gilbert et al. 2012 and El-Sherbiny 2005):

$$s_u = \frac{(F_{total} - F_{rod})}{N_c \times A} \tag{3.1}$$

Where

F_{total}: total measured resistance during t-bar insertion,

F_{rod}: rod resistance (measured by the separate penetration test)

A: projected t-bar area (4 in^2= 2580 mm^2)

N_c: bearing capacity factor for t-bar which is 10.5 (Stewart and Randolph 1994)

Remolded soil test beds were prepared by mixing the soil by using a steel paddle attached to a drill. For preparing soil test beds with sensitivity greater than one, the soil test bed was initially remolded and left undisturbed for couple of days to weeks. All 3 cycles of the t-bar test conducted at the same location resulted in the same strength profile. For calculating the soil sensitivity, the t-bar test was conducted at least for 4-6 cycles at the same location. It was measured that 4-6 cycles of penetration resulted in an asymptotic value, which is assumed as the residual strength. The soil sensitivity is calculated as the ratio of the undisturbed undrained shear strength to the remolded undrained shear strength (El-Sherbiny, 2005). Example strength profiles of remolded soil test bed and a soil test bed with sensitivity greater than one are presented in Figure 3.7 and Figure 3.8 respectively.
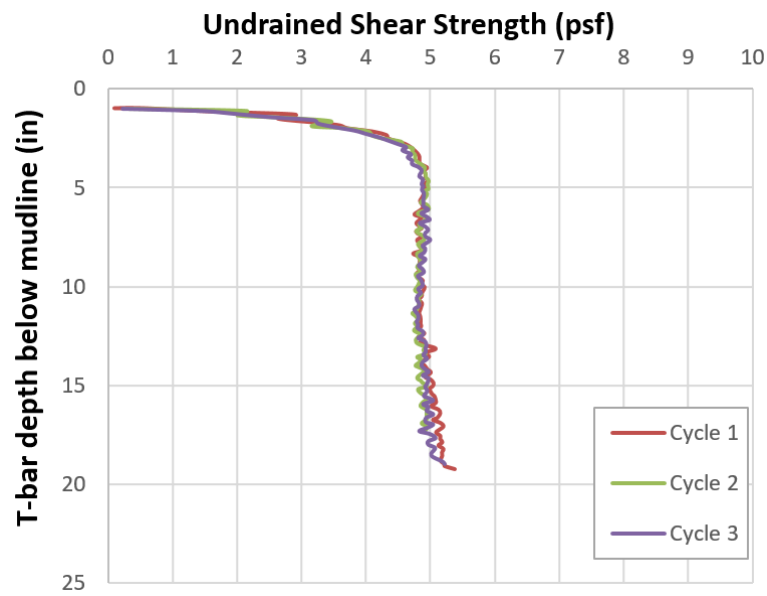
Figure 3.7: Example remolded soil strength profile, measured with t-bar
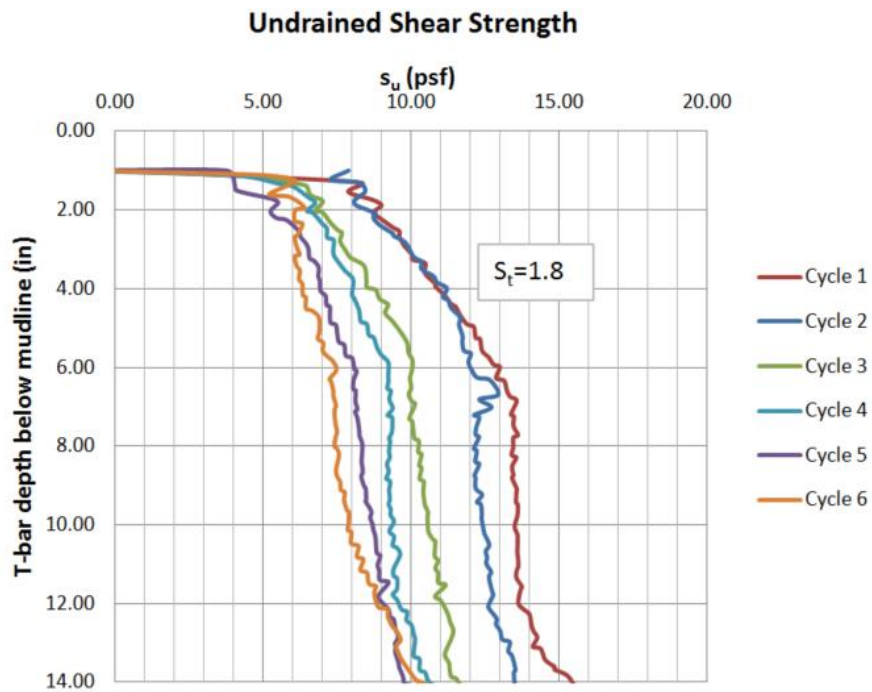
Figure 3.8: Example soil profile with sensitivity greater than one, measured with t-bar

The overconsolidated soil test beds were prepared by mixing the soil at c/p ratio's (undrained shear strength to effective overburden stress ratio) greater than 0.25. The soil was air dried to decrease the water content and obtain stiffer soil layers. Soil was remolded by mixing with the paddle to obtain uniform soil profiles. A split-spoon sampler was built using a PVC pipe to obtain water content samples throughout the soil layer. The unit weight of the soil with changing depth is calculated by:

$$\gamma = \frac{(1+w)G_s\gamma_w}{1+wG_s} \tag{3.2}$$

Where:

γ: Unit weight of soil

w: Water content

G_s: Specific Gravity

γ_w : Unit weight of water

The over consolidation ration (OCR) is calculated using the equation developed by Ladd et al. (1977):

$$\left(\frac{s_u}{\sigma_v'}\right)_{OC} = \left(\frac{s_u}{\sigma_v'}\right)_{NC} OCR^m \tag{3.3}$$

The undrained shear strength is measured by the t-bar test, the vertical effective stress (σ_v') is calculated by multiplying the buoyant unit weigth ($\gamma_b = \gamma - \gamma_w$) with the soil depth and m value is assumed as 0.8.

3.3 LOAD FRAMES

The load frames were built to connect test setup with the loading devices. Acrylic and steel pulleys were used to change the direction of loading. The aluminum loading frame was built using 4 in. wide channels that form a 5 ft wide and 4.7 ft tall loading frame on the steel tank. The frame can slide along the sides of the steel tank (Lee, 2008). The aluminum frame was extended 5 ft to the side by using an 8 ft long wooden strut that transfers the loading line to the wooden frame of the thermoplastic soil tank. This wooden frame with a platform was built using 2x4 lumbers for models tests in the 100-gallon thermoplastic tank. The load frames are presented in Figure 3.9.

Figure 3.9: Load frames

3.4 ELECTRIC MOTOR

A stepper motor (powered by a Superior Electric SLO-SYN MH112-ff-206) was used to control the displacement of loading lines. The motor is mounted on an aluminum plate suspended from the side of the steel tank, attached to the aluminum loading frame (Figure 3.10). This motor was initially used by tests for El-Gharbawy (1998) and El-Sherbiny (2005). The electric motor system has two linear actuators, two stepper motors,

two translator drivers and a computer controller card. The vertical displacement of the stepper motor is limited to 12.5 inches. The concentric pulley ratio of 3.25 was used to extend the loading line displacement to 40.63 inches. A data acquisition system was used to control the motor displacement rate while recording the motor position with respect to time. The 127 RPM (rounds per minute) corresponds to line displacement rate of 0.8 in/sec with the pulley system used in this research.
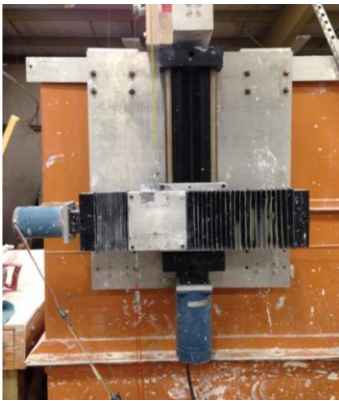
Figure 3.10: Stepper motor (Huang, 2015)

3.5 LOAD CELL

Two load cells, with maximum load capacities of 100 lbs and 200 lbs, manufactured by Lebow Products Inc. were used to measure the loads during testing (Figure 3.11). The compressive load results in a positive voltage output while the tensile load results in a negative voltage output. The load in pounds is calculated by subtracting a zero voltage from the output and multiplying the result with a calibration factor (Huang, 2015).

Figure 3.11: Load cell (Huang, 2015)

3.6 LINEAR MOTION TRANSDUCER

The linear motion transducer (LMT) is used to measure displacements ranging between 0-50 inches. The LMT is a RayecoTM model P-50. The LMT is attached moveable to a track system on the aluminum load frame (Figure 3.12). For calibration purposes, a steel tape measure was placed next to this track system to visually observe the displacement of the LMT sensor. The sensor is attached to the test system by a fishing line to minimize possible frictions along directional pulleys.
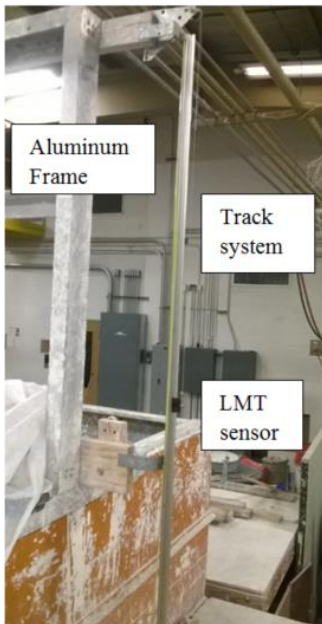
Figure 3.12: Linear Motion Transducer

3.7 MAGNETOMETER

The six-degree-of-freedom magnetic tracker (magnetometer) was used to measure position and orientation of the anchor as it moves through the soil in real time. The magnetometer was developed by Polhemus and the model number is Patriot P/N 4A0520-01, S/N 256B00086. The magnetometer consists of a sensor, source, electronics unit and a software (PiMgr) to transform measurements (Patriot User Manual, 2008). The source receives the electromagnetic waves coming from the sensor. To reduce the noise in the date, the magnetic objects are avoided from the test area and the source is placed close to sensor during experimental testing. Placing the source within 5 ft of sensor reduces the noise caused by magnetic objects significantly. When the distance is higher than 5 ft, the noise in measurements become more significant. Also using the magnetometer when the stepper motor is active causes a significant noise in data. This noise can be reduced by placing the source and sensor as close to each other as possible. The magnetometer source and the sensor are presented in Figure 3.13.

Figure 3.13: Magnetometer Source and Sensor

It is important to understand how the magnetometer measures the rotation and translation before using the magnetometer output for anchor tests. The magnetometer the translation output is measured with respect to the center of source. The +X and +Y directions are marked on the sensor and right hand rule is used to determine +Z direction. The rotational angles are presented with Euler angles which are expressed in terms of the rotating frames. The yaw is rotation around z-axis (azimuth), pitch is rotation around y-axis (elevation) and roll is rotation around x-axis (Polhemus T.M., 2013). The measurement order of the magnetometer is:

- First the yaw angle is measured with respect to external frame of xyz.

- Second, a new x′y′z′ coordinate system is set and the pitch rotation is measured with respect to this new frame.

- Third, a new frame of x″y″z″ is set and roll rotation is measured.

If the change in anchor rotation between recorded frames is of interest, using Euler angles to understand the exact physical behavior of anchor can be misleading. For the anchor drag embedment tests, the main focus was to analyze how much anchor rotates in each direction when the load acting on the anchor was changing in increments. To measure the change in each rotation at a given interval, the rotational angles should be measured with respect to a fixed axis of xyz rather than rotating axes. It is possible to calculate the change in rotations with respect to an external initial axes system by using magnetometer outputs of Euler angles or Direction Cosine Matrix. The direction cosine matrices are calculated depending on the measurement order of rotations. This magnetometer measures the rotations in the order of yaw-pitch-roll. The direction cosine matrix (R_{zyx}) for this measurement order is calculated by using the cosine (c) and sine (s) of yaw (ψ), pitch (θ) and roll (φ) as:

$$R_{zyx} = \begin{bmatrix} c\psi c\theta & c\psi s\theta s\varphi - s\psi c\varphi & c\psi s\theta c\varphi + s\psi s\varphi \\ s\psi c\theta & s\psi s\theta s\varphi + c\psi c\varphi & s\psi s\theta c\varphi - c\psi s\varphi \\ -s\theta & c\theta s\varphi & c\theta c\varphi \end{bmatrix} \tag{3.4}$$

Direction cosine matrix of each measurement frame (yaw-pitch-roll Euler angle output) is calculated. This direction cosine matrix is multiplied by the inverse of the matrix (R_{zyx}^{-1}) to obtain the original measurement frame. Each frame is recalculated by using this method. Summing the change in angles calculated with respect to this original frame gives the change in yaw, pitch and roll angles with respect to a fixed axis that is used to obtain first measurement frame. The yaw, pitch and roll angles presented in this study show the real time anchor rotation in each direction calculated by using magnetometer Euler angle outputs.

3.8 DATA ACQUISITION AND MOTION CONTROL PROGRAMS

The data acquisition and motion control system developed on LabVIEW platform was used to record data from the Data Acquisition (DAQ) hardware and motion control card which are both produced by National Instruments. The Data Acquisition program records the measurements from the load cell and the LMT sensor with respect to time and saves in text data file format. The DAQ user interface has a control area, file input area, calibration factors input area, load and displacement output area, load-displacement output area. The control area enables the user to start recording data, write and save text files, and stop data acquisition. The file input area enables user to input the file path and operator name. The calibration factors input area is used to type calibration factor that are used to convert voltage measurements to calibrated values of load, displacement etc. The output areas show calibrated load and displacement values and synchronous load-displacement graphs. The details of the DAQ and motion control are described in detail by Huang (2015).

59

3.9 CONCLUSIONS

The experimental testing facility includes the soil test beds of kaolinite and Gulf of Mexico marine clay. The experimental tests are performed using load frames, electric motor, load cells, linear motion transducer, magnetometer and the Data Acquisition and Motion Control programs. Properties and the operational details of the equipment are presented in details in this chapter.

Chapter 4: Pure Loading Yield Thresholds of Bearing Plates

4.1 INTRODUCTION AND OBJECTIVES

The objective of this chapter is to develop the understanding of pure loading yield thresholds of simple geometry bearing plates, that are symmetrical along the longitudinal axis, in clay under undrained loading. The yield thresholds of bearing plates in each of the six-degree-of-freedom are measured experimentally and calculated theoretically. The yield thresholds show the resistance of the plate to yielding when subjected to pure loading in that direction. When the yield threshold of the plate is exceeded, it mobilizes the capacity in that direction and starts to move. Yield thresholds are expressed in terms of non-dimensional factors that are obtained by experimental measurements and theoretical calculations. The six-degree-of-freedom loading directions are: normal, in-plane shear, out-of-plane shear, yaw, pitch and roll loading.

This chapter describes the experimental testing setup used to apply pure loading in each six-degree-of-freedom direction, properties of the model anchors, experimental and theoretical calculation of non-dimensional yield thresholds and factors affecting the non-dimensional yield thresholds.

4.2 SCALED MODEL ANCHORS

4.2.1 BEARING PLATES WITH SIMPLE GEOMETRIES

Bearing plates with simple geometries of circle, square, triangle and diamond were built using plywood or aluminum plates with constant thicknesses. The selected simple shapes are all symmetrical along the longitudinal axis of the bearing plate. This longitudinal axis is parallel with the in-plane shear loading direction.

The fluke areas of the bearing plates ranged between 8 in^2-20in^2 that correspond to equivalent fluke widths (B) between 2.83 inch-4.47 inch. The models have constant

thicknesses ranging from B/6-B/9. Different geometry models were built in equal fluke areas and thicknesses. The triangle model was built as an equilateral triangle. The diamond model was designed to have a smaller triangular area at the lower part and larger triangular area at the upper part. The ratios of dimensions were kept constant when building different scale diamond anchor models. The plywood models were painted with spray paint to decrease water absorption. Sample plywood and aluminum bearing plates are presented in Figure 4.1 and Figure 4.2 respectively. Holes were drilled on the models to insert penetration rods during pure loading tests. Bearing plates were tested in kaolinite and Gulf of Mexico marine clay. The aluminum models are significantly more durable than the plywood models. But plywood models are easily modified with the available tools at the laboratory. Also if magnetometer is being used, even though the aluminum models do not cause a significant noise they affect the magnetometer calibration significantly.
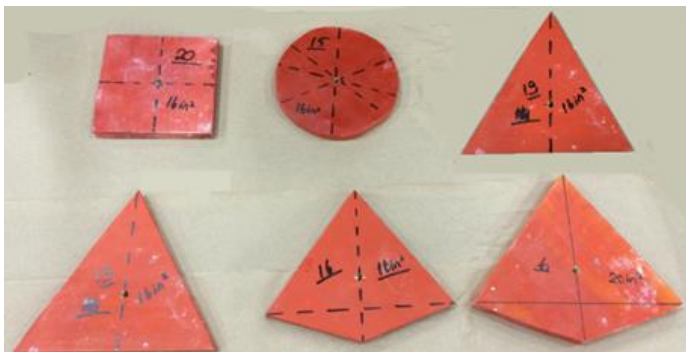
Figure 4.1: Plywood bearing plates
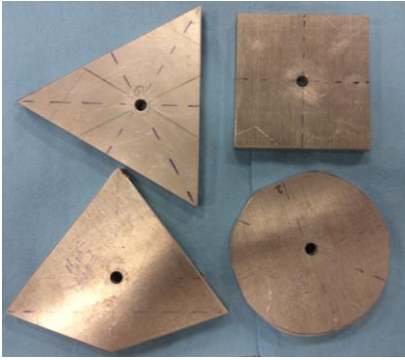
Figure 4.2: Aluminum bearing plates

4.3 TESTING SETUP AND PROCEDURES

The anchor scaled models are tested under translational and rotational pure loading conditions in different soil test beds under undrained conditions. Kaolinite and Gulf of Mexico marine clay soil test beds with different undrained soil strength profiles and soil sensitivities are prepared as test beds.

Remolded soil test beds were prepared by mixing the soil in the 100 gal thermoplastic thank or in soil barrels. The relatively bigger anchor models (such as $20in^2$ fluke area) are not tested in the soil barrels to avoid side effects. Soil was mixed between testing cycles to avoid sensitivity built up. For testing the anchors in soil test beds with sensitivity greater than one, the soil test bed was initially prepared by remolding the soil and embedding the anchor into soil. The testing setup was prepared and the soil was left undisturbed with the anchor model ready to be tested in it. After waiting for several days to obtain higher sensitivity soil, the test is started without disturbing the soil or the anchor model. T-bar test is conducted at a location away from the anchor test to measure the soil strength and sensitivity of the undisturbed soil without interacting with the remolded zone during anchor testing. Each loading test was repeated at least 3 times at equal testing conditions to obtain repeatable data.

The pure translational and rotational loading setups are prepared to load the anchor in one loading direction only. The testing setup is modified for testing different models and the effect of modifications are considered during the calculation of results. This section describes the main components of the loading setups and testing methods.

4.3.1 TRANSLATIONAL PURE LOADING TESTS

Direction of Loading

Translational pure loading tests consist of loading the anchor in normal, in-plane shear and out-of-plane shear directions. The pure loading directions are defined depending on the direction that anchor fluke is loaded to yield. The normal loading is described as the load being applied perpendicular to fluke plane such that the resistance of the anchor is obtained through the bearing of the fluke surface. The in-plane shear loading is described as the load applied in the plane of the major axis of the anchor (Gilbert et al., 2009). The out-of-plane shear loading direction is defined as the load applied at an angle from the plane of major axis.

The schematic drawing of a simple geometry anchor: diamond-shaped plate is presented in Figure 4.3. The top view shows the anchor orientation during free-fall such that when anchor embeds into soil the smaller height triangular part of the diamond is embedded deeper than the bigger height triangular part. The normal, in-plane shear and out-of-plane shear loading directions for this diamond-shaped plate are shown in Figure 4.4. Example testing photos of the diamond shaped bearing plate during insertion into kaolinite and the extraction of a square shaped bearing plate from kaolinite are presented in Figure 4.5.
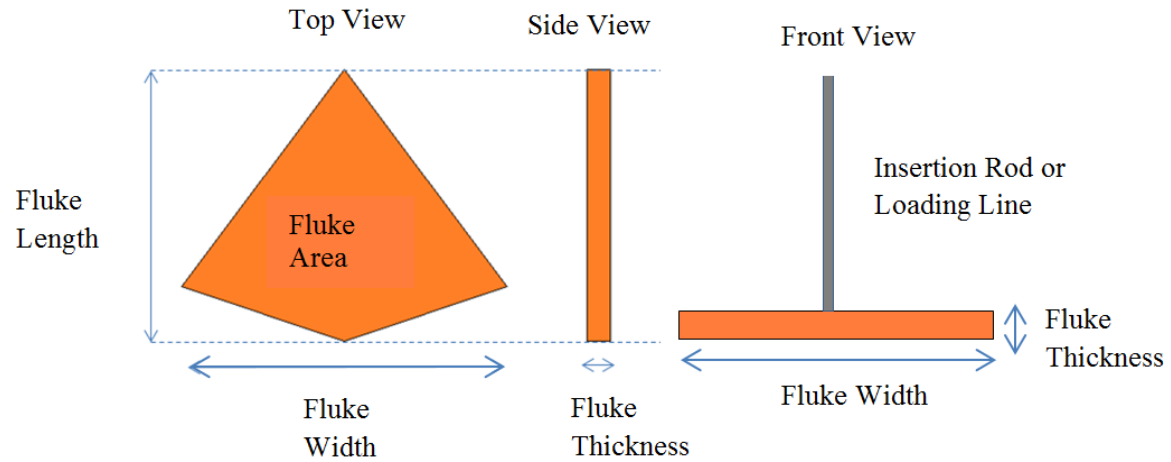
Figure 4.3: Schematic drawing of the diamond-shaped bearing plate
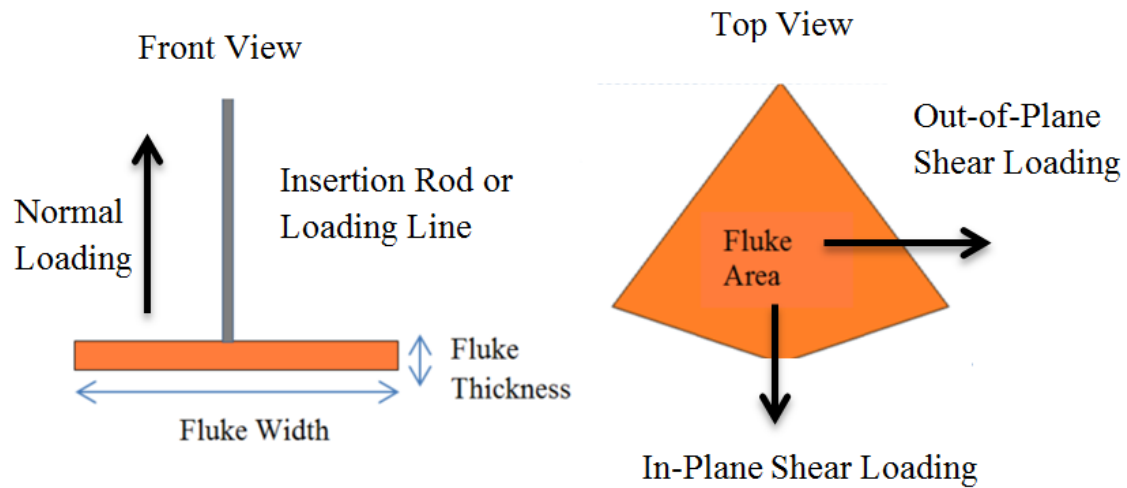
Figure 4.4: Translational pure loading directions of the diamond-shaped plate
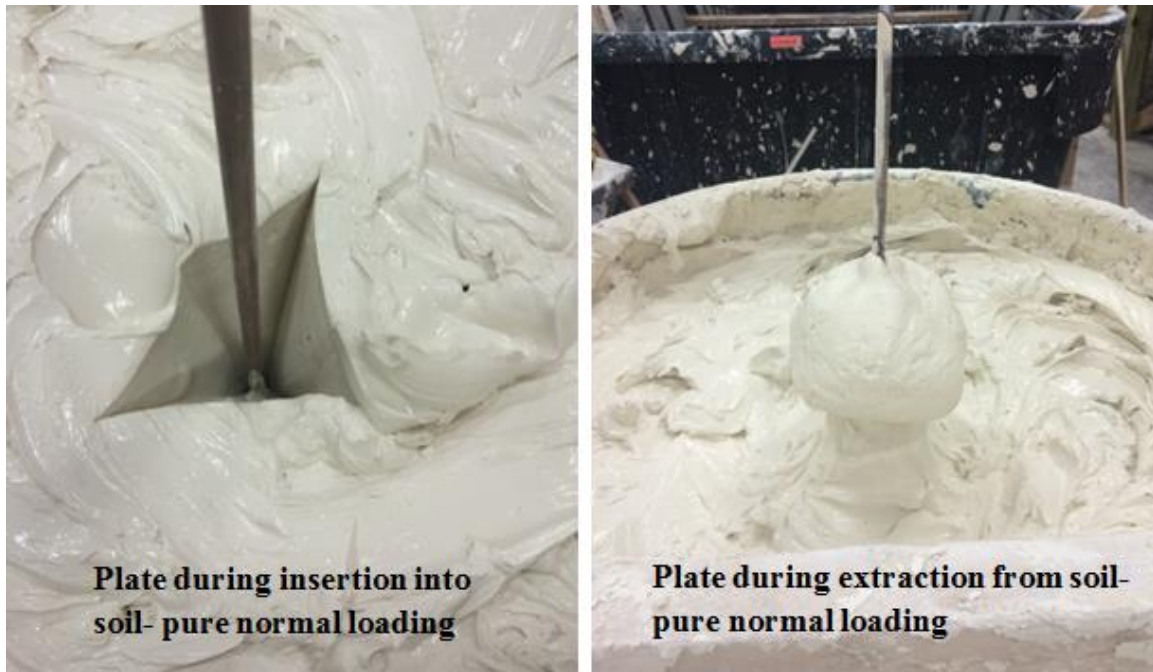
Figure 4.5: Normal loading test photo, simple shaped bearing plate in kaolinite

Testing Setup

To be able to load the anchor model in one direction only, two testing setups were developed: with insertion rod and with loading line. The testing setup with the insertion rod (Figure 4.6) is similar to the t-bar test setup. The t-bar insertion rod was mounted into the anchor model and the anchor is either pushed into the soil or pulled out of soil by displacing the electric motor at a rate equal to the t-bar test rate (0.8 in/sec) with the help of additional weights stacked on top of the insertion rod. The insertion rod is levelled prior to pushing the anchor into or out of soil. A load cell is attached on top of the insertion rod to measure anchor forces. The load cell recordings are saved during pushing the anchor into soil and pulling it out of soil. The friction along the insertion rod is measured by a separate insertion rod test and measured anchor loads are corrected for the friction along the rod. The load cell measurements are corrected for testing setup frictions (insertion rod,

66

plate-rod insertion pieces), insertion weights and the buoyant weight of the plate depending on the direction of the loading. All the loads presented in the context of this research are the net resistances.

Figure 4.6: Pure loading test setup for translational loading with insertion rod

4.3.2 ROTATIONAL PURE LOADING TESTS

The anchor models were loaded in pure pitch, roll and yaw directions to experimentally measure the anchor yield behavior under pure rotational loads. The rotational loading directions for the diamond-shaped plate (Figure 4.3) are presented in Figure 4.7.
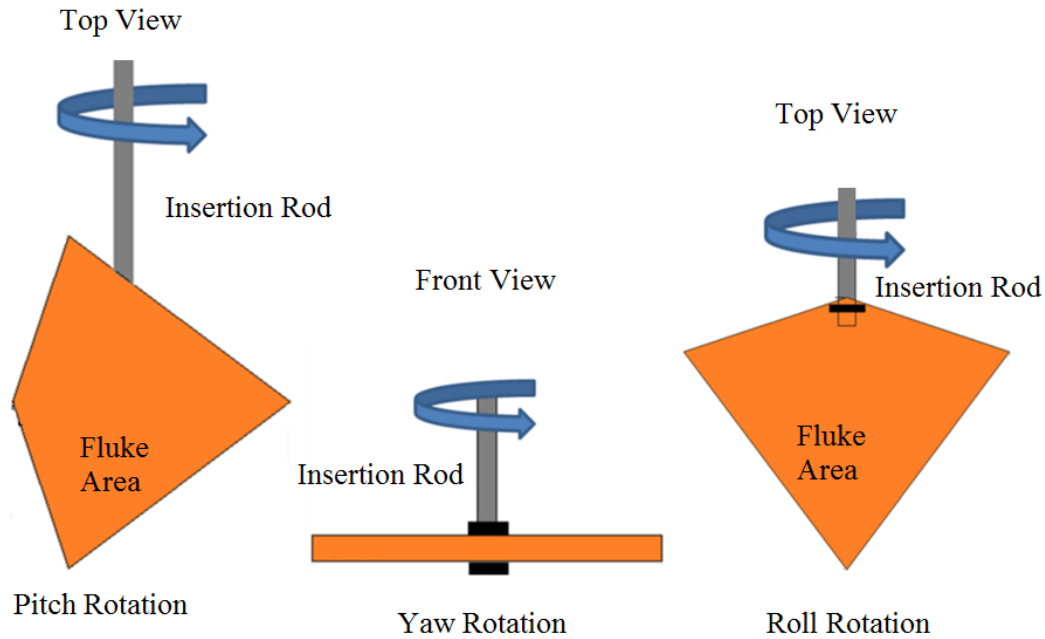
Figure 4.7: Rotational pure loading directions

The rotational pure loading test setup consists of a loading line attached to the electric motor on one side and an acrylic pulley on the other side. Acrylic pulley is mounted on a steel rod at its center and the steel rod is inserted into the anchor model. As the motor pulls the loading line at a rate of 8 in/sec, a moment equal to line load times pulley radius is applied to the anchor. A directional pulley is used to align the line attached between the load cell and the rotational pulley with the rotational pulley. The setup is shown in Figure 4.8. Once the moment resistance of the anchor is exceeded, the anchor starts rotating in the direction of rotational loading. The load cell measurements are corrected for testing setup frictions (insertion rod, plate-rod insertion pieces). All the loads presented in the context of this research are the net resistances.
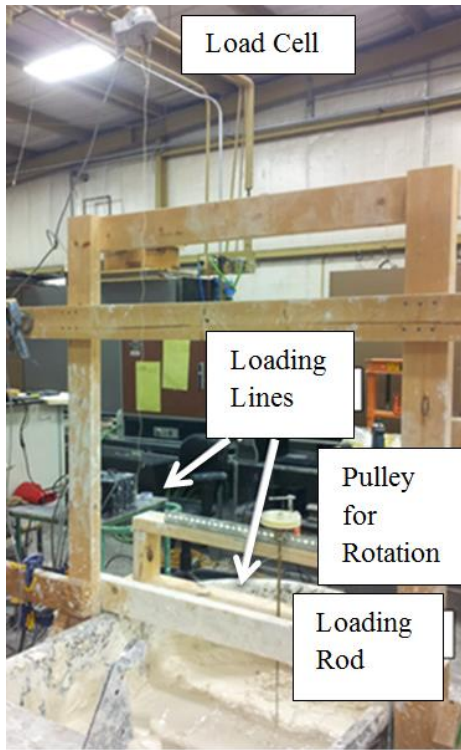
Figure 4.8: Pure loading test setup for rotational loading

4.4 PURE LOADING YIELD THRESHOLDS

4.4.1 EXPERIMENTALLY MEASURED PURE LOADING YIELD THRESHOLDS

The anchor pure loading test results are used to calculate the non-dimensional anchor yield thresholds. The measured anchor resistances are corrected for additional resistances due to testing setup (insertion rod, pulley friction, anchor supports during loading etc.) to obtain net anchor resistance. The net resistance is normalized by the undrained shear strength of soil and the anchor fluke area to calculate the non-dimensional yield thresholds. The pure loading yield thresholds for normal, in-plane shear and out-of-plane shear loading are calculated by Equation 4.1. The non-dimensional bearing capacity factors for pitch, yaw and roll loading are calculated by Equation 4.2. The resulting pure

loading yield thresholds were calculated by averaging the pure loading yield thresholds calculated for each testing cycle.

$$N_c = \frac{F}{A_f s_u} \tag{4.1}$$

$$N_c = \frac{M_{max}}{A_f s_u B} \tag{4.2}$$

Where:

F: Net anchor resistance

M_{max}: Maximum moment

B: Equivalent fluke width $= (A_{fluke})^{1/2}$

s_u: Undrained shear strength

It is important to normalize the anchor resistances with the accurate undrained shear strength. For soil profiles with constant undrained shear strength profile with depth, the s_u is calculated by averaging the s_u along the soil depth. If the undrained shear strength profile is not constant but linearly increasing with depth, Davis and Booker (1973) method is used to calculate the equivalent undrained shear strength to normalize the measured anchor resistance. According to this method, the limit unit bearing capacity of a strip footing on the surface of a deposit with increasing strength with depth is calculated by Equation 4.3.

$$q = \frac{Q}{B} = F\left[s_{u0}N_c + \frac{1}{4}\rho B\right] \tag{4.3}$$

Where:

Q: the total load at failure

B: width of the footing

s_{u0}: the undrained shear strength of the clay at depth $z_f=0$ below the base of foundation.

N_c: 5.14

ρ: rate of increase of the undrained shear strength with depth (ds_u/dz)

F: correction factor

The equivalent undrained shear strength is calculated by

$$s_{u,eq} = \frac{q_{bL}}{N_c} \qquad\qquad\qquad (4.4)$$

For applying this method to anchor tests, the $s_{u,0}$ is the undrained shear strength value corresponding to the depth which the anchor force to be normalized is measured at. The B is as the equivalent fluke length ($A_{fluke}^{0.5}$) of the scaled anchor model. The anchor resistance at a certain depth is obtained by correcting the load cell recording for additional resistances due to testing equipment. It is important to choose a load value that is representative of the full flow failure mechanism during pure loading test. Thus the load values recorded when the anchor is close to the bottom or the top of the soil tank are avoided.

An example calculation is presented for a 16 in^2 diamond shaped plate tested in remolded Gulf of Mexico marine clay test bed. The bearing force measured during pure normal loading is presented in Figure 4.9. First step is to decide the plate bearing force that will be normalized to calculate pure loading yield thresholds. The arrows pointed on the graphs show the load recorded at 7 inches of embedment (41.1 lbs) was the maximum. The undrained shear strength at the mudline was 17 psf and increases at a gradient of 14.45

71

psf/ft. The undrained shear strength measured 7 inches from mudline was approximately 25 psf. By using the Davis and Booker (1973) method, the strength of the soil deeper than 7 inches below mudline is considered (Figure 4.10). The units in kPa and meters are used to calculate F correction factor using the recommended method by API 2GEO (2011). The F correction factor can be calculated by:

$$F \approx a + bx - ((c + bx)^2 + d^2)^{0.5} \tag{4.5}$$

$$x = \frac{\rho B}{s_{u0}} \text{ for } 0 \le x \le 25 \tag{4.6}$$

The a, b, c and d coefficients are 1.372, 0.07, -0.128 and 0.342 for fully smooth interface (API 2GEO, 2011).
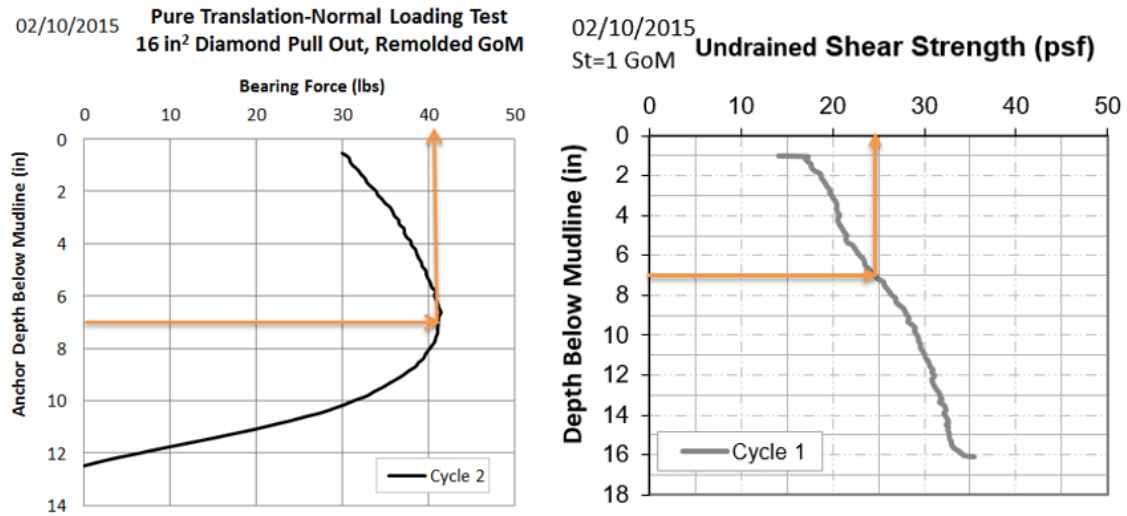
Figure 4.9: Example $s_{u,eq}$ calculation by Davis and Booker (1973) Method step 1
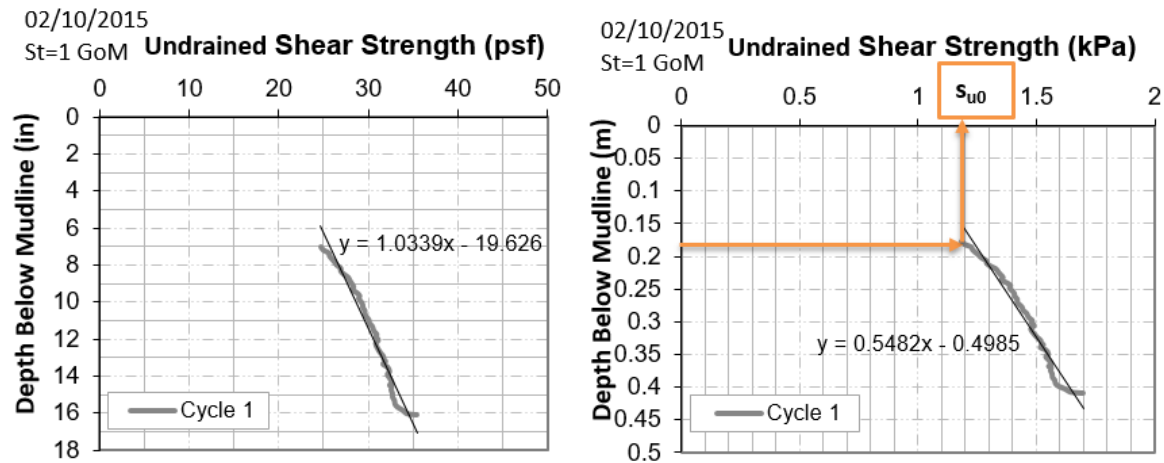
Figure 4.10: Example $s_{u,eq}$ calculation by Davis and Booker (1973) Method step 2

The B is the equivalent fluke length of 10.16 cm (4 in.) calculated for the 16 in^2 fluke area. The ρ is the equal to 1/0.5482=1.824 kPa/m. The s_{u0} is the undrained shear strength at the mudline but since the soil deeper than 7 inches is considered, the s_{u0} is equal to 1.19 kPa. By using Equation 4.3, $s_{u,eq}$ is calculated as 1.22 kPa which is equal to 25.6 psf. Normalizing the anchor resistance of 41.1 lbs with the $s_{u,eq}$ of 25.6 and A_f of 16 in^2 results in pure normal loading yield threshold of 14.5 for the 16 in^2 diamond shaped bearing plate.

4.4.2 SIMPLIFIED THEORETICAL PURE LOADING YIELD THRESHOLD CALCULATIONS

The theoretical pure loading yield thresholds were calculated for translational and rotational pure loading conditions. The total resistance to loading was theoretically calculated by accounting the areas acting in bearing resistance and those acting in shear; and assigning pure loading yield thresholds to those areas.

During pure normal loading, the fluke area is acting in bearing and fluke sides are acting in shear. The illustration of a solid square bearing plate subjected normal loading with areas assigned for shear and bearing resistances are presented in Figure 4.11. The

73

yield threshold for a square plate subjected to pure normal loading is 12.5 (Gilbert et al., 2009). The shear resistance is calculated as the product of an adhesion (α) factor, the undrained shear strength and the area acting in shear. For the completely remolded soil, α of 1 is used. For the tests in soil with sensitivity of S_t, α of $1/S_t$ is used.
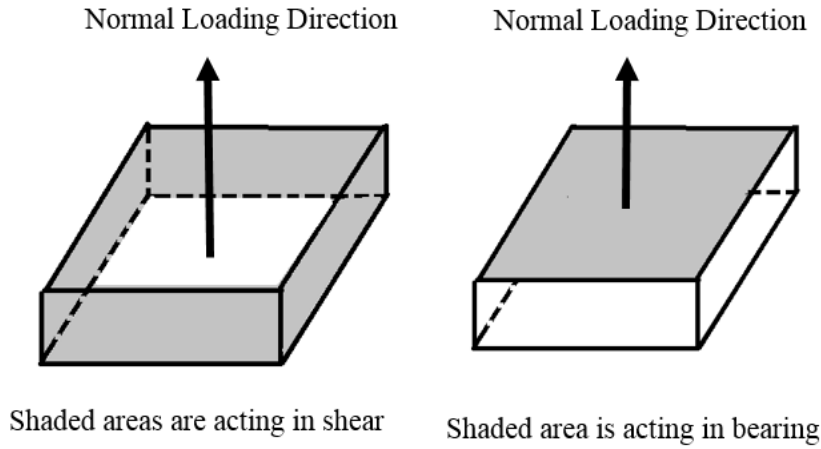
Figure 4.11: Solid square subjected to normal loading

Neglecting the suction behind the anchor, the non-dimensional yield threshold for pure normal loading (N_{normal}) for an anchor model with thickness of t and equivalent fluke width of B is calculated as:

$$N_{normal} = 12.5 + 4\times(1/S_t)\times(t/B) \tag{4.7}$$

When the anchor is loaded in shear loading, the top and bottom fluke areas and fluke side areas are acting in shear. The projected front area is acting in bearing. The illustration of a solid square bearing plate subjected to shear loading with areas assigned for shear and bearing resistances are presented in Figure 4.12. For the side of the fluke (i.e. thickness) the width of the side is small relative to the length of the bearing area, so the

bearing capacity factor for a buried strip footing of 7.5 is assigned to calculate the bearing resistance of projected area (Aubeny et al., 2011).
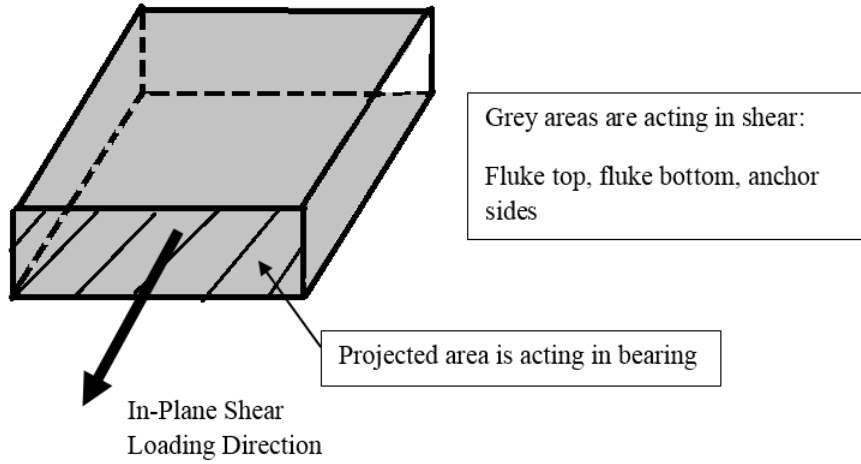
Figure 4.12: Solid square subjected to in-plane shear loading

Assuming the back side of the fluke is also providing bearing resistance, the non-dimensional yield threshold for pure shear loading (N_{shear}) for an anchor model with thickness of t and equivalent fluke width of B is calculated as:

$$N_{shear} = 2(1/S_t) + 2 \times 7.5 \times (t/B) \tag{4.8}$$

The upper bound solution estimated the moment bearing capacity factor of 1.9 for a thin circular plate (Yang et al., 2008). Illustration of a solid square subjected to rotational loading is presented in Figure 4.13 showing the moment contribution of fluke edges with constant fluke thicknesses.
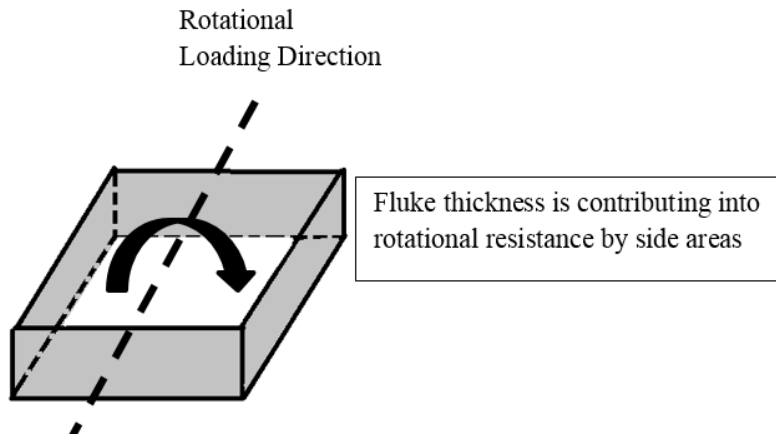
Figure 4.13: Solid square subjected to rotational loading

The non-dimensional yield threshold for pure moment loading (N_{moment}) for an anchor model with thickness of t and equivalent fluke width of B is calculated as:

$$N_{moment,one-wing} = 1.9 + 1.5 \times (1/S_t) \times (t/B) \tag{4.9}$$

4.5 RESULTS OF PURE LOADING YIELD THRESHOLD ANALYSIS OF BEARING PLATES

4.5.1 YIELD THRESHOLDS OF BEARING PLATES IN CLAY

The non-dimensional pure loading yield thresholds calculated for simple shaped bearing plates symmetrical along the longitudinal axis are measured experimentally and calculated theoretically. The results obtained by testing bearing plates of circle, square, triangle and diamond shaped anchor flukes are presented in Figure 4.14, Figure 4.15 and Figure 4.16 for pure normal, shear and rotational loading respectively. For anchor fluke areas between 8 in^2 to 20 in^2, the pure normal loading yield threshold (N_{normal}) in the range of 10-15, the pure shear loading yield threshold (N_{shear}) 3.3-4.4 and the pure rotational loading yield threshold in the range of (N_{moment}) 1.9-2.6 were measured during the tests in

remolded clay. The theoretical non-dimensional yield thresholds are in good agreement with the experimentally measured yield thresholds.

The measured and theoretically calculated pure normal loading yield thresholds (Figure 4.14) compare well with the theoretical values calculated from the finite element methods (FEM) for thin symmetrical plates; N_{normal} of 12.4-13.1 (Martin and Randolph, 2001), 11.87 (O'Neill, et al., 2003), 12 (Aubeny and Chi, 2014), 12.5 (Yang, et al., 2010).
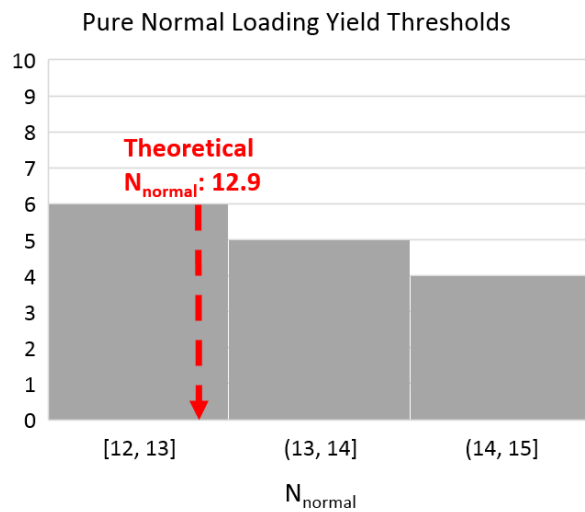
Figure 4.14: Pure normal loading yield thresholds for bearing plates

The measured pure shear loading yield thresholds for the bearing plates are also comparable to theoretical predictions and approximately 1/3rd of the pure normal loading yield thresholds. The pure shear loading yield threshold measurements and theoretical predictions for simple shaped bearing plates (Figure 4.15) match well with the theoretical values calculated with finite element modeling. Example FEM N_{shear} results obtained for flukes with constant thickness are 4.39 (Yang et al., 2010), 4.29 (O'Neill et al., 2003), 3.9 (for t=0.5 in, L=4 in square) (Gilbert et al., 2009) and 3.38 (Elkhatip and Randolph, 2005).
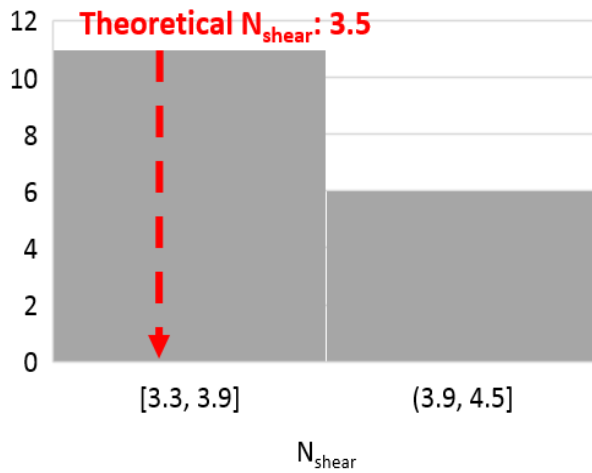
Figure 4.15: Pure shear loading yield thresholds for bearing plates

The measured pure rotational loading yield thresholds for the bearing plates (Figure 4.16) are comparable to theoretical values calculated by finite element methods for thin plates such as N_{moment} of 1.7-1.9 (Yang, et al., 2010; Gilbert, et al., 2009; Aubeny and Chi, 2014). The experimental measurements are slightly higher than theoretical N_{moment} values since the constant fluke thickness increases the rotational yield thresholds.
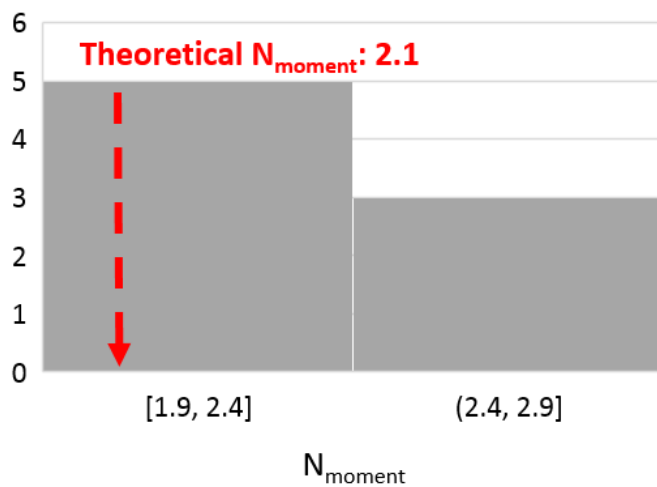
Figure 4.16: Pure rotational loading yield thresholds for bearing plates

4.5.2 EFFECT OF GEOMETRY

The results show that the shape of the bearing plate does not have a significant effect on the pure loading resistance for simple geometry bearing plates that are symmetrical along the longitudinal axis. Comparing a set of yield thresholds experimentally measured in kaolinite testing triangle, circle, square and diamond anchor models with 16 in^2 fluke areas and constant thickness of 0.5 in are presented in Figure 4.17. The same anchor models are also tested in Gulf of Mexico marine clay and pure normal loading non-dimensional yield thresholds are presented in Figure 4.18 and pure shear loading yield thresholds are presented in Figure 4.19. The results show that, for the same soil and testing conditions, plate area and plate thickness, there is no significant effect of anchor shape on the anchor yield threshold for simple geometry bearing plates that are symmetrical along the longitudinal axis.
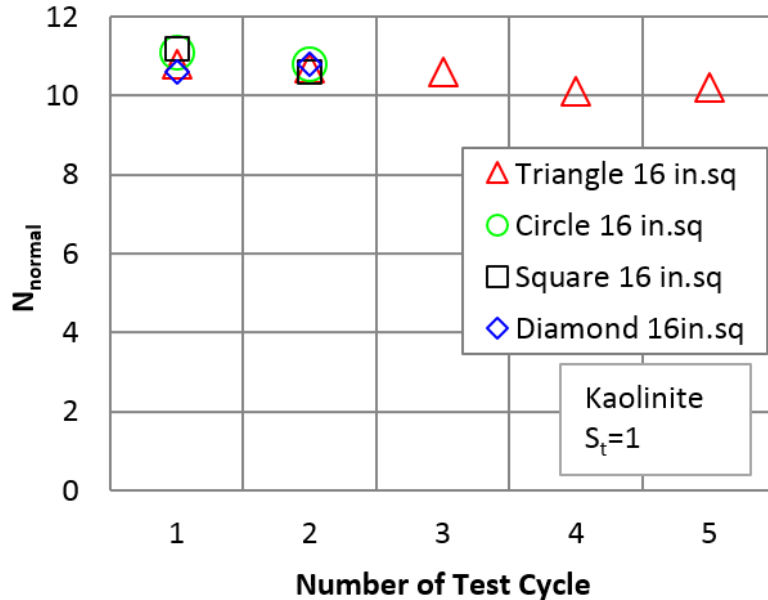
Figure 4.17: Effect of geometry on yield thresholds, pure normal loading in kaolinite
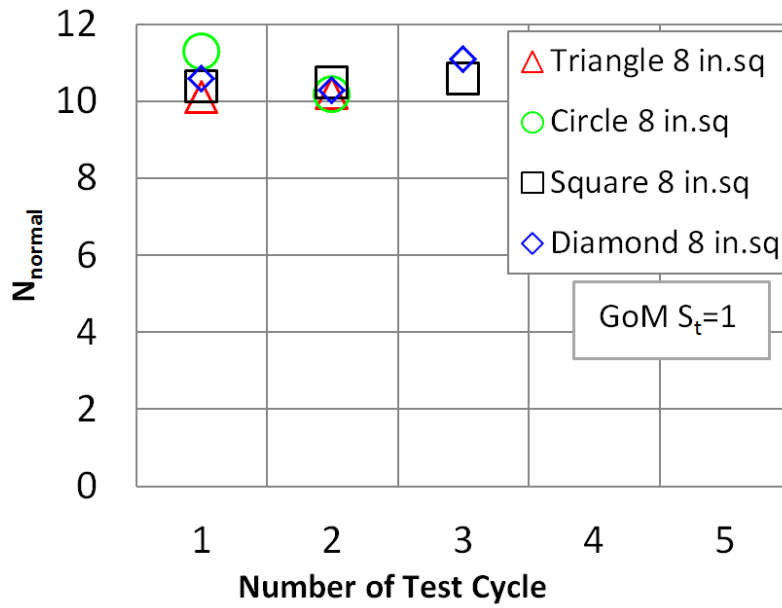
Figure 4.18: Effect of geometry on yield thresholds, pure normal loading in Gulf of
Mexico (GoM) marine clay
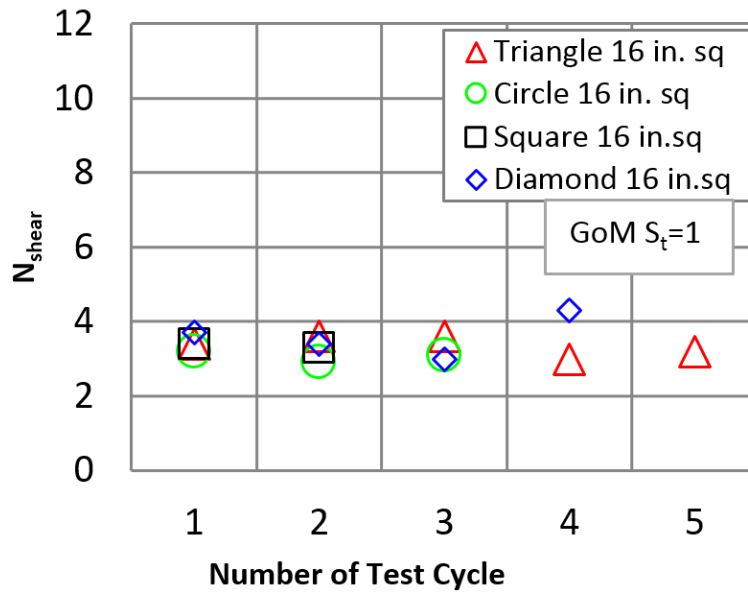
Figure 4.19: Effect of geometry on yield thresholds, pure shear loading in Gulf of Mexico
(GoM)marine clay

The yield thresholds experimentally measured for pure in-plane shear loading are analyzed to study the calculation method of theoretical in-plane shear yield thresholds. For an anchor fluke area presented in Figure 4.20, the fluke width is B, length is L and side is x. Assuming the θ angle starts from 30 degrees (equilateral triangle) and increases to 90 degrees (square) with keeping B constant.
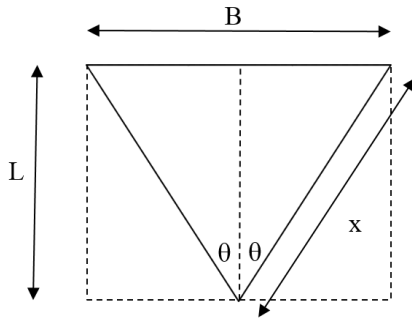
Figure 4.20: Anchor dimensions for theoretical calculations of in-plane shear yield
threshold

The theoretical N_{shear} is calculated by considering the contribution of top and bottom fluke areas, the contribution of sides and with or without including the reverse bearing (suction) at the back of the anchor. If there is a gap left behind the anchor during yielding in in-plane shear direction, bearing contribution from the back of the anchor is not mobilized. The contribution of the fluke sides for a bearing plate shape with $30° \leq \theta \leq 90°$ can be calculated in two different ways: either assuming the shear resistance acts along an area equal to the x.t (Figure 4.21) or assuming the bearing resistance acts along the projected area of B.t (Figure 4.22) where t is the constant fluke thickness. The x distance can be calculated as B/2sinθ.
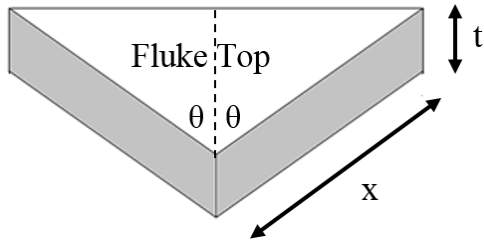
Figure 4.21: Anchor sides providing shear resistance
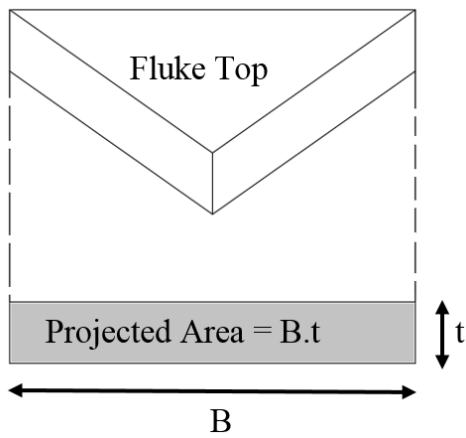
Figure 4.22: Anchor projected area acting in bearing

The theoretical N_{shear} values can be calculated without including the contribution of the back of the fluke by Equation 4.10 if the assumption is that anchor sides provide shear resistance and by Equation 4.11 if the assumption is assuming the projected area provides bearing resistance.

$$N_{shear} = \frac{2.\alpha.s_u.A_f + 2.x.t.\alpha.s_u}{A_f} \qquad (4.10)$$

$$N_{shear} = \frac{2.\alpha.s_u.A_f + N_c.B.t.s_u}{A_f} \qquad (4.11)$$

The experimental values obtained by testing the equilateral triangle ($\theta=30°$), diamond anchor ($\theta=71°$), reversed diamond anchor ($\theta=37°$) and square ($\theta=90°$) in in-plane shear loading are presented in Figure 4.23 with theoretical calculations. The theoretical N_{shear} values for experimentally tested bearing plates are calculated by both methods of assuming the front area is providing shear resistance or assuming the projected area is providing bearing resistance. The higher theoretical N_{shear} values are calculated when Equation 4.11 is used since bearing resistance of the projected area contributes more than the shear resistance of the side areas. Results show that there is no significant difference in measured N_{shear} for $30°\leq\theta\leq90°$. Calculating the N_{shear} by assuming the projected area is proving bearing resistance (Equation 4.11) results in better match of theoretical and experimental N_{shear} values. The experimental N_{shear} values higher than the theoretical N_{shear} values indicate additional resistance was obtained from the suction at the back of the anchor during those tests.
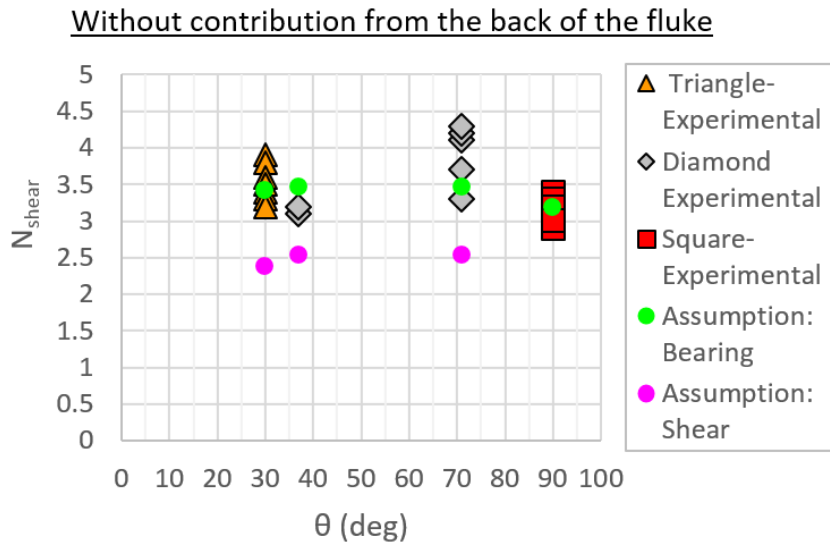
Figure 4.23: Comparison of N_{shear} values for different θ angles, without contribution of the back of the fluke

When the contribution of the back of the fluke is included in the theoretical calculations, depending on the geometry of the anchor, it can be assumed as the back of the anchor is contributing with bearing resistance (square, triangle) or in shear resistance (diamond). The theoretical N_{shear} equations can be modified to assume both front and back projected areas are acting in shear (Equation 4.12), both front and back projected areas are acting in bearing (Equation 4.13) or one projected area is acting in bearing and the other projected area is acting in shear (Equation 4.14).

$$N_{shear} = \frac{2.\alpha.s_u.A_f + 2.2.x.t.\alpha.s_u}{A_f} \tag{4.12}$$

$$N_{shear} = \frac{2.\alpha.s_u.A_f + 2.N_c.B.t.s_u}{A_f} \tag{4.13}$$

$$N_{shear} = \frac{2.\alpha.s_u.A_f + .2.x.t.\alpha.s_u + N_c.B.t.s_u}{A_f} \tag{4.14}$$

Comparisons of theoretical calculations including the contribution of the back of the anchor with experimental measurements are presented in Figure 4.24. The results show that assuming both front and back projected areas are acting in shear under-predicts while assuming both areas act in bearing over-predicts N_{shear}. The assumption of one projected area contributes in shear resistance while the other projected area contributes in bearing resistance results in good match with experimental measurements.

It can be concluded that, if the reverse end bearing is included in the calculations assuming the front projected area is acting in shear estimates the anchor pure shear loading

yield threshold accurately. If the contribution from the back of the anchor is not included in the calculations (assuming a gap has formed behind the anchor), then assuming the front projected area is acting in bearing results in good match with experimental measurements. Since the equilateral triangle has a flat back area during in-plane shear loading tests, theoretical calculations assumed that the back area provides reverse end bearing. The experimental triangle data (Figure 4.24) show that measurements can be lower than both theoretical calculations. This indicates a gap can form at the back of the anchor during testing. The formation of the gap can be explained by the fast loading of bearing plates in the experimental setup and high undrained shear strength of the soil around the anchor.
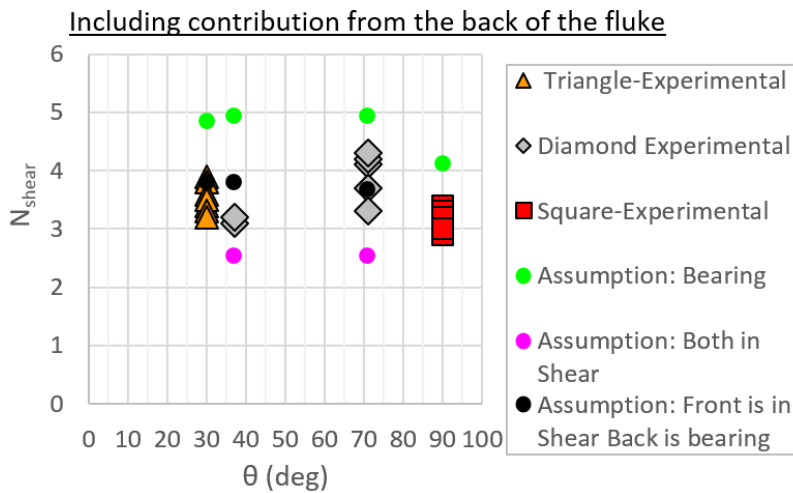
Figure 4.24: Comparison of N_{shear} values for different θ angles, including contribution of the back of the fluke

Comparison of theoretical calculations and experimental measurements show that there is no significant difference in measured N_{shear} for $30°\leq\theta\leq90°$. Since the formation of gap behind the anchor depends both on the soil and the loading conditions, not relying on the contribution of the reverse end bearing and assuming the front projected area is acting in bearing provides better estimates.

85

4.5.3 TYPE OF CLAY

The pure loading yield thresholds measured by testing simple shaped bearing plates that are symmetrical along the longitudinal axis are similar for both the tests in remolded kaolinite and remolded Gulf of Mexico marine clay. Result show that the plasticity of the clay does not affect the pure loading yield thresholds in each of the six-degree-of-freedom. Figure 4.26 shows the undrained shear strength profile with depth of a kaolinite test bed and a Gulf of Mexico marine clay test bed. Both test beds have similar undrained shear strength profiles. Bearing plates with simple geometries, equal fluke areas and thickness were tested in those soil test beds. The non-dimensional pure loading yield thresholds calculated for the mentioned tests are presented in Figure 4.26. The results show that simple bearing plates have similar yield thresholds both in kaolinite and Gulf of Mexico marine clay.
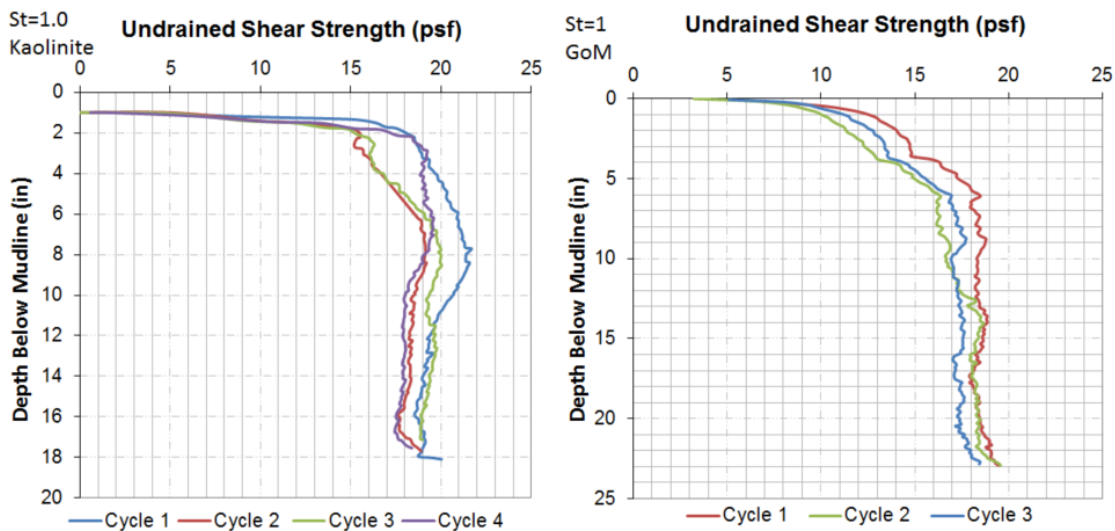
Figure 4.25: Undrained shear strength profiles for kaolinite and Gulf of Mexico (GoM) marine clay
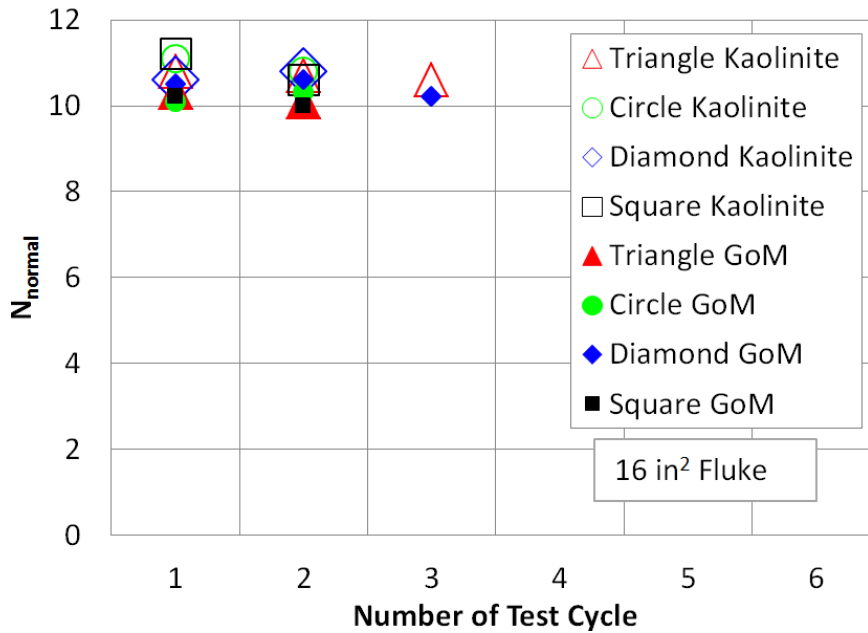
Figure 4.26: Effect of clay type, pure normal loading yield thresholds of bearing plates

4.5.4 UNDRAINED SHEAR STRENGTH PROFILE

Similar pure loading yield thresholds were measured for simple geometry bearing plates, symmetrical along the longitudinal axis, tested in soil test beds with constant undrained shear strength profiles or linearly increasing undrained shear strength profiles. Figure 4.27 shows two different soil strength profiles of remolded Gulf of Mexico marine clay and test results of simple bearing plates with equal fluke area and thickness tested in pure shear loading. The results show that having a constant undrained shear strength profile or increasing shear strength profile did not affect the measured non-dimensional yield thresholds in pure shear loading significantly. On the other hand, it is important to choose the accurate undrained shear strength value to normalize measured anchor resistance to calculate the pure loading yield thresholds, especially for linearly increasing soil profiles. If the anchor resistance to be normalized is picked when the anchor is deeply embedded

87

into soil and if the undrained shear strength at a shallow depth is used to normalize, the calculated yield thresholds can be significantly higher.
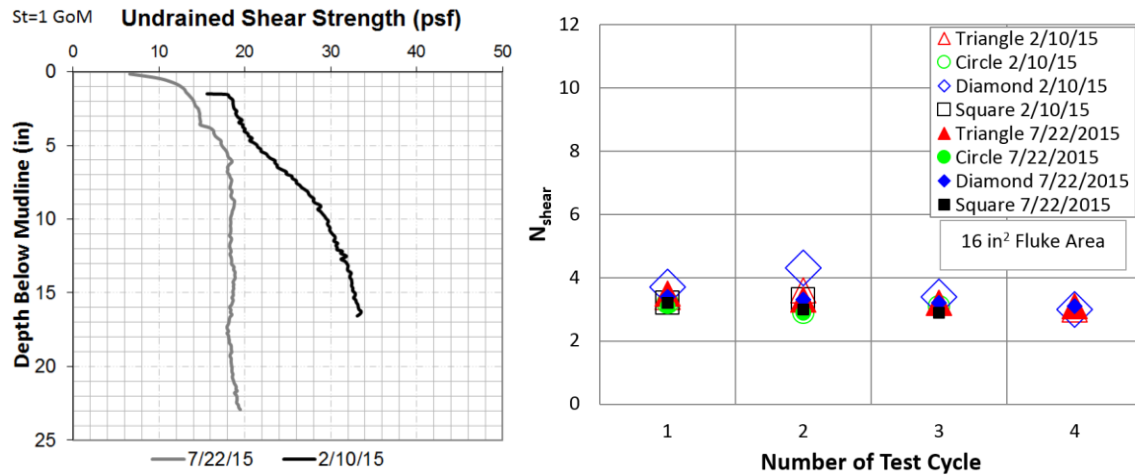
Figure 4.27: Effect of soil strength profile on anchor yield threshold

4.5.5 EFFECT OF SOIL SENSITIVITY

The results presented in Figure 4.28, Figure 4.29, and Figure 4.30 show increase in soil sensitivity decreases the measured and calculated pure loading yield thresholds. The results are obtained by testing anchor models in kaolinite and Gulf of Mexico marine clay with remolded soil ($S_t= 1$) and sensitivity soil ($S_t=1.7$) and by theoretical calculations. The effect of soil sensitivity on the pure shear loading yield threshold is significant while it is negligible on the pure normal loading and pure pitch loading pure yield thresholds. The theoretical calculations are consistent with experimental measurements.
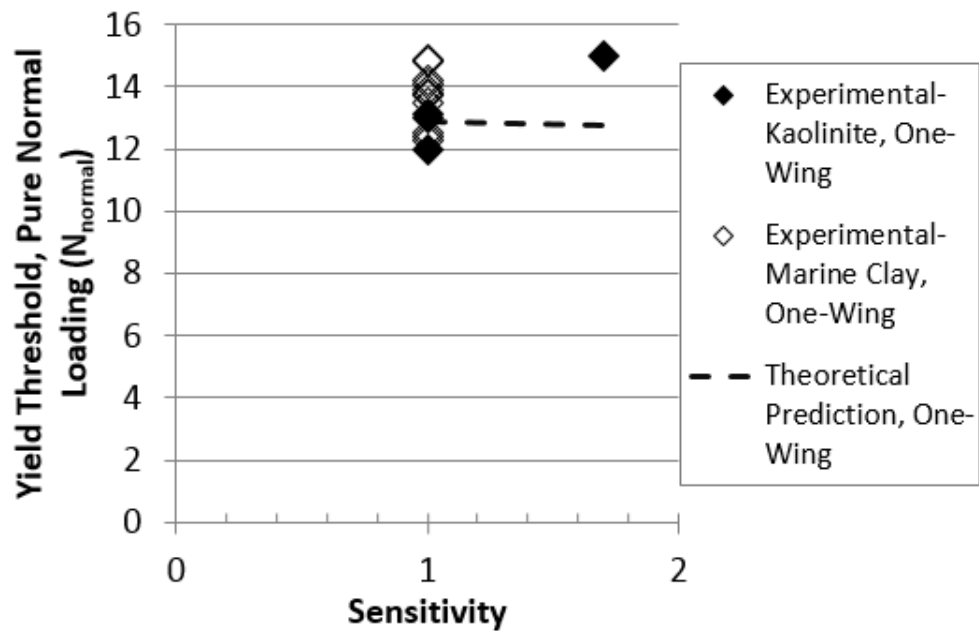
Figure 4.28: Effect of soil sensitivity on pure normal loading yield thresholds for bearing plates
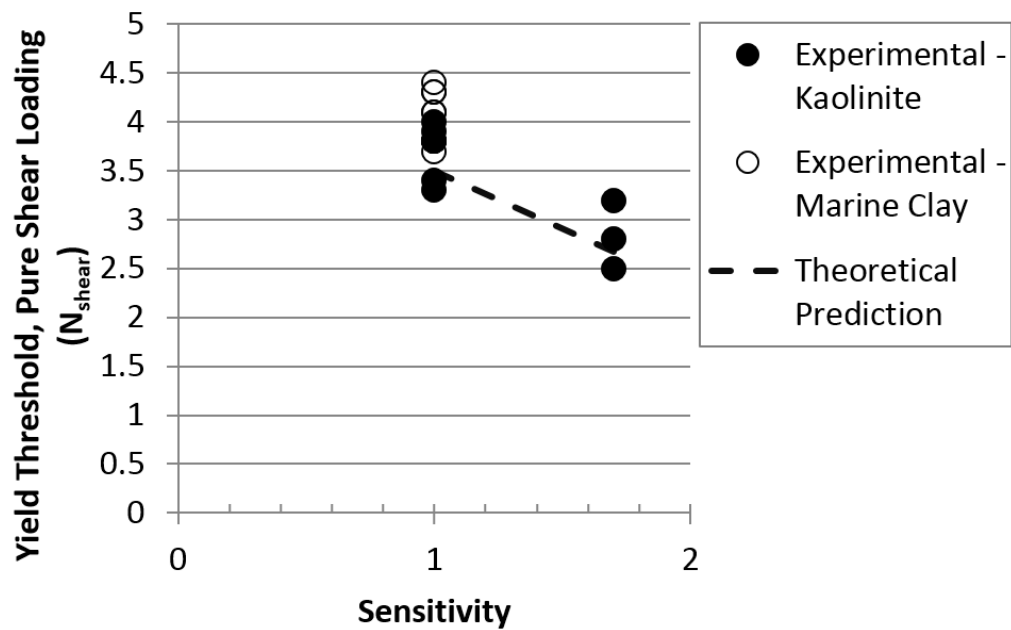
Figure 4.29: Effect of soil sensitivity on pure shear loading yield thresholds for bearing plates
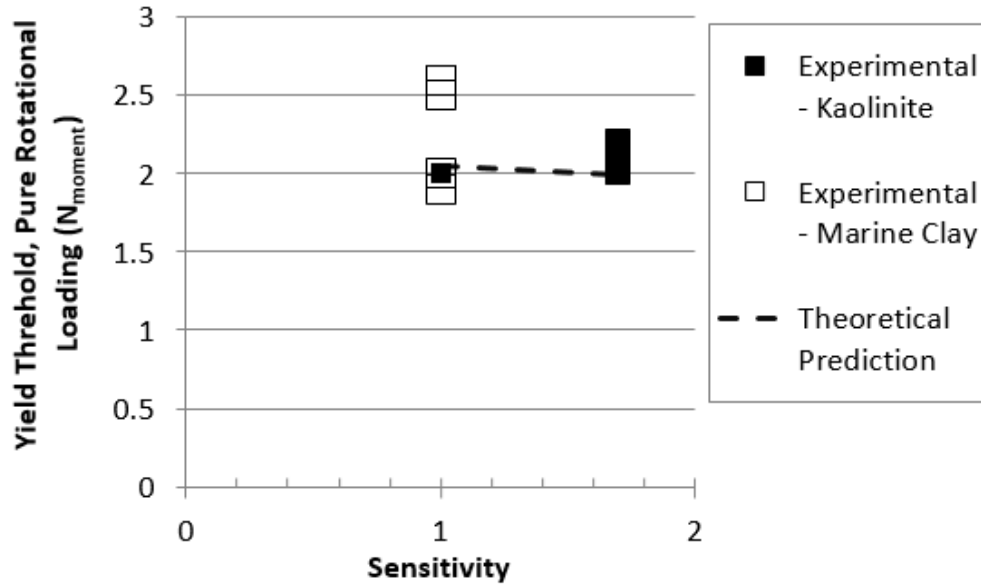
Figure 4.30: Effect of soil sensitivity on pure rotational loading yield thresholds for bearing plates

4.5.6 EFFECT OF LOADING ROD

For the normal loading tests, the same insertion rod was used for all anchor models. The insertion rod was levelled at the beginning of the test to make sure it is vertical (angle with the mudline is 90 degrees). Comparing the tests conducted in the same test soil bed and under the same loading conditions, the insertion rod's effect on the formation of full-flow mechanism is more significant for smaller anchor models (Figure 4.31). The net t-bar resistance calculated by removing the friction of the insertion rod during insertion and extraction are presented in Figure 4.32. T-bar results show that when the t-bar is pushed into soil with the insertion rod behind it, the measured resistance is higher than the extraction resistance measured as the t-bar is pulled out with the insertion rod in front of it. This shows during t-bar testing, having the insertion rod in front of the displacement direction also causes the insertion rod to interact with the soil failure mechanism and decreases the measured resistance.
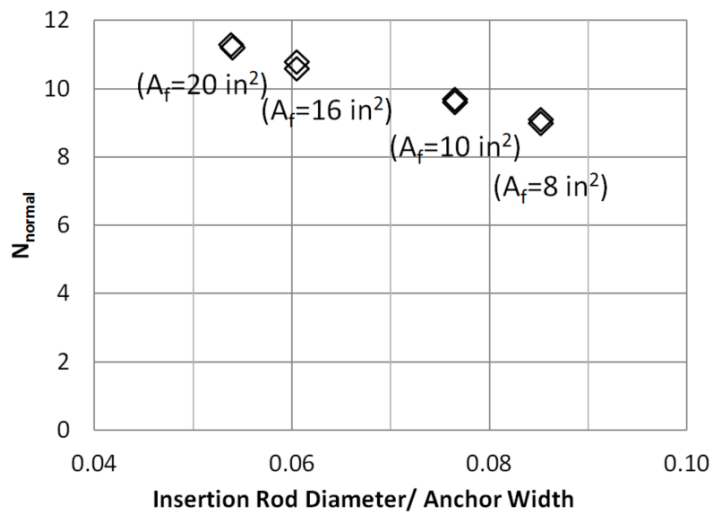
Figure 4.31: Effect of insertion rod size on the anchor resistance to pure normal loading
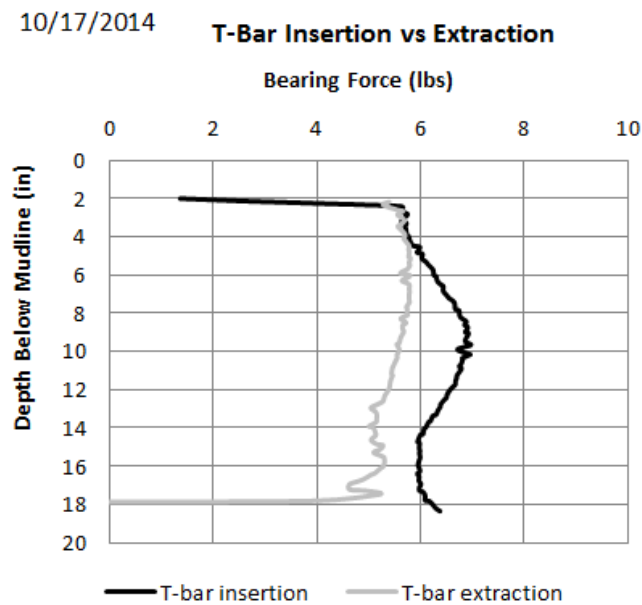
Figure 4.32: Comparison of t-bar insertion and extraction resistances

A 4 in^2 circle bearing plate was prepared and tested in the kaolinite to compare the differences between push-in and pull-out resistances with the insertion and extraction resistances of the t-bar, which also has a projected area of 4 in^2. The pull-out and push-in

91

resistances during pure normal loading of circle shaped bearing plates with fluke areas of 4 in^2 and 16in^2 are presented in Figure 4.33 and Figure 4.34. The t-bar insertion and extraction resistances measured in the same soil test bed are presented in Figure 4.35. The same insertion rod is used for all tests. Results show that for circle plate with 4 in^2 fluke area and the t-bar, the resistances during pulling out of the soil are less than the resistances measured during pushing into soil. The insertion rod is in front of the plate/t-bar during pulling out while it is behind it during pushing in. Comparing the push-in and pull-out net anchor resistances with the 16 in^2 fluke area bearing plate, the differences in resistances are less significant than the differences measured with testing 4 in^2 fluke area bearing plates.
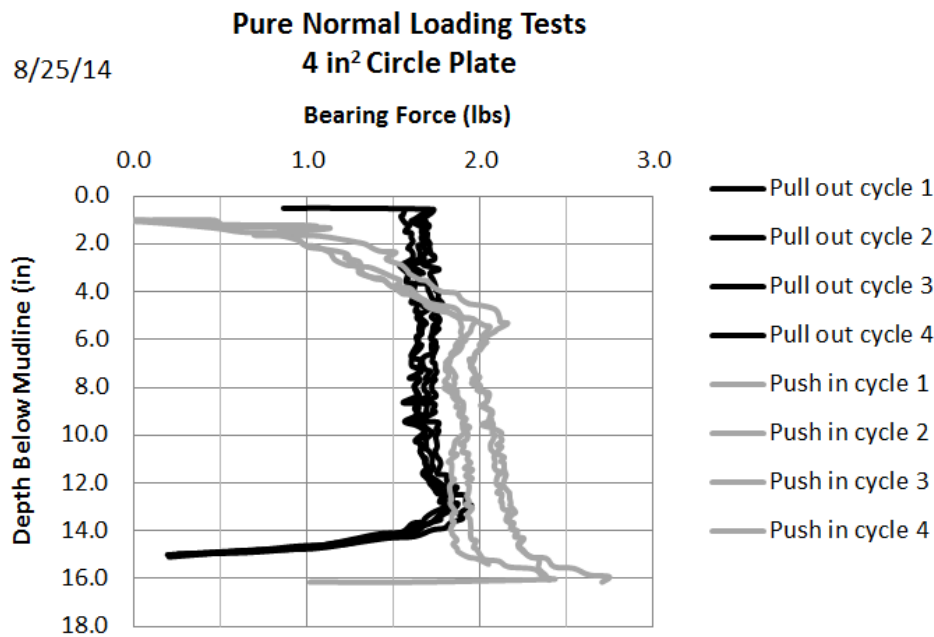
Figure 4.33: 4in^2 circle bearing plate push-in and pull-out resistances
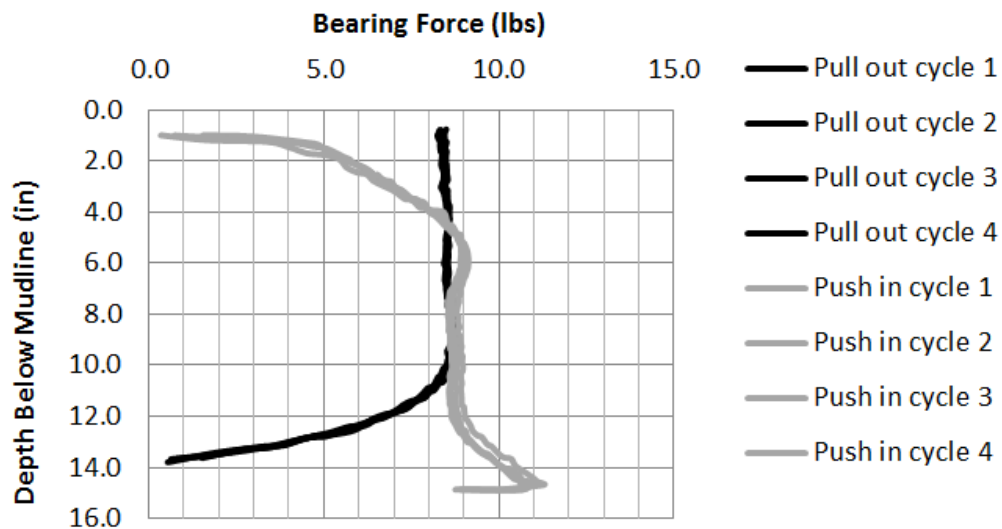
Figure 4.34: 16in^2 circle bearing plate push-in and pull-out resistances
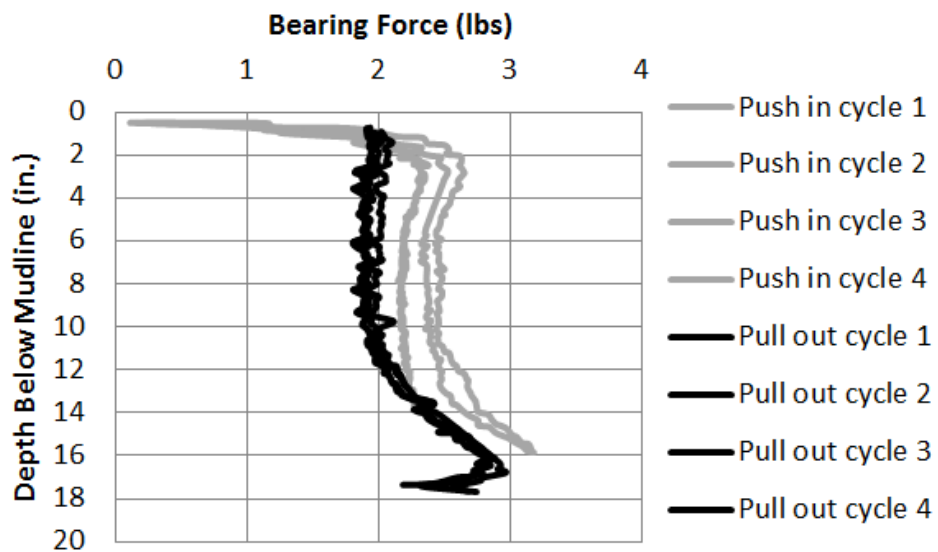
Figure 4.35: Insertion and extraction resistances during t-bar test

93

Results show that having an insertion rod in front of the plate during testing can significantly affect the measured resistances by interacting with the soil failure mechanism if the plate area is small. This interaction can be minimized by increasing the bearing plate area, using a thinner rod or a loading line, or keeping the insertion rod behind the plate during loading. If a larger bearing area is chosen, the main limitation is the soil tank dimensions. Using a thinner rod may not be feasible in the experimental testing conditions since it is mounted to the load cell on the other side. Other option is to use a loading line but in that case it is important to restrict anchor tilt during testing to ensure anchor is loaded in pure loading rather than combined loading. Having the insertion rod behind the plate is not always feasible since pushing plates into soil may require high loads. This also explains the lower N_{normal} values between 10-12 compared to the values between 12-15. When the plate fluke area is smaller (4-10 in^2) and the plate is pulled out of soil with the insertion rod in front of the plate, N_{normal} values between 10-12 are calculated. When larger fluke areas (such as 20 in^2) are pushed-in or pulled-out, the effect of insertion rod on the measured N_{normal} is negligible and values between 12-15 are measured. Simple bearing plates with 16 in^2 area resulted in N_{normal} of 10-12 when pulled-out of soil and 12-14 when pushed-into soil.

4.5.7 EFFECT OF LOADING RATE ON ROTATIONAL PURE LOADING TESTS

The rotational pitch, yaw and roll loading tests are conducted by using a loading line displacement rate of 0.8 in/sec to pull the pulley that rotates the simple bearing plate attached to it. This rate is used as it is also the loading rate for t-bar and pure translational loading tests. The loading rate was selected to have fast loading such that undrained loading conditions occur. To study the effect of rotational rates on the anchor rotational yield threshold, the line displacement rates of 0.4 in/sec and 0.2 in/sec are used to test the

diamond bearing plate with 20 in^2 fluke area. Figure 4.36 shows that the tested loading rates did not affect the measured anchor resistance. At higher rates, increase in the anchor resistance is expected as the shear strength of the soil increases with increasing shear strain rate but the tested line displacement rates resulted in similar pure loading yield thresholds.
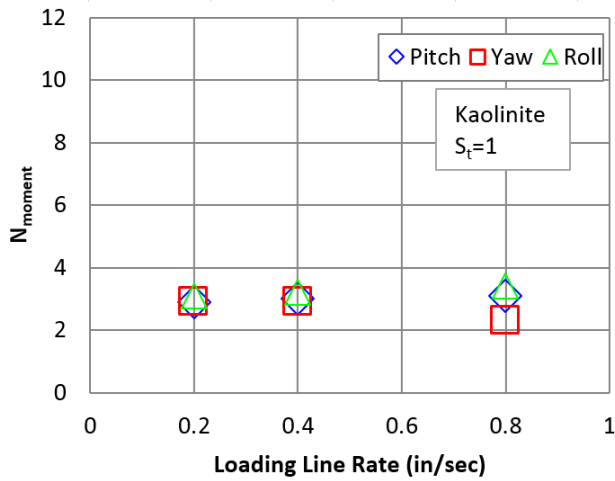
Figure 4.36: Effect of loading rate on rotational pure loading

4.6 CONCLUSIONS

This chapter presents the experimental and theoretical studies conducted to develop the understanding of pure loading yield thresholds of simple shaped bearing plates that are symmetrical along the longitudinal axis in remolded clay under undrained loading. The anchor resistances under pure loading conditions are presented in terms of non-dimensional pure loading yield thresholds that are calculated by normalizing the net anchor resistance with the anchor fluke area and the undrained shear strength of the soil.

The simple shaped bearing plates are tested in remolded clay under undrained loading and pure loading yield thresholds are calculated as: N_{normal} in the range of 10-15, N_{shear} in the range of 3.3-4.4 and N_{moment} in the range of 1.9-2.6 were measured during the

tests in remolded clay. The measured pure shear loading yield thresholds for the bearing plates are also comparable to theoretical predictions and approximately 1/3rd of the pure normal loading yield thresholds.

The results show that, for the same soil and testing conditions, plate area and plate thickness, there is no significant effect of the anchor shape on the anchor yield threshold for simple geometry bearing plates that are symmetrical along the longitudinal axis. Comparing triangle, diamond and square shaped bearing plates, it is decided that the most accurate way to theoretically calculate pure shear loading yield threshold is to ignore the contribution of the reverse end bearing and assumd the front projected area is acting in bearing. Also the calculation method does not depend on the geometry of the anchor front area while tested in shear loading.

Results show that the undrained shear strength of the soil, or the type of the clay (kaolinite vs Gulf of Mexico marine clay) does not affect anchor yield thresholds significantly. Experimental measurements and theoretical calculations show that the pure loading yield thresholds decrease with increasing soil sensitivity. This decrease is negligible for pure normal and pure moment loading but it is significant for pure shear loading. The loading rod size can affect the measured pure normal loading yield thresholds significantly by interacting with the failure mechanism of the soil around the bearing plate depending on the direction of loading. When the insertion rod is in front of the bearing plate during loading, it interacts significantly with the soil failure mechanism if the plate bearing area is small. This effect can be minimized by either using small diameter insertion rods (such as loading line) if the insertion rod is going to be in front of the plate during loading or by placing the insertion rod behind the plate during loading. The loading line displacement rates of 0.2 in/sec, 0.4 in/sec and 0.8 in/sec did not result in a significant difference for the measure pure rotational loading yield threshold (N_{moment}).

Chapter 5: Post-Yield Movement of Bearing Plates

5.1 INTRODUCTION AND OBJECTIVES

The objective of this chapter is to assess the post-yield movement and dive trajectory of simple shaped bearing plates that are symmetrical along the longitudinal axis under undrained loading conditions. When the pure loading yield threshold of a simple shaped bearing plate in any of the six-degree-of-freedom direction is mobilized, plate starts to yield in that direction. When the yield thresholds in multiple directions are mobilized simultaneously, the interaction between resistances result in yielding under combined loading. This section initially focuses on experimentally testing and theoretically calculating the mechanics of initiation of post-yield movement for drag embedment anchors and vertically loaded anchors. Based on the initiation of post-yield movement understanding developed by testing the scaled DEA and VLA models, simple shaped bearing plates symmetrical along the longitudinal axis are tested. The post-yield movement of bearing plates are experimentally measured and the results are summarized.

5.2 INITIATION OF POST-YIELD MOVEMENT

To understand the initiation of post-yield movement, drag embedment anchor (DEA) and vertically loaded anchor (VLA) scaled models were tested experimentally. The forces acting on the anchor models were calculated theoretically to the utilization ratios that initiate post-yield movement of conventional anchor models are analyzed.

5.2.1 PRELIMINARY TESTS WITH DEA AND VLA MODELS

Preliminary anchor drag embedment tests were performed by using the 1:30 scale Drag Embedment Anchor model and Vertically Loaded Anchor model to develop the understanding of initiation of anchor dive penetration with a fixed shank and a freely rotating shank (Figure 5.1).

97
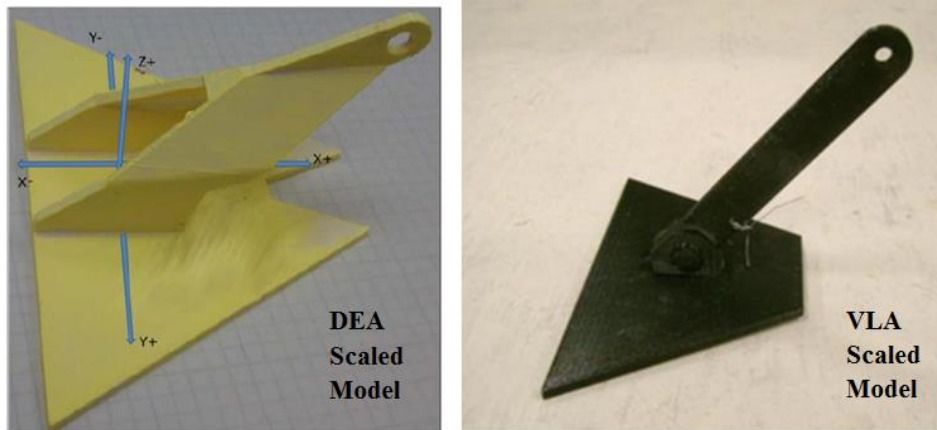
Figure 5.1: The Scaled DEA and VLA models (Aubeny et al., 2011)

Both scaled models were fabricated from acrylic by 3D printing. The angle between fluke and shank of the DEA model is approximately 50 degrees and the anchor weighs 0.072 lbs in air (Aubeny et al., 2011). The anchor model ratio of fluke width to fluke length is 1.5 and which is within the typical range of 1-2 for commercial anchors. The ratio of fluke length to fluke thickness of the fluke is 29, which is on the higher side of the typical range of 5-30 for commercial anchors (McCarthy, 2011). The scaled VLA model weighs 0.109 lbs in air and the volume of the anchor is approximately 2.74 in^3.

Case 1: The DEA model was placed at the mudline with pitch angles between 30 to 90 degrees. The pitch angle of 90 degrees corresponds to vertical fluke while pitch angle of 0 means the anchor fluke is horizontal (Figure 5.2). The increase in pitch angle (clockwise rotation) refers to anchor getting vertical and the decrease in pitch angle (counter-clockwise rotation) refers to anchor getting horizontal. The loading line angle from horizontal changed between 6-10 degrees. Illustration of the testing configuration is schematically presented in Figure 5.3.
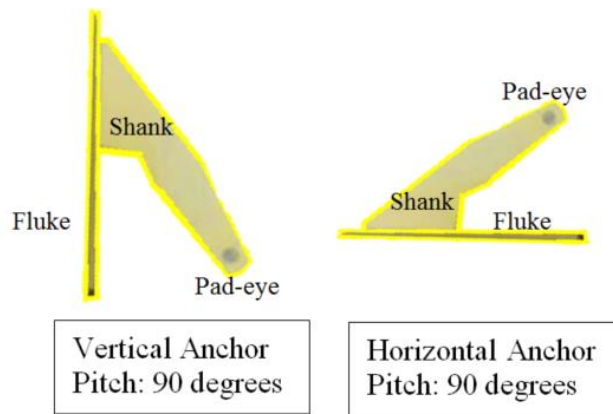
Figure 5.2: DEA model orientations with pitch angle

It is observed that when the anchor initial pitch is between 30-90 degrees, anchor embedded deeper and the anchor pitch was between 30-45 degrees during diving. The pitch kept decreasing (anchor rotates counter clockwise) as the anchor reaches ultimate embedment. McCarthy (2011) previously conducted drag embedment tests using the same DEA scaled model and reported that for initial anchor pitch between 15-80 degrees, the increase in the initial pitch angle resulted in slightly deeper maximum embedment.
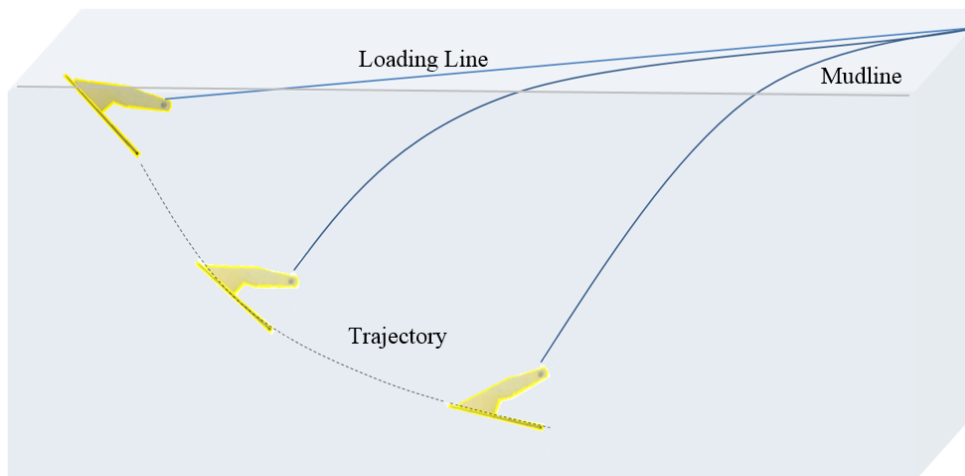
Figure 5.3: Illustration of DEA scaled model testing configuration

Case 2: The VLA scaled model was placed into soil at different penetration depths and initial pitch value with a shank free to move. An illustration example is presented in Figure 5.4. The observations are:

- When the anchor is placed vertically into soil at a depth of 1 fluke length with a shank free to rotate, independent of whether the shank was closed or at an angle from fluke initially, the shank opened up with increasing line load and the anchor rotated clockwise (pitch angle from horizontal increased to 135 degrees). As the fluke-shank angle increased to 90-180 degrees, the fluke was pulled out of soil.

- When the anchor was placed vertically at a depth of 3-4 fluke lengths, with further increase in the line load the shank opened while rotating the anchor (decreasing pitch direction). Anchor did not dive deeper but also it did not get pulled out of the soil and plowed with the shank near perpendicular to fluke.

- When the shank angle was restricted to a maximum of 75 degrees, the VLA model behaved like a DEA. Placing the anchor vertically into soil or at a pitch of approximately 45 degrees, resulted in shank opening up to the 75 degrees. When the shank reached the maximum fluke-shank angle, the anchor started rotating with further loading and dove deeper at a pitch angle approximately equal to 45 degrees.

- The VLA model was placed into soil with an upside-down fluke orientation such that the longer edge of the trapezoid was located deeper than the shorter edge (Figure 5.5). The fluke-shank angle was initially zero and shank was free to rotate. Anchor was placed into soil vertically and fully covered with soil at various embedment depths. With increasing line load, the shank opened and the anchor pitch angle increased up to approximately 135 degrees (clockwise rotation of the anchor), and the anchor got pulled out of soil. It is important to note that when the fluke is placed upside-down, the fluke area above the fluke-shank attachment point is less than the fluke area below the fluke-

100

shank attachment point. Assuming a constant undrained shear strength profile, the soil resistance acting on the fluke area above the fluke-shank attachment point is lower than the soil resistance acting on the fluke area below that point. This shows that the-fluke shank attachment point is very important to avoid anchor rotation in the reverse direction that results in anchor being pulled out of soil.
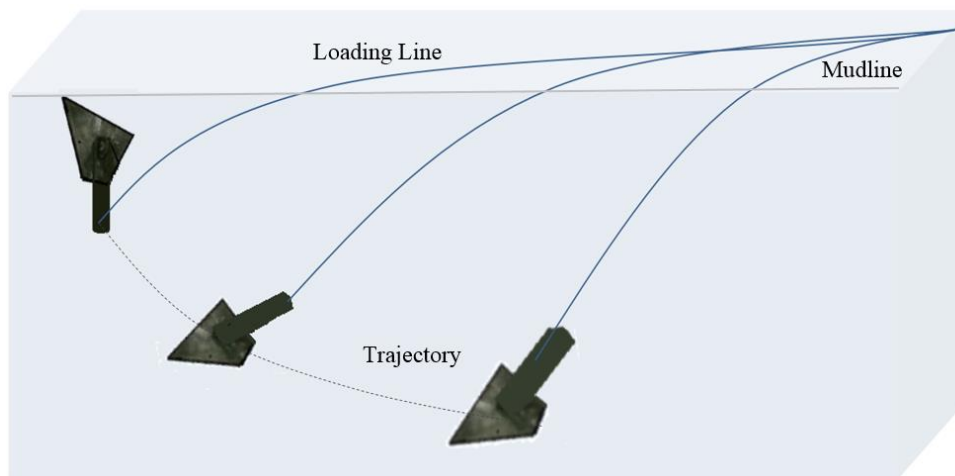
Figure 5.4: Illustration of VLA scaled model testing configuration
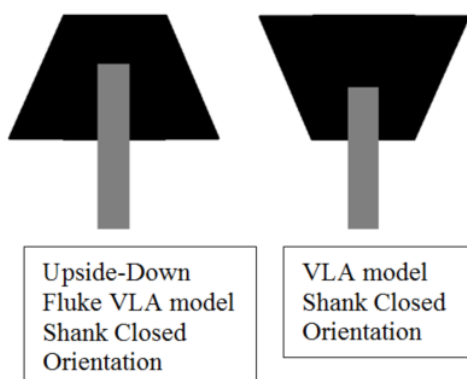
Figure 5.5: Illustration of VLA model fluke upside-down orientation

5.2.2 THEORETICAL CALCULATION OF FORCES

The force mechanics of the scaled DEA and VLA models were calculated to understand the forces acting on the anchor models during dive penetration. The mechanical model developed by Liu et al. (2012) based on the Neubecker and Randolph (1996) model was used to calculate the forces acting on the anchor. This model focuses on the two main structural parts of the anchor: the fluke and the shank. Anchor movement only refers to penetration of the fluke parallel to fluke plane due to drag loading. The detailed anchor areas of the 1:30 scale VLA and DEA models are presented in Figure 5.7 and Figure 5.7. The areas providing shear resistance and bearing resistance were determined for different loading directions and anchor orientations. By assigning theoretical yield thresholds on those areas, the anchor resistance was calculated theoretically.
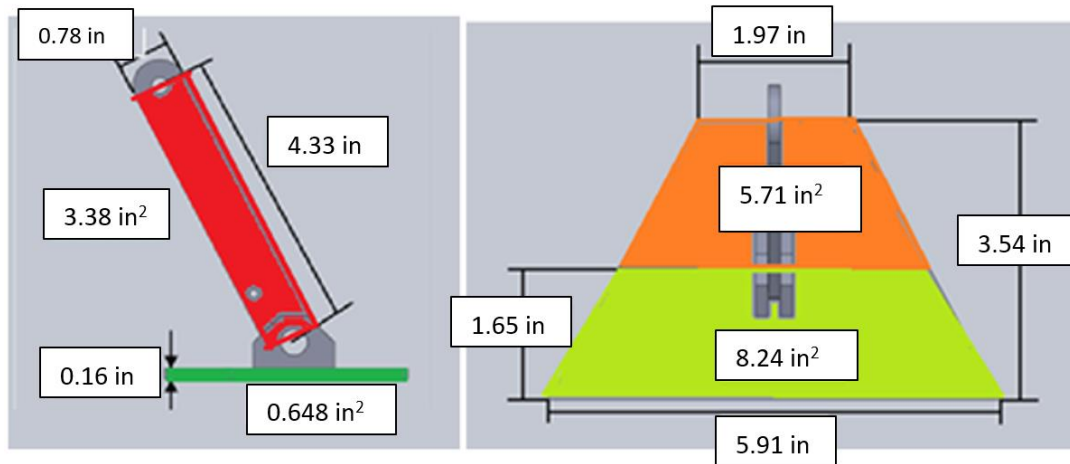
Figure 5.6: VLA 1:30 scaled model dimensions in details
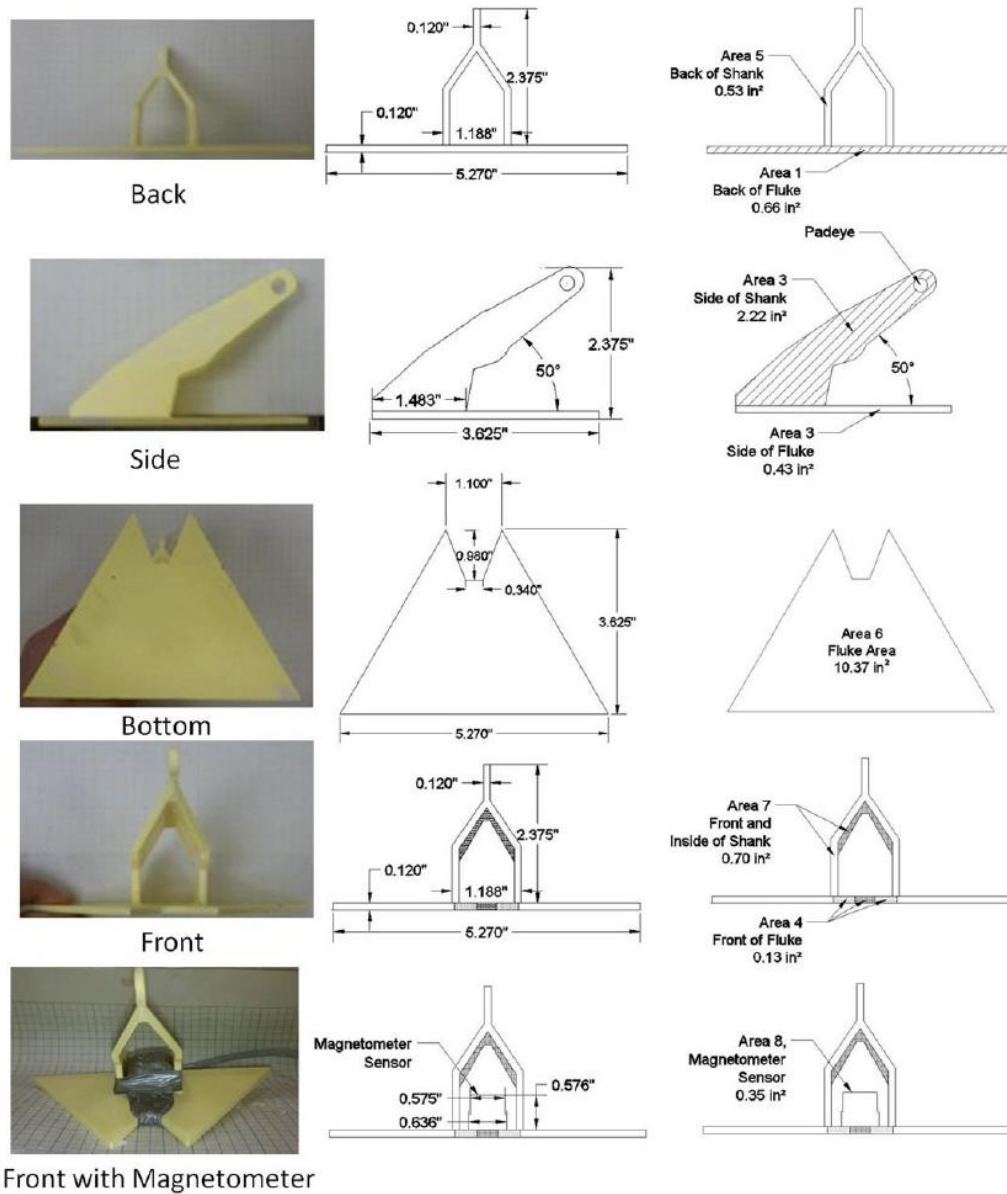
Figure 5.7: DEA 1:30 scaled model dimensions in details (McCarthy, 2011)

Ignoring the anchor weight, forces acting on the scaled anchor model are presented in Figure 5.8. F_a is the line force acting on the pad-eye, F_t and F_n are the components of the line force acting in the fluke parallel and fluke normal directions respectively. The bearing resistance of the anchor (F_b) is the sum of the bearing resistances of the fluke and shank

respectively. The shearing resistance (F_s) is the sum of the shear resistances of fluke and shank respectively.
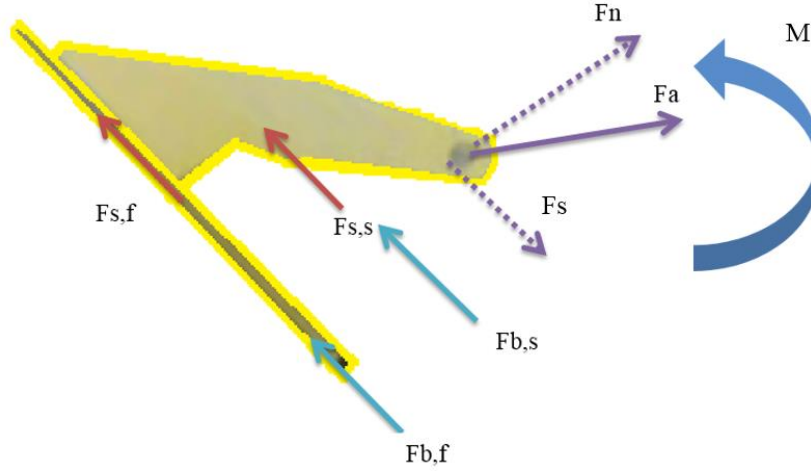
Figure 5.8: Forces acting on the scaled DEA model

The resistance of the anchor model to pure normal, shear and moment loading are calculated by:

$$F_{n,max} = N_{normal} s_u A_f \tag{5.1}$$

$$F_{s,max} = N_{shear} s_u A_f \tag{5.2}$$

$$M_{max} = N_{moment} s_u A_f \sqrt{A_f} \tag{5.3}$$

The post-yield movement initiates when the load acting on the anchor exceeds the anchor threshold in the direction of loading. The experimentally measured N_{normal} of 11, N_{shear} of 4 and N_{moment} of 2.4 (Aubeny et al., 2011) are used to calculate the theoretical yield

thresholds under pure loading conditions. Since the tests are conducted in remolded soil, α is assumed as 1. For the DEA model and VLA with restricted shank rotation, the eccentricities with respect to centroid of the fluke are measured to calculate the applied moment. The utilization ratios for each loading conditions are calculated to determine the primary mode of failure. The utilization ratios are calculated by dividing the applied load in the given direction by the resistance of the anchor in that direction as:

$$u_m = \frac{M}{M_{max}} \tag{5.4}$$

$$u_s = \frac{F_s}{F_{s,max}} \tag{5.5}$$

$$u_p = \frac{F_n}{F_{n,max}} \tag{5.6}$$

where:

u_m: utilization ratio for moment loading

M: applied moment

M_{max}: anchor resistance to pure rotational loading

u_s: utilization ratio for shear loading

F_s: applied shear force

$F_{s,max}$: anchor resistance to pure shear loading

u_p: utilization ratio for normal loading

F_n: applied bearing force

$F_{n,max}$: anchor resistance to pure normal loading

Assuming the line load increases incrementally, the utilization ratios in each of the normal, shear and moment loading are calculated for the given initial anchor orientation

until one of the utilization ratios (u_m, u_s, or u_p) exceeds 1 to theoretically calculate the initial direction of yield for a given pitch angle and shank condition. The calculation stopped when one of the utilization ratios reached 1. The comparison of experimental observations and theoretical calculations with and without including the buoyant weight of the anchor (W') for analyzed orientation and shank condition are presented in Table 5.1 and Table 5.2 for DEA and VLA with free shank. The schematic drawings of the anchor orientations from side view are also included to show anchor initial and final orientation. The straight line refers to mudline. The drawings are not to scale.

Experimental Observations				Calculation		
Initial Orientation		Final Embedment	Observation	Type of Loading	U.R. (%)	
					With W´	Without W´
	Shank at the mudline, fluke is at 45 degrees from vertical, initial pitch is approximately -45°	Embedded Deeper	Movement starts with yielding in shear, pitch decreased to approximately 30° 	In-Plane Shear	100	87.60
				Normal	4.65	4.85
				Moment	50.52	
	Vertical fluke, initial pitch -90°	Embedded Deeper	Movement starts with rotation. Pitch decreased to 45° 	In-Plane	3.42	3.37
				Normal	24.33	24.33
				Moment	100	

Table 5.1: Comparison of experimental observations and theoretical calculations for DEA model

Experimental				Calculation		
Initial Orientation		Final Embedment	Observation	Type of Loading	U.R. (%)	
					With W′	Without W′
	Shank at the mudline, initial pitch is 45 degrees	Embedded Deeper	Movement starts with yielding in shear, pitch decreases to approximately 30 degrees (like the DEA)	In-Plane Shear	**100**	100
				Normal	46.58	46.98
				Moment	5.85	
	Vertical fluke, fluke-shank angle is 45 degrees, initial pitch 90 degrees	Pulled out	Movement starts with yielding in bearing. Shank opened more than 90 degrees. Fluke turned to the opposite direction, anchor got pulled out	In-Plane Shear	54.66	53.53
				Normal	**100**	100
				Moment	22.72	
	Shank and fluke are vertical, initial pitch 90 degrees, initially shank is closed Fully embedded			In-Plane Shear	70.25	70.25
				Normal	**100**	100
				Moment	22.20	
	Vertical fluke horizontal shank (90 degrees from fluke), fully embedded			In-Plane Shear	64.83	61.83
				Normal	**100**	100
				Moment	23.13	
	Vertical shank, fluke-shank angle is 92 degrees, concentric loading, zero moment case, fully embedded			In-Plane Shear	59.81	56.60
				Normal	**100**	100
				Moment	0	

Table 5.2: Comparison of experimental observations and theoretical calculations for VLA model with free shank

The results can be summarized as:

- For the DEA model with a fixed shank and VLA model with a free shank, when the anchor is initially embedded at a pitch angle of approximately 45 degrees with

the shank at the mudline, the initial mode of failure is yielding in in-plane shear direction as u_s exceeds 1 before u_m or u_p equals to 1.

- When the DEA model with fixed shank is placed vertically into soil, with increasing line load the initial mode of failure is anchor rotation from vertical as u_m exceeds 1 before u_s or u_p equals to 1.

- When the VLA model with free shank is placed vertically into soil, the initial mode of failure is bearing failure as u_p exceeds 1 before u_m or u_s equals to 1.

5.2.3 RESULTS OF THE INITIATION OF ANCHOR DIVE ANALYSIS

The initiation of anchor dive analysis is conducted to understand the force mechanics that initiate the post-yield movement for drag embedment anchors and vertically loaded anchors. Experimental tests conducted by scaled DEA and VLA models were used to test different anchor pitch angles and shank conditions. Utilization ratios in direction of shear, normal and moment loading were calculated. Theoretical results were compared with experimental observations to check if the initiation of anchor dive penetration can be predicted by the calculated utilization ratios. Results show that calculating the utilization ratios is an accurate way of predicting initiation of anchor dive penetration. For an anchor embedded into soil with a shank free to rotate, the anchor dive initiation depends on multiple variables, such as:

- Anchor loading line geometry and load,

- Shank restriction and shank angle from fluke,

- Fluke-shank attachment point,

- Anchor pure loading capacity in shear, normal and moment loading,

- Anchor initial pitch,

108

- The initial embedment of the anchor; if it is fully embedded or partially embedded.

Analyzing the experimental results and theoretical calculations the results can be summarized as:

(1)   The initial mode of failure is important for understanding if the anchor will be pulled out of soil or embed deeper with further loading.

(2)   When the anchor models with fixed shank were embedded into soil at a pitch angle between 30-60 degrees, the post-yield movement initiated with in-plane shear movement. The anchor continued diving deeper with further loading.

(3)   When the VLA model was initially embedded into soil vertically with a shank free to rotate, increasing line tension rotated the shank. The shank opened up to an angle greater than 90 degrees from fluke plane and the anchor was pulled out of soil by clockwise rotation (increasing pitch) and shear in reverse direction (Figure 5.9). Theoretical calculations show the anchor normal resistance was mobilized before shear resistance thus anchor was not able to embed deeper.
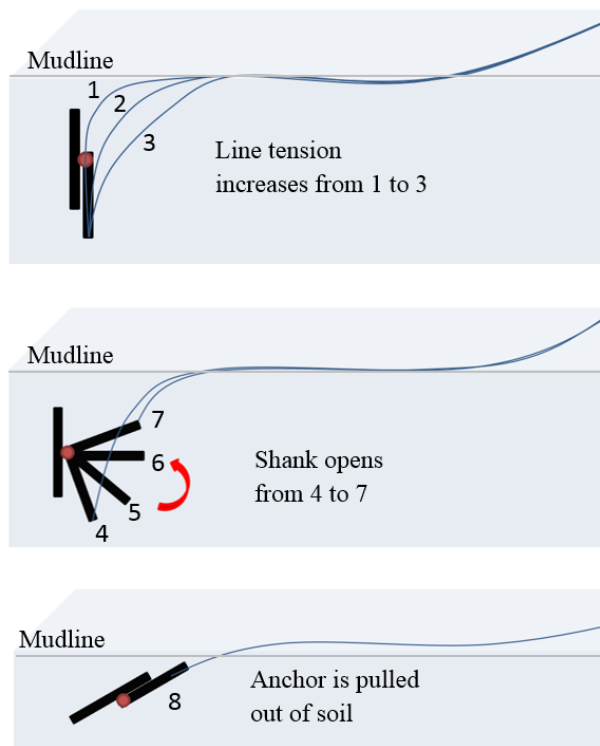
Figure 5.9: Anchor pull-out with free shank after free-fall penetration

(4)   When the anchor models were initially vertical, the anchor needs to rotate in the counter clock-wise rotation to achieve dive penetration with further loading.

(5)   When the shank is connected at the anchor center of resistance and free to rotate, it does not transfer any moment that can rotate the anchor.

(6)   To have rotation as the initial mode of failure, the shank should be held attached to fluke at the beginning of loading. The distance between anchor shackle and fluke-shank connection point creates an eccentricity. The load applied at the shackle applies a moment at the fluke-shank connection point. Anchor starts to rotate from vertical (counter-clock wise rotation, decreasing pitch) when the moment capacity of the anchor is exceeded. If the shank is released after the fluke pitch is between 30-60 degrees, the rotation stops and anchor starts to dive deeper.

110

(7) The fluke-shank attachment point affects anchor behavior significantly. For a vertically embedded anchor, if the shank is attached above center of resistance, the soil pressure acting on the fluke area lower than the shank attachment point rotates the anchor in the clock-wise rotation. This causes anchor to be pulled out of soil.

(8) Having a free shank when the anchor pitch is approximately 45 degrees, causes anchor to dive deeper if there is no eccentricity to cause moment. In that case shank gets aligned with the loading line, the utilization in shear loading is mobilized before the utilization in normal loading is mobilized. The anchor starts to dive in the direction parallel to fluke.

(9) When the opening degree of the shank of the VLA is restricted to a certain degree from fluke plane, the VLA anchor performs like a DEA. With increasing line load, the shank opens until the restriction angle and anchor post-yield movement initiates with rotation. Once the anchor pitch is approximately 45 degrees; it starts to yield in shear direction. It continues diving deeper while pitching until the ultimate embedment is reached.

(10) To initiate dive penetration after anchor starts to move, the shear capacity of the anchor should be mobilized before its normal loading capacity is mobilized. The line force should have a component parallel to anchor fluke plane that tries to embed the anchor deeper. The anchor configuration with a free shank aligned with loading line is presented in Figure 5.10. The magnitude of this force depends on the line load (F_a), line angle from horizontal (θ_a), shank angle from fluke plane ($\theta_{fs} = \theta_a + \theta_f$), and the fluke pitch from horizontal (θ_f). For a given line load, the utilization ratios are calculated for shear loading and normal loading as:

111

$$u_s = \frac{F_s}{F_{s,max}} = \frac{T_s \cos\theta_{fs}}{N_{shear} s_u A_f} \qquad (5.7)$$

$$u_p = \frac{F_n}{F_{n,max}} = \frac{T_a \sin\theta_{fs}}{N_{normal} s_u A_f} \qquad (5.8)$$

Mudline
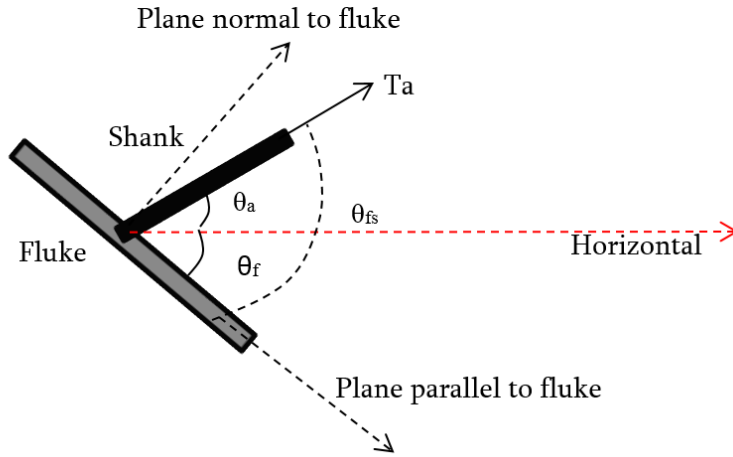
Figure 5.10: Anchor configuration after shank is released

If the utilization ratio in shear direction is mobilized before the utilization in normal direction, then the anchor starts diving deeper. This depends on the shank angle from fluke plane and the anchor yield thresholds in pure normal and pure shear loading directions.

5.3 POST-YIELD ANALYSIS OF BEARING PLATES

Simple geometry bearing plates symmetrical along the longitudinal axis were tested under drag embedment loading to observe dive trajectory. The testing setup, scaled model properties, and results are summarized in this section.

5.3.1 TESTING SETUP AND BEARING PLATE MODELS

Preliminary drag embedment tests were performed with using simple geometry one-wing and bi-wing bearing plates that are symmetrical along the longitudinal axis. Test models were: diamond shaped bearing plate with 20 in^2 fluke area and 0.43 in thickness (Figure 5.13); diamond, trapezoid, triangle and bi-wing bearing plates (two trapezoids connected) with 14 in^2 fluke areas and 0.2 in thickness (Figure 5.11). A very thin loading line (nylon rope with a diameter of 0.025in.) was used to reduce soil friction along the loading line. The magnetometer was not used during these tests to eliminate any effects that might be caused by attaching the magnetometer sensor on the anchor model or the thick magnetometer line. The 0.1 in. thick rods with measurement marks were attached at the back of the bearing plates. The measurement rods were used to observe the change in plate rotation and penetration depth during drag embedment loading. Also it provides visual observation of the initiation of post-yield movement. The bearing plates were fully embedded at the beginning of the test and the measurement rod extended outside of soil (Figure 5.12).

The loading line acts like a shank free to rotate and connects directly to the bearing plate. The loading line was attached to different locations on the bearing plate line of symmetry to study the difference in post-yield movement caused by changing the fluke-shank attachment location. Figure 5.13 shows the loading line attachment points on the diamond shaped bearing plate. The c_m represents the center of mass of the constant thickness bearing plates. The model presented in Figure 5.13 shows the direction it is embedded into soil: point 1 was above the center of mass and points 2-5 are below the center of mass when the plate was embedded near vertically into soil after free-fall penetration.

113
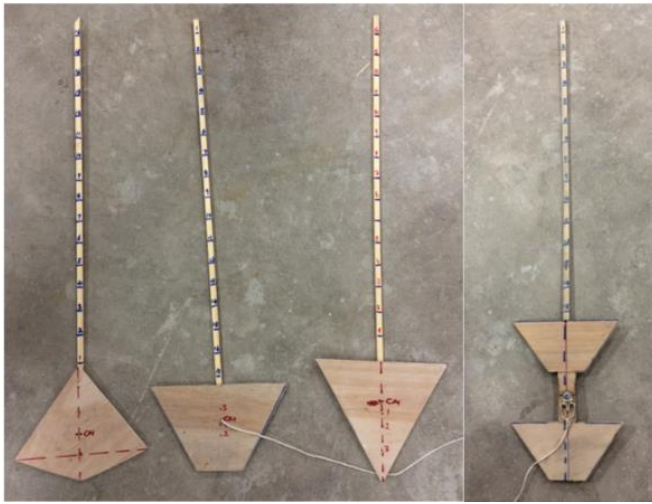
Figure 5.11: Bearing Plates for preliminary drag embedment tests
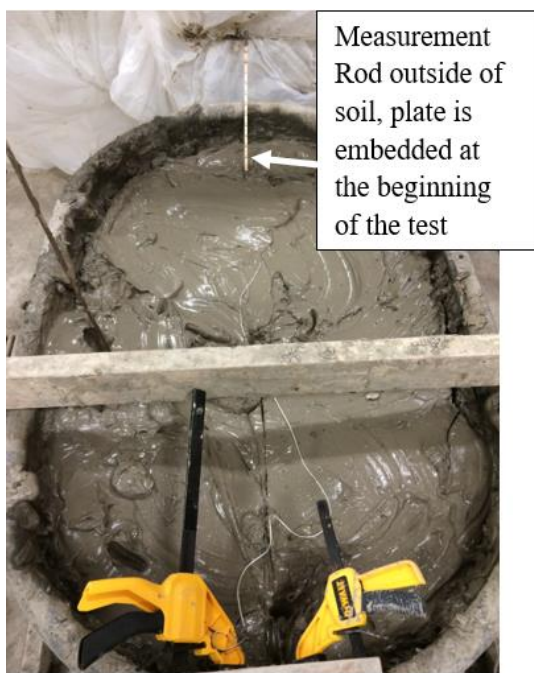
Figure 5.12: Measurement rod attached to bearing plate, beginning of test
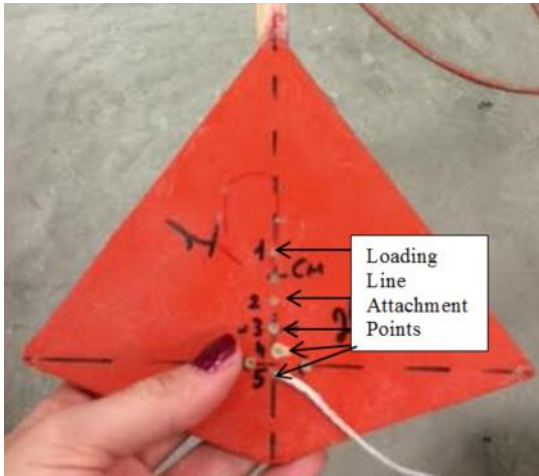
Figure 5.13: Diamond bearing plate with different line attachment points

The bearing plates were placed fully embedded into soil at pitch angles of 30, 45, and 60 degrees. The initial pitch was measured approximately by measuring the measurement rod angle from horizontal by using a protractor. The bearing plates were placed at different initial depths. The initial depth of the anchor was calculated by measuring the depth of soil layer located on the highest point of the anchor. It varied from 0.5 inches to 3 inches. The illustration of anchor orientation at the beginning of the test is presented in Figure 5.14.
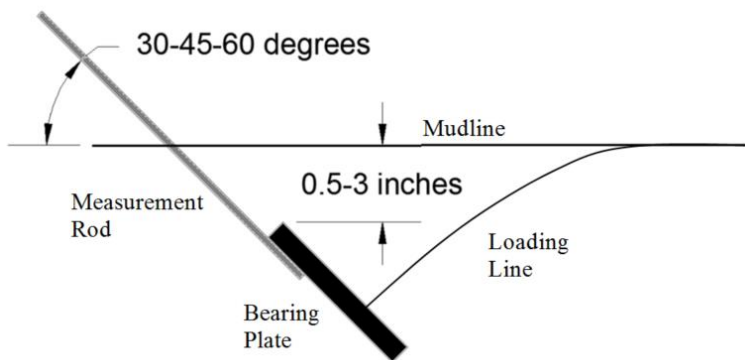
Figure 5.14: Illustration of the initial anchor orientation

115

The anchor models were tested in Gulf of Mexico marine clay test bed with constant shear strength profile. An example undrained shear strength profile is presented in Figure 5.15.

Since some of the tests were conducted by placing the anchor close to mudline, it is important to know the undrained shear strength profile couple of inches below the mudline as well. It is not possible to accurately measure the undrained shear strength of the soil within 4 inches from mudline since the full-flow failure mechanism cannot be fully formed while using a t-bar test. Water content samples taken by a custom-made split spoon sampler was used to measure the water content throughout the depth of the soil layer. As Figure 5.15 shows, the water content was almost constant throughout the soil test bed which indicates the undrained shear strength was also constant. It shows that the undrained shear strength of the soil within 4 inches of depth from mudline was also similar to the rest of the soil depth.
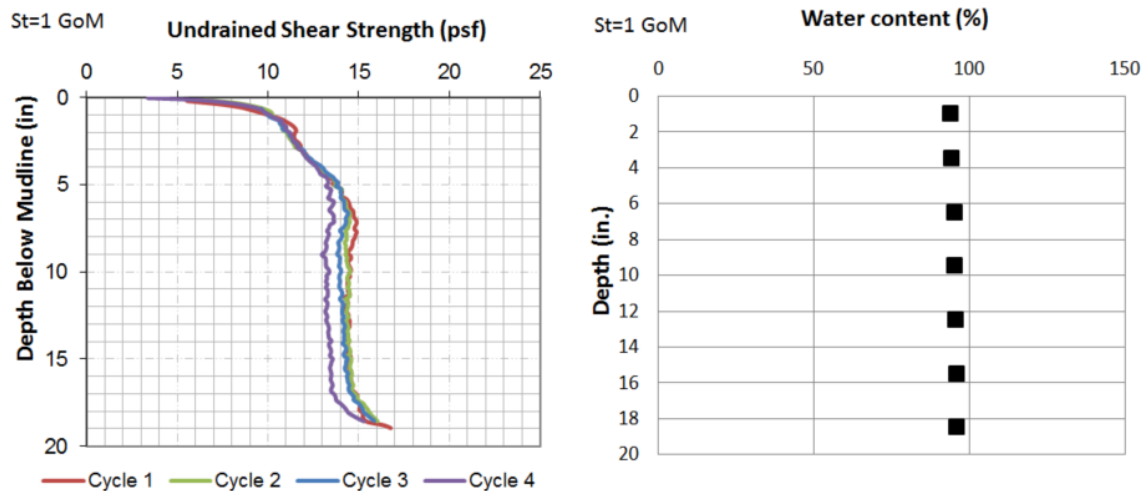
Figure 5.15: Undrained shear strength and water content profile, Gulf of Mexico (GoM)test bed

5.3.2 RESULTS OF PRELIMINARY POST-YIELD ANALYSIS OF BEARING PLATES

After the anchors were placed at their initial locations, they were dragged up to 4.5 equivalent fluke lengths horizontally. The results obtained by the bearing plate dive trajectories are:

(1)   The bearing plate post-yield movement was initiated by rotation from the initial pitch angle. This rotation was followed by yielding in the in-plane shear direction when the plate pitch was approximately 45 degrees. For all initial pitch angles, plate pitch decreased slowly (anchor gets closer to being horizontal) while the plate was penetrating deeper. This approximate angle of 45 degrees was measured for models with pure normal loading yield threshold to pure shear loading yield threshold ratio of approximately 3.

(2)   The anchor trajectory did not change significantly for different geometry bearing plates symmetrical along the longitudinal axis with shapes of diamond, trapezoid, triangle and bi-wing.

(3)   Plates embedded deeper if the loading line was attached at the fluke center of mass or any point below that.

(4)   When the loading line was attached above the fluke center of mass, the plate was pulled out of soil during drag embedment loading.

(5)   The maximum embedment depths were achieved when the loading line was attached at the anchor center of resistance.

(6)   Using a thin loading line minimized the soil friction acting on the loading line. Also the thin loading line obtained a taut configuration resulted in more accurate calculations of the line angle.

The post-yield movement analysis of simple shaped bearing plates show that the plates initially rotated to approximate pitch angle of 45 degrees and failed in in-plane shear

117

loading. The post-yield movement is depended on the loading line attachment point on the bearing plate. The maximum penetration depths were obtained when the line was attached on the plate center of resistance.

For a constant thickness bearing plate, the center of area and center of pressure are identical. The change in the center of pressure location for increasing undrained soil strength is analyzed theoretically. The diamond, trapezoid, triangle and bi-wing shapes tested experimentally are analyzed theoretically based on the calculations prepared by Giampa (2015) that focuses on the soil pressures acting on a bearing plate embedded fully into soil. Giampa (2015) divided each plate length into 20 equal slices and calculated the net pressures acting on each slice when the plate has initial pitch angles of 30, 45, 60 and 90 degrees (90-degree: vertical plate). The z distance is measured from the top of the anchor such that maximum z equals to the plate length (Figure 5.16). For a plate embedded at a certain pitch angle, the vertical and horizontal soil stresses acting on an example slice at the plastic equilibrium state are presented in Figure 5.17.
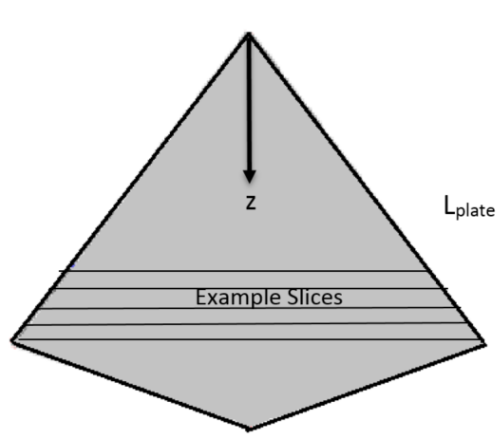
Figure 5.16: Diamond shape front view, measurement of z
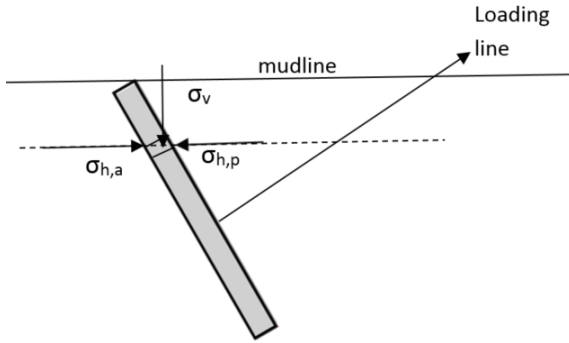
Figure 5.17: Soil stresses acting on a slice

The horizontal active and passive pressures are calculated by using Rankine's Theory (1857). For the undrained clay (ϕ=0) condition the coefficient of Rankine's active earth pressure (K_a) and coefficient of Rankine's passive earth pressure (K_p) are equal to 1. Thus the net horizontal stress can be calculated as:

$$\sigma_v = \gamma z \tag{5.9}$$

$$\sigma_{h,a} = \sigma_v - 2c \tag{5.10}$$

$$\sigma_{h,p} = \sigma_v + 2c \tag{5.11}$$

$$\sigma_{h,net} = 4c = 4s_u \tag{5.12}$$

where γ is the unit weight of soil and c is the cohesion. Giampa's (2015) analysis of center of pressure of plates in soil test bed with constant undrained shear strength profile are extended to soil test beds with linearly increasing soil strength profile. Assuming different $s_{u,0}$ (undrained soil strength at the mudline) and k gradient (increase in soil

strength with depth), the center of pressure (COP) are calculated for each pitch angles. Cheon (2010) presented in Figure 5.18 as the undrained shear strength profile with depth for Gulf of Mexico marine clay site. To study the effect of k on the location of center of pressure, the k values between lower and upper bounds of 10-14 psf/ft for the Gulf of Mexico marine clay are analyzed. The $s_{u,0}$ of 0, 5 and 10 psf are studied.
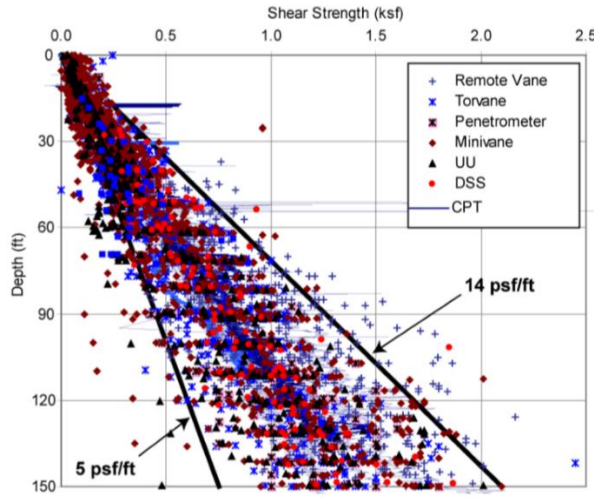
Figure 5.18: An example undrained shear strength profile for Gulf of Mexico

Giampa (2015) calculated the center of pressure (COP) for the plate by calculating the sum of the forces acting on each slice (F_i) and multiplying with the moment arm (x_i) then dividing the resultant with the sum of forces (ΣF_i).

$$COP = \frac{\sum_{i=1}^{20} F_i x_i}{\sum_{i=1}^{20} F_i} \qquad (5.13)$$

The comparison of results is presented in Figure 5.19-Figure 5.22 for diamond, trapezoid, triangle and bi-wing shaped plates. In all cases, the center of pressure does not change with increasing pitch angle. When the undrained shear strength profile is constant

with depth, the center of pressure coincides with the center of area. The center of pressure shifts below when the plate is in soil test bed with undrained shear strength profile linearly increasing with depth. For the mudline strength of 0, the k between 5-14 psf/ft did not cause any difference for the analyzed plates. For a constant k gradient, increasing mudline strength also causes the center of pressure to shift further down as the lower part of the anchor is subjected to higher soil stresses.
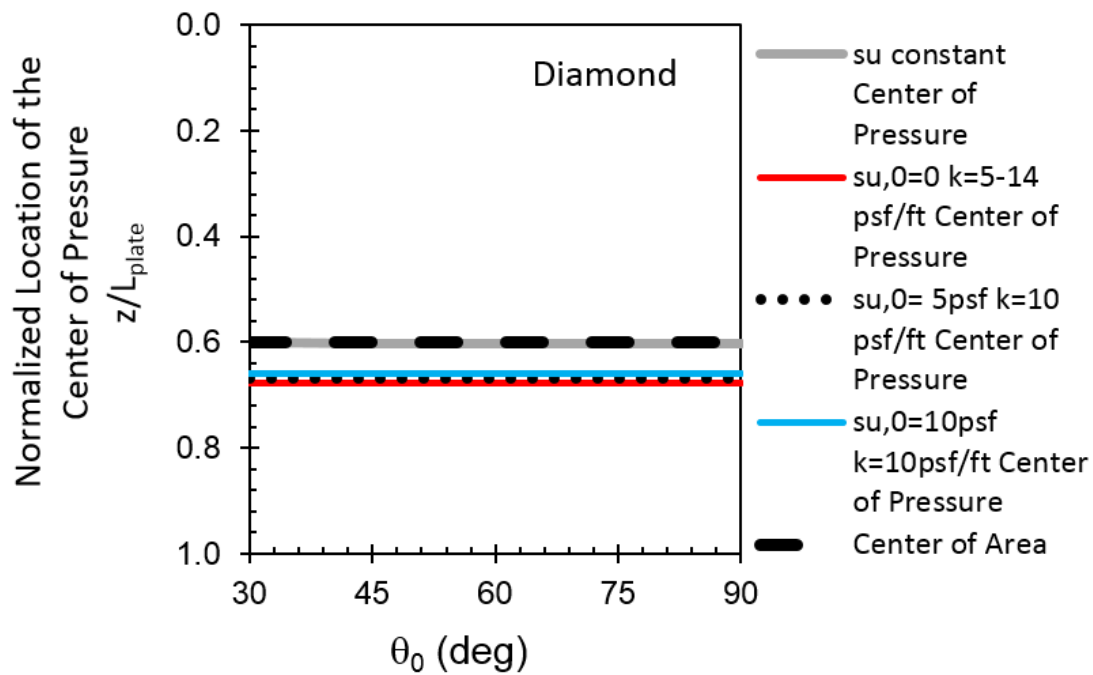
Figure 5.19: Change in center of pressure diamond plate
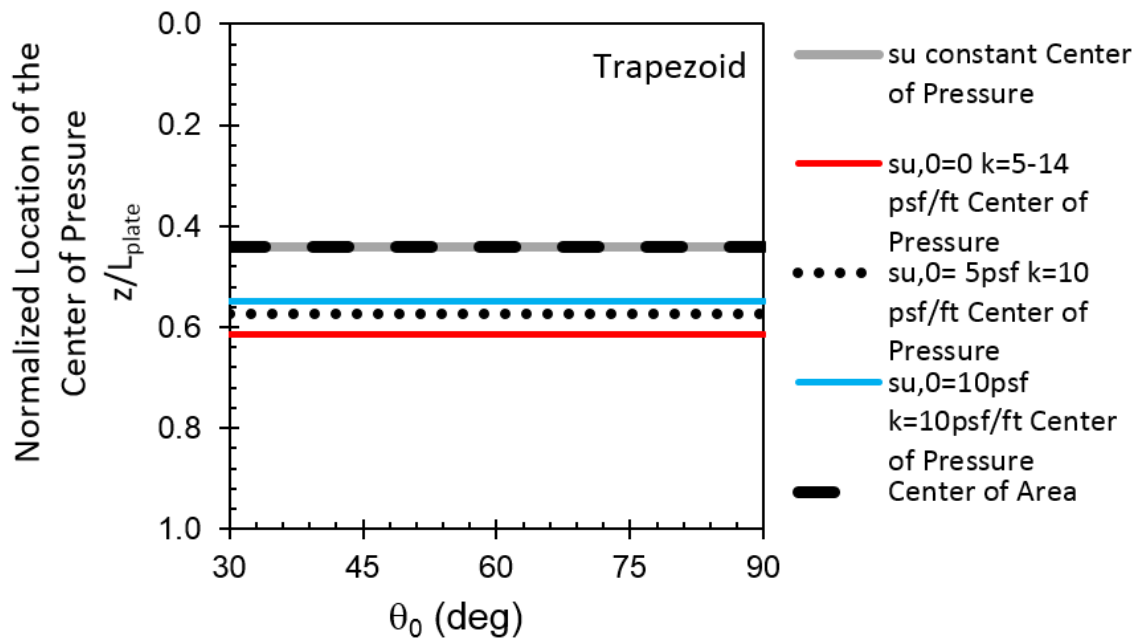
Figure 5.20: Change in center of pressure trapezoid plate
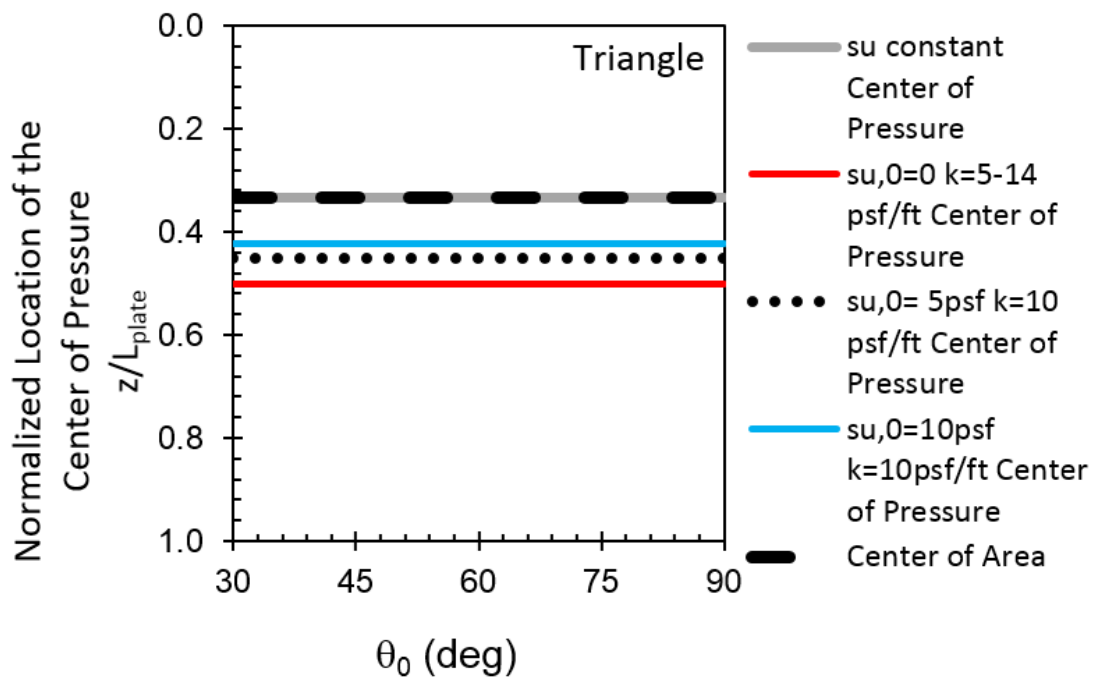
Figure 5.21: Change in center of pressure triangle plate

122
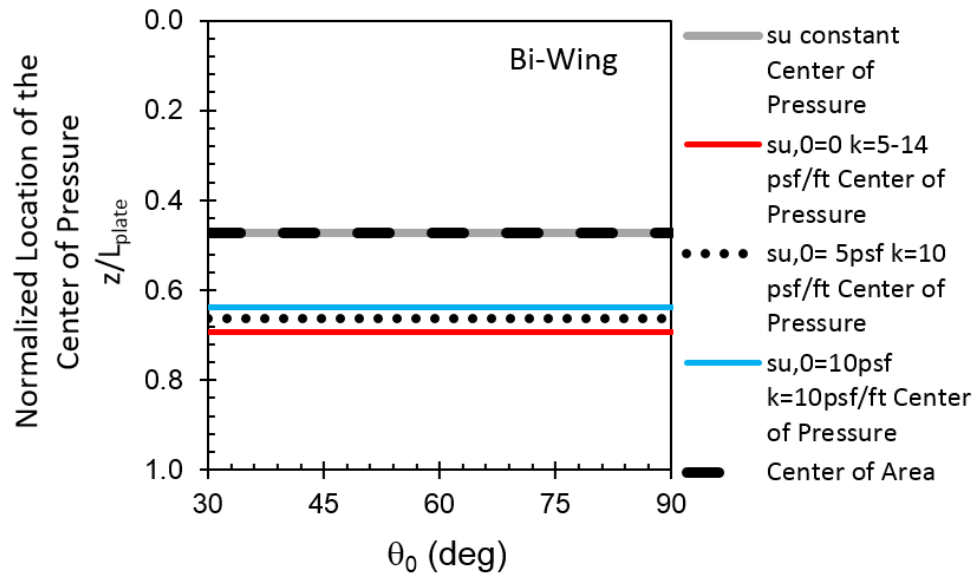
Figure 5.22: Change in center of pressure bi-wing plate

5.4 CONCLUSIONS

This chapter presented the post-yield movement analysis of the simple shaped bearing plates that are symmetrical along the longitudinal axis. The results are:

- Experimental testing of scaled drag embedment anchor (DEA) and vertically loaded anchor (VLA) models and theoretical calculations show that a plate anchor vertically embedded into soil should be rotated to a certain pitch angle with the shank attached to fluke. At that pitch angle, releasing the shank results in anchor penetration with increasing loading line. Releasing the shank at this pitch angle causes line load to be transferred to fluke plane in components parallel and perpendicular to fluke.

- Anchor post-yield movement initiates depending on the angle between fluke and shank, and the yield thresholds in pure shear and pure normal loading. Mobilizing

123

the anchor shear loading capacity before anchor normal loading capacity is mobilized, provides dive penetration during drag embedment loading.

- Theoretical calculations of the initiation of post-yield movement are consistent with the experimental observations.

- The post-yield movement of bearing plates show the plates initially rotate to a pitch angle and then start diving deeper if the loading line is attached on the plate center of resistance or below the center of resistance. This pitch angle during the dive penetration depends on the anchor resistances in normal and shear loading. For simple shaped bearing plates with approximate ratio of pure normal loading yield threshold to pure shear loading yield threshold of 3, this angle was approximately measured as 45 degrees. Attaching the loading line above center of area causes plate to rotate in the reverse direction and pulled out of soil.

- Initiation of post-yield movement and the dive trajectory are similar for tested simple bearing plates with shapes of diamond, trapezoid, triangle and bi-wing.

- Theoretical calculations show that when the simple shaped bearing plates with constant thicknesses are tested in soil test bed with constant undrained shear strength, the center of area and center of pressure coincide. When the undrained shear strength of the soil test bed is linearly increasing with depth, the center of pressure is located lower than center of area. The center of pressure does not change with changing plate pitch angle.

Chapter 6: Experimental Testing of the Flying Wing Anchor® Concepts

6.1 INTRODUCTION AND OBJECTIVES

The objective of this chapter is to optimize the new anchor concept, the Flying Wing Anchor®, based on the pure loading yield thresholds, initiation of post-yield movement and the dive trajectory in clay under undrained conditions. The Flying Wing Anchor® is developed as a sustainable anchor concept for deep-water offshore wind turbines. This new concept draws on the best attributes of torpedo piles and vertically loaded plate anchors. It relies on the gravitational and environmental loads for installation and mobilizing anchor holding capacity. The details of this concept: installation steps, mobilization of capacity and developed structures are presented. The design principles of the installation and mobilization of capacity are explained. The experimental testing and theoretical calculations to obtain the pure loading yield thresholds, initiation of post-yield movement, the post-yield performance and the optimization of the Flying Wing Anchor® concepts are presented in this chapter.

6.2 INSTALLATION AND MOBILIZATION OF CAPACITY

The installation of the anchor has two main steps: free-fall through water column like a torpedo anchor and dive penetration into soil like a plate anchor. The installation steps of the Flying-Wing Anchor are presented in Figure 6.1. The initial anchor penetration into soil is achieved by releasing the anchor from a significant height above the seafloor and it dives after free-fall through water column. Due to its hydrodynamic stability, it penetrates near vertically into soil silently and efficiently, like a torpedo pile. As the tension in the mooring line connecting the anchor to the offshore wind turbine platform increases due to environmental loads, the anchors starts to rotate from vertical (pitch rotation) with the shank attached to fluke when the moment capacity of the anchor is exceeded. A fluke-

125

shank coupling mechanism has been designed to hold the shank attached to fluke until the anchor reached the design pitch angle (Gilbert et al., 2015). At this angle, the coupling mechanism (Iturriaga Flores, 2016) releases the shank and the shank gets aligned with the loading line. Once the shank is free to rotate, the anchor starts to act as a vertically loaded anchor. With further increase in the line tension, anchor starts to dive and pitch toward the horizontal in service. When the shank angle from fluke plane is almost 90 degrees, the available holding capacity of the anchor is maximized over the full fluke surface in bearing at an extreme load condition.
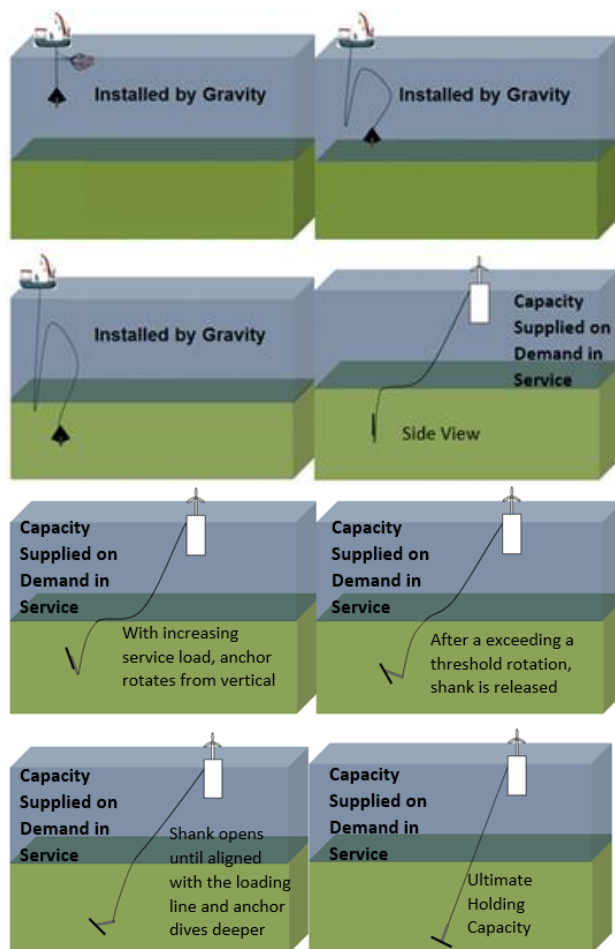
Figure 6.1: Installation and service for the Flying Wing Anchor®

6.2.1 FREE-FALL EMBEDMENT

The anchor embedment starts with free-fall through water after being released from a certain water depth. Depending on the anchor geometry and the direction of falling, the anchor is subjected to hydrodynamic forces. The surface integral of the pressure field around the anchor results in the hydrodynamic forces. The longitudinal component of the hydrodynamic force is the drag force acting collinear with the direction of movement and the lift force acting perpendicular to movement. The stability of the anchor during free-fall through water was analyzed by calculating the magnitude and locations of forces acting on the anchor during an angle of attack. The schematic drawing of the hydrodynamic forces and their locations acting on the anchor during free fall through water are presented in Figure 6.2. The anchor design is considered hydrodynamically stable if the resultant moment due to lift and drag forces with respect to the center of gravity can reduce the angle of attack bringing the anchor back to vertical (Iturriaga Flores, 2016).
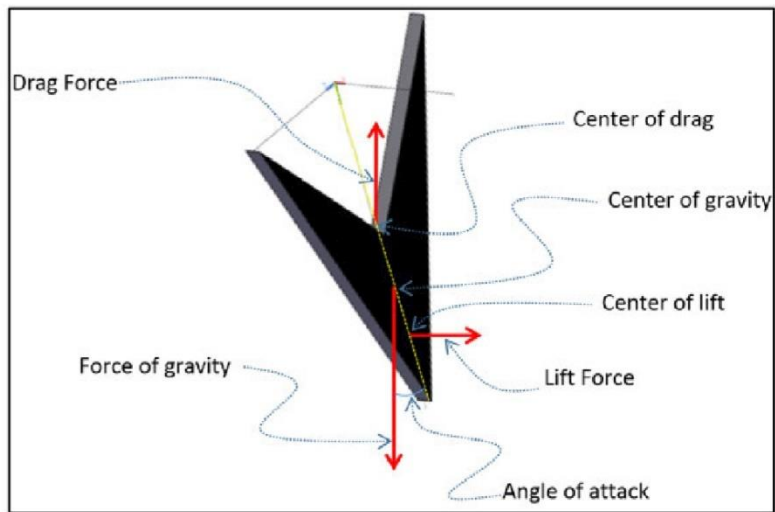
Figure 6.2: Forces acting on the anchor during free-fall (Iturriaga Flores, 2016)

During free-fall through water, the resisting force on the anchor is the drag force. As the anchor starts embedding into soil, the soil resistance acting on the anchor reduces the anchor speed until it reaches its ultimate free-fall embedment. Gilbert et al. (2009) used the API 2 GEO (2011) design method for driven piles to calculate the soil resisting force acting on a torpedo pile during penetration into soil after free-fall through water. The same method can be used to calculate the Flying Wing Anchor® penetration depth after free-fall. The API 2GEO (2011) calculates the soil resistance as the sum of end and side resistances:

$$F_{resistance} = F_{end} + F_{side} \qquad (6.1)$$

$$F_{end} = N_c s_{u(v),undisturbed} A_{end} \qquad (6.2)$$

$$F_{side} = \alpha s_{u(v),remolded} A_{side} \qquad (6.3)$$

where:

F_{end}: tip resistance of the anchor

F_{side}: shear resistance of the anchor

N_c: bearing capacity factor

α: side shear factor

$s_{u(v)}$: undrained shear strength of the soil as a function of penetration velocity

A_{tip}: projected tip area of the anchor

A_{side}: shear area of the anchor

The soil resistance slows the anchor as it enters into soil and the anchor finally completes the free-fall installation when its velocity is zero. The preliminary free-fall tests resulted in penetration depths of up to 2.4 equivalent fluke lengths (Gerkus et al., 2016).

6.2.2 ANCHOR DRAG EMBEDMENT

The hydrodynamic stability of the anchor will provide near vertical embedment into soil after free-fall through water. After the free-fall penetration is completed, anchor is attached to the floating platform via mooring lines. The mooring line is connected to the anchor shackle on the other side. As the environmental loads start to act on the floating platform, the mooring line tension increases and the load is transferred to the anchor.

The shank is designed to be held attached to the anchor fluke during free-fall penetration. Keeping the shank attached to fluke during free-fall penetration reduces the shank resistance during dive. The shank is connected to the anchor center of resistance and held attached to the fluke by the fluke-shank coupling mechanism at the tip of the anchor. This distance between the fluke-shank connection and the coupling mechanism creates eccentricity for rotational loading. Anchor starts to rotate from vertical when the yield threshold of the anchor in pure pitch loading is exceeded. The post-yield movement of the anchor initiates with pitch rotation.

Experimental measurements and theoretical calculations of post-yield movement of bearing plates show that after the anchor reaches a certain pitch angle, it starts to yield in-shear with increasing line load. The dive penetration at this pitch angle depends on the anchor loading line angle and the yield thresholds of the anchor in pure shear and pure normal loading. The fluke-shank coupling mechanism is designed to keep the shank attached to fluke until the design rotation angle from vertical is reached (Gilbert et al., 2015). The fluke-shank coupling mechanism designed by Iturriaga Flores (2016) is

presented in Figure 6.3 and Figure 6.4. When the angle between the mooring line and the fluke plane reaches a threshold value of 60-degrees, the hook inside the coupling mechanism sets the shank free to rotate by releasing the bearing roll and the mechanic shackle. This 60-degree angle is achieved both by the anchor pitch and the change in the loading line angle at the pad-eye. When the shank opens, it gets aligned with the loading line and the load is transferred from the mooring line to the anchor center of resistance through the shank (Iturriaga Flores, 2016).

The purpose of the coupling mechanism is to enable anchor dive penetration without pulling the anchor out of soil. It is designed as a mechanical system and triggered by the anchor and the loading line orientation.
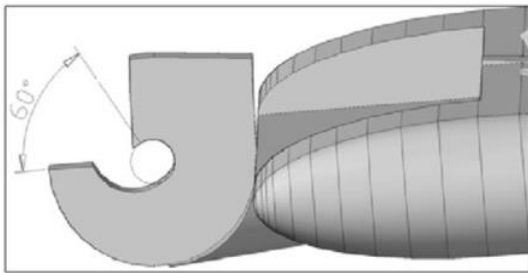
Figure 6.3: Fluke-shank coupling mechanism (Iturriaga Flores, 2016)
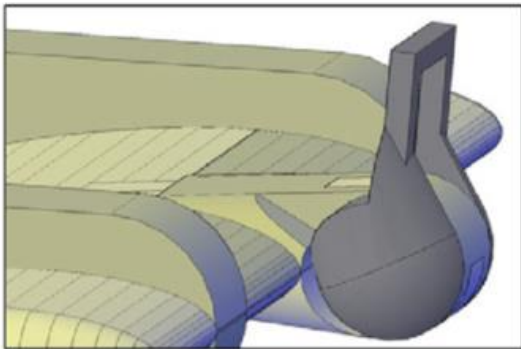
Figure 6.4: Fluke-shank coupling mechanism, mechanic shackle (Iturriaga Flores, 2016)

When the anchor shank is free to rotate, it starts to act as a vertically loaded anchor. Figure 6.5 shows the force equilibrium of a plate anchor rotated α degrees from vertical and has a freely rotatable shank attached at the anchor center of resistance.
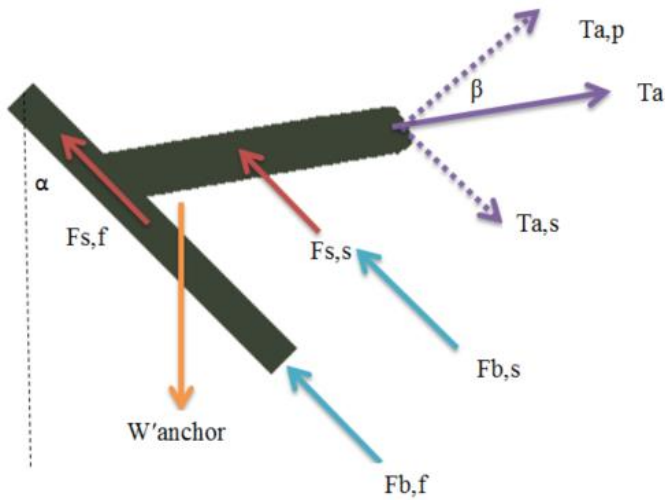
Figure 6.5: Forces acting on the anchor with free shank

where;

W'_{anchor}: submerged weight of the anchor (which is ignored in the calculations)

$F_{s,f}$: shear resistance of the fluke

$F_{s,s}$: shear resistance of the shank

$F_{b,f}$: bearing resistance of the fluke

$F_{b,s}$: bearing resistance of the shank

T_a: is the mooring line load

$T_{a,p} = T_a.\cos\beta$: component of the mooring line load perpendicular to fluke plane

$T_{a,s} = T_a.\sin\beta$: the component of the mooring line load parallel to fluke plane

When the force applied in each direction exceeds the anchor yield threshold in that direction, anchor starts to yield. Experimental tests using scaled model VLA showed that

if the shank is free to rotate when the anchor is vertical, anchor yields in the normal direction and gets pulled out of soil. At this configuration the component of the line load parallel to fluke plane is in the direction of pulling the anchor out of soil rather than embedding it deeper. When the shank is released the angle between fluke and loading line gets equal to 60-degrees. For a line load of T_a, the force to yield the anchor in shear direction is equal to $T_a.\cos(60)$ which is $0.5\ T_a$ and the force to yield the anchor is $T_a.\sin(60)$ which is $0.87\ T_a$. Assuming the anchor concept has a ratio of pure normal loading yield threshold to pure shear loading yield threshold of 3:1. Which means when $T_{a,s}$ exceeds $(0.87\ T_a)/3=0.29\ Ta$, the anchor starts to yield in shear direction and anchor embeds deeper before the capacity in pure normal loading is mobilized.

As the anchor dives deeper into soil, the mooring line transverses more and it rotates the shank further away from the fluke plane. When the shank reaches its ultimate position of being near vertical to the fluke plane, the ultimate holding capacity in bearing is maximized over the anchor fluke surface (Gilbert et al., 2015). It is possible to retrieve the anchor by pulling from the opposite direction to slice back up through soil and failing the anchor in shear since the shear resistance of the anchor is $1/3^{rd}$ of the bearing resistance.

6.3 DEVELOPED FLYING WING ANCHOR® CONCEPTS

The Flying Wing Anchor® was developed as one-wing and bi-wing concepts. The structural design details and hydrodynamic stability calculations are presented in Iturriaga Flores (2016).

The anchor concepts developed as one-wing and bi-wing Flying Wing Anchors® have main components of: anchor fluke, shank, fluke-shank attachment mechanism, and shackle. Fluke is the bearing plate that mobilizes anchor holding capacity over its surface. Shank provides the connection between anchor fluke and the loading line and transfers the

132

environmental loads to the anchor fluke. The shank is attached at the anchor center of resistance assuming a constant soil strength profile (Iturriaga Flores, 2016). The fluke-shank coupling mechanism is attached at the tips of the shank and fluke, to hold the shank attached to fluke during initial pitch rotation. When the coupling mechanism releases the shank, it starts to open up and at the final configuration the shank is almost perpendicular to the fluke to maximize the holding capacity of the anchor. The loading line is attached to the anchor at the shackle.

6.3.1 ONE-WING FLYING WING ANCHOR®

The one-wing Flying Wing Anchor® concept has been developed to have one diamond shape fluke (Figure 6.6). The hydrodynamic stability, structural design details and coupling mechanism are presented in details in Iturriaga Flores (2016). The main components of the Diamond Flying Wing Anchor® concept are presented in Figure 6.7. The diamond shaped fluke has additional weights attached at the lower part of the fluke to provide hydrodynamic stability during free-fall. The structure has rigid I-beams and thin steel plates. The coupling mechanism is located at the lower part of the anchor, at the tip. Shank is attached at the fluke center of resistance by two arms (Iturriaga Flores, 2016).

Anchor efficiency is defined as the anchor holding force (ultimate holding capacity) divided by anchor dry weight (O'Neill et al., 2003). Using additional weights to provide hydrodynamic stability increased the anchor weight in air. But this added weight had a negligible contribution to anchor holding capacity. To achieve hydrodynamic stability with higher anchor efficiency, the concept of using two fluke areas was introduced.

| Diamond-7 | Diamond-7 shank open |
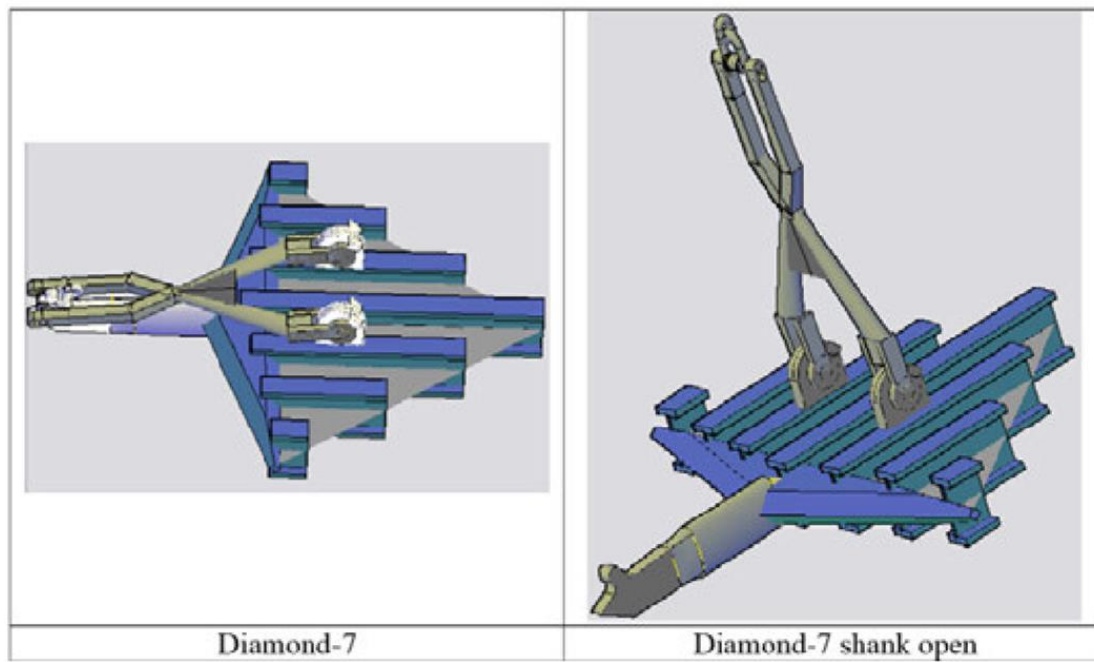
Figure 6.6: One –Wing Diamond Anchor (Iturriaga Flores, 2016)

Shackle

Shank

Coupling
Mechanism
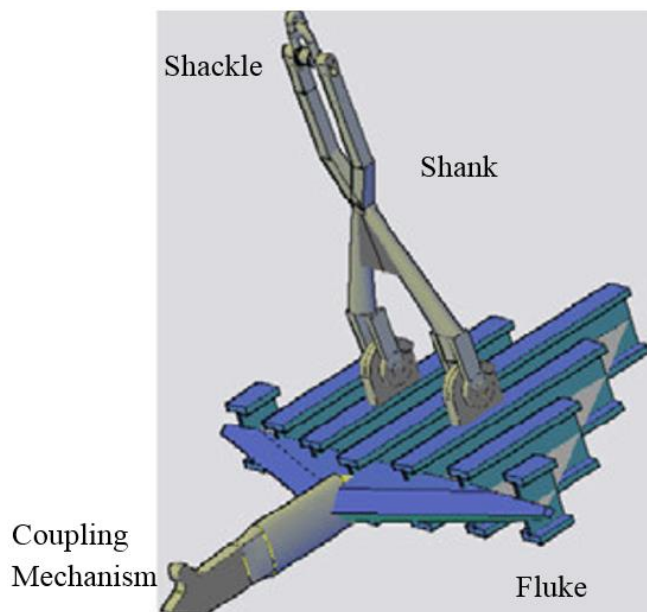
Fluke

Figure 6.7: Parts of Diamond one-wing anchor (Iturriaga Flores, 2016)

134

6.3.2 BI-WING FLYING WING ANCHORS®

The idea of using independent control surfaces for hydrodynamic stability introduced the Flying Wing Anchor® with two fluke surfaces separated from each other. The developed bi-wing concepts are presented in Figure 6.8 and Figure 6.9. The Paloma design of the bi-wing concepts was developed for the scaled model offshore testing in Ireland lead by project collaborators in University College Dublin (Iturriaga Flores, 2016). The main anchor components for the Paloma anchor are presented in Figure 6.10. The shank is connecting to the fluke on the beams by two arms. The shank arms connect with each other at the anchor tip and shank is held attached to fluke with the dove-head coupling mechanism.

| Bi-Wing-1[1] | Bi-Wing-1 shank open[3] |
| Bi-Wing-2 shank open | Guillotine[2] |
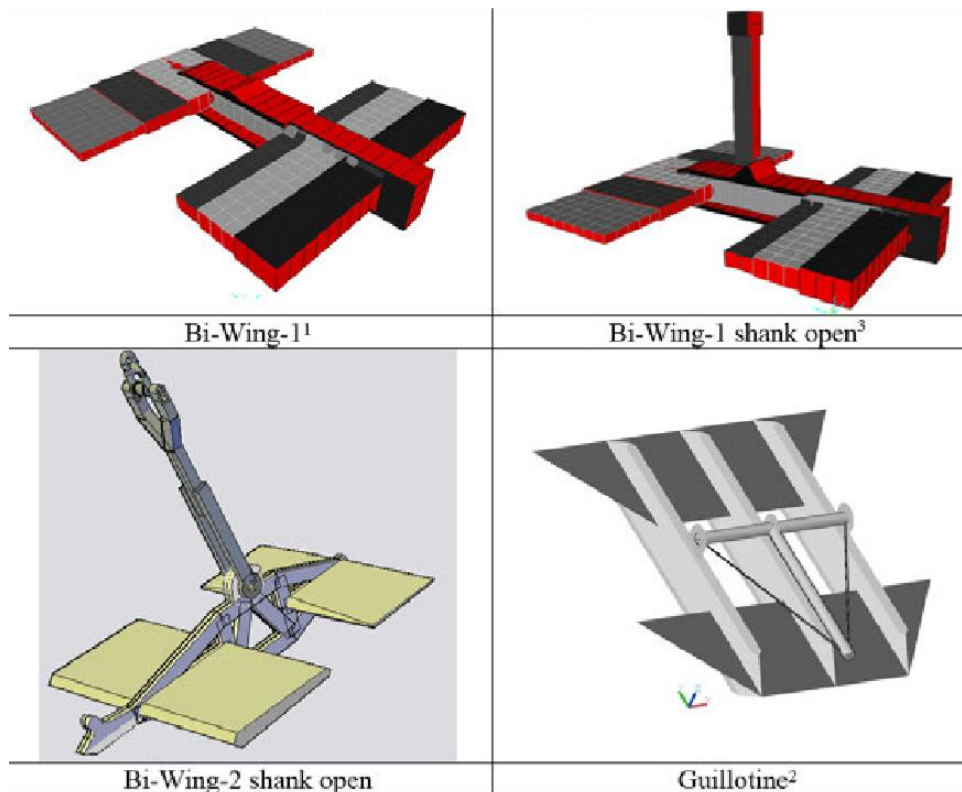
Figure 6.8: Bi-wing Anchor Designs (Iturriaga Flores, 2016)
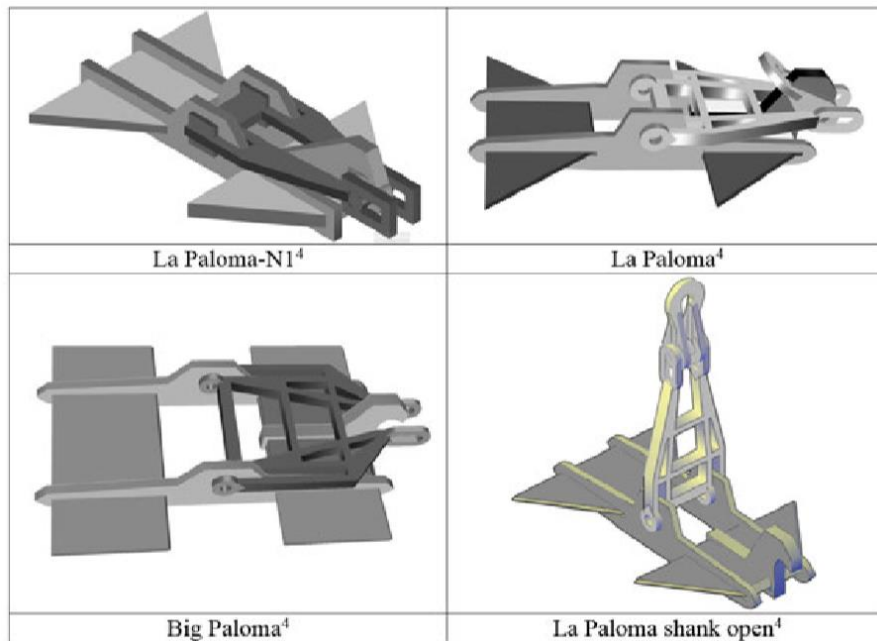
Figure 6.9: Bi-wing Paloma anchors (Iturriaga Flores, 2016)
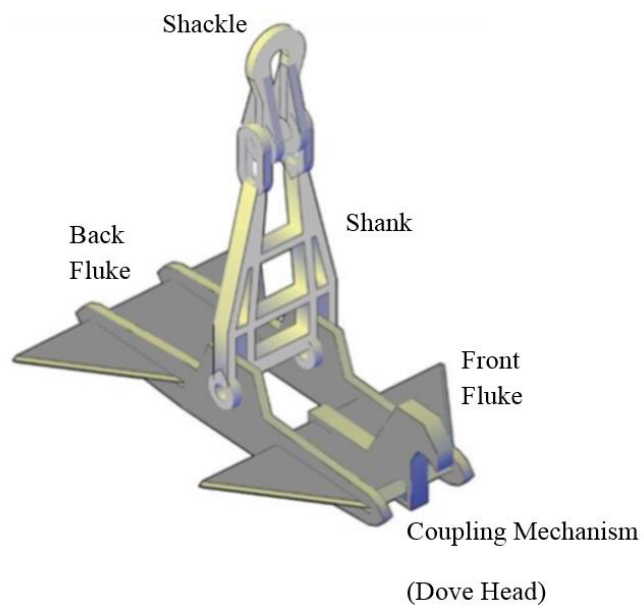
Figure 6.10: Parts of Paloma bi-wing anchor (Iturriaga Flores, 2016)

The fluke-shank coupling mechanism of the Paloma anchor (dove head-Figure 6.10) increased the shear resistance of the anchor due to robust geometry. The Paloma anchor design was modified with a smaller fluke-shank coupling mechanism, tear-drop shape fluke thickness and additional fins for hydrodynamic stability and different size flukes. The new design is the final bi-wing Flying Wing Anchor® concept of Speedy-1-K (Speedy) (Figure 6.11). It optimizes the hydrodynamic stability with the additional help of fins. The shear resistance was also decreased with the hidden fluke-shank coupling mechanism, fluke-shank configuration, and the teardrop-shaped fluke profiles. The main components of the Speedy anchor are presented in Figure 6.12 (Iturriaga Flores, 2016).
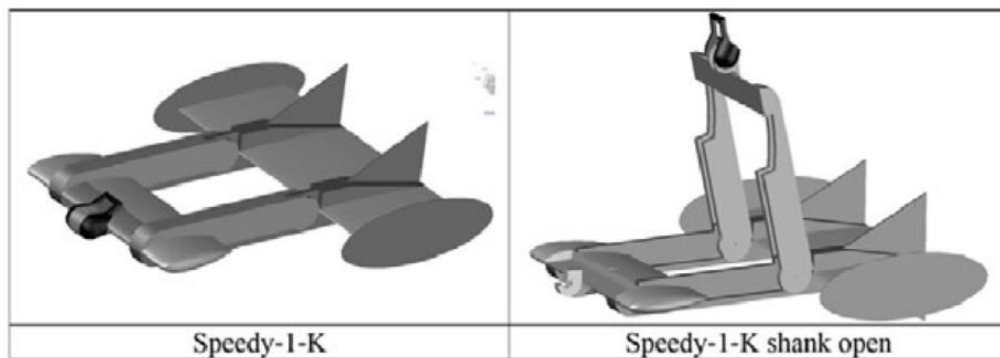
Figure 6.11: Speedy-1-k final design (Iturriaga Flores, 2016)
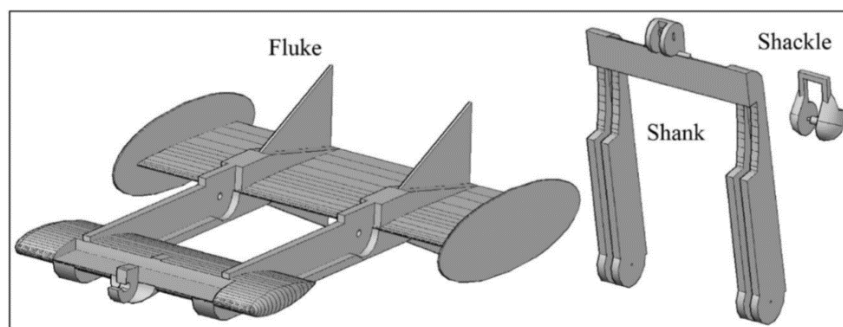
Figure 6.12: Parts of Speedy bi-wing anchor (Iturriaga Flores, 2016)

6.4 SCALED MODELS OF THE FLYING WING ANCHOR® CONCEPT

6.4.1 PLYWOOD MODELS

The plywood diamond-shaped bearing plate with a fluke area of 20 in^2 and constant fluke thickness of 0.2 in was built to measure anchor post-yield movement with the magnetometer attached on it (Figure 6.13). The model was painted to reduce water absorption. This model was thinner than the diamond shaped bearing plates used for pure loading yield threshold testing to reduce resistance of the anchor during drag embedment installation.

Figure 6.13: Diamond-shaped bearing plate with magnetometer attached

The plywood bi-wing Paloma model with a fluke area of 12 in^2 and a constant fluke thickness of 0.2 in was built to measure anchor post-yield movement with the magnetometer attached on it (Figure 6.14). The magnetometer was placed inside the slot cut on the front fluke. The shank arms were attached with additional plywood pieces and modified throughout the test as required. Bolts and nuts made of wood were used to avoid magnetometer noise.

Figure 6.14: Plywood Paloma anchor models

6.4.2 ACRYLIC MODELS

The Flying Wing Anchor® concept scaled anchors were built in acrylic using 3D printers. The anchor models were built in scales ranging from 1/30-1/5. The scales are calculated approximately and the exact scales can be determined depending on the prototype anchor size. The scaled laboratory models of the one-wing concept diamond-shaped anchor, bi-wing concepts Paloma and Speedy-1-K (Speedy) (Iturriaga Flores, 2016) are presented in Figure 6.15.

Diamond Anchor

The one-wing concept Diamond scaled models were built in acrylic by 3D printers. The models have fluke areas of 11.44 in^2, weight in air of 0.114 lbs and fluke thickness varying between 0.1-0.75 inch (Figure 6.16). The models were built identical and modified during testing as required. The acrylic Paloma scaled model built by 3D printing (Figure 6.17) and weighs 0.12 lbs in air.

139
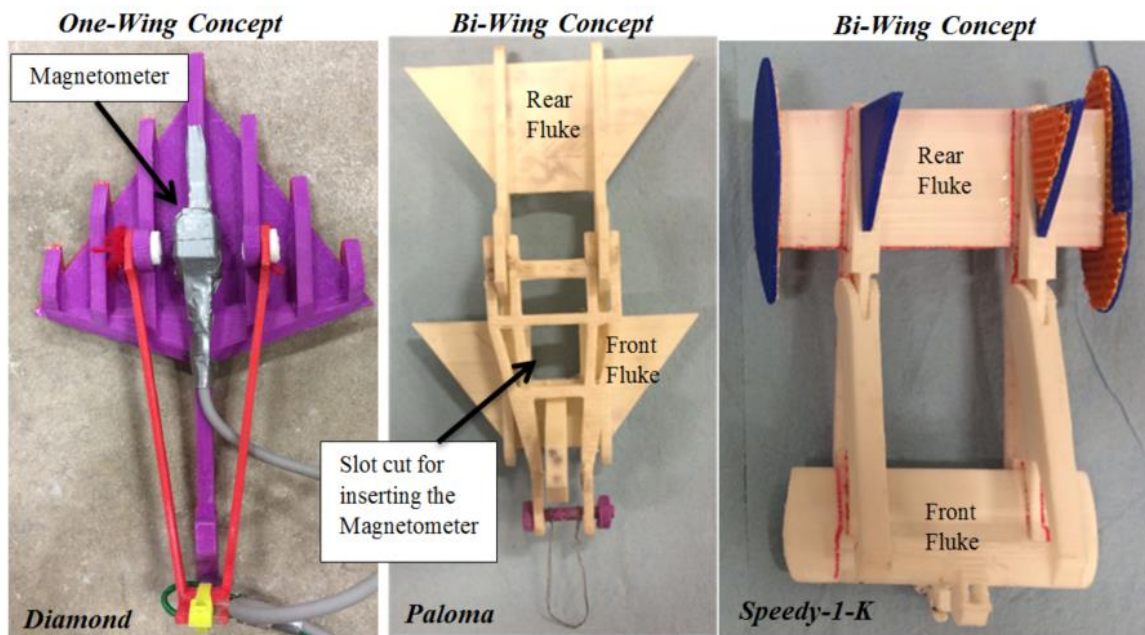
Figure 6.15: Acrylic Flying Wing Anchor® concepts

Figure 6.16: Acrylic Diamond models

Paloma Anchor

The acrylic Paloma scaled models were built in acrylic by 3D printing (Figure 6.17) and weigh 0.12 lbs in air. Total fluke area is 12 in^2. Anchor models were smoothed by filing to reduce friction along the surface. Also shank has no resistance to opening at the fluke-shank connection. The fluke was printed in one piece together with the beams and dove head. The dove head was built with the 60-degree angle release mechanism to check the fluke-shank coupling mechanism shank release angle. The magnetometer was placed inside the slot cut on the front fluke during post-yield movement measurements. Using a bi-wing mechanism enables magnetometer line to be free during testing and go to the mudline through the gap between flukes. It does not increase the loading line diameter or interact with anchor during pitch rotation.
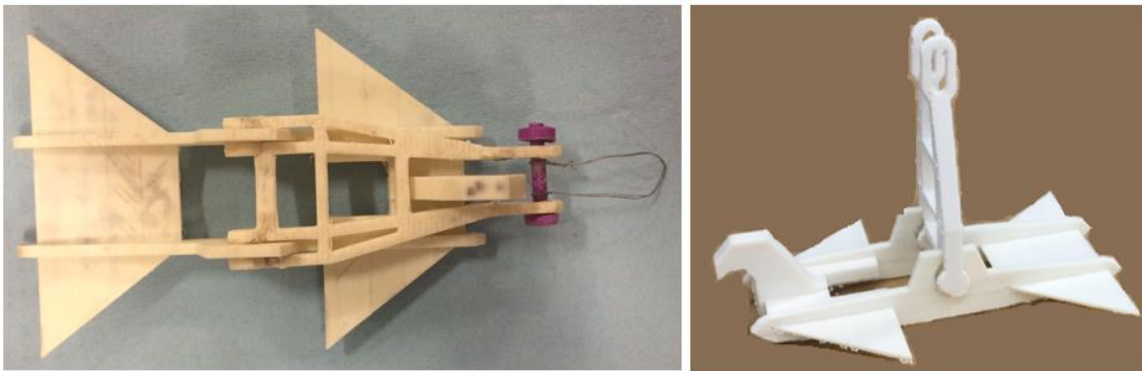
Figure 6.17: Acrylic Paloma models

Speedy Anchor

The bi-wing concept Speedy anchor has fluke areas ranging from 9.7-19.29 in^2. The fluke area sizes were restricted by the 3D printer dimensions and printing time limitations. Different fluke sizes were built and the models were modified depending on the testing

requirements. The parts were attached with epoxy or glue. The surfaces were smoothed by filing and modifications were made by melting or drilling anchor pieces. The model was filed by sand paper to ensure there is no gap remaining between the shank and the front fluke when the shank is closed.

Additional Speedy models are printed to study the effect of fluke separation distance on the ratio of anchor shear resistance to anchor normal resistance. One model was built as the scaled model of the original Speedy design and the other model had flukes further separated from each other. Both models have equal fluke areas (total of 9.7 in^2) and fins but the anchor with modified fluke separation has longer beams connecting the flukes (Figure 6.18).
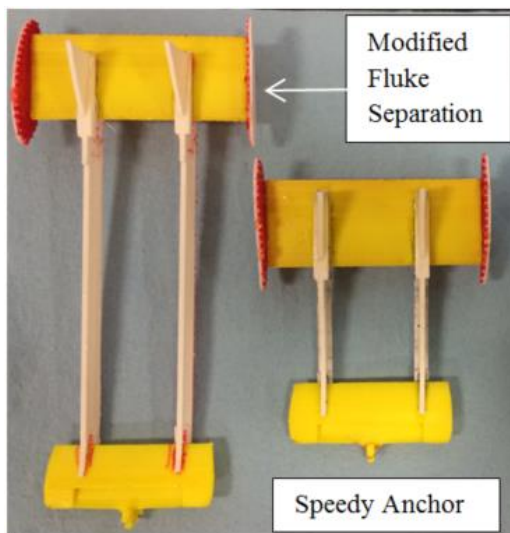
Figure 6.18: Speedy anchor models with designed and modified separation distance

The modified separation distance was chosen based on the Finite Element calculations presented by Gilbert et al. (2009) to determine soil failure mechanism during failure in bearing. The failure mechanism presented in Figure 6.19 shows that for an anchor width of B, the plastic strain contours extend to approximately 0.87 B from the edges of

the fluke plane displaces. The anchor with the modified separation distance was built by separating the anchor flukes at a distance of equal to the sum of the fluke lengths of both rear ($B_{rear} = A^{0.5}_{rear\ fluke}$) and front fluke planes ($B_{front} = A^{0.5}_{front\ fluke}$). The objective of this test is to understand how the normal resistance to shear resistance ratio of the anchor will be affected if the interaction between the full-flow soil failure mechanism around each fluke is minimized.
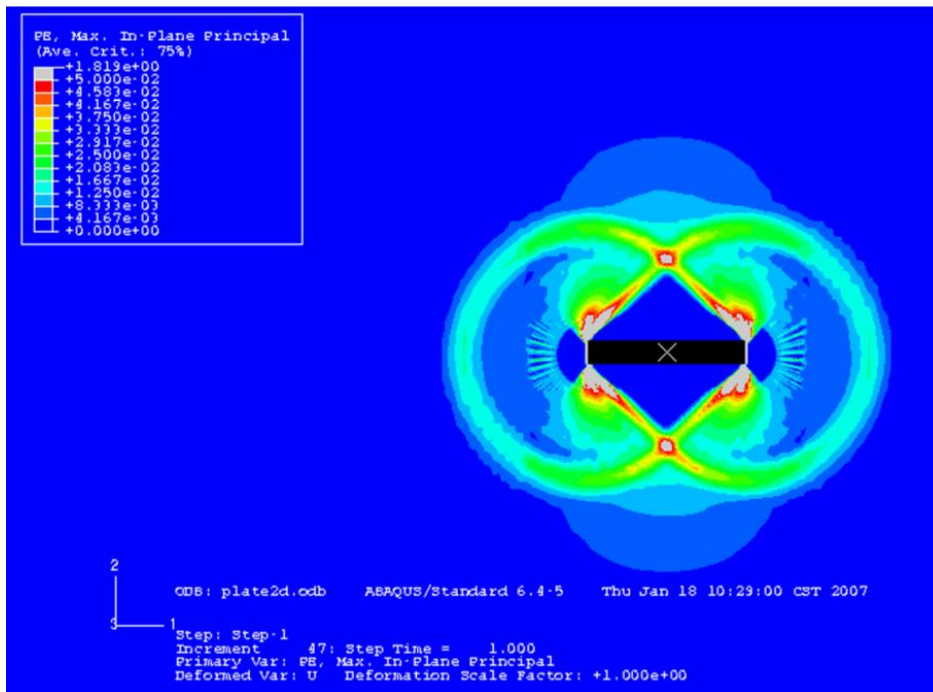
Figure 6.19: Finite element results for infinitely-long bearing plate, plastic strain contours at yield (Gilbert et al., 2009)

For experimental measurement of the Speedy concept post-yield movement, 1/5 scale of the Speedy anchor was built in acrylic. The model has a fluke area of 19.29 in^2 and it weighs 0.204 pounds in air. The Speedy model with the magnetometer attached and hydrodynamic fins removed is presented in Figure 6.20. The anchor model was tested with

the 0.025 in diameter white nylon rope. The Speedy anchor model was built without the coupling mechanism since the 3D printer precision was not enough to print a very small detailed piece that corresponds to the 1/5 scale of the coupling mechanism in prototype Speedy. The magnetometer was placed inside the slot cut on the front fluke. The magnetometer line went through the fluke separation distance and was free on the mudline.
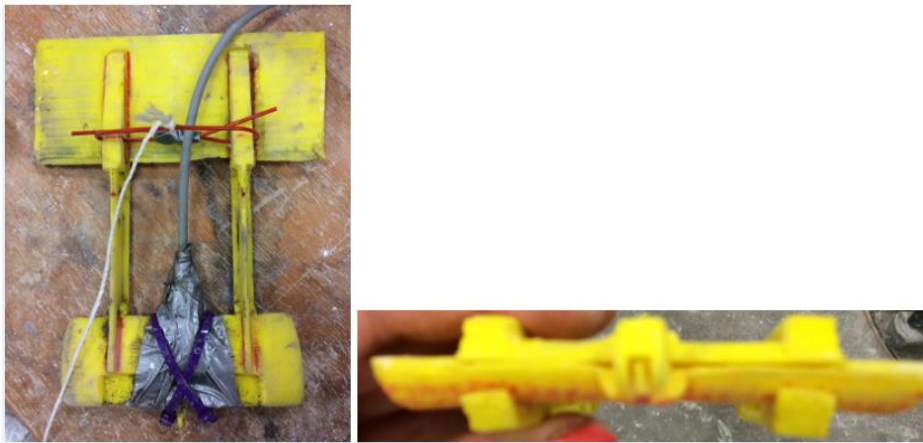
Figure 6.20: Speedy acrylic model without fins, with magnetometer

6.5 PURE LOADING YIELD THRESHOLDS

This section describes the experimental measurements and theoretical calculations of pure loading yield thresholds of the Flying Wing Anchor® concepts. The scaled model Diamond anchor, bi-wing concepts of Paloma and Speedy are tested in the Gulf of Mexico marine clay to measure the pure loading yield thresholds of the one-wing and bi-wing shaped Flying Wing Anchor® concepts. The experimental measurements and theoretical results are compared with the pure loading yield thresholds of simple shaped bearing plates that are symmetrical along the longitudinal axis.

6.5.1 EXPERIMENTAL TESTING SETUP

The scaled model Flying Wing Anchor® concepts were tested in the remolded Gulf of Mexico marine clay. Translational loading tests were conducted by initially embedding the anchor into soil and pulling out at a constant rate of 0.8 in/sec equal to the t-bar test rate. The translational loading was applied by either attaching the scaled models on the t-bar insertion rod or using a loading line to load the anchor model. The experimental tests with simple bearing plates showed the insertion rod diameter size relative to the fluke area can affect the measured pure normal loading yield thresholds. Also it was not feasible to attach more complicated geometries of Flying Wing Anchors® with varying thicknesses to an insertion rod. The loading line was either attached directly on the anchor or on the frame built to keep the anchor stable during testing.

shows the anchor scaled model before and after normal loading test using a loading line attached on the anchor. Figure 6.22 shows the Speedy anchor model with a plywood support frame attached on it for attaching the line during translational loading tests. The measured anchor resistance was corrected to account for the contribution of support frame. The soil friction along the line is calculated by multiplying the line's perimeter, line length covered in clay and the undrained shear strength of the soil. The line friction is minimized by using thin loading lines. The load cell measurements are corrected for additional frictions caused by the testing setup (insertion rod/line, anchor-rod insertion pieces), insertion weights and the buoyant weight of the plate depending on the direction of the loading. All the loads presented here are the net resistances.
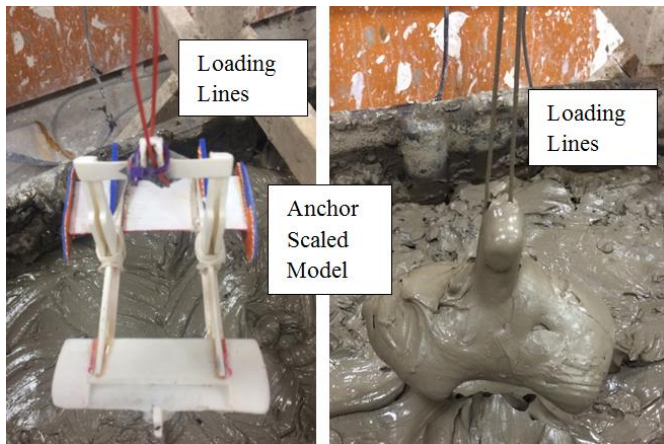
Figure 6.21: Pure loading test setup for translational loading with loading line
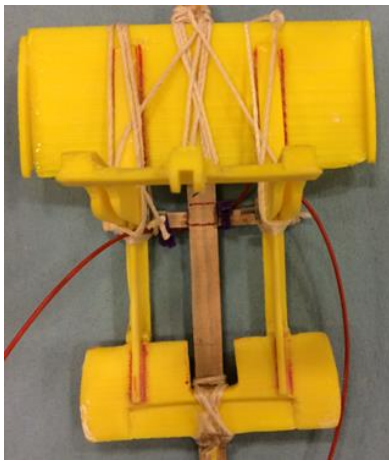
Figure 6.22: Speedy anchor model with support frame for pure loading tests

To apply rotational loading, the Flying Wing Anchor® 3D models were tested with the magnetometer attached. The anchors were initially placed vertically into soil. The loading line was attached at the pad-eye and the initial loading line angle was measured. The anchor line had a constant displacement rate of 0.8 in/sec. The change in load cell and magnetometer recordings were compared simultaneously. The resistance recorded at the start of anchor rotation was used to calculate the yield threshold in pure rotational loading.

6.5.2 OPTIMIZATION OF FLYING WING ANCHOR® CONCEPTS AND MEASURED YIELD THRESHOLDS

The development of Flying Wing Anchor® concepts follows as: Diamond anchor, Paloma anchor and Speedy Anchor. The development of designs highly depends on the yield threshold measurements as well as the hydrodynamic stability concerns.

The baseline of the design was to develop an anchor that has a normal resistance to shear resistance ratio of approximately 3:1, as measured for the simple bearing plates. The initial design developed by Iturriaga Flores (2016) is the diamond shaped one-wing Flying Wing Anchor® concept. Experimental testing of the simple shaped bearing plates symmetrical along the longitudinal axis showed that there is no significant advantage of using either of the tested geometries. The diamond shaped fluke was designed with additional weight on the lower part of the anchor for the hydrodynamic stability and has structural I-beams on the fluke surface. The measured N_{shear} is 4.2 and N_{normal} is 11, resulting in a ratio of normal resistance to shear resistance of 2.62. Results show attaching additional weights and beams increased the shear resistance of the Flying Wing Anchor® concept.

The bi-wing anchor concept was designed to provide the hydrodynamic stability by using two control surfaces rather than additional weight. The aim is to increase the efficiency of the Flying Wing Anchor® concept while decreasing the shear resistance. The measured ratio of normal resistance to shear resistance is 2.43 for Paloma anchor. Theoretical calculations showed that the fluke-shank coupling mechanism has a robust structure (dove head-Figure 6.23) and it increased the shear resistance significantly. By removing the coupling mechanism and the anchor shank (Figure 6.24), the measured yield threshold in pure in shear loading was decreased from 5.6 to 3.6 and anchor normal resistance to shear resistance ratio was measured as 3.8.
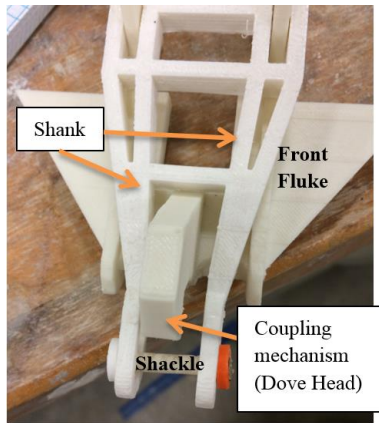
Figure 6.23: Paloma Anchor Coupling Mechanism and Shank

Figure 6.24: Paloma model without shank and coupling mechanism

The Speedy model was designed to reduce the shear resistance of bi-wing Paloma anchor concept. The steps of changing the design from Paloma to Speedy anchor included: changing constant fluke thickness into tear-drop shape, reducing the coupling mechanism size and embedding shank into front fluke (Iturriaga Flores 2016). The initial design has triangle and elliptical fins (Figure 6.25) to increase the hydrodynamic stability. Testing the anchor model with fins resulted in N_{shear} of 6.75 and N_{normal} of 13.6.
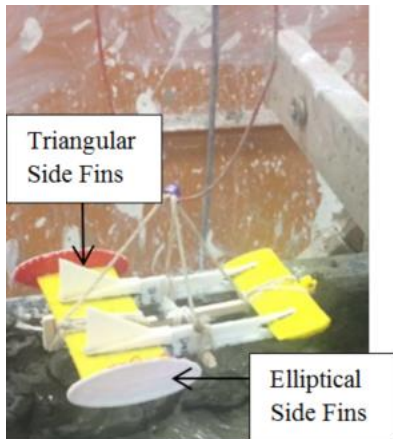
Figure 6.25: Scaled model Speedy-1-K anchor without shank

To decrease the shear resistance of Speedy, the triangle fins on the rear fluke are removed and the elliptical side fin sizes were reduced. The Speedy model with refined fins (Figure 6.22) was tested with the wooden support frame attached on it to prevent anchor tilt during pure normal loading tests. Speedy scaled model with refined fins was built at a scale of 1/5 of the prototype anchor but the back fluke thickness and elliptical fins thicknesses were increased since 3D printers were not able to print plates as thin as the 1/5 scale model requires. For the scaled model with refines fins, the yield threshold calculated theoretically for pure shear loading was calculated as 4.0. The experimental bearing capacity factor in pure shear loading of 4.2 can be explained by the increased surface roughness of the acrylic model and the increased fluke thickness due to 3D printing. The measured N_{shear} is 4.2 and N_{normal} is 15.1, resulting in a ratio of normal resistance to shear resistance of 3.6 for the scaled model Speedy anchor. Fixing the Speedy anchor shank as perpendicular to fluke increased the pure shear loading yield threshold to 5.3 due to bearing resistance of shank arms.

The theoretical pure shear loading yield threshold for the prototype Speedy is calculated as 3.5 resulting in theoretical normal resistance to shear resistance ratio of 4.3

149

for the prototype Speedy. Since shear resistance is much lower than the normal resistance, anchor can be reused by pulling it from the opposite direction to close the shank and yield the anchor in pure shear loading until it is out of soil. This enables anchor to be reused in another location or project.

The Speedy anchor model built with modified fluke separation distance (Figure 6.18) was tested to study the effect of separation distance on normal resistance to shear resistance ratio. The results show that separating the flukes further apart increased the pure normal loading yield threshold. Figure 6.26 shows the measured net anchor resistances during the pure normal loading tests of anchor models with original fluke separation distance and with the flukes separated further apart. The theoretical line was calculated by adding the increased resistances of additional length of beams due to further fluke separation, to the measured resistance of the original design anchor. Results show that the theoretical line and the peak net anchor resistance measured experimentally with anchor model that has further separated flukes, match well. This indicates the increase in pure normal loading yield threshold was mostly due to increased beam lengths. But increasing the beam lengths also increased the shear resistance. The normal resistance to shear resistance ratio is calculated as 2.9 for the original design and 2.7 for the anchor with the modified fluke separation distance. It is measured that separating the anchor flukes further did not increase the ratio of pure normal loading yield threshold to the pure shear loading yield threshold.

Pure Normal Loading Test

Net Bearing Force (lbs)
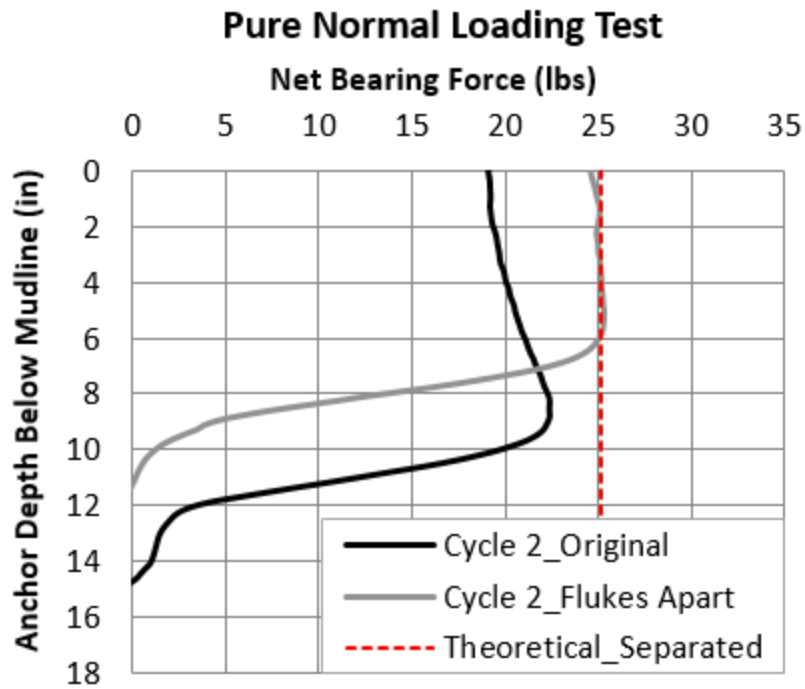
Figure 6.26: Anchor pure normal loading resistance, modified fluke separation distance

The experimentally measured yield thresholds of the scaled Flying Wing Anchor® concepts and the ratios of normal resistance to shear resistance are summarized in Table 6.1.

Bearing Factor	One-Wing Concept: Diamond Anchor	Bi-Wing Concept: Paloma	Bi-Wing Concept: Speedy
N_{normal}	11	13.6	15.1
$N_{in\text{-}plane\ shear}$	4.2	5.6	4.2
N_{normal}/N_{shear}	2.62	2.43	3.6

Table 6.1: Bearing capacity factors for one-wing and bi-wing scaled anchor models

6.5.3 RESULTS OF THE FLYING WING ANCHOR® YIELD THRESHOLDS

The experimentally measured and theoretically calculated pure loading yield threshold results for simple geometry bearing plates, one-wing and bi-wing Flying Wing Anchor® concepts are compared in this section. The results presented as one-wing include the simple bearing plates tested (Chapter 4) and the Diamond Flying Wing Anchor® concept. The results presented as bi-wing concepts are Paloma and Speedy Flying Wing Anchors®.

The theoretical pure loading yield thresholds are calculated by using Equation 4.5 for pure normal loading yield threshold and Equation 4.6 for pure shear loading yield threshold. Equation 4.7 was modified to account for two fluke areas. The non-dimensional yield threshold for pure moment loading (N_{moment}) for bi-wing anchor models with thickness of t and equivalent fluke width of B is calculated by:

$$N_{moment,bi\text{-}wing} = 2 \times 1.9 + 2.8 \times (1/S_t) \times (t/B) \tag{6.4}$$

The comparison of experimental and theoretical bearing factors for normal loading is presented in Figure 6.27. The results are obtained by testing simple bearing plates and the scaled Flying Wing Anchor® models in kaolinite and Gulf of Mexico marine clay with remolded soil ($S_t = 1$) and sensitivity soil ($S_t = 1.7$). The measured pure normal loading yield thresholds of bi-wing and one-wing concepts are between 12-15 and match well with the theoretical pure loading yield thresholds and the pure loading yield thresholds of simple shaped bearing plates (between 10-15). The N_{normal} values measured experimentally and calculated theoretically are on the higher side of the one-wing N_{normal} values. Experimental measurements and theoretical predictions show that the decrease in pure normal loading bearing capacity factors with increasing soil sensitivity is negligible.
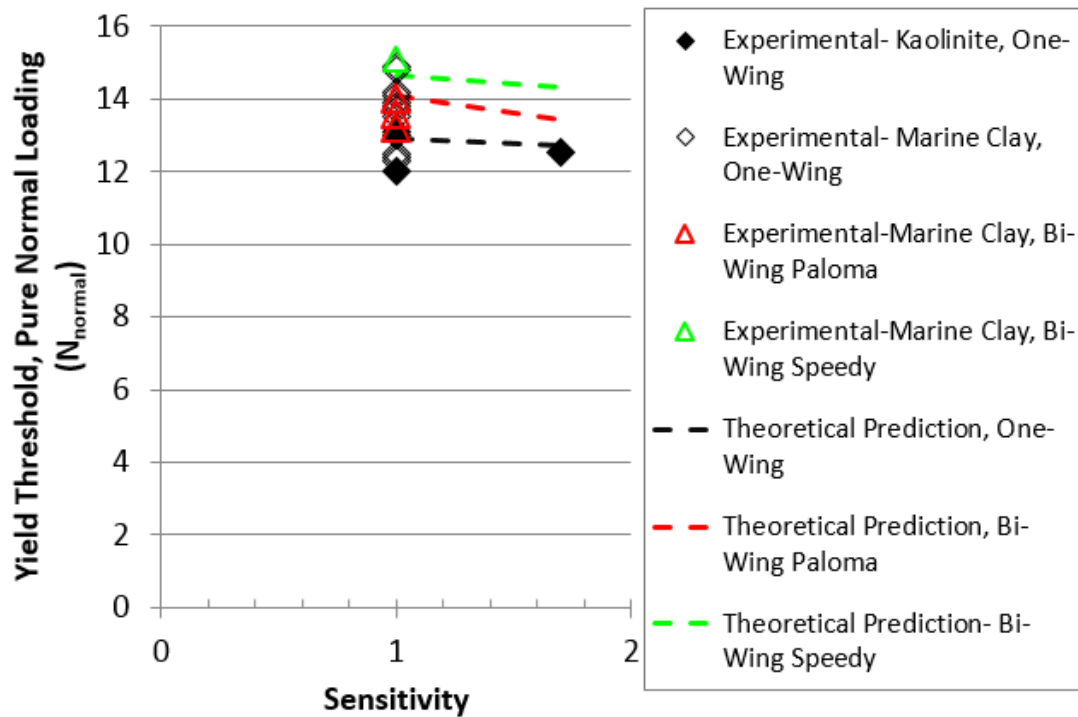
Figure 6.27: Pure normal loading yield thresholds, bearing plates and anchor concepts

The pure shear loading yield thresholds are presented in Figure 6.28. Results show that the experimental results are in good agreement with the theoretical calculations. The pure shear loading yield thresholds are approximately $1/3^{rd}$ of the pure normal loading yield thresholds. The experimental results for the bi-wing concepts are slightly higher than the predicted values for the remolded soil. This can be explained by the increased surface roughness of 3D printed models. The models are smoothed by filing to decrease the contribution of surface roughness on the anchor shear resistance. While the Paloma anchor has the highest pure shear loading yield threshold, the N_{shear} for Speedy and one-wing concepts are between 3.3-4.4. Both experimental measurements and theoretical

calculations show that the pure shear loading yield threshold decreases significantly with increasing soil sensitivity.
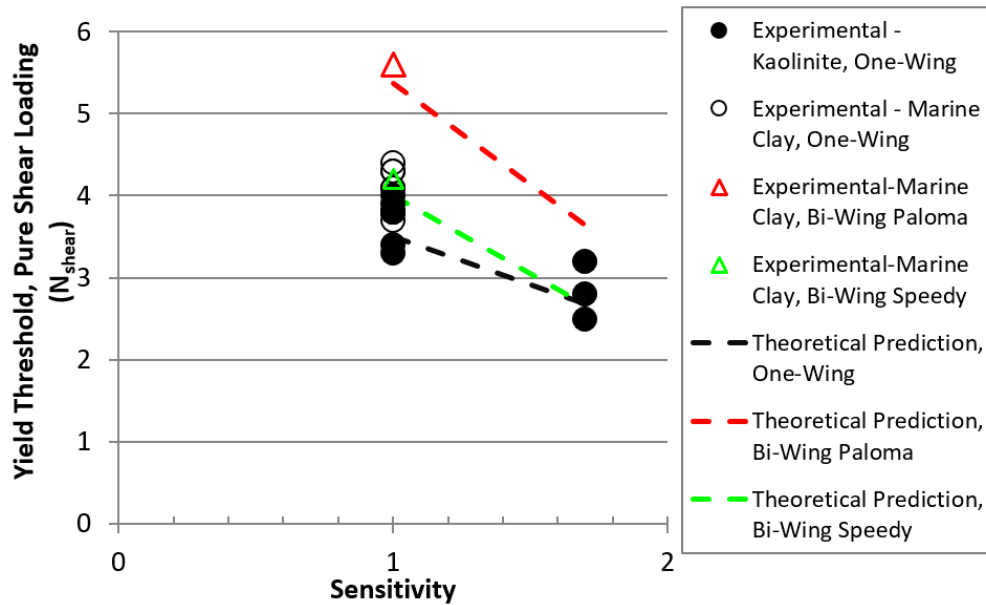
Figure 6.28: Pure shear loading yield thresholds, bearing plates and anchor concepts

The measured N_{moment} for the bi-wing anchor is almost twice the N_{moment} for the one-wing anchor due to the flukes (wings) located at a distance from the anchor center of mass. It can be seen that experimental measurements match well with the theoretical calculations. Both experimental results and theoretical calculations show that the decrease in pure rotational bearing capacity factor with increasing soil sensitivity is negligible.
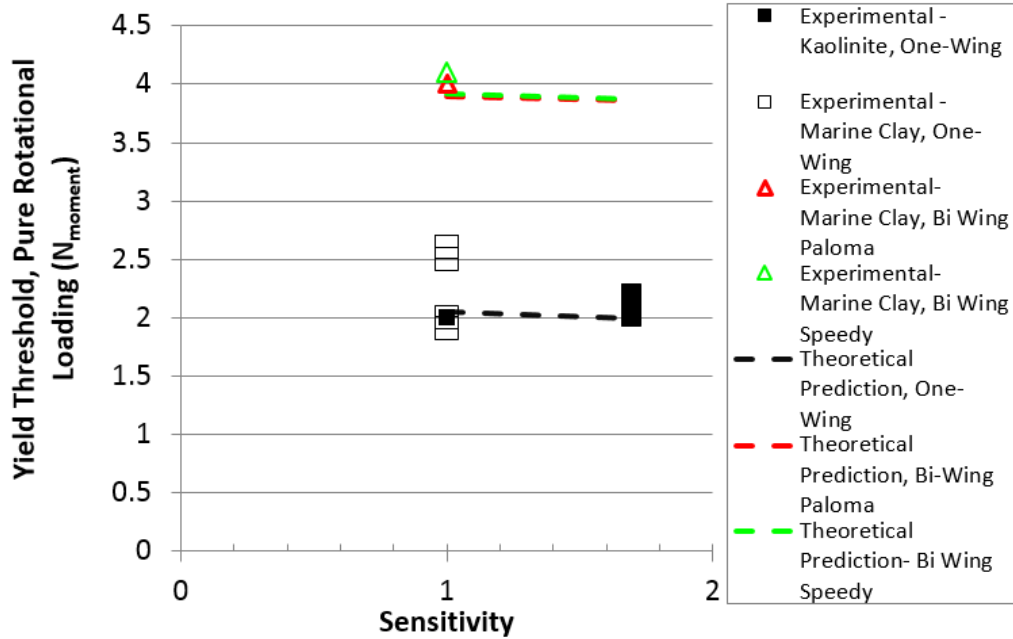
Figure 6.29: Pure rotational loading yield thresholds, bearing plates and anchor concepts

6.6 POST-YIELD MOVEMENT

This section describes the post-yield movement of the Flying Wing Anchor® concepts of the one-wing Diamond anchor and the bi-wing Paloma and Speedy anchors. Based on the understanding developed by the initiation of post-yield movement and the post yield movement analysis of simple shaped bearing plates, the Flying Wing Anchor® concepts were optimized. By experimental measurements and theoretical calculations, the post-yield movement performances of the scaled Flying Wing Anchor® concepts are presented.

The challenge in experimentally measuring the anchor post-yield movement while optimizing the Flying Wing Anchor® concepts was understanding if the test results are affected by the defects caused by the scaled models, testing setup or loading conditions. This section mainly focuses on the repeatable data obtained after several modifications of anchor models and testing setup. Even though the tests failed to obtain repeatable results

155

are not presented here, the key outcomes from the failures are addressed to provide advice for researchers.

The post-yield movement analysis of the Flying Wing Anchor® concept focuses optimizing anchor concepts to achieve installation and mobilization of ultimate capacity as planned. The installation starts with free-fall embedment and continues with drag embedment. This section focuses on the anchor performance and installation during drag embedment. Experimental measurements of anchor resistance and six-degree-of-freedom behavior are presented. The loads presented here are corrected for testing setup frictions (such as pulley friction) and represent the net anchor resistances.

The main goals for the post-yield analysis can be grouped as:

1. Initiation of the post-yield movement: During free-fall penetration, the shank needs to be attached to the fluke to reduce penetration resistance and achieve deeper penetration after free-fall. The loading line attached at the shackle is dragged into soil with the anchor. After the free-fall embedment, anchor line forms a reverse catenary geometry with increasing tension. As the loads acting on the wind turbine start to increase, the mooring line transfers the load to the anchor. For an anchor near vertically embedded into soil, it is important to ensure anchor dives deeper without being pulled out of soil. The initiation of post-yield movement analysis of the DEA and VLA scaled model showed that the initial anchor yield must be in pitch rotation while the shank is attached to the fluke. Scaled anchor models were tested experimentally to measure the initial mode of failure during the initiation of post-yield movement.

2. Coupling mechanism shank release angle: The coupling mechanism designed by Iturriaga Flores (2016) releases the shank when the target pitch angle is achieved. When the shank gets released, it aligns itself with the loading line and the angle

156

between fluke and shank increases to 60-degrees. The angle coupling mechanism releases the shank is measured using scaled anchor models.

3.   Anchor dive trajectory: After the shank is released, anchor starts to yield in shear direction when anchor capacity in shear loading is mobilized. With further increase in the line load, anchor embeds deeper while the fluke-shank angle increases. When the shank angle from the fluke plane is approximately 90 degrees, the anchor mobilizes its ultimate holding capacity. The dive trajectory of the scaled anchor models were measured experimentally.

6.6.1   EXPERIMENTAL SETUP FOR DRAG EMBEDMENT LOADING

Anchor post-yield movement was measured by drag embedding scaled anchor models with the magnetometer attached on them to measure six-degree-of-freedom behavior. The tests were conducted in the thermoplastic soil tank with a wooden frame. The magnetometer source is placed as close to the soil test bed as possible to reduce the noise caused by the stepper motor. The anchor model was initially fully embedded into soil. Depending on the anchor model thickness, geometry and material; the magnetometer sensor is either placed on the anchor model or inserted into a cut on the anchor model to avoid increasing the anchor resistance due to magnetometer sensor. The magnetometer line was either attached to the anchor loading line or placed on the soil layer by passing through the fluke separation distance (bi-wing models) such that it won't affect anchor pitch rotation.

The drag embedment test setup, presented in Figure 6.30, shows that anchor was dragged in the +Y direction and the soil depth increases in the +Z direction. The X, Y and Z directions depend on the orientation of the magnetometer sensor. To avoid confusion, the +Y direction is presented as the direction of drag, +X is the out-of-plane direction and

157

+Z is the vertical direction of embedment into soil. Drag embedment tests were performed by placing the anchor into soil with 0.5-6 in. of soil layer covering the highest point of the anchor. The depth of soil layer covering the anchor was measured by inserting a measurement stick and finding the depth of the highest anchor point. The Gulf of Mexico marine clay soil test bed was remolded at the beginning of the test and when the waiting period exceeds couple of minutes, the soil test bed was also remolded in between testing cycles.

Anchor loading lines of 50 lb-rated 0.025 in. diameter nylon rope and 160-lb rated 0.092 in diameter nylon coated wire are used. When the magnetometer line was attached to the nylon rope, it was covered with a duct type increasing the total line diameter to 0.16 inches. The thinner loading line was preferred to reduce the soil friction along the loading line and to avoid a complex connection at the pad-eye. The drag distance was limited to the length of the soil tank. The loading line angle at the mudline was minimized by placing a directional pulley close to mudline. To increase the drag distance, a hole was drilled on the side of the anchor to place the directional pulley outside of the soil bed. Both pulley locations are presented in Figure 6.31. The pulley friction was measured with a separate test and the pulley friction coefficient is calculated. Pulley friction was subtracted from the load cell measurements to calculate the net anchor resistance. All the load measurements presented in this section show the net anchor resistances. Anchors were pulled at line displacement rates between 0.04-8.0 in/sec to assess the anchor post-yield behavior under different loading rates.
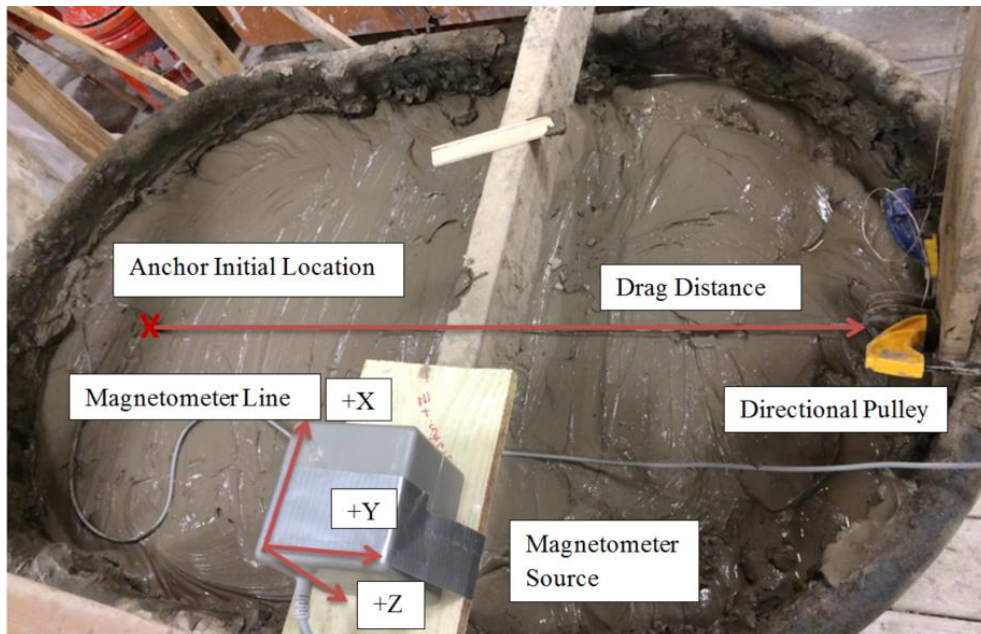
Figure 6.30: Drag embedment loading test setup

Figure 6.31: Location of directional pulley for drag embedment tests

6.6.2 POST-YIELD MOVEMENT OF THE DIAMOND ANCHOR

The post-yield movement of the diamond-shaped Flying Wing Anchor® model was measured by experimentally testing the diamond shaped bearing plate (Figure 6.13) and the acrylic diamond models (Figure 6.16). The models were initially embedded into soil

and dragged at a constant rate of 0.8 in/sec. The dive trajectory and the anchor resistance were measured during the drag embedment. Example test results are analyzed here and repeat tests are presented in the Appendix.

The diamond shaped bearing plate was fully embedded into soil with the fluke center located approximately 0.6 B below mudline. The initial loading line (0.025 in diameter white nylon rope) angle from horizontal was approximately 5 degrees. The loading line angle was attached at the fluke center of mass. The magnetometer recordings were used to calculate the location of anchor center throughout the test. The t-bar tests were performed at two different locations in the remolded soil test bed along the drag distance. The horizontal distance between location 1 and location 2 was measured as 2.2 B. The undrained shear strength profile shows that the soil strength profile does not change within drag path.
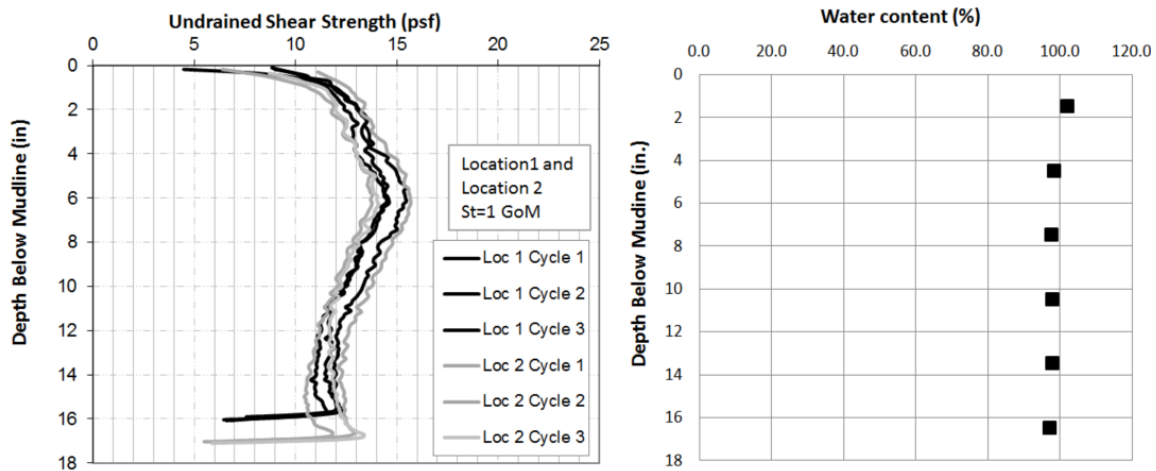
Figure 6.32: Soil strength and water content profile

Example dive trajectory results for the diamond-shaped bearing are presented in Figure 6.33 for an initial anchor pitch of approximately 45 degrees from horizontal and in

Figure 6.34 for an initial anchor pitch of approximately 30 degrees from horizontal. The net load acting on the anchor, depth of anchor center, pitch angle and the changes in yaw and roll angles are presented with respect to anchor drag distance in terms of equivalent anchor fluke length (B).

The trajectory shows the diamond-shaped bearing plate embedded deeper while the pitch angle was increasing. The tests were continued until the anchor was nearly vertical (pitch angle of 90 degrees) and plowing in the soil. The anchor with initial pitch of 45 degrees was able to embed 0.8B and 1.5B deeper resulting in final embedment depths of 1.4 B and 2.1 B of the anchor center. The anchor with initial pitch of 30 degrees was able to embed 0.7 B and 1.1 B deeper resulting in final embedment depths of 1.2 B and 1.7 B of the anchor center. The equivalent non-dimensional yield capacity (N_e) shows mobilized anchor capacity during dive penetration. It is calculated by normalizing the net anchor resistance with the undrained shear strength of the soil and the fluke area. For tests with initial pitch of 45-degrees, the N_e increases to 6.5-7 and decreases slightly to 5 as anchor pitches and fails. For tests with initial pitch of 30-degrees, the N_e increases to 5 and decreases slightly to 4.3 as anchor pitches and fails. As the N_e value is slightly higher than the N_{shear}, it shows the interaction between anchor resistances to shear and normal loading.

The increase in yaw and roll rotations can be explained by attaching the loading line on the anchor without using a shank. If the anchor model is not perfectly aligned with the rotational pulley at the beginning of the test, then the line angle applies an out-of-plane drag loading as the anchor approaches the pulley. Not having a shank caused anchor to yaw and roll. Those yaw and roll rotations affected the dive trajectory of the anchor. Even though the change in pitch angles were the same when the tests were repeated (cycle 1 vs cycle 2) the difference in final embedment depths can be explained by difference in yaw

and roll rotations. Especially yaw rotations caused anchor to go sideways instead of diving deeper.

      Additional tests were performed by varying the initial pitch angles but repeatable data was not obtained. Results show that changing the initial pitch angle from 30 degrees to 45 degrees did not cause a significant difference in the anchor trajectory or the ultimate load capacity.
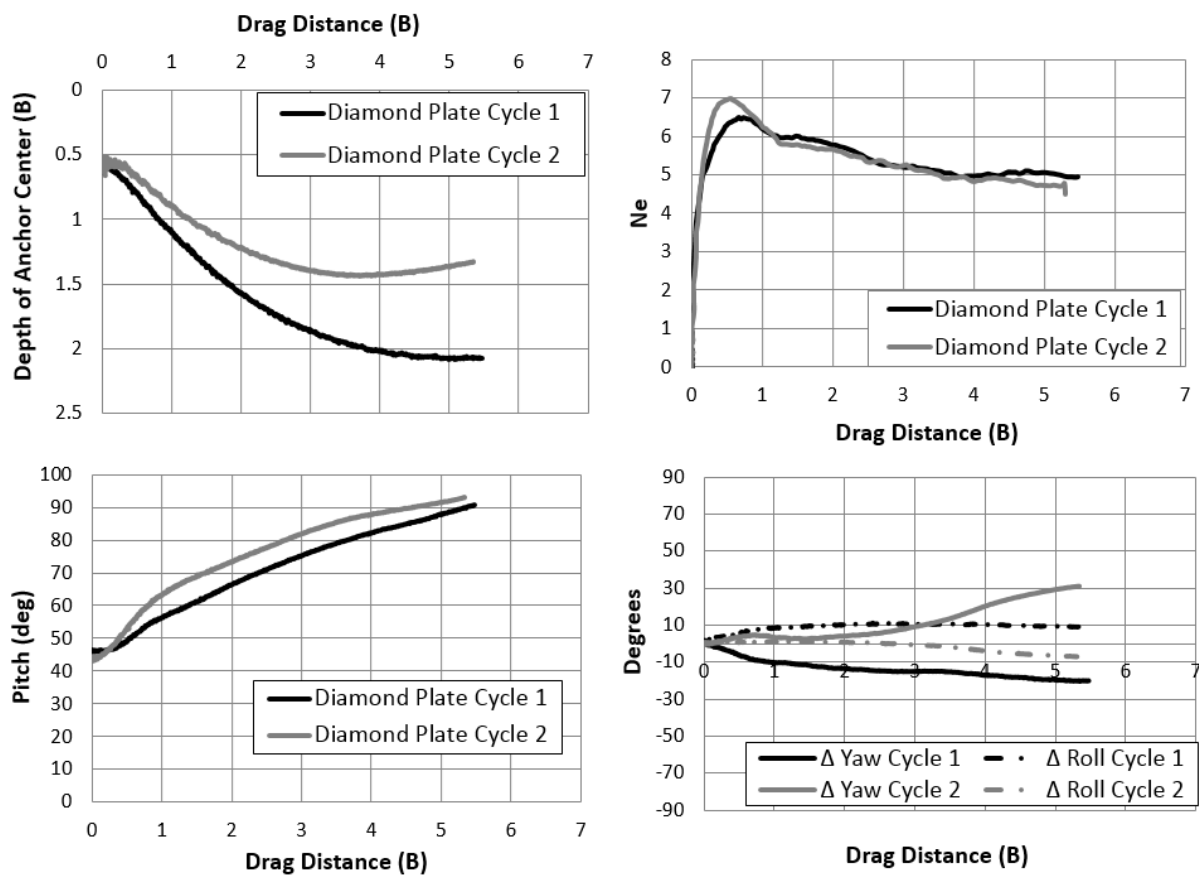
Figure 6.33: Diamond bearing plate dive trajectory, initial pitch 45 degrees
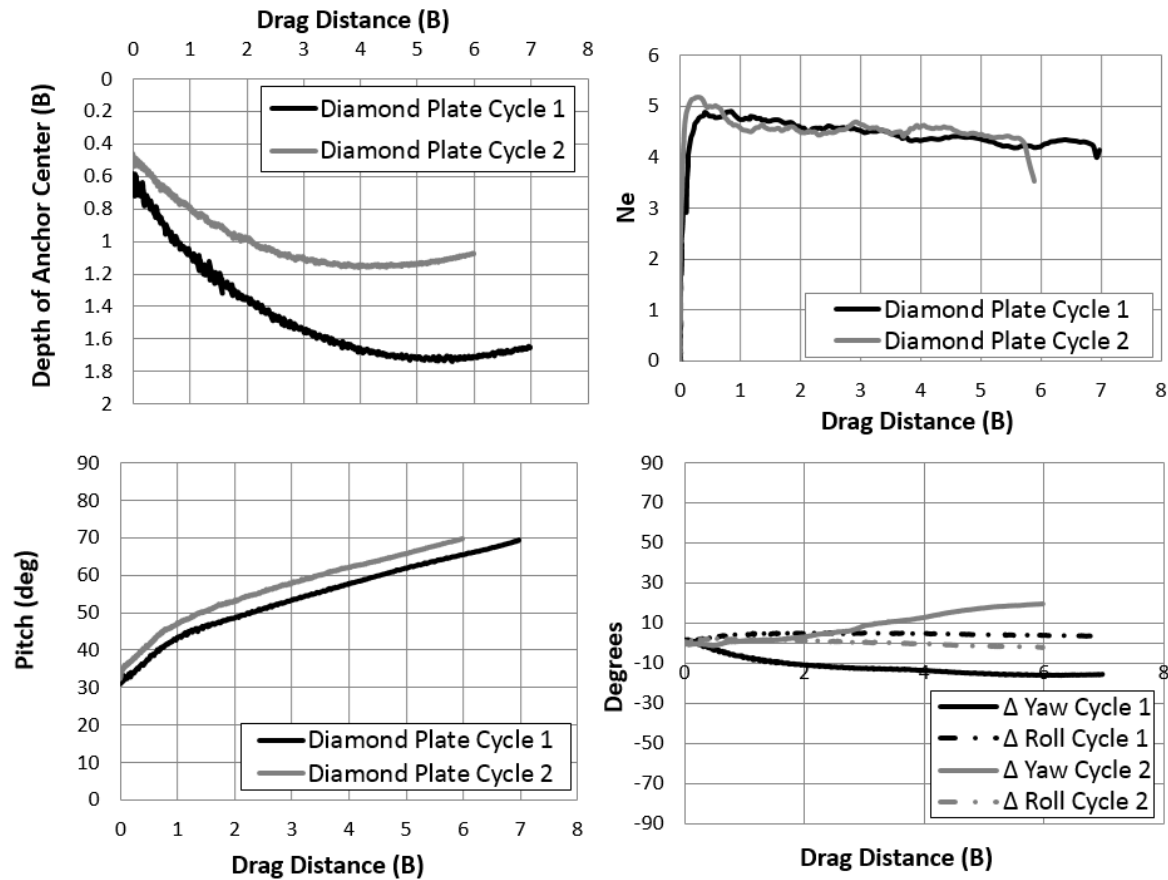
Figure 6.34: Diamond bearing plate dive trajectory, initial pitch 30 degrees

The diamond shaped one-wing Flying Wing Anchor® was tested in drag embedment loading to measure the anchor post-yield movement. The orange colored anchor model (Figure 6.16) has a beam attached at the front part of the anchor and it was tested without a shank. The other anchor model's (purple and red in color, Figure 6.16) beam was cut off to reduce anchor shear resistance and it was tested with a freely rotatable shank attached at the anchor center. The nylon coated wire with 0.092 in diameter was used as the loading line.

Anchor drag tests performed using the orange 3D printed one-wing Flying Wing Anchor® model did not result in anchor embedment. The anchor model yawed and rolled

163

significantly during testing. Attaching the magnetometer sensor close to anchor center of resistance caused loading line to interact with magnetometer sensor. Also the pure loading tests showed the ratio of pure normal loading yield threshold to pure shear loading yield threshold decreased to 2.4 from the target value of 3. This increase is mostly due to increases shear area by the I-beams on the fluke and the lower beam attached to fluke. Those beams were designed to contribute to the hydrodynamic stability but affected the dive trajectory adversely by increasing the shear resistance. Repeatable dive trajectory measurements were not obtained by testing this model.

To reduce acrylic model's shear resistance, a part of the purple anchor model's lower beam was cut off from the model. Shank was attached to model on the I-beams from two points. Shank is used to reduce the yaw and roll rotations and keep the loading line away from the magnetometer sensor. This model was tested in the remolded Gulf of Mexico marine clay test bed. The undrained shear strength profile measured at two different locations 2.36 B apart from each other along the drag path of the anchor model are presented in Figure 6.35. The model was tested by initially embedding into soil with the anchor center at approximately 1.9-2 B at pitch angles of 30-35 degrees. The anchor was able to embed 0.3-0.55 B deeper while the pitch angle was increasing to approximately 40 degrees (Figure 6.36). The final anchor center location was 2.2 B and 2.55 B below mudline. Attaching the loading line through a shank to the anchor fluke helped reduce the yaw and roll rotations during testing. Also cutting a part of the lower beam reduced anchor shear resistance and provided deeper anchor penetration with in-plane drag loading.
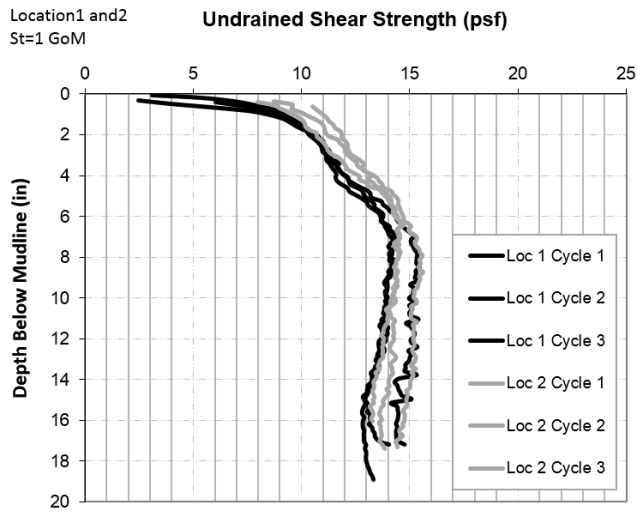
Figure 6.35: Undrained soil strength profile for acrylic Diamond model testing
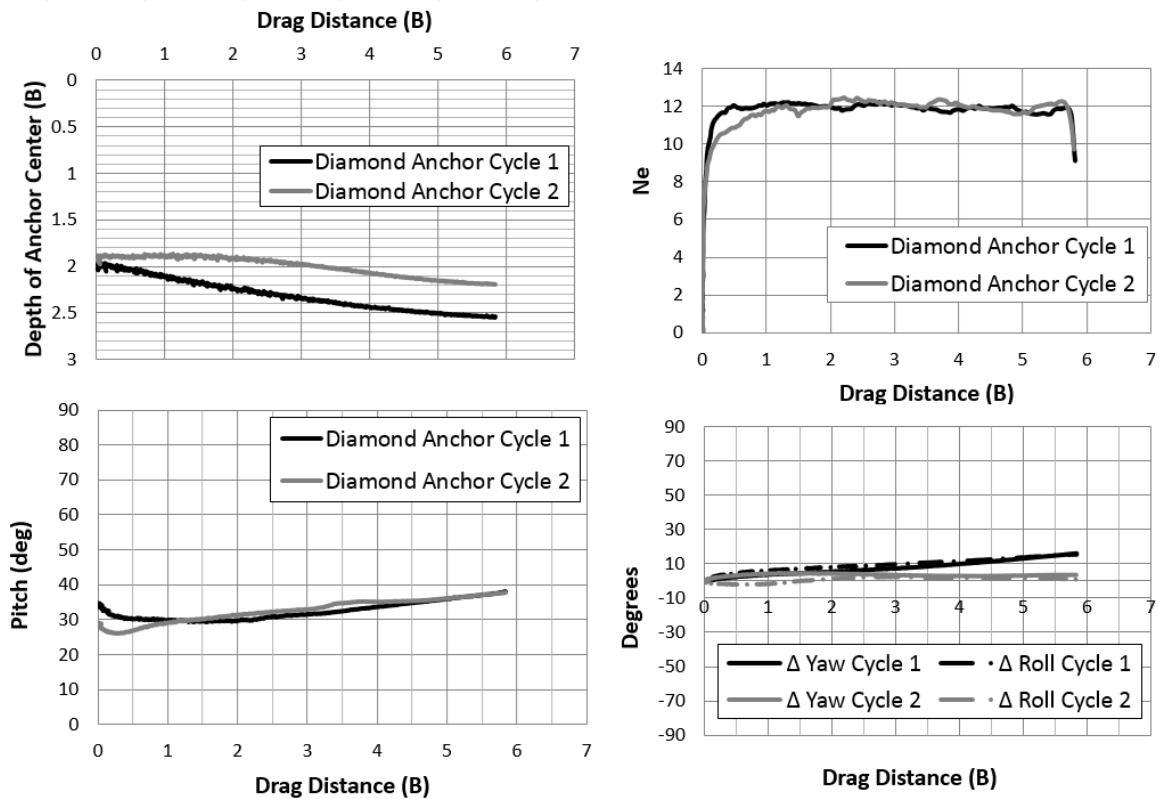
Figure 6.36: One wing Diamond anchor dive trajectory

165

The ratio of the change in displacement normal to the fluke (dn) to the change in displacement parallel to the fluke (ds) with the drag embedment is presented in Figure 6.37. The scatter in the experimental data is due to high frequency of measurements with the magnetometer. The results show that the dn/ds points are concentrated around the value of 0.5 which indicates anchor displacement in direction parallel to fluke is 2 times the displacement in direction normal to fluke.
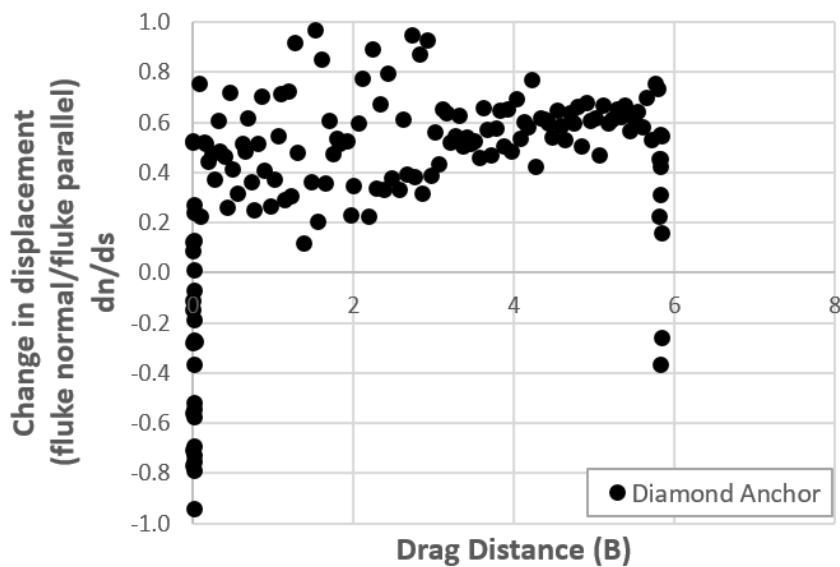
Figure 6.37: Change in dn/ds with drag, Diamond anchor

6.6.3 POST-YIELD MOVEMENT OF THE PALOMA ANCHOR

The bi-wing Flying Anchor Concept of Paloma anchor was tested using scaled anchor models built in plywood and acrylic. The models were subjected to small modifications during testing as needed. Magnetometer was attached to a slot cut on the fluke plane and the six-degree-of-freedom behavior was recorded during drag embedment along with the anchor resistance.

166

The initial drag embedment tests were conducted by using the plywood model (Figure 6.14). The dove head and the rod mechanism represent the fluke-shank coupling mechanism of the prototype. The loading line (0.025 in diameter white nylon rope) was inserted into a notch made on the rod to avoid line movement along the rod serving as the shackle. The model was tested at different initial pitch angles and embedment depths. The results showed that using the plywood model caused testing errors as plywood absorbed the water and swell. The swelling of the wood bolts at the fluke-shank connection increased shank's resistance to opening. The shank arms were held together with plywood pieces and detaching of those plywood pieces during testing resulted in termination of the tests for several times. Repeatable data was not obtained due to testing model failure and it is decided to build acrylic models (Figure 6.17) using the 3D printers.

The acrylic Paloma scaled models were used to measure initiation of anchor pitch rotation, fluke-shank coupling mechanism shank release angle, in-plane and out-of-plane drag loading, and the effect of loading rates on anchor dive performance.

Initiation of Anchor Pitch Rotation

The Flying Wing Anchor® concept requires anchor movement to initiate with pitch rotation. If anchor can yield in rotation before bearing, it can dive deeper with drag loading. If the anchor yields in bearing, this results in anchor to be pulled out of soil. The Paloma model's dove head fluke-shank coupling mechanism was designed to hold the shank attached at the anchor front fluke to ensure the post-yield movement initiates with pitch rotation.

The initiation of anchor pitch rotation was experimentally measured by testing the acrylic Paloma anchor with magnetometer attached and measuring the anchor resistance to pitch rotation. The scaled anchor models were initially embedded into soil near vertically.

167

The shank was held attached to fluke by the fluke-shank coupling mechanism. The anchor loading line angle from the horizontal was minimized by the directional pulley that is attached on the side of the soil tank at the end of drag distance. By using the electric motor, the loading line was pulled to load the anchor at a constant rate.

Anchor is designed to start pitching when the moment applied at anchor center of resistance exceeds the pitch resistance of the anchor. The moment applied to rotate the anchor is calculated by multiplying the eccentricity caused by holding the shank attached to front fluke with the line load's component perpendicular to fluke plane. The pitch rotation is expected to continue until the fluke-shank coupling mechanism releases the shank. The design fluke-shank release angle of 60 degrees is controlled by the geometry of the dove-head mechanism (Iturriaga Flores, 2016). The roller rod (purple rod in Figure 6.17) serves as the shackle and the loading line is attached at the middle of the rod. The shackle rolls inside the dove-head mechanism while anchor pitches from vertical. The illustration of the anchor pitch rotation with the closed shank configuration is presented in Figure 6.38. As the loading line is pulled in +Y direction, the anchor rotates counter clockwise in the Y-Z plane until the shank is released. Once the shank is released, the pitch rotation stops and the shank gets aligned with the taut loading line.
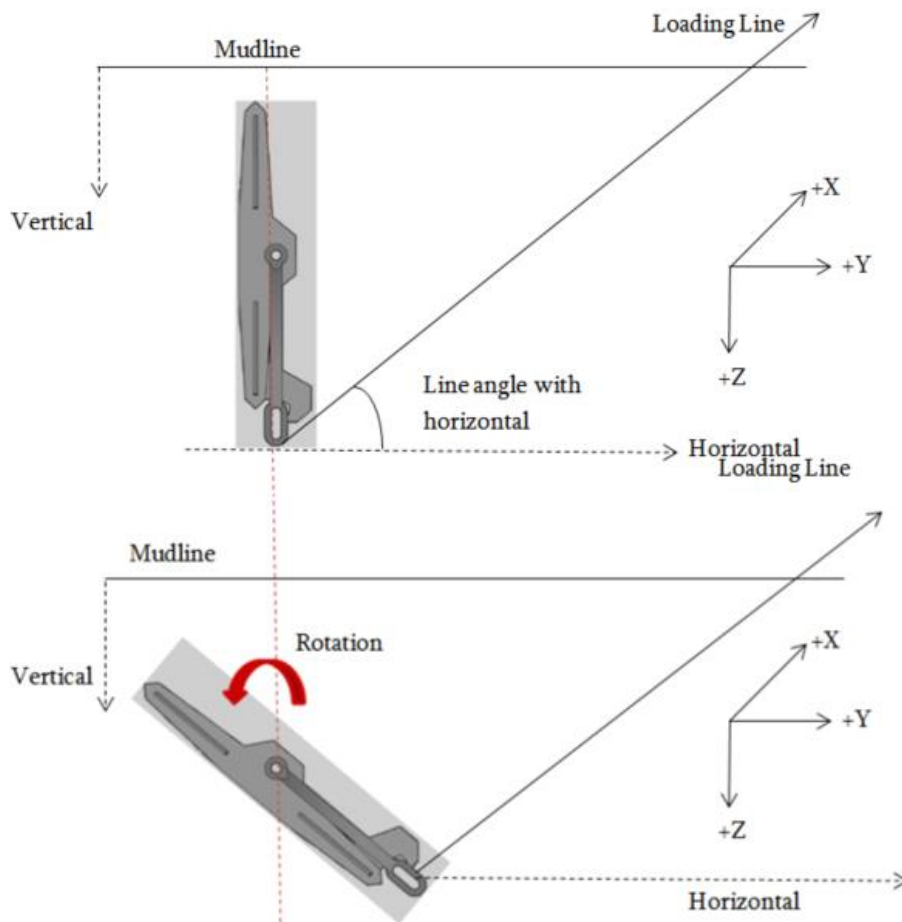
Figure 6.38: Paloma anchor initial pitch rotation

An example test result and the theoretical calculation for that test are presented below. The acrylic bi-wing model with the fluke area of 12 in.[2] was tested in the soil test bed with constant undrained shear strength of 14 psf. The anchor line displacement rate was reduced to 0.04 in/sec (1/20th of the t-bar testing rate) to capture anchor pitch rotation with the magnetometer and load cell measurements during testing. The net anchor resistance and anchor pitch angle are presented in Figure 6.39. Initially the anchor was vertical (87 degrees) in soil. As the load increases to approximately 1 lb, the anchor starts to pitch very slowly. Tangent 1, 2 and 3 are added on the figure to show the change in pitch

angle with increasing load. The highest slope of tangent 3 indicates that the anchor reached its maximum pitch rotation rate when the load exceeded approximately 3.5 lbs. The red point on the curve shows shank release. When the shank is released, the load dropped suddenly since the resistance from the dove-head mechanism was overcome. Then the load started to increase at a constant pitch angle as the shank opens and gets aligned with the loading line. By the end of the test, anchor started to pitch slightly at a constant load of approximately 12 lbs. The sudden drop from 12 lbs to 10 lbs was due to the termination of the test.

Figure 6.39: Initiation of anchor pitch rotation

The force required to initiate pitch rotation for this scaled anchor model can be calculated theoretically by:

$$M = F_{net} \cdot e \tag{6.5}$$
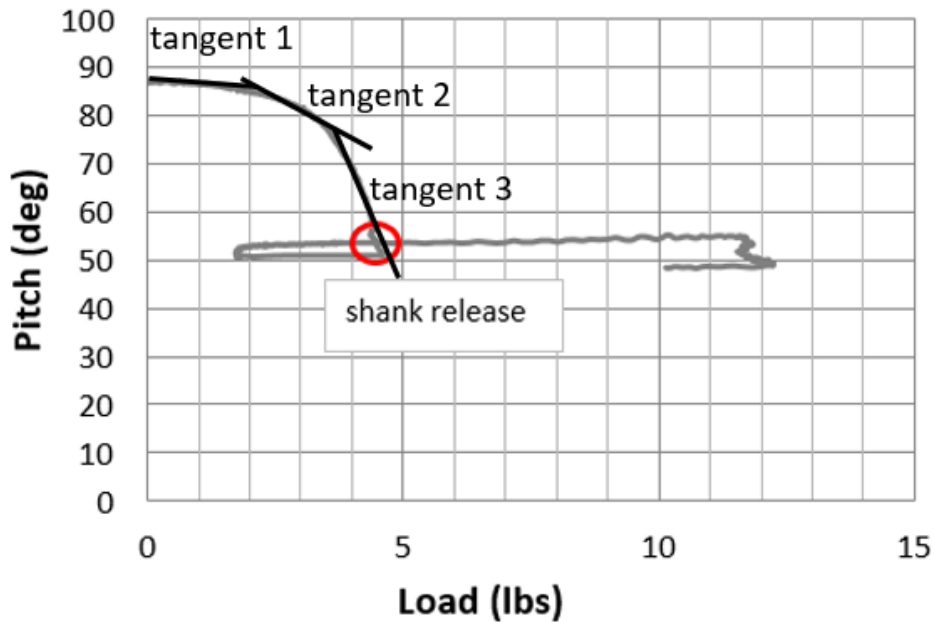
170

$$N_{pitch} = \frac{M_{max}}{A_f s_u L_f}$$
(6.6)

where:

F_{net}: the net load ($F_{line}.\cos$(line angle from horizontal))

e: eccentricity (the distance from pad-eye to fluke-shank attachment)

A_f: Fluke area

L_f: Equivalent fluke length ($\sqrt{A_f}$)

For the acrylic bi-wing anchor model with the fluke area of 12in.^{2}, equivalent fluke length of 3.46 in., eccentricity of 4.5 in. and N_{pitch} between 4-4.5; constant undrained shear strength of 14 psf, it can be predicted that when the net load exceeds 3.6-4 lbs, the anchor will start rotating. The initial line angle was measured approximately 10-degrees for this test. The corresponding line load can be calculated as 3.66-4.06 lbs. It can be concluded that the experimental results are similar to predicted results.

Fluke-Shank Coupling Mechanism Shank Release Angle

The fluke-shank coupling mechanism is designed to release the shank mechanically depending on the anchor pitch angle from horizontal and anchor line angle at the shackle from horizontal. When the coupling mechanism releases the shank, the angle between the shank and the fluke plane is equal to 60-degrees (shank is at 30-degrees from fluke normal). The 3D printed scaled Paloma anchor model was tested experimentally to measure the angle between fluke plane and shank when the shank is released by the coupling mechanism. The 60-degree angle is measured in two steps: first the anchor is placed into soil and the line angle from horizontal is calculated for a taut line configuration.

171

The anchor starts to rotate from vertical with the increasing line load. As the magnetometer is inserted into the anchor fluke, the pitch angle of the anchor is measured simultaneously with anchor resistance. Assuming the change in line angle from horizontal is negligible during anchor rotation, the sum of anchor pitch from horizontal (magnetometer recording) and the initial line angle from horizontal gives the angle between shank and fluke immediately after the coupling mechanism released the shank. The angle configuration right after the shank is released is presented with an illustration in Figure 6.40.
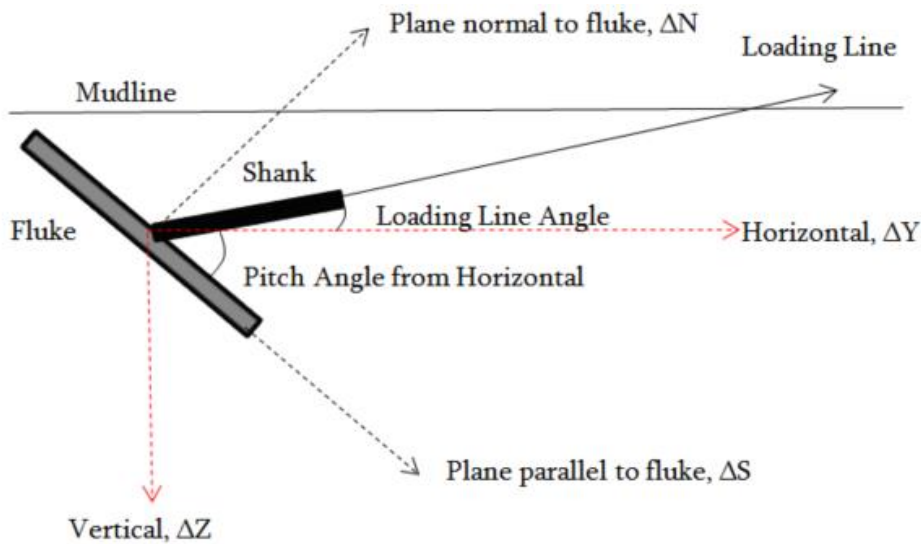
Figure 6.40: Anchor angle configuration after the shank is released

By experimental tests, the angle when the fluke-shank coupling mechanism releases the shank is measured. Initially the line release angle was checked by a protractor when the anchor was out of soil and the dove head was filed until the target angle of 60-degrees was measured outside of soil. The anchor loading line displacement rate during anchor pitch and shank release was reduced to 0.04 in/sec ($1/20^{th}$ of the t-bar testing rate).

Since dove head-roller mechanism was built by acrylic, the roller was not able to roll inside the dove head smoothly. When the anchor is loaded fast, the roller might not have enough time to align itself. Also when the anchor is loaded slowly during the pitch rotation and shank release, the changes in the load cell and magnetometer measurement can be observed easier during testing such as the shank release can be observed as a sudden drop in the measured load before the load starts to increase again.

An example test result is presented in Figure 6.41. The pitch-load graph shows that the anchor was initially embedded near vertically into soil (pitch of 83 degrees). As the load increased, anchor started to pitch and the pitching stopped when the load was approximately 4.3 lbs. The sudden drop in the load to 1.7 lbs at anchor pitch of 45 degrees indicates that the shank was released. The initial line angle was measured as 13 degrees. This means right after the coupling mechanism released the shank, the angle between fluke and shank was equal to 58 degrees which is very close to the design angle of 60 degrees. The difference of 2 degrees can be explained by the approximation in the measurement of the initial line angle and the assumption of constant line angle from horizontal during anchor pitch rotation. The change in yaw and roll angles are presented with respect to pitch angle. The magnetometer recordings show that anchor was only rotating in the pitch direction; yaw and roll angles were constant. It can be inferred that using a shank during testing significantly reduces anchor yaw and roll rotations during in-plane drag loading.
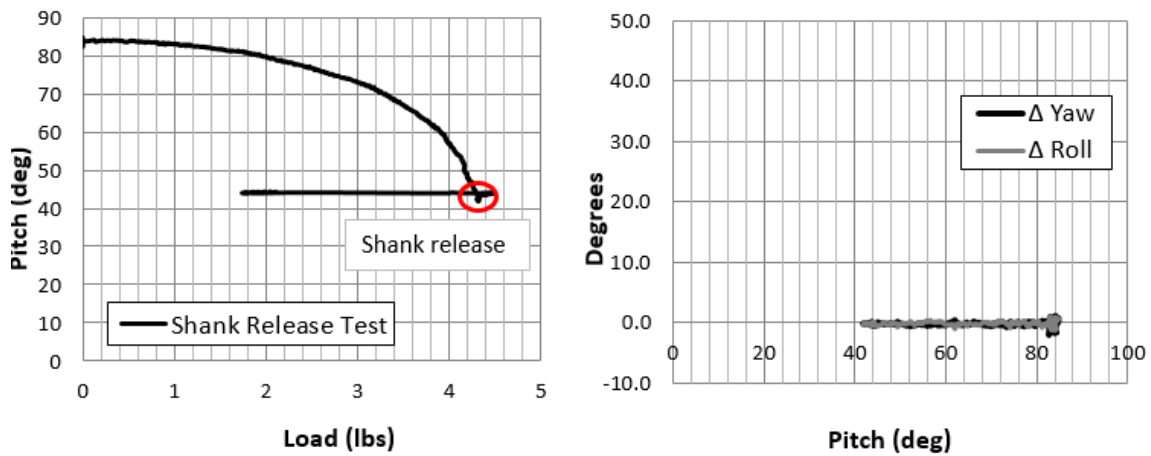
Figure 6.41: Coupling mechanism shank release angle test results

In-Plane Drag Embedment Installation

The acrylic Paloma anchor was loaded by in-plane drag to measure anchor dive trajectory after shank release. The scaled anchor model was dragged several fluke lengths horizontally while measuring the six-degree-of-freedom behavior by the magnetometer and the anchor resistance by the load cell. The undrained soil strength profile of the remolded Gulf of Mexico marine clay test bed is presented in Figure 6.42.

Figure 6.42: Undrained soil strength profile of the remolded clay test bed

174

An example test results is presented in Figure 6.43. The test was started by initially embedding anchor into soil with the anchor center located at 1.15 B near vertically (initial pitch of 87 degrees). Initially the anchor line load was pulled at a rate of 0.04 in/sec until the shank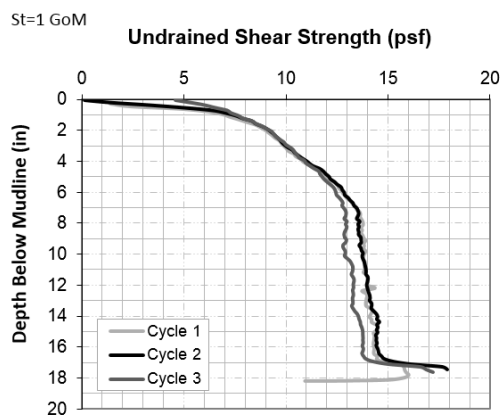 was released. The anchor dive trajectory was measured by dragging the anchor further after the shank was released. The results show that the fluke-shank coupling mechanism released the shank when the load was around 4.2 lbs and the anchor pitch was around 52 degrees. The initial line angle was measured as approximately 10 degrees which shows when the shank was released; the angle between fluke plane and shank was increased to 62 degrees (Figure 6.44). The shank release was observed in the load graph as a sudden drop in the load from 4.2 lbs to 1.9 lbs. The loading line displacement rate was increased to 0.4 in/sec (1/2 t-bar loading rate), after the shank was released (the point marked with red circle on load and pitch graphs). The net anchor resistance was normalized by the fluke area and the undrained shear strength of the soil to calculate the equivalent non-dimensional yield threshold. The N_e value increased to 4 when anchor was rotating and the sudden drop to 1.8 indicates the shank release. The resistance immediately picks up and increases to 10. This value being in between N_{shear} and N_{normal} shows that anchor yields in both shear and normal directions. The anchor capacity is mobilized and Ne stayed constant when anchor was failing. At the end of the test: anchor pitch angle from horizontal was 50 degrees, anchor center was at a depth of 1.55 B from the mudline and anchor equivalent bearing capacity factor of 10 was measured. Anchor was able to embed 0.4 B deeper when subjected to in-plane drag loading.

Results show that when the anchor trajectory became horizontal by the end of the test (indicating anchor plowing in failure), the ultimate holding capacity of the anchor was still maintained. There is no significant yaw or roll during the test and the anchor dive trajectory shows anchor was embedded deeper by in-plane drag loading.
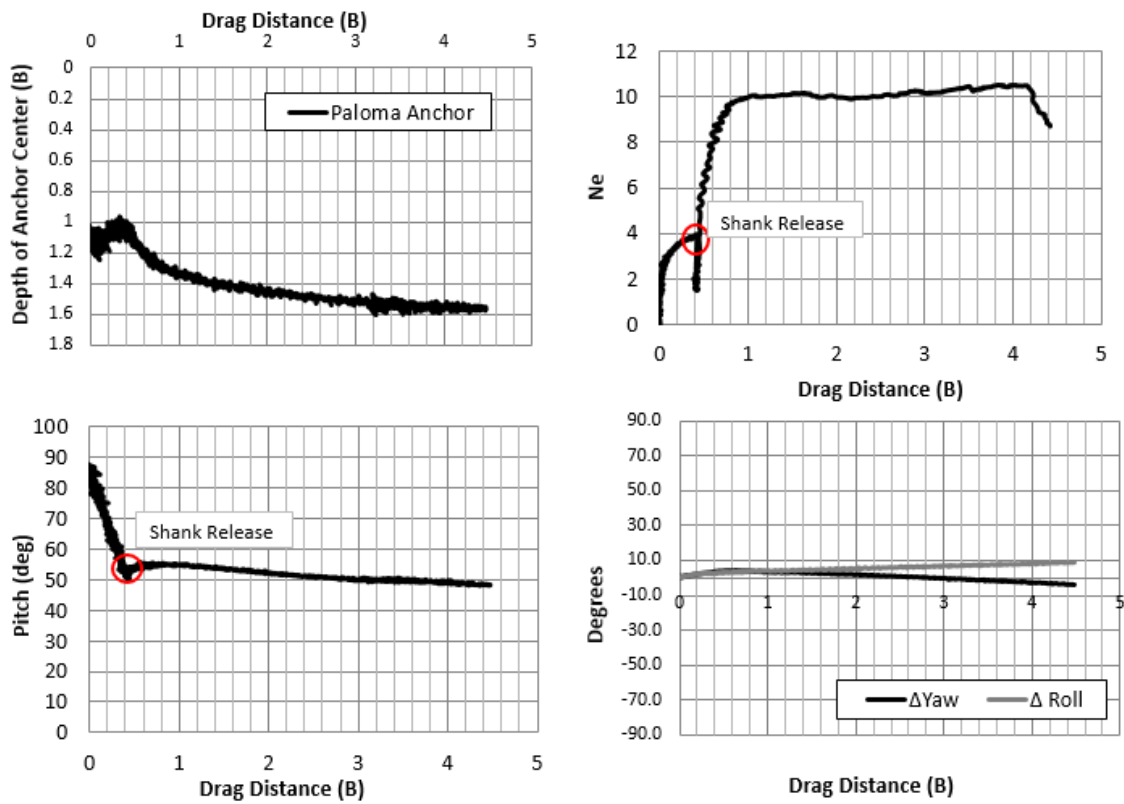
175

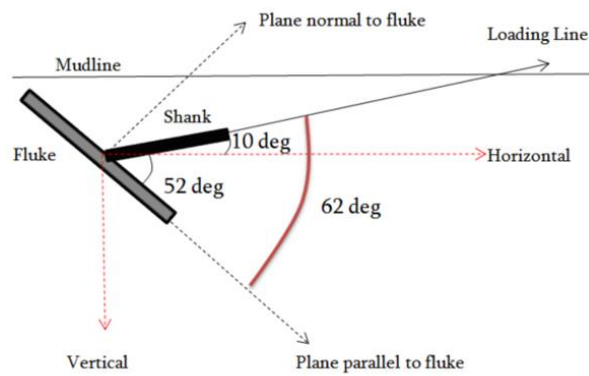Figure 6.43: Bi-wing Paloma anchor post-yield movement

Figure 6.44: Bi-wing Paloma, angle configuration after shank was released

The magnetometer presents anchor displacements with respect to X-Y-Z plane. Another way of presenting anchor trajectory is to translate those displacements into anchor plane. The magnetometer measurements are used to calculate anchor displacement in directions parallel (S) to fluke and perpendicular (N) to fluke, for a constant anchor pitch. The sign conventions and displacement directions are presented in Figure 6.45. The calculated displacements in S and N directions with horizontal drag distance (in Y direction) for the test results presented in Figure 6.43 are shown in Figure 6.46. The anchor moved in the direction parallel to fluke for 3.3 B while it was dragged in the horizontal direction for 4.5 B. It shows majority of anchor displacement was yielding parallel to fluke which is failure in the in-plane shear direction. The displacement in the direction parallel to fluke was around -0.3 B meaning that the anchor was slightly yielding in the normal loading direction.
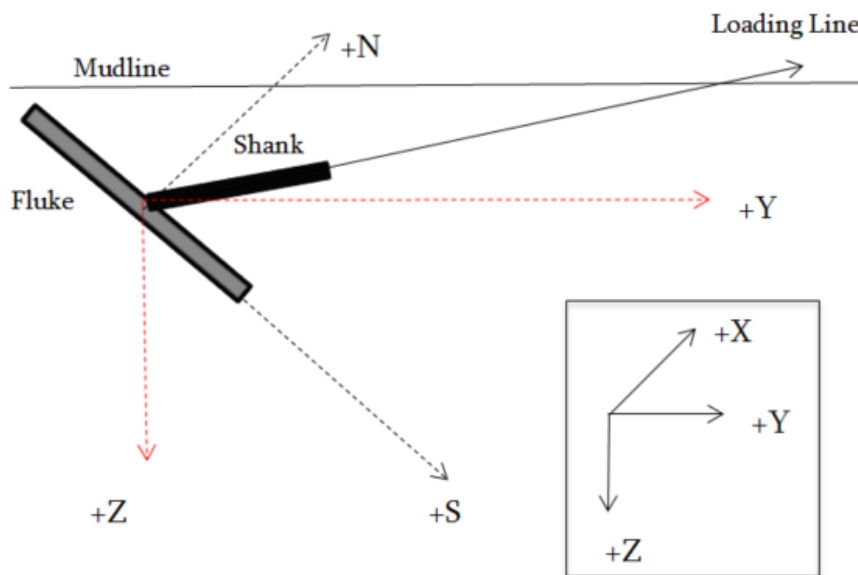

Figure 6.45: Bi-wing Paloma anchor displacement directions and sign convention
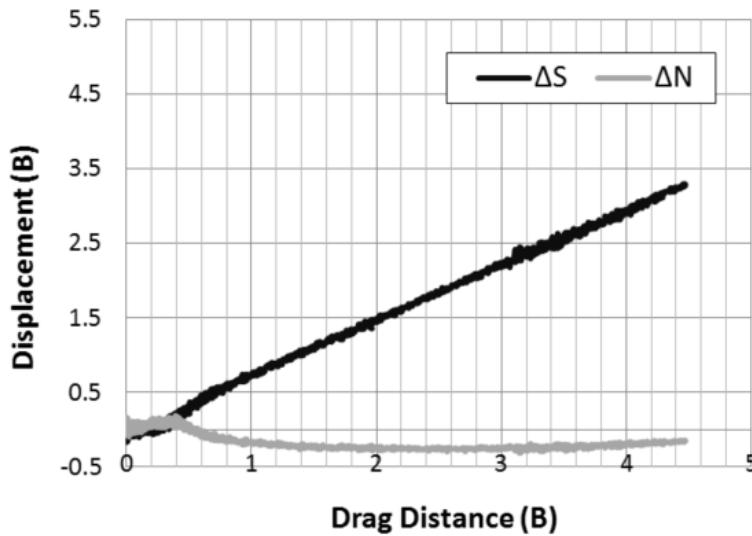
Figure 6.46: Bi-wing Paloma displacement in direction parallel and perpendicular to fluke

In-plane drag embedment installation after shank release was also measured by a separate test focusing on the anchor performance after shank release. The scaled Paloma anchor model was embedded into soil at the pitch angle that represent the anchor configuration at the moment of shank release. For the initial line angle of approximately 5 degrees from horizontal, the anchor fluke was placed at an initial pitch angle of 50 degrees. Shank is released from the coupling mechanism and placed in resting position on the anchor coupling mechanism. Increase in line tension increased the shank angle from fluke as the shank got aligned with the loading line.

The anchor center was initially located at a depth of 0.8 B below the mudline and the anchor loading line was pulled at a displacement rate of 0.4 in/sec. An example set of test results are presented in Figure 6.47. The anchor was embedded deeper with further drag while the pitch angle was changing slightly. The N_e increased to 9.5 and the mobilized anchor resistance was maintained while the anchor was diving deeper. The change in yaw and roll angles were around 10 degrees in each direction by the end of the test. The yaw

178

and roll angles started to increase gradually after a horizontal drag distance of 1 B and reached maximum of 10 degrees by the end of the test. The anchor embedded 0.7 B and the final anchor center location was 1.5 B in 3.5 B horizontal drag distance.
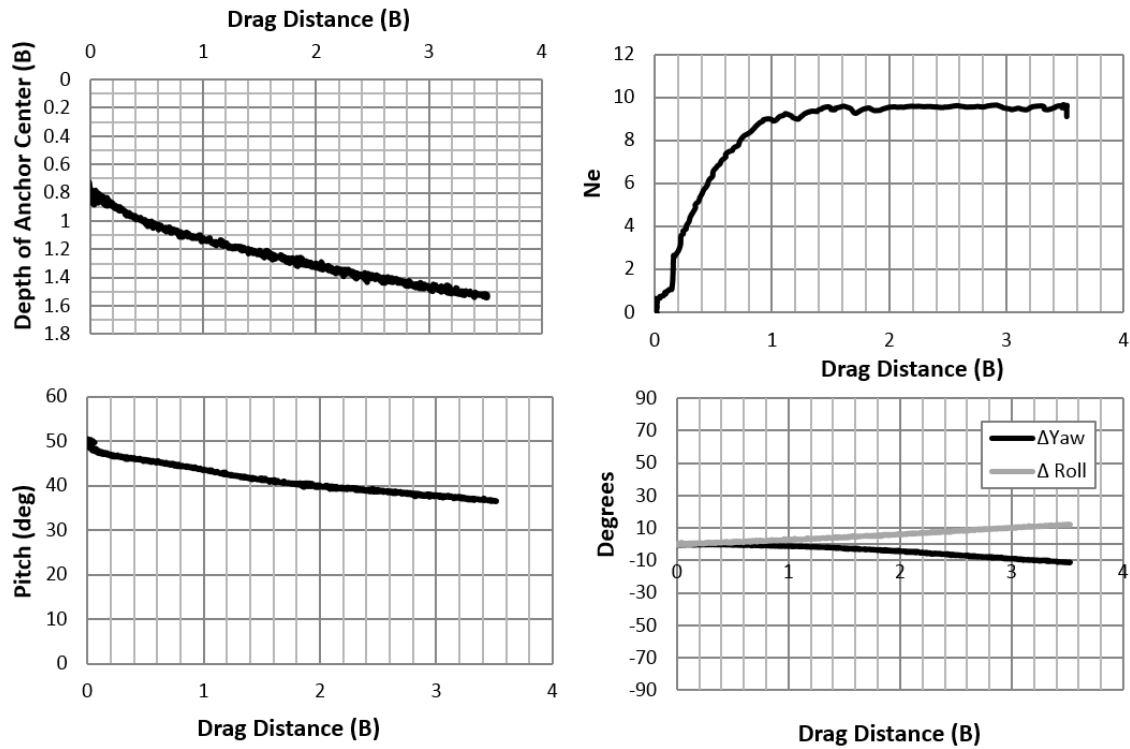
Figure 6.47: Bi-wing Paloma dive trajectory after shank was released

Out-of-Plane Loading during Drag Embedment Installation

The scaled anchor model dive trajectory was measured when the anchor is subjected to out-of-plane drag embedment loading. The anchor can be subjected to out-of-plane drag loading immediately after free-fall embedment if the anchor rolls during free-fall penetration. To analyze the ability of the anchor to correct itself and release the shank at the target angle affects anchor dive trajectory.

179

The bi-wing Paloma anchor was initially placed vertically (84 degrees pitch) and fully embedded into soil with the anchor center 1.2 B below mudline with the initial roll angle of 30 degrees. Figure 6.48 schematically shows the top view and side of how Paloma anchor is loaded in out-of-plane loading direction. The top view shows the back of the anchor and how it was rotated 30-degrees from the axis perpendicular to loading direction to give an initial roll of 30 degrees. The initial line angle from horizontal was measured as 10 degrees. The side view shows that anchor was initially embedded near vertical.
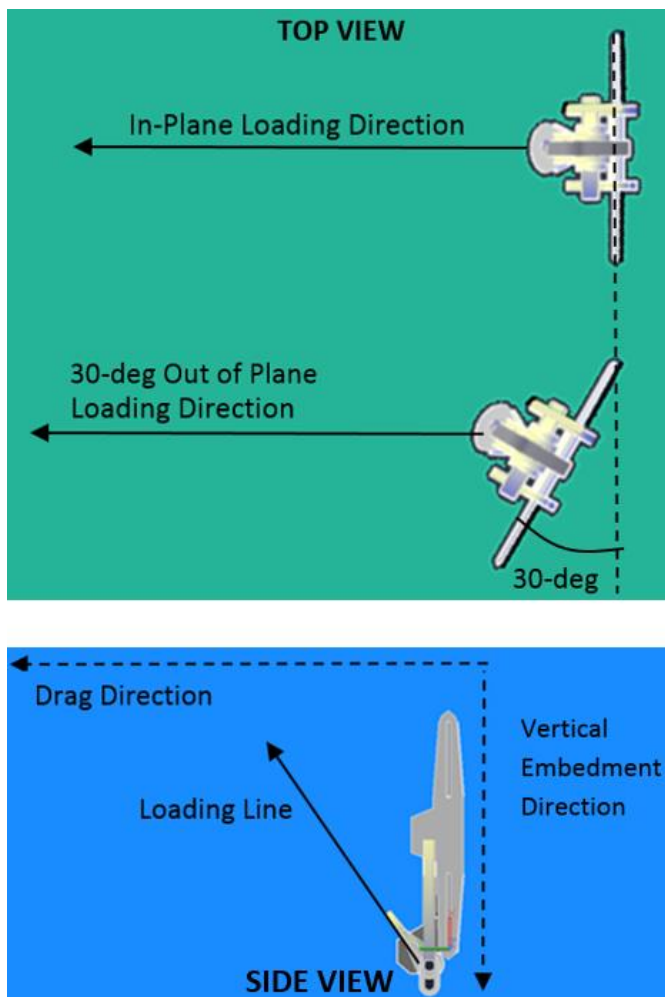

Figure 6.48: Initial bi-wing Paloma orientation for out-of-plane drag test

An example set of test results of the out-of-plane drag loading tests are presented in Figure 6.49. The anchor resistance is presented in terms of the equivalent bearing capacity factor. Initially N_e increased to 4 and dropped to 1.7 indicating the shank was released. After the shank release, N_e increased to 11 and the holding capacity of the anchor was maintained until the test was terminated. N_e of 11 was in between N_{shear} and N_{normal} for the Paloma anchor indicating the anchor was failing in shear and normal loading directions simultaneously. During the drag embedment loading, anchor pitch changed from 84 degrees to 50 degrees. The shank was released from the coupling mechanism when the anchor pitch from horizontal was 50 degrees. Neglecting the small change in anchor line angle during this rotation, the angle between fluke and shank became 60 degrees immediately after shank was released. It shows the coupling mechanism released the shank at the angle it was designed to release. With further drag loading, anchor started to yaw and roll approximately 10 degrees in each rotational direction with the shank free to move. The anchor did not diver deeper but yielded in the horizontal plane, plowing while anchor pitch was changing from 50 degrees to 40 degrees. Anchor was able to maintain the holding capacity during plowing.

The comparison of initial and final anchor positions is presented with schematic Paloma drawings from different views. The results show that when the anchor was loaded up to 30 degrees out-of-plane, the fluke-shank coupling mechanism released the shank at as designed and the anchor was able to correct itself with yaw and roll rotations after the shank was released. The anchor was aligned with the loading line at the end the of the test indicating further loading would have loaded the anchor in the in-plane shear direction.
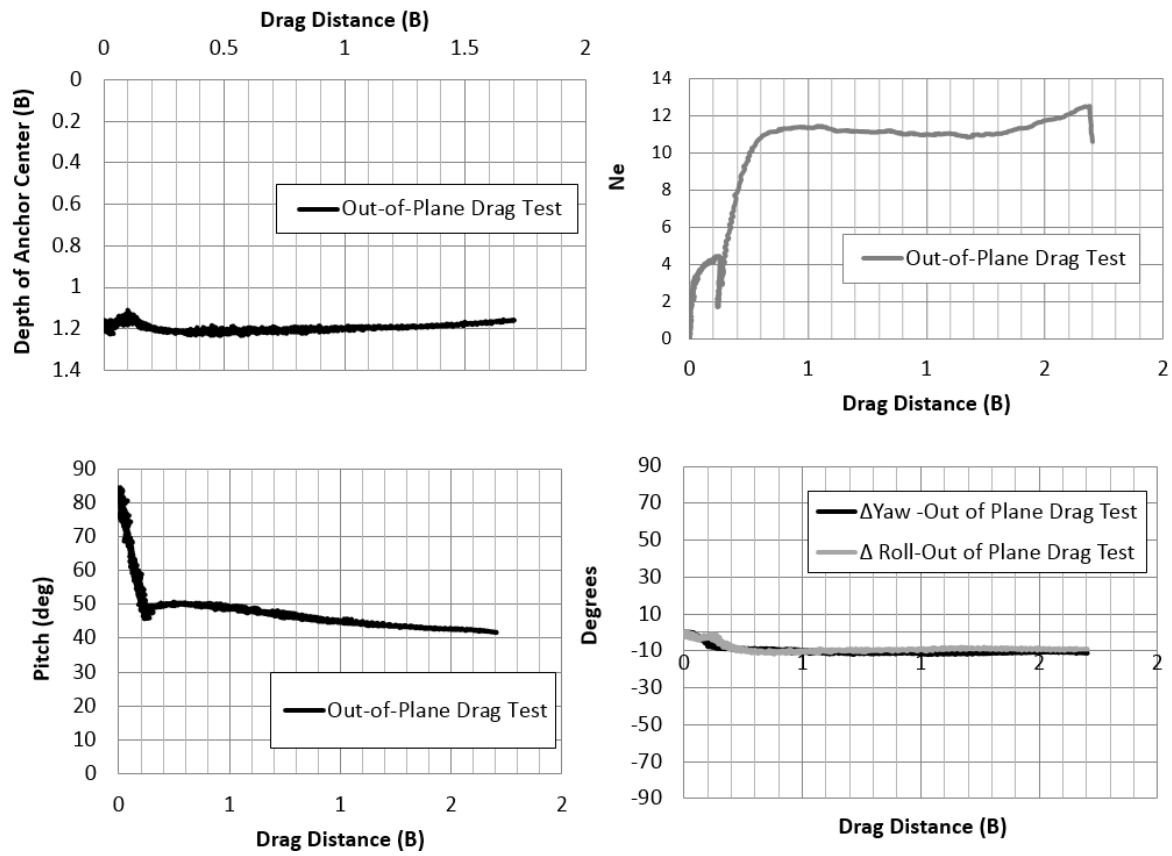
Figure 6.49: Bi-wing Paloma out-of-plane drag loading test results

Position	Side View	Top View	Front View	Back View
Initial Position				
Final Position				

Table 6.2: Initial and final position of Paloma anchor, out-of-plane drag loading test

Effect of Line Displacement Rate on Measured Anchor Dive Performance

The anchor drag embedment tests were performed with initially pulling the loading line at a displacement rate of 0.04 in/sec until the shank was released, then increasing the line displacement rate to 0.4 in/sec during anchor dive penetration. The reason for initially using a small loading rate is to make sure shank release is observed during testing by the load and magnetometer measurement. The rest of the test was continued at a higher rate to have undrained testing conditions, to save from testing time and to have a feasible data analysis process. To analyze the effect of anchor loading line displacement rate, that determine anchor rotational and translational displacement rates, drag embedment tests were performed at different loading rates.

The tested line displacement rates of 0.04, 0.4, 0.8 and 4.0 in/sec correspond to anchor rotational rates of 0.25, 2.5, 5 and 25 deg/sec for the bi-wing Paloma anchor scaled model with 12 in^2 fluke area. The tests were conducted in the remolded Gulf of Mexico marine clay test bed with average undrained shear strength of 19 psf. The thin loading line of nylon rope was used for drag loading and recordings were corrected for pulley friction. The line displacement rate was kept constant during the test and the bi-wing Paloma model was tested for anchor pitch rotation, shank release and dive trajectory.

The change in anchor pitch and load for each loading rate is presented in Figure 6.50. The results show that the sudden drop in the load was recorded for all tests indicating the shank was released at the target angle. The measured net anchor resistance (load) increased slightly with the increasing loading line displacement rate when the rate was increased to 4.0 in/sec. For loading line displacement rates of 0.04 in/sec, 0.4 in/sec, 0.8 in/sec and 4.0 in/sec; the change in load and pitch are similar: the anchor rotated until pitch was around 52-55 degrees, followed by shank release and load increased while pitch angle was almost constant. At all of the loading rates, anchor kept plowing with further drag

loading after shank was released. The results show that performing the drag embedment loading tests with a loading line displacement rate of 0.04 in/sec, 0.4 in./sec, 0.8 in/sec or 4.0 in/sec do not cause a significant difference in the anchor dive trajectory. The measured anchor resistances were similar for loading line displacement rates of 0.04 in/sec, 0.4 in./sec and 0.8 in/sec while it was slightly higher for 4.0 in/sec. Anchor resistance and dive trajectory measurements are presented with repeat tests in details in the Appendix.
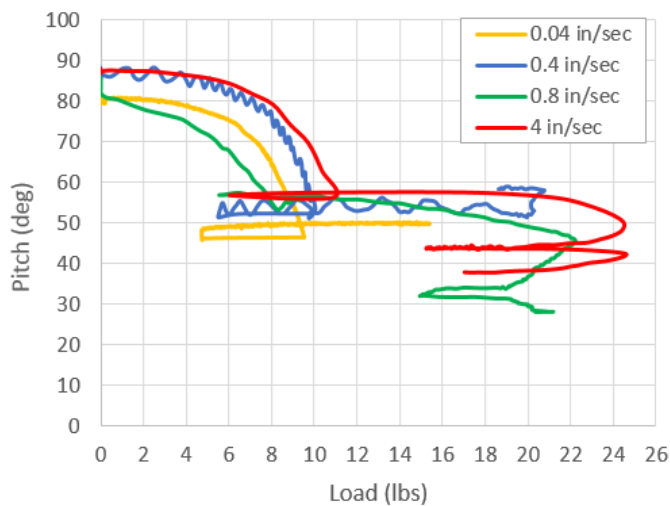

Figure 6.50: Effect of loading rate on pitch and load

Post-Yield Behavior in Normally Consolidated Soil

The bi-wing Paloma anchor model was tested in normally consolidated kaolinite soil test bed. The test bed had undrained shear strength of 0 at the mudline and linearly increasing with depth with a gradient of 24 psf/ft. The anchor model was tested with the magnetometer attached on it but since the test was conducted inside steel tank, pulling the loading line with the stepper motor caused significant noise in the magnetometer data. To avoid noise in measurements, the anchor was loaded manually and this is the reason of the fluctuation in the load data (Figure 6.51).

184

The anchor was initially embedded into soil at a pitch angle of 78 degrees and the anchor center located at approximately 2.6 B below mudline. The loading line angle from horizontal was approximately 8 degrees. The anchor rotated until the pitch angle reached 50 degrees and the anchor shank was released. With further loading, anchor dove 0.35 B deeper, resulting in anchor center embedment at 2.9 B from mudline. The measurements show that when the load exceeded 40 lbs, the anchor pitch started to increase to 65 degrees. This indicates anchor was trying to embed into stiffer soil layer and the applied load was not high enough for further dive penetration. Instead, anchor started to get vertical while failing in bearing. Since anchor was being loaded manually, the load was not increased more than 60 pounds.

By using the measured displacements, the ratio of the change in displacement normal to the fluke (dn) to the change in displacement parallel to the fluke (ds) with the drag embedment is calculated and presented in Figure 6.52. It can be seen that most of the data points are concentrated around dn/ds value of 1. The ratio of the change in vertical translation (dz) to the change in horizontal translation (dy) is presented in Figure 6.53. Results show most of the data points are concentrated around dz/dy value of 0.5.
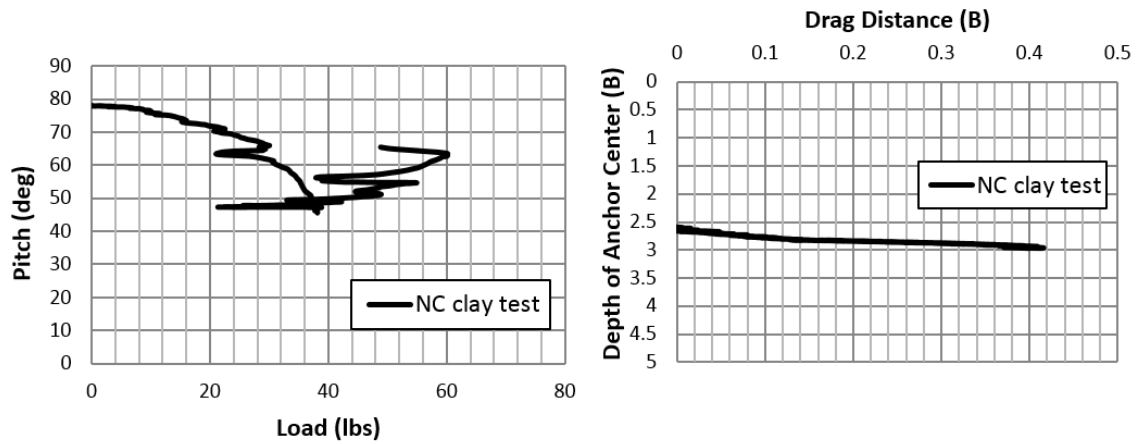
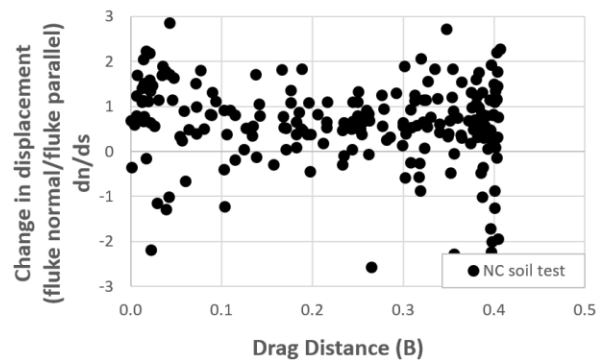Figure 6.51: Results of anchor drag embedment test in NC kaolinite

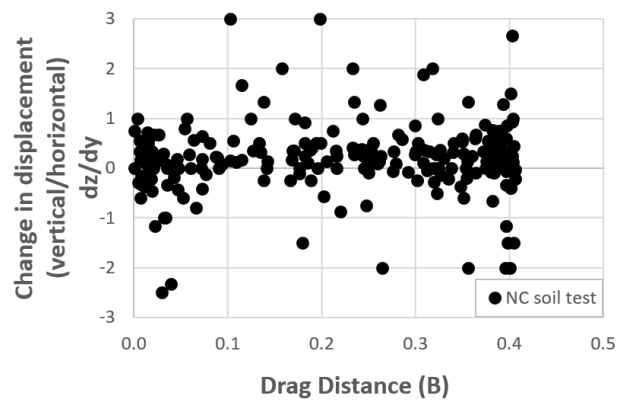Figure 6.52: Change in dn/ds with drag in normally consolidated test bed

Figure 6.53: Change in dz/dy with drag in normally consolidated test bed

186

6.6.4 POST-YIELD MOVEMENT OF SPEEDY ANCHOR

The acrylic scaled model Speedy anchor was built using 3D printing and tested for the in-plane drag embedment loading and the dive trajectory. The anchor model was loaded by the 0.025 in diameter white nylon rope. Tests with Paloma anchor showed that using a line displacement rate of 0.4 in/sec or 0.8 in/sec did not cause a significant difference in the anchor dive trajectory. Thus loading line displacement rate of 0.8 in/sec (t-bar loading rate) was used during drag embedment loading tests.

This model was tested by changing initial pitch angles, initial embedment depths, shank resistance to opening and the fluke-shank attachment location.

Different Initial Embedment Depths

The anchor free-fall penetration results in different initial embedment depths depending on the drop height, soil conditions and anchor characteristics. Dive trajectory of the anchor models embedded at different depths were tested by in-plane drag loading. Initial embedment depths are representative of the free-fall penetration but also restricted with the depth of soil test bed. The Speedy model with a fluke area of 19.29 in^2 was tested with the magnetometer attached. The thin loading line with a diameter of 0.025 in was used to minimize loading line effects. This model's shank was placed resting (partially embedded into front fluke plane) on the fluke without being held by the coupling mechanism at the beginning of the test. The shank was free to move but there is a friction between the shank and the fluke-shank connection location that slows the shank opening. The soil profile has constant undrained shear strength profile and the undrained soil strength was approximately 20 psf.

The initial pitch angles were between 52-56 degrees and the initial line angles were between 8-14 degrees. The drag embedment test results with initial embedment

depths of 0.7 B, 1.2 B and 1.7 B are presented in Figure 6.54. The change in depth of anchor center with drag distance shows the trajectory followed during drag embedment loading. The shapes of the trajectory curves are similar. Anchor centers embedded between 0.6 B-1.2 B deeper. The anchor with the deepest initial embedment achieved the deepest penetration. In all of the tests, the trajectory gets almost horizontal with further drag which means anchor was plowing at the end of the test. The change in N_e with drag distance shows that the equivalent bearing capacity factor between 10-12 was reached in all tests. The measured N_e was between the pure loading yield thresholds (N_{normal} of 15.1 and N_{shear} of 4.2) indicating the interaction between normal and shear loading capacities during failure. Also the decreasing pitch angle indicates that the anchor was becoming horizontal.

The change in line angle was included in the calculations to measure the angle between fluke and shank throughout the test. The line angle from horizontal was calculated by measuring the horizontal and vertical distances of the shank attachment point from the directional pulley and by translating magnetometer measurements to shank attachment point for a shank totally aligned with the loading line. As anchor penetrates deeper, the line angle from horizontal increases with further drag due to limited soil test bed distance. This change in the loading line angle is compensated by anchor pitch. This results in shank-fluke angles between 65-50 degrees. Change in yaw and roll rotations were less than 10 degrees for all tests. The increase up to 10 degrees were measured by the end of drag distance.
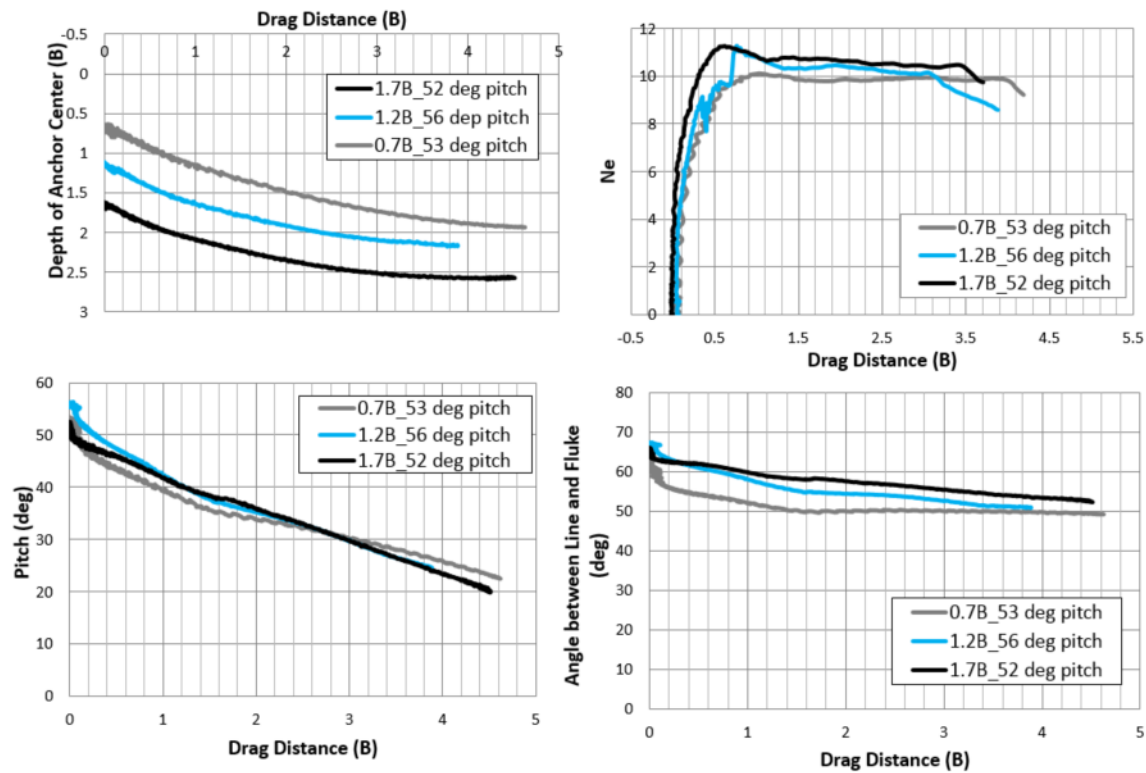
Figure 6.54: Bi-wing Speedy different initial embedments, shank resistance

To have a better understanding of anchor pitch during diving, the friction between shank arms and the fluke connection locations were decreased by filing the acrylic model. Tests were repeated for approximately same initial depths, pitch and line angles. The results are presented in Figure 6.55. The models were able to dive 0.5B-1B deeper while N_e between 10-12 was measured during dive trajectory. Anchor pitch decreased to 10-20 degrees by the end of the test indicating the fluke was almost horizontal. Angle between line and the fluke also decreased to 30-40 degrees. Even though the shank was not perpendicular to the fluke by the end of the test, the mobilized anchor holding capacity was mostly maintained.
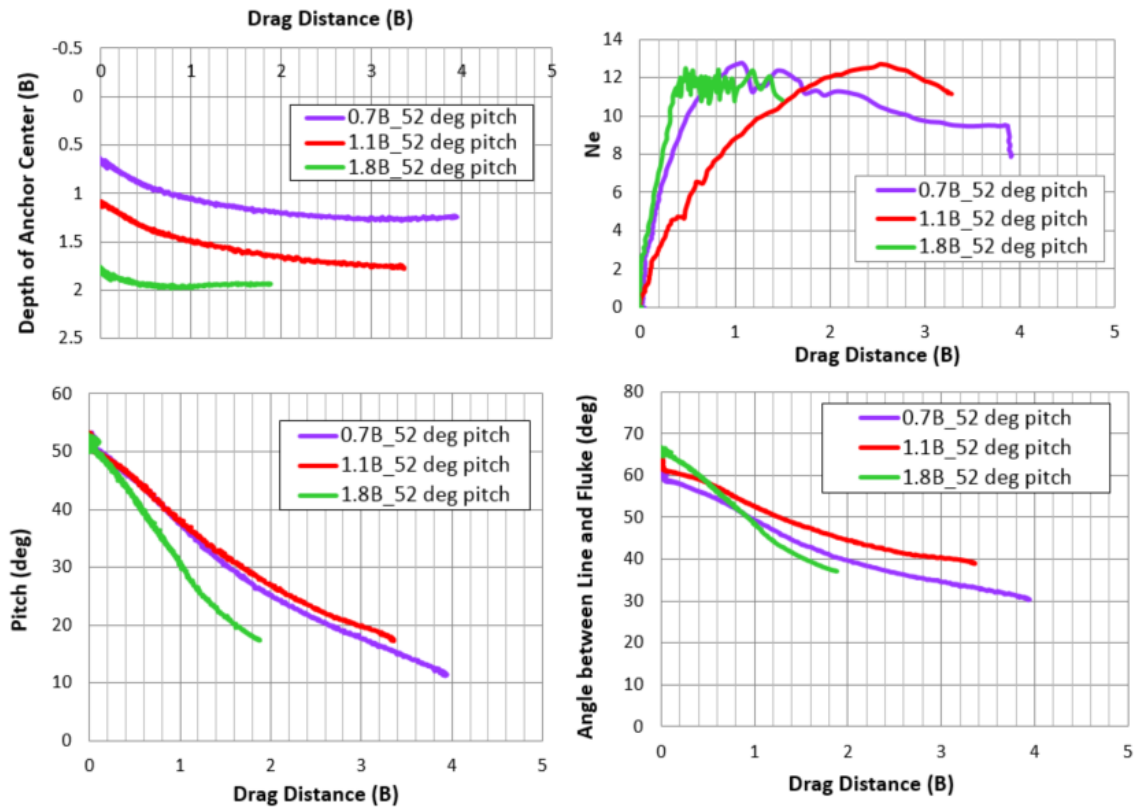
Figure 6.55: Bi-wing Speedy different initial embedment depths, reduced shank resistance

The test results of both cases (shank with some resistance to opening and shank completely free to open) are compared in Figure 6.56. The comparisons show that reducing the shank resistance to opening caused anchor to pitch faster. Anchor continued diving deeper while pitching. By the end of the test, anchor had a horizontal trajectory with approximately horizontal fluke. Due to faster pitching, the angle between shank and fluke also changed faster when the shank resistance to opening was reduced. The mobilized anchor resistance is presented in terms of N_e. The N_e values are between 10 and 12, showing even when it's failing, the anchor was able to provide a resistance in between pure shear and pure normal loading yield thresholds.

190
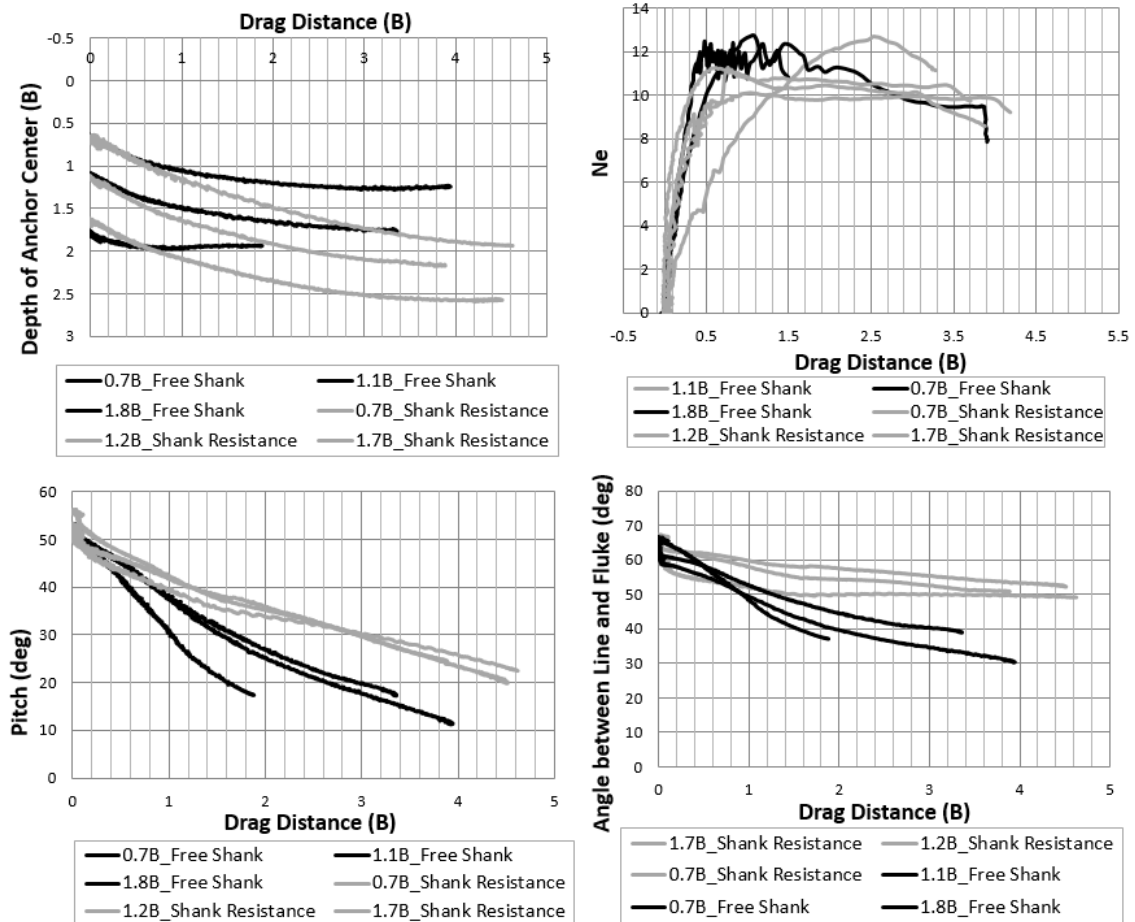
Figure 6.56: Bi-wing Speedy anchor, shank resistance effect

Different Initial Pitch Angles

The bi-wing Paloma anchor was tested with changing the initial pitch angle. The anchor center was located at the same depths for both tests (1.7 B) and the shank was resting on the fluke. The initial pitch angles of 40 and 52 degrees were tested. The initial line angle at the beginning of the test was approximately 14 degrees from horizontal at the shackle. The test results were compared in Figure 6.57. The results show that anchor kept pitching while diving deeper until the anchor fluke was almost horizontal. Anchor with the higher initial pitch angle was able to dive deeper since the pitching rate was approximately

191

the same for both cases. It took longer time for the steeper anchor to get horizontal thus it resulted in more penetration of the steeper anchor until its fluke was almost horizontal.

The change in undrained soil strength profile with depth (in terms of equivalent fluke length, B) is presented in Figure 6.58. The undrained shear strength of the soil test bed did not change significantly between 2.25 B and 2.5 B, the final depth of anchor center for each test. The difference between mobilized N_e of 9 and 11 as the anchor trajectory gets horizontal can be explained by the angle between the fluke and the shank. As the fluke-shank angle increases from 0 to 90 degrees, the failure mechanism changes from failure in in-plane shear direction to normal loading direction. Thus higher fluke-shank angle resulted in higher anchor resistance.

Comparing both tests, the dive trajectory and the ultimate load capacity obtained in both cases were not significantly different.
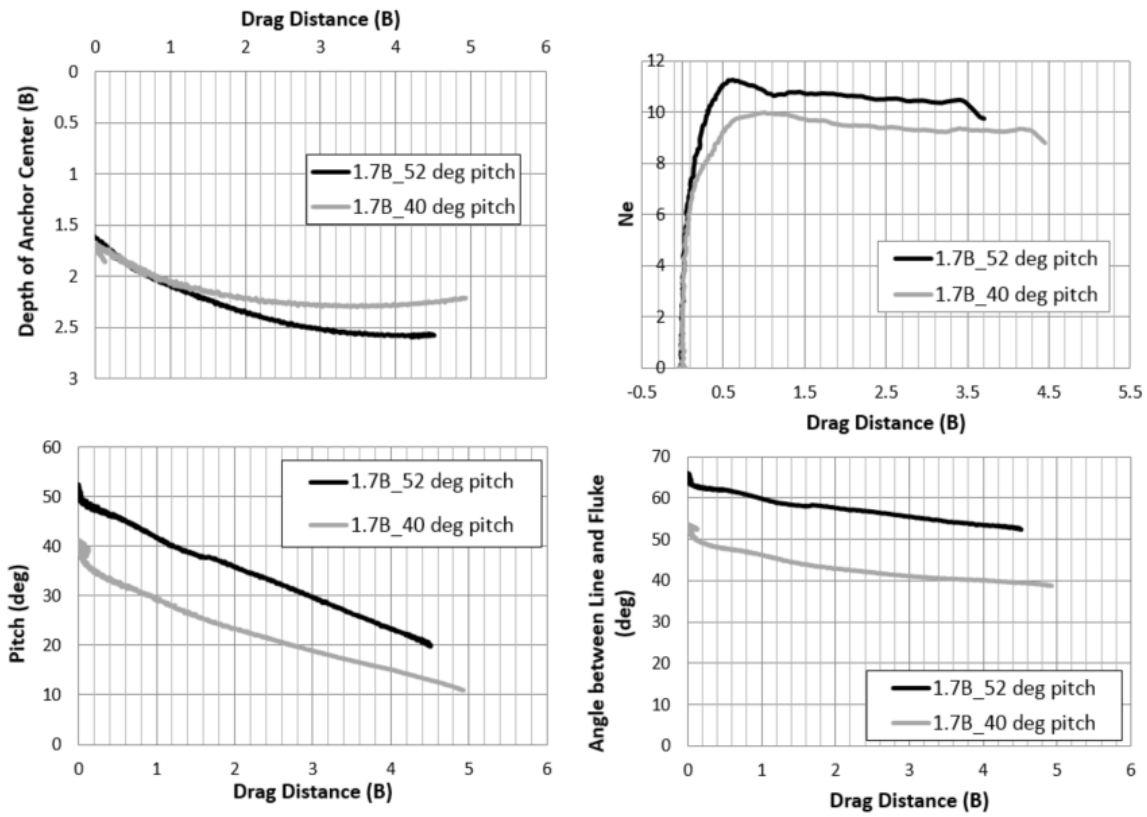
Figure 6.57: Bi-wing Speedy anchor, different initial pitch angles
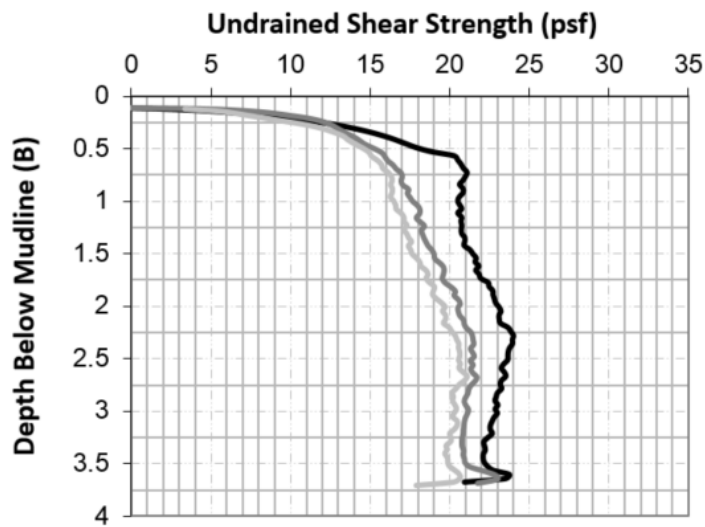

Figure 6.58: Undrained soil strength profile

193

Effect of the Fluke-Shank Attachment Location

It is important to have the shank attached at the anchor center of resistance to avoid pitch rotation after the shank was released. Preliminary tests with bearing plates showed if the shank is attached away from the anchor center of resistance, the eccentricity of the line load will cause a moment resulting in anchor rotation. The direction of rotation significantly effects anchor dive trajectory. It is difficult to attach the anchor shank at the anchor center of resistance using the scaled anchor model. Experimental tests require modifications, such as cutting a slot for magnetometer, filing the model, melting or gluing different pieces. And those modifications may shift the anchor center of resistance away from the designed location.

The fluke-shank attachment point was moved 0.03 B closer to the back fluke (upper than the original point) and tested under the same conditions (anchor center at 1.1B below mudline with initial pitch of 52 degrees and line angle of 14 degrees). The results are presented in Figure 6.59. The results show that dive trajectory was exactly the same for both anchors. The mobilized load capacity was also similar but moving the shank further up decreased the rate of anchor pitch. The capacity was mobilized sooner when the shank was attached further up but since the soil depth, pitch angle, and fluke-shank angle are all the same after 1B drag distance, this does not seem like the reason of capacity being mobilized faster. It must be due to a testing error that caused "shank original" test cycle to mobilize its capacity relatively slower. The same test was compared in Figure 6.55 (1.1B_52 deg pitch) previously and it can be see that the rate of mobilizing the anchor capacity is not dependent on the shank location. It is important to note that changing the shank attachment point did not affect the anchor capacity or dive trajectory significantly but reduced the pitch rotation rate during anchor failure. This indicates placing the magnetometer into a slot cut in the front fluke changed the exact location of center of

resistance slightly. Additional tests were performed by moving the shank attachment location further up. In those tests, anchor started to pitch in the opposite direction. This analysis shows the original location and the new tested location can both be used as a fluke-shank attachment point. Tests performed by attaching the shank at the original location are representative of the anchor dive trajectory as slight changes in the fluke-shank attachment point do not result in a significant difference in anchor dive trajectory or mobilized anchor capacity.
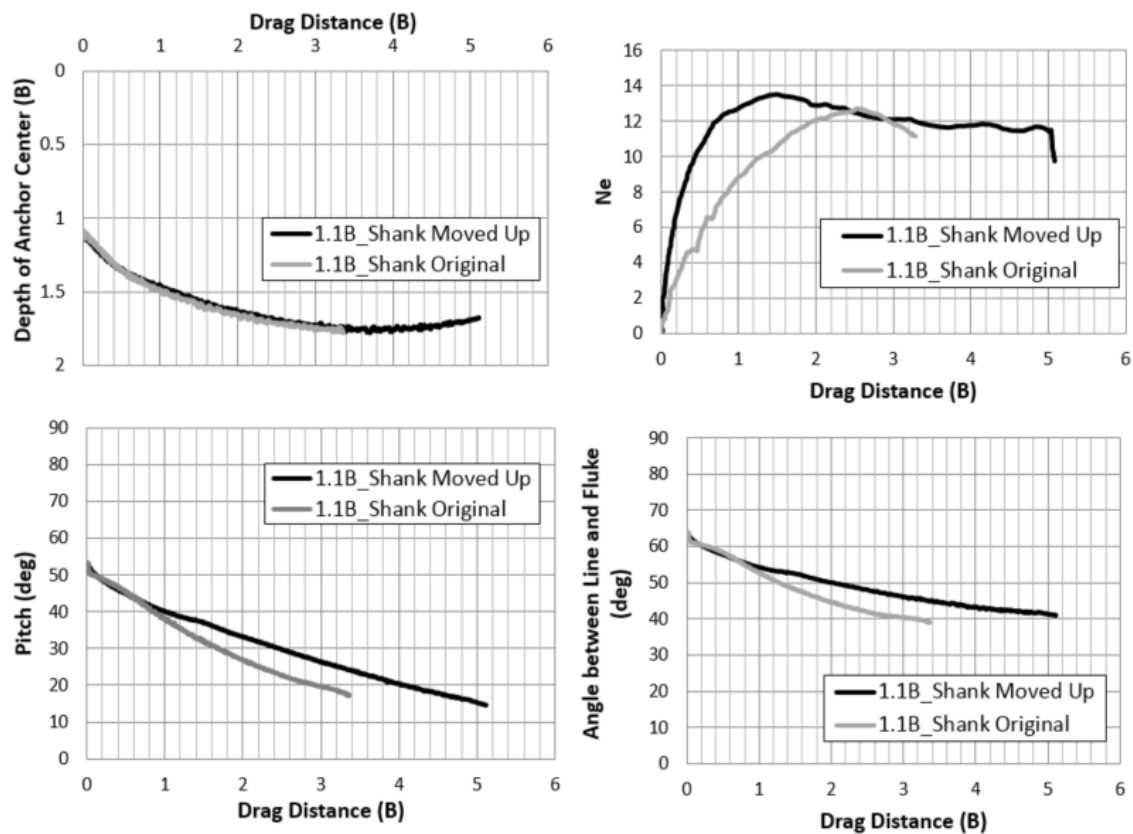
Figure 6.59: Bi-wing Speedy, different shank attachment location

Comparison of Speedy Anchor with Drag Embedment Anchors

The measured Speedy Flying Wing Anchor® concept post-yield movement is compared with the measured and predicted post-yield movement of Drag Embedment Anchor 1:30 scaled model (DEA model on Figure 5.1) tested by McCarthy (2011). The dive trajectory and the mobilized anchor capacity in terms of equivalent non-dimensional yield threshold (N_e) during dive penetration in terms of line displacement are presented in Figure 6.60 (Aubeny et al., 2011). The test was conducted in kaolinite soil test bed with undrained shear strength of 0.8 psf at the mudline and a strength gradient of 8 psf/ft. The initial pitch of the fluke was approximately 45 degrees. The measured pure normal loading yield threshold (N_{normal}) is 11 and the pure shear loading yield threshold (N_{shear}) is 4.2 for the DEA scaled model.

The dive trajectory measurement shows the horizontal line displacement that indicated drag distance and the vertical embedment. The anchor capacity is presented in terms of the equivalent non-dimensional yield threshold (N_e). The N_e measured during drag embedment anchor penetration reached a maximum of 6 during dive penetration. It is stated that the N_e was relatively constant after a drag distance of approximately 4.2 fluke lengths and vertical embedment of 2 fluke lengths.

Comparing results obtained by Speedy anchor drag embedment loading, it can be concluded that the mobilized anchor capacity is almost the double of conventional drag embedment anchors. While both the DEA and the Speedy model has N_{shear} of 4.2, the Speedy anchor model has higher N_{normal} value of 15, which is almost 36% higher than that the pure normal loading yield threshold of the DEA model. N_e was measured between 10-12. The N_e of 10-12 was mobilized after 0.5 fluke lengths of drag that resulted in 0.3-0.5 fluke lengths of embedment. The decrease in Speedy anchor pitch during drag embedment installation provides anchor trajectory to get horizontal and result in near horizontal

movement during failure. This prevents Speedy anchor to turn up and slide out of soil. The experimental measurements show that the mobilized anchor capacity is sustained (constant N_e) during pitch rotation while dive penetration.
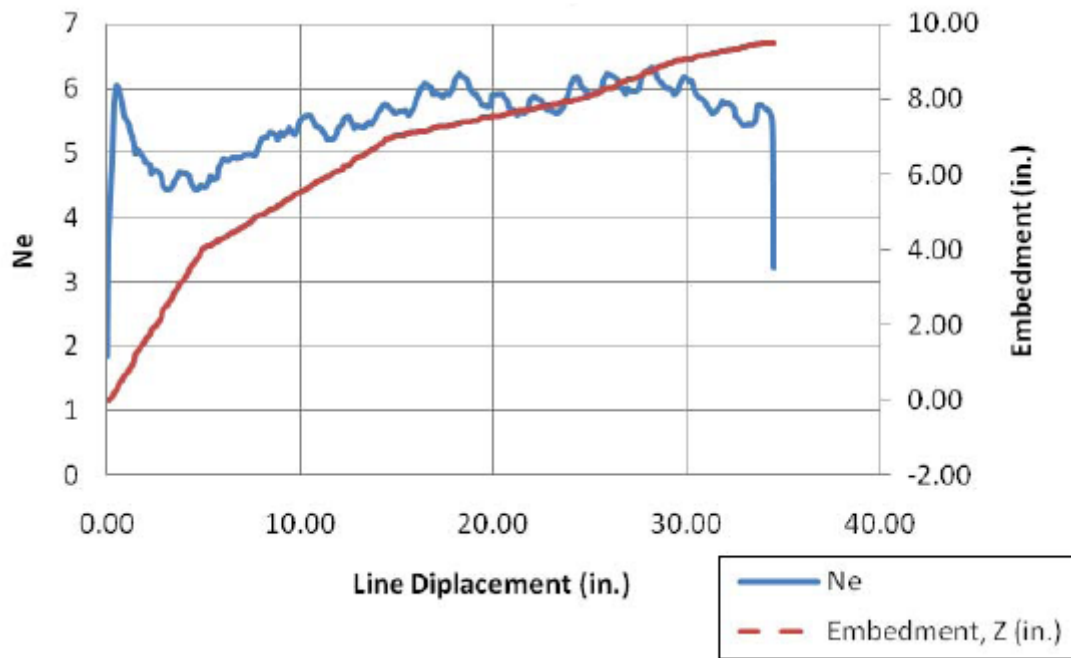

Figure 6.60: Mobilized anchor capacity and trajectory during drag embedment (Aubeny, ve diğerleri, 2011)

6.6.5   RESULTS OF THE FLYING WING ANCHOR® POST-YIELD MOVEMENT ANALYSIS

The post-yield movement of the Flying Wing Anchor® concepts are assessed by testing plywood and acrylic scaled models of one-wing and bi-wing concepts. The results are summarized below.

The results obtained by testing the one-wing Diamond anchor model are:

1.   Testing the diamond shaped bearing plate with initial pitch angles of 30 and 45 degrees resulted in anchor diving 0.7 B-1.5 B deeper. Changing the initial pitch angle did not cause a significant difference in the trajectory. Both tests continued until the anchor pitch increased and the anchor fluke was near vertical which indicated anchor was failing and plowing.

2.   It is observed that testing the anchor model with attaching the loading line directly on the anchor fluke (without using a shank) increased yaw and roll rotations. Those rotations affected anchor dive trajectory when the same test was repeated.

3.   Two diamond acrylic models were used for drag embedment testing. The main difference between testing a Diamond shaped bearing plate and the scaled model Diamond Anchor is the structural components of the Diamond Anchor for hydrodynamic stability. The additional weight, I-beams on the fluke and lower beam increased the shear resistance of the acrylic model. Anchor normal resistance to shear resistance ratio decreased to 2.4 from the initial target ratio of 3.

4.   When the scaled model was tested without a shank, it did not embed deeper due to both increased shear resistance and the loading line interaction with the magnetometer.

5.   The diamond acrylic model was tested by attaching a shank and cutting the lower bea partially to reduce shear resistance. Anchor center penetrated 0.3 B-0.55 B deeper by the in-plane drag loading.

6. It was hard to obtain repeatable data by testing the diamond anchor model.

Results obtained by testing the bi-wing Paloma scaled model are:

1. The bi-wing Flying Wing Anchor® concept Paloma anchor was built using plywood and acrylic. Repeatable data was not obtained testing the plywood model due to model failure during testing. The acrylic model provided repeatable data.

2. The bi-wing Paloma has the fluke-shank coupling mechanism attached. The line displacement rate of 0.04 in/sec was used before the shank was released from the fluke-shank coupling mechanism. When the anchor is loaded slowly at the beginning of the test, it is possible to visually observe the shank release as a sudden drop in measured load values. The line displacement rate was increased to 0.4 in/sec after the shank was released.

3. Initiation of pitch rotation was studied by initially embedding the anchor at a near vertical orientation. Anchor started to rotate in pitch direction when the moment capacity was exceeded. The moment capacity was calculated using the pure moment loading yield threshold (N_{moment}). The load that was expected to start the pitch rotation was compared with the measured load that started the pitch rotation during scaled model testing. The experimental results are in good agreement with the theoretical predictions.

4. The fluke-shank coupling mechanism is geometrically designed to release the shank such that the angle between the shank and the fluke equals to 60 degrees when shank is released. This angle was determined experimentally by approximately calculating the initial line angle from horizontal and measuring the exact anchor pitch angle using magnetometer. The shank release was captured from the load cell measurements momentarily as a sudden drop in load. Results showed that the fluke-shank coupling mechanism released the shank at the designed angle.

199

Following the release, shank got aligned with the loading line. The angle between fluke-shank was within couple of degrees from 60 degrees. The interval of +/- couple of degrees is due to approximate measurement of the initial loading line angle from horizontal and assumption of no change in the loading line angle during anchor pitch rotation.

5. It is observed that using a shank with two arms significantly reduced the yaw and roll rotations compared to diamond anchor tests performed without a shank (with directly attaching the loading line on the anchor fluke).

6. In-plane drag embedment tests resulted in up to 0.7 B anchor dive penetration with 3.5B drag embedment. The holding capacity of the anchor is presented in terms of the equivalent bearing capacity factor. Results show N_e of 9-10 was mobilized during anchor dive penetration and anchor was able to maintain the holding capacity during dive penetration.

7. The out-of-plane drag loading tests were performed to study anchor dive trajectory when the anchor was subjected to out-of-plane drag loading (i.e. during a hurricane). Also a possible roll during free-fall penetration can cause anchor to be loaded in out-of-plane. Thus anchor installation steps and dive trajectory were both tested by loading the anchor with 30 degrees out-of-plane drag loading. The fluke-shank attachment mechanism was able to release the shank at the designed angle. When the shank was free, anchor corrected itself with yaw and roll rotations and got aligned with the loading line. Anchor was not able to embed deeper but it also did not get pulled out of soil. N_e value of 11 shows anchor was able to mobilize the holding capacity in combination of resistance to shear and normal loading.

8. The bi-wing Paloma anchor models were tested with varying the loading line displacement rate. The result showed that for the loading line displacement rates of

0.04-0.4-0.8-4.0 in/sec, anchor pitched when the moment capacity was exceeded, and the shank was released at the design angle. The load increased slightly when the displacement rate was increased to 4.0 in/sec but using a line displacement rate of 0.04 in/sec, 0.4 in/sec or 0.8 in/sec did not cause a significant change in the measured anchor resistance.

9. The bi-wing Paloma anchor was tested in normally consolidated kaolinite. The anchor model embedded 0.35 B vertically with horizontal drag of 0.4 B. Further dive penetration was not obtained due to manually applied line load was not enough to embed the anchor into stiffer soil layer.

Bi-wing Speedy Scaled Model Tests:

5. The bi-wing Flying Wing Anchor® concept Speedy anchor was built in acrylic. The line displacement rate of 0.8 in/sec was used for drag embedment tests. This model does not have the fluke-shank coupling mechanism. The tests were started with initially embedding the model at different penetrations. The anchor was placed at pitch angles between 40-56 degrees with the shank resting freely on the coupling mechanism. Anchor was initially embedded into soil at embedment depths between 0.7 B-1.2 B and vertical embedment of up to 1.2 B was measured with 4.6 B horizontal drag.

6. Deeper initial embedment results in deeper penetration during drag embedment as the dive trajectories are similar for all initial embedment depths.

7. Anchor was pitching while embedding deeper since the anchor capacity was mobilized. The rate of pitch rotation was faster when the shank had no frictional resistance to opening. Friction between the shank arms and fluke connection locations decreased the rate of pitch and resulted in deeper anchor penetration. This is due to line load component parallel to fluke being in the direction of providing

further penetration. When the anchor is completely horizontal, line only drags it in in-plane shear direction.

8. The Speedy model was tested with pitch angles of 40 degrees and 52 degrees at the same initial embedment depth. The rate of pitch rotation was the same for both cases so anchor with higher initial pitch angle was able to embed deeper since it had more time to dive deeper before the fluke was almost horizontal. The soil profile was at the final embedment depths were approximately the same for both tests. The anchor with 52 degree initial pitch was able to mobilize N_e of 11 while test with 40 degree initial pitch was able to mobilize N_e of 9. The difference in the mobilized capacity can be explained by the shank-fluke angle. As the angle gets closer to 90 degrees (shank is perpendicular to fluke), the mobilized anchor capacity gets closer to pure bearing.

9. The effect of fluke-shank connection point was studied by attaching the shank higher (closer to back fluke) than the original attachment location of anchor center of resistance. The trajectory and mobilized anchor resistances were similar and the anchor pitch rotation was slower with the new shank location. This indicates cutting a slot for the magnetometer and placing the magnetometer might have changed anchor center of resistance slightly. But both attachment locations were appropriate as fluke-shank attachment points. Moving the shank further closer to back fluke resulted in pitch rotation in the opposite direction and that should be avoided to achieve dive penetration.

10. Anchor post-yield movement tests with Speedy anchor model showed the anchor mobilized the holding capacity in combination of shear and bearing resistances. The anchor holding capacity drops only slightly after reaching a peak value and

anchor was able to maintain most of the holding resistance while it pitched until fluke was horizontal.

11. This change in pitch angle can be explained by the anchor mobilizing full capacity, the increase in line angle with increasing drag distance and the slight change in anchor center of resistance caused by modifying the anchor model for experimental testing.

12. Results show that when anchor was failing, it did not get pulled out of soil but rather moved horizontally while maintaining the holding capacity.

13. Comparison of Speedy anchor measurements with the conventional Drag Embedment Anchor measurements show that the Speedy anchor can mobilize double the DEA capacity by embedding $1/4^{th}$ of vertical penetration in $1/8^{th}$ of a drag distance than what requires the DEA to mobilize the anchor capacity.

6.7 CONCLUSIONS

This chapter introduces the new offshore anchor concept, the Flying Wing Anchor®. Initially the concept is introduced by explaining the installation steps and the mobilization of anchor capacity. The developed Flying Wing Anchor® concepts and structural parts are presented. The focus of this chapter is the experimental testing and the theoretical calculations of the pure loading yield thresholds, initiation of post-yield movement and the anchor dive trajectory. The initial Flying Wing Anchor® concept is developed as the one-wing Diamond Anchor. Further improving resulted in the bi-wing anchor concepts of Paloma anchor and the final concept of Speedy anchor. The experimental testing and theoretical calculation results that contributed to the optimization

of the Flying Wing Anchor® concepts are explained in this chapter. The optimization steps based on these results are summarized below.

The initial Flying Wing Anchor® concept is the Diamond anchor that is developed as a one-wing concept. The minimum normal resistance to shear resistance ratio of 3:1 was planned to achieve during optimization of designs to obtain deeper dive penetrations with drag embedment. Pure loading yield thresholds (N_{normal} of 11 N_{shear} of 4.2) show the anchor shear resistance is increased due to structural additions for hydrodynamic stability. The increased shear resistance prevents deeper drag embedment penetration. Also those structural additions increased the anchor weight with a minor contribution to anchor capacity that conceptually decreased the anchor efficiency.

The concept of using two control surfaces to provide hydrodynamic stability resulted in bi-wing Flying Wing Anchor® concept of Paloma anchor. The N_{normal} of 13.6 and N_{shear} of 5.6 are measured in remolded clay under undrained loading conditions. Initiation of anchor pitch rotation, and fluke-shank coupling mechanism concepts were confirmed with experimentally testing the Paloma anchor model. The in-plane drag embedment installation measurements resulted in deeper dive penetration than Diamond anchor. Experimental measurements show if anchor rolls up to 30-degrees during free-fall embedment, it corrects itself with yaw and roll rotations once the shank is released during installation.

The bi-wing concept of Speedy anchor was developed to decrease the shear resistance of the Paloma anchor model. The pure loading yield thresholds resulted in a theoretical normal resistance to shear resistance ratio of 4.3 for the Speedy anchor. Experimental measurements of the dive trajectory show the Speedy anchor embeds deeper than both Diamond and Paloma anchor models during drag embedment loading. The

Speedy anchor starts to pitch during failure until it gets close to horizontal while maintaining the holding capacity.

Comparison of Speedy anchor measurements with the conventional Drag Embedment Anchor measurements show that the Speedy anchor can mobilize double the DEA capacity by embedding $1/4^{th}$ of vertical penetration in $1/8^{th}$ of a drag distance than what requires the DEA to mobilize the anchor capacity.

Chapter 7: Simplified Plasticity Model to Predict Anchor Dive Trajectory

7.1 INTRODUCTION AND OBJECTIVES

The objective of this chapter is to develop a simplified plasticity model that calculates the interactions between the anchor, the loading line, and the soil around the line and the anchor to predict the initiation of post-yield behavior, dive trajectory and the ultimate holding capacity of the new anchor concept in clay under undrained conditions. The developed simplified plasticity model is calibrated with experimental measurements of pure loading yield thresholds. The non-dimensional pure loading yield thresholds and the dive trajectory measured for the Flying Wing Anchor® concepts (Chapter 6) are used to calibrate the Simplified Plasticity Model.

As a result of free-fall, anchor embeds into soil near vertically with the shank attached to fluke. The Simplified Plasticity Model focuses on the anchor performance after it has completed the free-fall penetration. The simplified plasticity model was initiated by Huang (2015) and calibrated with the experimental testing results obtained by scaled model testing of the Flying Wing Anchor® concepts. This chapter includes the calculation steps of the Simplified Plasticity Model and the comparison of results with experimental measurements. The detailed information about the Simplified Plasticity Model can be found in Huang (2015).

7.2 CALCULATION OF ANCHOR-LINE INTERACTION

For calculating the anchor line profile and the line load acting at the mudline, the Neubecker and Randolph (1995) and Aubeny and Chi (2014) models were used. The input parameters are:

- Undrained shear strength profile: the input parameters are the undrained shear strength at the mudline (s_{u0}), and the soil strength gradient (k).

- Anchor line characteristics: the input parameters are the bearing capacity factor for calculating the normal resistance of the anchor line/chain (N_c), effective line width (b), line multiplier ($E_n=1$ for mooring line, 2.5 for chain), line diameter (d), line friction coefficient (μ).

- Anchor location: depth of anchor pad-eye (z_a), depth that N_c rises from 5.1 at the mudline to 7.6 (z_{break}).

- Anchor line load at the pad-eye (T_a) and anchor line angle at the mudline (θ_0).

The anchor line geometry is calculated by horizontal (x) and vertical (z) coordinates as follows:

(1) The depth between mudline and the pad-eye is divided into small increments to analyze line geometry in small increments. The calculations are performed for increasing z, anchor line vertical coordinate (depth).

(2) The change in N_c from 5.1 to 7.6 is calculated with increasing depth. For depths greater than 2.4b, N_c of 7.6 is used.

(3) For the assumed T_a, the normalized soil resistances due to mudline strength (Q_1) and due to soil strength gradient (Q_2) are calculated by:

$$Q_1 = \frac{E_n N_c s_{u0} z_a}{T_a} \tag{7.1}$$

$$Q_2 = \frac{E_n N_c b k z_a^2}{2 T_a} \tag{7.2}$$

(4) Using Q_1, Q_2, θ_0 and Equation 2.8, the normalized horizontal coordinate (x*) and the horizontal coordinate (x) are calculated.

After the line geometry is obtained, next step is to calculate the line angle at the shackle (pad-eye) (θ_a) and the line load at the mudline (T_0). The calculation steps are:

(1)   For small increments of line, by using the x and z coordinates, calculate small line segments with the line length of $l^2 = \Delta z^2 + \Delta x^2$.

(2)   For each line segment whose length is calculated in the previous step, the bearing resistance (Q) and the shear resistance (F) of the line are calculated by Equations 2.2 and 2.3.

(3)   The load of the anchor line at the mudline is calculated by adding the line friction to the anchor line load at the shackle (pad-eye):

$$T_0 = T_a + \sum_{i=1}^{n} F_i \tag{7.3}$$

(4)   The line angle at the pad-eye (θ_a) is calculated from the geometry of the line segment attached at the pad-eye as:

$$\theta_a = atan\left(\frac{dz}{dx}\right) \tag{7.4}$$

7.3 CALCULATION OF ANCHOR PITCH ROTATION

For calculating the anchor pitch rotation with the shank attached to fluke by the fluke-shank coupling mechanism, the input parameters are:

•   Anchor-line interaction calculation module described in the previous section.

•   Undrained shear strength profile: the input parameters are the undrained shear strength at the mudline (s_{u0}), and the soil strength gradient (k).

•   Anchor characteristics: depth of anchor pad-eye (z_a), anchor fluke area (A_f), eccentricity (e: distance between pad-eye and fluke-shank attachment point), the yield thresholds for pure normal (N_{normal}), shear (N_{shear}) and moment (N_{moment})

loading measured experimentally, fluke-shank coupling mechanism shank release angle ($\beta_{threshold}$).

The anchor pitch rotation is calculated by:

(1)   It is assumed that the line load at the pad-eye (T_a) starts from zero and increases in small increments.

(2)   For each line load at the pad-eye, the corresponding line angle at the pad-eye (θ_a) is calculated by the anchor-line interaction module.

(3)   The horizontal component of the line load at the pad-eye, T_{ah} is calculated as $T_{ah}=T_a.\cos\theta_a$

(4)   The moment acting on the anchor center for moment rotation is calculated as $M=T_{ah}.e$

(5)   The utilization ratio in moment is calculated by:

$$u_m = \frac{M}{Mmax} = \frac{T_{ah}.e}{N_{moment}s_u A_f} \tag{7.5}$$

The T_a is increased until the utilization ratio in moment is greater than 1, as pitch rotation starts when the moment capacity of the anchor is exceeded. If $u_m>1$ is obtained, corresponding T_a and θ_a values are transferred to the next calculation step: dive initiation. If $u_m<1$, the T_a is increased in small increments and the calculation steps are repeated until $u_m>1$ is obtained.

(6)   At the T_a and θ_a that starts the anchor pitch, assuming both values stay constant, the anchor rotation from vertical starts to increase in small increments. The vertical anchor orientation means α is equal to zero (Figure 7.1). For a constant θ_a and increasing α; β, the angle between fluke normal plane and loading line, is calculated by $\beta=\alpha-\theta_a$. The α is increased until β reached the $\beta_{threshold}$ value of 30 degrees.
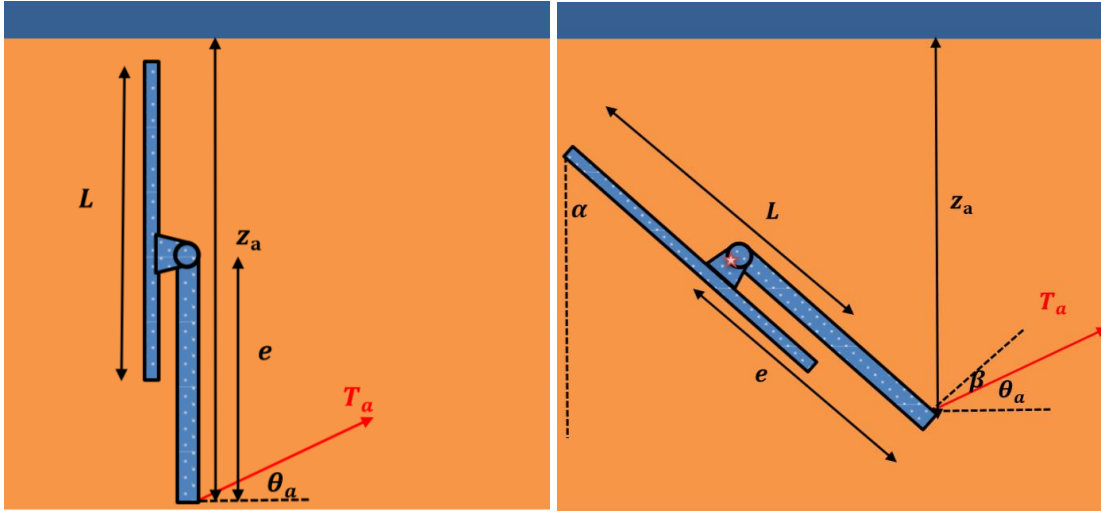
Figure 7.1: Anchor pitch rotation (Huang, 2015)

(7)   The α rotation, T_a load, and θ_a angle resulting in $\beta_{threshold}$ values are transferred to the next step: dive penetration calculation.

7.4 CALCULATION OF DIVE PENETRATION AND ULTIMATE LOADING CAPACITY

When the shank is released, it aligns itself with the loading line. Assuming the shank is attached to the fluke at the anchor center of mass, and assuming shank has no resistance to rotation; the anchor rotation stops. The load at the pad-eye is transferred to fluke plane by the shank. The input parameters are:

• Anchor-line interaction calculation module described in the previous section.

• Undrained shear strength profile: the input parameters are the undrained shear strength at the mudline (s_{u0}), and the soil strength gradient (k).

• Anchor characteristics: depth of anchor pad-eye (z_a), anchor fluke area (A_f), the yield thresholds for pure normal (N_{normal}), and shear (N_{shear}) loading measured experimentally, line angle from fluke normal at the pad-eye (β), anchor rotation from vertical (α).

210

The calculation steps for dive penetration are:

(1)   The dive initiation calculation starts with the α anchor rotation from vertical, T_a line load at the pad-eye, and θ_a line angle at the pad-eye. The T_a line load is increased incrementally while α stays constant. The corresponding θ_a is calculated for the T_a load. The β line angle from fluke normal is calculated as $\beta=\alpha-\theta_a$. The free-body diagram prepared of the anchor dive penetration by Huang (2015) is presented in Figure 7.2.
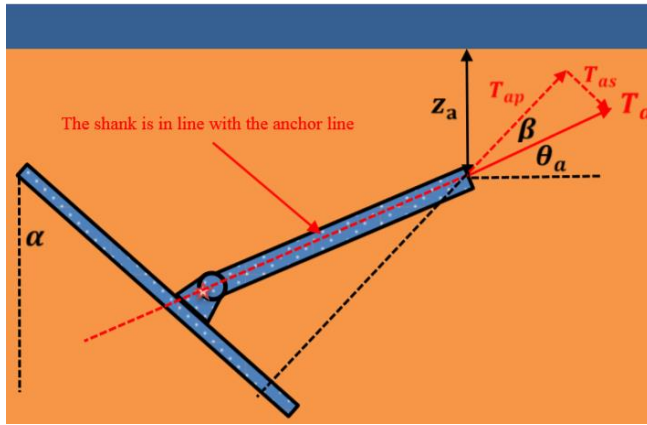
Figure 7.2: Free-body diagram of the anchor during dive penetration (Huang, 2015)

(2)   For the assumed T_a, the components acting in shear direction to fluke plane (T_{as}) and in bearing direction to fluke plane (T_{ap}) are calculated by:

$$T_{as} = T_a \sin \beta \tag{7.6}$$

$$T_{ap} = T_a \cos \beta \tag{7.7}$$

(3)   The utilization ratios in shear loading (u_s) and normal loading (u_p) corresponding to the T_{as} and T_{ap} calculated in previous step are calculated by:

$$u_s = \frac{T_{as}}{N_{shear}S_u A_f} \tag{7.8}$$

$$u_p = \frac{T_{ap}}{N_{normal}S_u A_f} \tag{7.9}$$

(4)   For the moment utilization (u_m) of zero, the yield locus is calculated by rewriting Equation 2.16 using Equations 7.8 and 7.9.

$$f = \left(u_p\right)^q + (u_s)^{n/p} - 1 = 0 \tag{7.10}$$

(5)   For a calculated u_p, the corresponding shear utilization ratio on the yield locus is calculated as:

$$u_s^* = \left[1 - \left(u_p\right)^q\right]^{p/n} \tag{7.11}$$

If this corresponding u_s^* is smaller than the u_s calculated by Equation 7.8, it means the anchor starts diving parallel to fluke plane. If not, T_a is increased until $u_s > u_s^*$ is achieved.

(6)   For calculating the anchor trajectory, a small displacement in the direction of fluke plane (Δs) is assumed.

(7)   The ratio of dn/ds is obtained by calculating the normal to the yield function as the finite-difference derivatives:

$$\frac{dn}{ds} = \frac{\frac{\delta f}{\delta u_p}}{\frac{\delta f}{\delta u_s}} \tag{7.12}$$

$$f(u_p, u_s) = u_s - 1 + \left(u_p^{\frac{qp}{n}}\right) = 0 \tag{7.13}$$

$$\frac{\delta f(u_p, u_s)}{\delta u_p} = \frac{pq}{n}\left(1 - u_p^q\right)^{\frac{p}{n}-1} u_p^{q-1} \tag{7.14}$$

$$\frac{\delta f(u_p, u_s)}{\delta u_s} = 1 \tag{7.15}$$

(8) The incremental displacement perpendicular to the fluke face (Δn) corresponding to the given Δs is calculated by rewriting Equation 2.24:

$$\Delta n = \left(\frac{\delta f}{\delta u_p} \middle/ \frac{\delta f}{\delta u_s}\right)\Delta s \tag{7.16}$$

(9) The horizontal (Δy) and vertical (Δz) displacements corresponding to Δs and Δn are calculated by using Equations 2.28-2.29 as:

$$\Delta y = \Delta s.\sin\alpha + \Delta n.\cos\alpha \tag{7.17}$$

$$\Delta z = \Delta s.\cos\alpha - \Delta n.\sin\alpha \tag{7.18}$$

(10) When the anchor reaches the maximum embedment depth (z_{max}), assuming shank is perpendicular to the fluke plane, the anchor mobilizes the ultimate holding capacity through bearing from full fluke surface. If the undrained strength of the

soil is s_u at the depth of z_{max}, the anchor ultimate holding capacity (UHC) can be calculated by:

$$UHC = s_u A_f N_{normal} \qquad\qquad (7.19)$$

7.5 RESULTS OF ANCHOR DIVE TRAJECTORY PREDICTIONS

The results obtained by the Simplified Plasticity Model for Paloma anchor are compared with experimental measurements. The anchor pure loading yield thresholds and post-yield movement analysis (Chapter 6) are used to calibrate the Simplified Plasticity Model.

The Simplified Plasticity Model predictions are compared with experimental measurements of the Paloma anchor model. The bi-wing Paloma anchor model was tested by initially embedding the anchor fully into soil near vertically. The anchor center was located at 1.15 B and the initial line angle was measured as 10 degrees. Initially the line load is increased in small increments and the corresponding line angle from horizontal is calculated. The pitch rotation initiated when the anchor capacity in moment loading is mobilized ($u_m>1$). The calibration model is initially calibrated with: pure loading yield thresholds measured for the acrylic Paloma anchor model, model dimensions, undrained strength profile of the soil test bed and loading line characteristics. The experimental pitch and line load on anchor are presented with the analytical load prediction for initiation of pitch rotation on Figure 7.3. The Simplified Plasticity model predicts the anchor starts rotating in the pitch direction when the load acting on the anchor exceeds 4.15 lbs. Experimental measurements show the pitch rotation started when the load exceeded 3.6 lbs. The predicted load is slightly higher than the experimental measurement.

214

After the pitch rotation starts, it continues until the shank is released by the fluke-shank coupling mechanism. The Simplified Plasticity Model rotates the model from vertical in small increments while assuming the line angle from horizontal and the line load are constant. The rotation stops when the threshold angle of 60-degrees between the fluke plane and the loading line is reached. It is assumed that the pitch rotation stops when the shank is released. The experimental measurements show the angle between fluke and shank was approximately 62-degrees right after the shank was released which is in good agreement with the analytical model assumption.

The Simplified Plasticity Model predicts the dive penetration starts when the anchor capacity in shear or normal loading is mobilized. The Simplified Plasticity model predicts the capacity in shear is mobilized before the capacity in normal loading and predicts the dive penetration starts when the line load acting on the anchor exceeds 11.12 lbs. The comparison of experimental measurements with the analytical prediction of dive initiation load are presented in Figure 7.4. The experimental measurements show that, after the shank was released (which corresponds to drag distance of 0.4B) the load increased from 2 lbs to 11.8 lbs as the shank gets aligned with the loading line. It is difficult to identify the exact load that initiates dive penetration with drag embedment since the load increases when shank gets aligned with the loading line. But as the rest of the dive penetration is measured at an approximately constant load of 11.8 lbs, it can be commented that the dive initiation started at a load close to 11.8 lbs. It can be concluded that analytical prediction of the load that initiates dive penetration is in agreement with the experimental measurements.
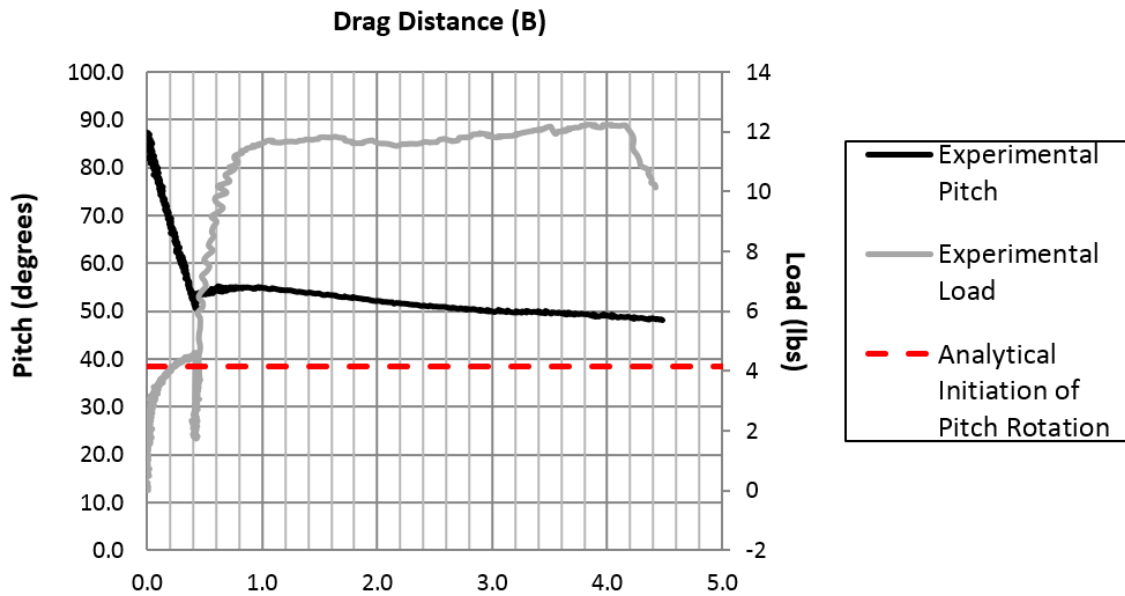
Figure 7.3: Simplified Plasticity Model prediction for the initiation of pitch rotation
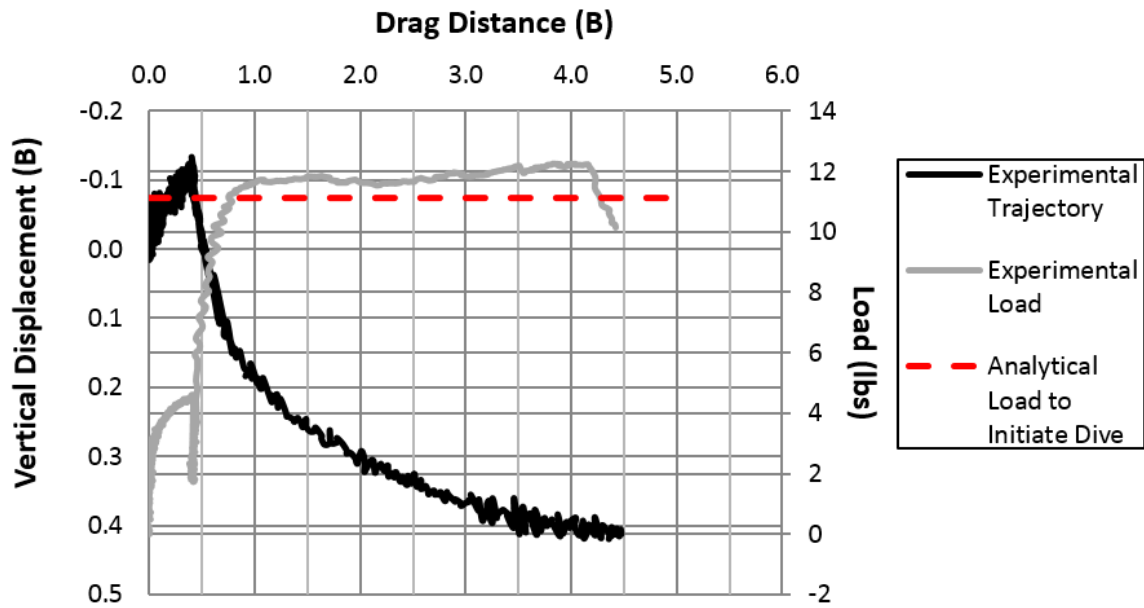
Figure 7.4: Simplified Plasticity Model prediction for the initiation of dive penetration

To focus on the dive trajectory, the same anchor model was tested in the same soil test bed only for the dive trajectory. The bi-wing Paloma anchor model was initially embedded fully into soil with the anchor center at a depth of 0.8 B from the mudline. The anchor fluke had an initial pitch angle of 50-degrees and the loading line angle from horizontal was approximately 5-degrees from horizontal. The shank was released and was resting on the fluke-shank coupling mechanism such that increasing line load initially opens the shank. The mobilized equivalent bearing capacity factor, N_e, during experimental testing (Figure 7.5) increased and stayed approximately constant at 9.4, which is in between the value for pure shear (5.6) and pure bearing (13.6) (Table 6.1). This indicates the interaction between shear and normal loads during anchor penetration.
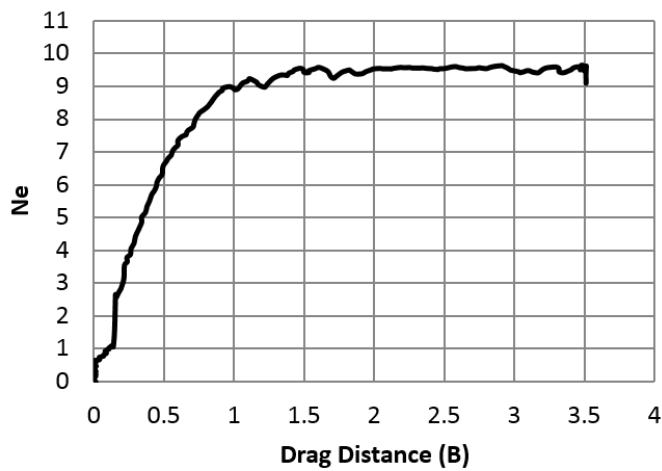
Figure 7.5: Experimentally measured N_e for bi-wing Paloma

The calibrated yield locus is obtained by calibrating the Simplified Plasticity Model with dive trajectory measurements obtained by testing Paloma anchor model. The calibration steps are:

(1) The yield thresholds experimentally measured for pure normal ($N_{normal,max}$), shear ($N_{shear,max}$) and moment ($N_{moment,max}$) loading are used as input values to the Simplified Plasticity Model calculation modules.

(2) The angle between fluke and shank (θ_{fs}) is equal to 60-degrees as set by the fluke-shank coupling mechanism. When the threshold of 60 degrees is reached, the rotation stops.

(3) The c_1 and c_2 coefficients are calculated as $\sin\theta_{fs}$ and $\cos\theta_{fs}$ by using Equation 2.18 and 2.19.

(4) The yield function equation presented in Equation 2.21 is modified to assume moment rotation is zero. It can be re-written as:

$$f = \left(\frac{|c_1|N_e}{N_{n,max}}\right)^q + \left[\left(\frac{|c_2|N_e}{N_{s,max}}\right)^n\right]^{1/p} - 1 \tag{7.20}$$

(5) The focus of calibration is to use experimentally measured N_e (9.4) value and change q and n/p ratios until yield function (f (V, H) = 0) calculated by Equation 7.18 is equal to zero.

(6) The second calibration is the ratio of normal displacement to shear displacement ratio (R_{ns}) calculated by Equation 2.27. Assuming moment is zero, the N_n and N_s values are calculated by using Equations 2.18 and 2.19 and the experimentally measured N_e value of 9.4.

(7) If f=0 is not obtained, then the N_e value is decreased or increased slightly to obtain f=0 and match calculated R_{ns} with the measured R_{ns}. The measured R_{ns} was approximately 0.5 for the Paloma anchor and McCarthy (2011) previously

measured R_{ns} of approximately 0.2 for drag embedment anchors. R_{ns} of 0.3 was used for calibration.

(8)   The n/p ratio and q value resulting in the best match of experimentally measured N_e and R_{ns} values are used for calculating the yield locus by using Equation 2.16 for the Simplified Plasticity Model predictions.

The calibrated interaction coefficients used for the simplified plasticity model prediction and the interaction coefficients by FEM for the plane strain conditions (Gilbert, et al., 2009) are summarized in Table 7.1.

Interaction factor	Calibrated Values	FEM Prediction (Plane Strain)
n/p	1.91	2.67
q	2.00	4.4

Table 7.1: Interaction coefficients used for predictions

Figure 7.6 shows the calibrated yield surface calculated using the calibrated interaction coefficients and the theoretical yield surface calculated using the FEM interaction coefficients.
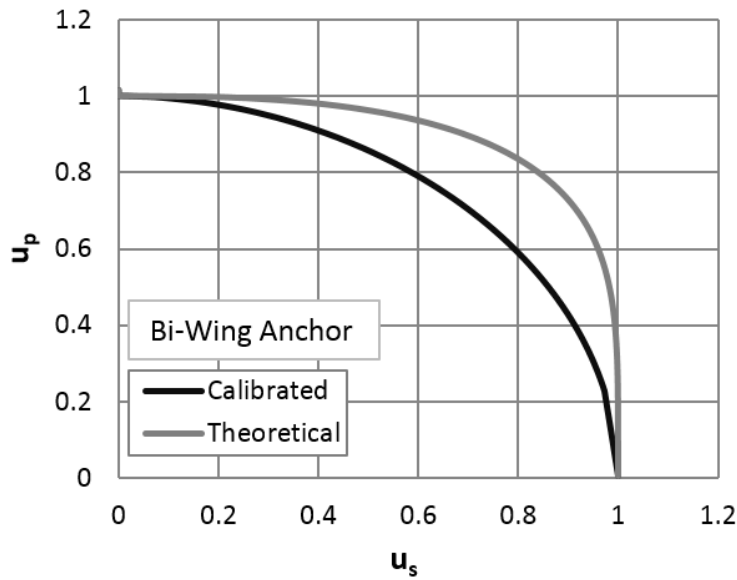
Figure 7.6: Calibrated and theoretical yield locus for the bi-wing Paloma anchor

The anchor dive trajectory calculated by the calibrated yield interaction coefficients and the interaction coefficients obtained by FEM for plane strain conditions (Gilbert, et al., 2009). The comparison of the measured and predicted anchor dive trajectories are presented in Figure 7.7. Results show that the Simplified Prediction Model dive trajectory results are similar to the experimental testing results when the change in pitch angle is small. The difference between the Simplified Plasticity Model prediction and the measured penetration depths at higher drag distances can be attributed to the change in pitch angle throughout the scaled model test and the assumption of constant pitch angle for the Simplified Plasticity Model calculations.
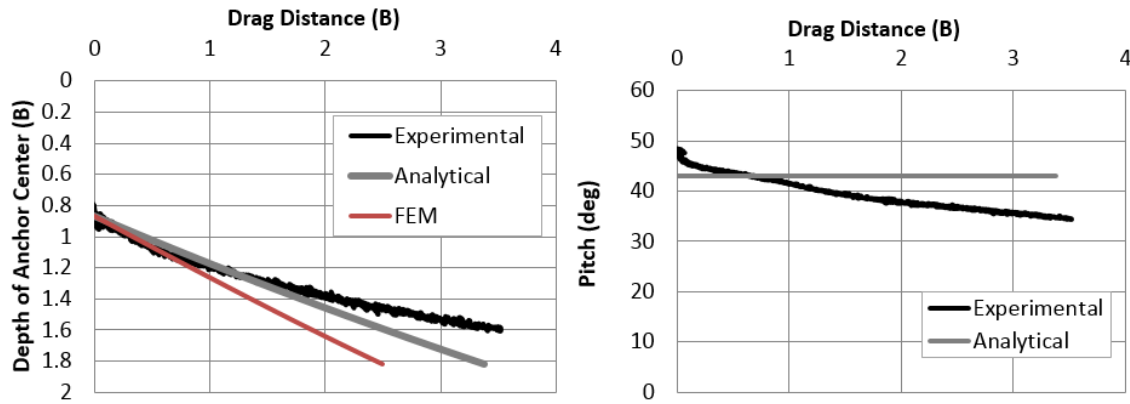
Figure 7.7: Dive trajectory, experimental results and analytical predictions

The change in pitch angle with translation parallel to fluke is presented in Figure 7.8.. While the analytical model assumes the pitch angle does not change with translation parallel to fluke (s direction), the experimental results show anchor pitch angle decreased with increasing translation.
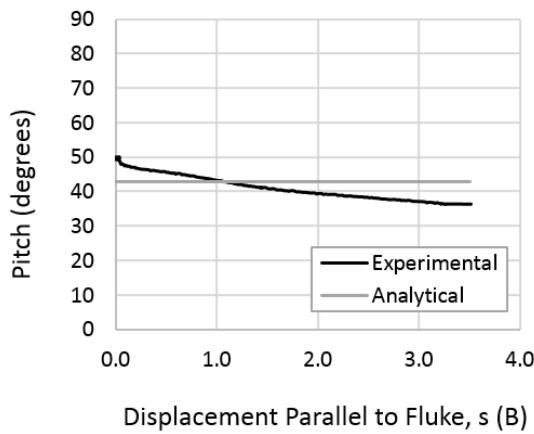
Figure 7.8: Change in pitch angle with translation parallel to fluke

The experimental measurements and analytical assumption of change in line angle from the plane parallel to fluke are presented in Figure 7.9. As the shank is free and aligned with the loading line this angle is also equal to the angle between fluke parallel and shank

(θ_{fs}). The slight drop in the analytical angle prediction is due to assuming the bearing capacity factor for calculating the normal resistance of the anchor line (N_c) is 5.1 at the mudline and increases to 7.6 for depths greater than 2.4 b (where b is the effective line width). Results show that the analytical model calculates a very slight change in the angle between fluke-line after the shank was released. The analytical line-fluke angle is approximately 57 degrees while the experimental line-fluke angle decreases from 56-degrees to 51-degrees then increases to 52-degrees during drag embedment. The difference is also related to the assumption of constant anchor pitch during analytical calculations while experimental measurements show decrease in anchor pitch with increasing drag distance. Even though the pitch angle decreases approximately 10-degrees during drag embedment, the 5 degree-maximum difference of line-fluke angle between predicted and measured values can be explained by the higher line angles measured during experimental testing.
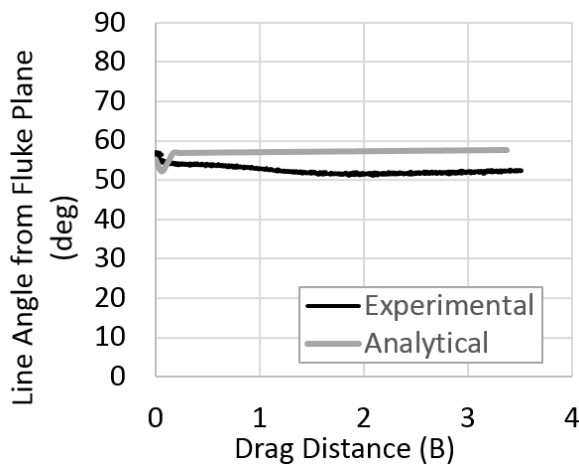
Figure 7.9: Change of angle between line and fluke parallel

The displacement normal to the fluke (n) versus the displacement parallel to the fluke (s) is presented in Figure 7.10. The analytical prediction matches well with the

experimental measurement. The change in R_{ns} ($R_{ns} = dn/ds$) with drag distance is presented in Figure 7.11 and it is approximately 0.5 both for the analytical prediction and the experimental measurement. Figure 7.11 shows the linear approximation of the experimental data match well with the analytical prediction. This is also consistent with the dn/ds ratio of 0.55 presented for the vertically loaded anchors by Aubeny and Chi (2014).
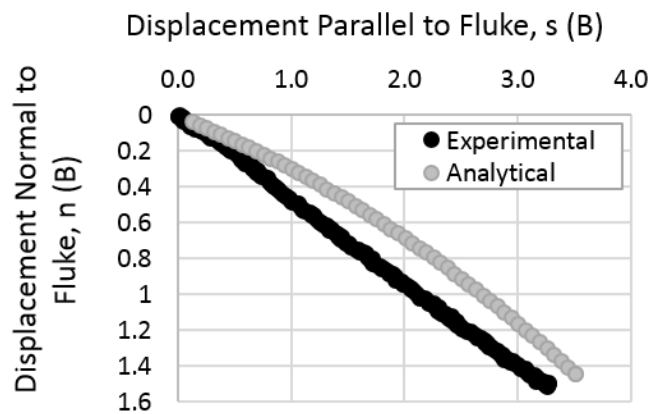
Figure 7.10: Displacement normal to fluke (n) versus displacement parallel to fluke (s)
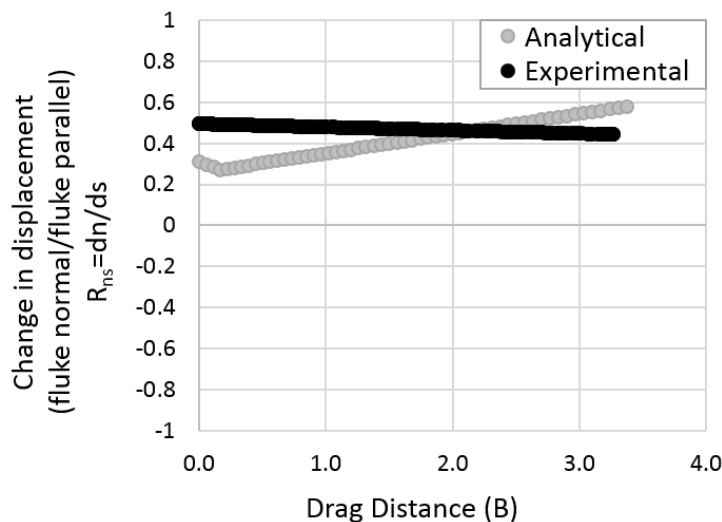
Figure 7.11: Change in dn/ds with drag

The ratio of the change in vertical displacement (dz) to the change in horizontal displacement (dy) with the drag embedment is presented in in Figure 7.12. Results show that experimental measurements and the analytical predictions match well. The experimental data show dz/dy is between 0 and 0.5. The analytical dz/dy decreases slightly with increasing drag distance.
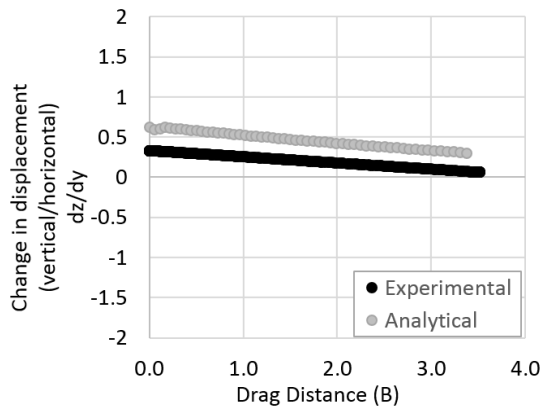
Figure 7.12: Change in dz/dy with drag

7.6 CONCLUSIONS

This chapter presents the Simplified Plasticity Model developed to predict the Flying Wing Anchor® dive trajectory and the ultimate holding capacity. The Simplified Plasticity Model calculates the interactions between the anchor, the loading line and the soil around the anchor and the loading line. The model calculation starts with increasing the line load. It is followed by the initiation of anchor pitch rotation when the load transferred eccentrically to the anchor exceeds the pure moment loading capacity of the anchor. The fluke-shank coupling mechanism is included in the calculations by increasing the rotation from vertical until the fluke-shank angle reaches a threshold value of 60-degrees. The dive trajectory is calculated by calculating the utilization in shear and normal

loading directions and comparing the results with the yield locus. The Simplified Plasticity Model is calibrated with experimental pure loading yield thresholds and the post-yield movement measurements of the Flying Wing Anchor®. The interaction coefficients to predict yield locus are calibrated with the measured dive trajectory and the calibration steps are described in detail.

The Simplified Plasticity Model prediction of line load to initiate pitch rotation is slightly higher than the measured load. After the pitch rotation starts, anchor pitch is decreased in small increments until the shank is released. The Simplified Plasticity Model assumes the angle between fluke and shank is equal to 60 degrees when the shank is released. The experimental measurements show the angle between fluke and shank was approximately 62-degrees right after the shank was released which is in good agreement with the analytical model assumption.

The anchor dive penetration initiates when the anchor capacity in shear loading is mobilized. The Simplified Plasticity Model predicts a load of 11.12 lbs. It is in good agreement with the experimental measurement of almost 11.8 lbs.

The Simplified Prediction Model dive trajectory predictions are similar to experimental testing results when the change in pitch angle is small. As the change in anchor pitch angle increases with further loading, the Simplified Plasticity Model predicts deeper penetrations than the experimental measurements. This can be explained by the Simplified Plasticity Model assumption of constant pitch angle during dive with the free-shank. The prediction model line angle from fluke plane is slightly higher than the experimentally measured line angle from fluke plane (which is also shank angle from fluke plane since shank is free). The same assumption also results in predicted anchor line-fluke angles approximately 5 degrees higher than the measured values. The predicted dn/ds and dz/dy ratios are in good agreement with the experimental measurements.

225

Chapter 8: Conclusions and Recommended Future Work

8.1 CONCLUSIONS

The future of wind energy is in deep-water where energy production can be maximized using larger wind turbines in an environment where winds are plentiful. The challenges of constructing deep-water wind turbines can be reduced with sustainable foundation concepts. This study focuses on experimental testing of a new offshore anchor that is developed as a sustainable and efficient foundation solution for deep-water wind turbines. The evolvement of the concepts focuses on not just anchor performance in soil but also the hydrodynamic stability and the structural capacity. This research focuses on anchor performance in soil, how it is measured and how results are used to optimize the Flying Wing Anchor® concepts. The main geotechnical objectives of the new anchor design are to have high efficiency, deeper drag embedment penetration, and "fly through the soil" during failure without getting out of soil.

This research presents the understanding of pure loading yield thresholds, initiation of post-yield movement and the post-yield movement with further loading of simple shaped bearing plates and the Flying Wing Anchor® concepts.

Objective 1 was to develop the understanding of the pure loading yield thresholds of simple shaped bearing plates that are symmetrical along the longitudinal axis in clay under undrained loading, study how the pure loading yield thresholds change for different geometries; investigate how the undrained shear strength, sensitivity and plasticity of soil and the loading rod and the rotational loading rates affects the pure loading yield thresholds of bearing plates and evaluate how experimental measurements compare with theoretical predictions. The simple shaped bearing plates are tested in remolded clay under undrained loading and pure loading yield thresholds are calculated as: N_{normal} in the range of 10-15, N_{shear} in the range of 3.3-4.4 and N_{moment} in the range of 1.9-2.6 were measured during the

tests in remolded clay. The results show that, for the same soil and testing conditions, plate area and plate thickness, there is no significant effect of anchor shape on the anchor yield threshold for simple geometry bearing plates that are symmetrical along the longitudinal axis. Results show that the undrained shear strength of the soil, or the type of the clay (kaolinite vs Gulf of Mexico marine clay) does not affect anchor yield thresholds significantly. Experimental measurements and theoretical calculations show that the pure loading yield thresholds decrease with increasing soil sensitivity. This decrease is negligible for pure normal and pure moment loading but it is significant for pure shear loading. The loading rod size can affect the measured pure normal loading yield thresholds significantly by interacting with the failure mechanism of the soil around the bearing plate depending on the direction of loading. The tested loading line displacement rates did not result in a significant difference for the measure pure rotational loading yield threshold (N_{moment}).

Objective 2 was to assess the initiation of post-yield movement and dive trajectory of simple shaped bearing plates that are symmetrical along the longitudinal axis under undrained loading conditions. Experimental testing of the scaled drag embedment anchor (DEA) and vertically loaded anchor (VLA) models and the theoretical calculations show that a plate anchor vertically embedded into soil should be rotated to a certain pitch angle with the shank attached to fluke. At that pitch angle, releasing the shank results in anchor penetration with increasing loading line. Releasing the shank at this pitch angle causes line load to be transferred to fluke plane in components parallel and perpendicular to fluke. Anchor post-yield movement initiates depending on the angle between fluke and shank, and the yield thresholds in pure shear and pure normal loading. Mobilizing the anchor shear loading capacity before anchor normal loading capacity is mobilized, provides dive penetration during drag embedment loading. The post-yield movement of simple shaped

bearing plates show the plates initially rotate to a pitch angle and then start diving deeper if the loading line is attached on the plate center of resistance or below center of resistance. This pitch angle during the dive penetration depends on the anchor resistances in normal and shear loading. For simple shaped bearing plates with ratio of pure normal loading yield threshold to pure shear loading yield threshold of approximately 3, this angle was approximately measured as 45 degrees. Attaching the loading line above center of area causes plate to rotate in the reverse direction and get pulled out of soil. Theoretical calculations show that the center of area and the center of pressure coincide when the bearing plates are tested in constant undrained shear strength but the center of pressure shifts below the center of area when the undrained shear strength linearly increases with depth. The center of pressure does not change with changing plate pitch rotation. Theoretical calculations of the initiation of post-yield movement are consistent with the experimental observations.

Objective 3 was to optimize the design of the Flying Wing Anchor® concept based on the pure loading yield thresholds, initiation of post-yield movement and the dive trajectory in clay under undrained conditions. The Flying Wing Anchor® concept, the design aspects of the installation steps, mobilization of anchor capacity and developed structures are presented. The initial Flying Wing Anchor® concept is the Diamond anchor that is developed as a one-wing concept. The minimum normal resistance to shear resistance ratio of 3:1 was planned to achieve during optimization of designs to obtain deeper dive penetrations with drag embedment. Pure loading yield thresholds (N_{normal} of 11 N_{shear} of 4.2) show the anchor shear resistance is increased due to structural additions for hydrodynamic stability. The increased shear resistance prevents deeper drag embedment penetration. Also those structural additions increased the anchor weight with a minor contribution to anchor capacity that conceptually decreases anchor efficiency. The

concept of using two control surfaces to provide hydrodynamic stability resulted in the bi-wing Flying Wing Anchor® concept of Paloma anchor. The N_{normal} of 13.6 and N_{shear} of 5.6 are measured in remolded clay under undrained loading conditions. The initiation of anchor pitch rotation, and the fluke-shank coupling mechanism concepts were confirmed with experimentally testing the Paloma anchor model. The in-plane drag embedment installation measurements resulted in deeper dive penetration than Diamond anchor. Experimental measurements show if anchor rolls up to 30-degrees during free-fall embedment, it corrects itself with yaw and roll rotations once the shank is released during installation. The bi-wing concept of Speedy anchor was developed to decrease the shear resistance of the Paloma anchor model. The pure loading yield thresholds resulted in a theoretical normal resistance to shear resistance ratio of 4.3 for the Speedy anchor. Experimental measurements of the dive trajectory show the Speedy anchor embeds deeper than both the Diamond and the Paloma anchor models during drag embedment loading. The Speedy anchor starts to pitch during failure until it gets close to horizontal while maintaining the holding capacity. Comparison of Speedy anchor measurements with the conventional Drag Embedment Anchor measurements show that the Speedy anchor can mobilize double the DEA capacity by embedding $1/4^{th}$ of vertical penetration in $1/8^{th}$ of a drag distance than what requires the DEA to mobilize the anchor capacity.

Objective 4 was to develop a simplified plasticity model that calculates the interactions between the anchor, the loading line, and the soil around the line and the anchor to predict the initiation of post yield behavior, dive trajectory and the ultimate holding capacity of the new anchor concept in clay; and evaluate how theoretical predictions compare with experimental measurements. The Simplified Plasticity Model calculates the interactions between the anchor, loading line and the soil around the anchor and the loading line. The model calculation starts with increasing line load followed by initiation of anchor

pitch rotation when the load exceeds the pure moment loading capacity of the anchor. The fluke-shank coupling mechanism is included in the calculations by increasing the rotation from vertical until the fluke-shank angle reaches a threshold value of 60 degrees. The dive trajectory is calculated by calculating the utilization in shear and normal loading directions and comparing the results with the yield locus. The Simplified Plasticity Model is calibrated with the experimental pure loading yield thresholds and the post-yield movement measurements of the Flying Wing Anchor®. The Simplified Prediction Model dive trajectory predictions are similar to the experimental testing results when the change in pitch angle is small. As the change in anchor pitch angle increases with further loading, the Simplified Plasticity Model penetration predictions get higher than the measured value due to the Simplified Plasticity Model assumption of constant pitch angle during dive trajectory with the free-shank. The experimentally measured and prediction model calculations of dn/ds and dz/dy ratios are in good agreement.

8.2 RECOMMENDED FUTURE WORK

The understanding of the Flying Wing Anchor® performance can be further improved by coupling the hydrodynamic stability analysis with the anchor performance in clay. Any structural modifications that can be done to improve the anchor holding capacity and the dive trajectory are restricted by the hydrodynamic stability of the anchor. The resistance of the anchor to shear loading can be further reduced to increase normal resistance to shear resistance ratio and improve dive penetration.

Testing the scaled model anchor in normally consolidated soil test beds with different forerunner diameters can produce important data to predict prototype anchor behavior in normally consolidated soil test beds. By using scaling relationships, important insight can be obtained about the prototype Flying Wing Anchor® performance in field.

The anchor can be tested by restricting one-degree-of-freedom in translational loading and subjected to the loading in the other two-degrees-of-freedoms. The interactions between pure loading pairs such as shear-normal, shear-rotation and normal-rotation can be obtained experimentally. The results can be used to improve the Simplified Plasticity Model.

Anchor dive trajectory can be modeled with finite element modeling and the interactions coefficients (m,n,p,q) can be calculated for the Flying Wing Anchor® concept.

Appendix

A.1 DIMENSIONS OF BEARING PLATES WITH SIMPLE GEOMETRIES
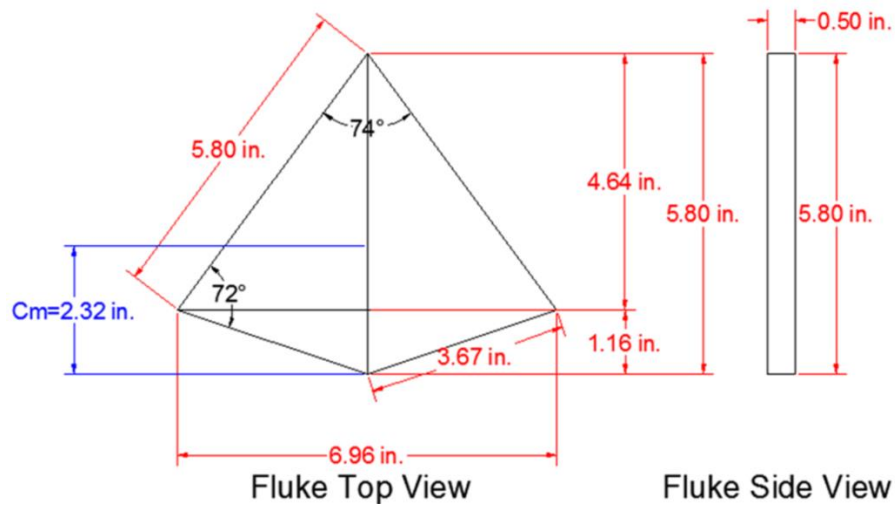
Figure A.1: Diamond 20 in^2 fluke area
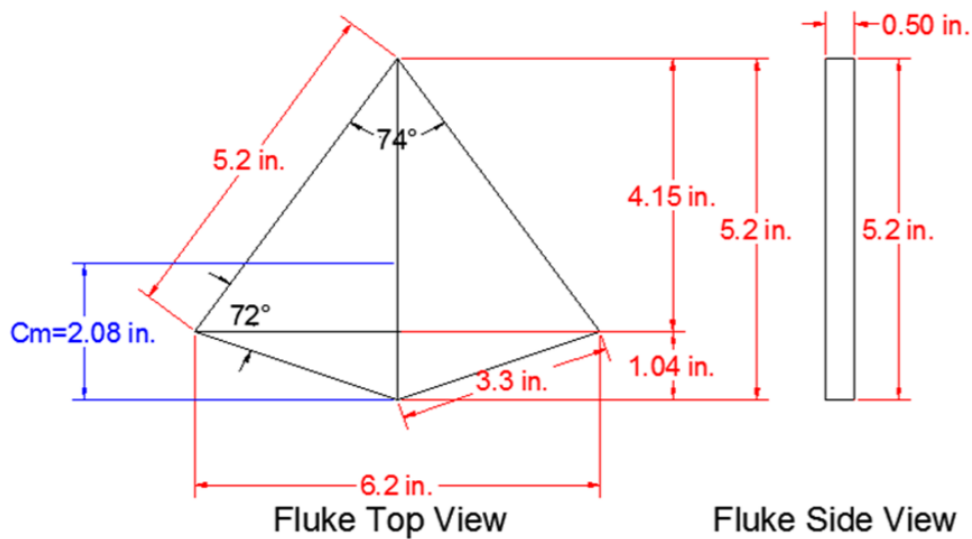
Figure A.2: Diamond model with 16 in^2 fluke area
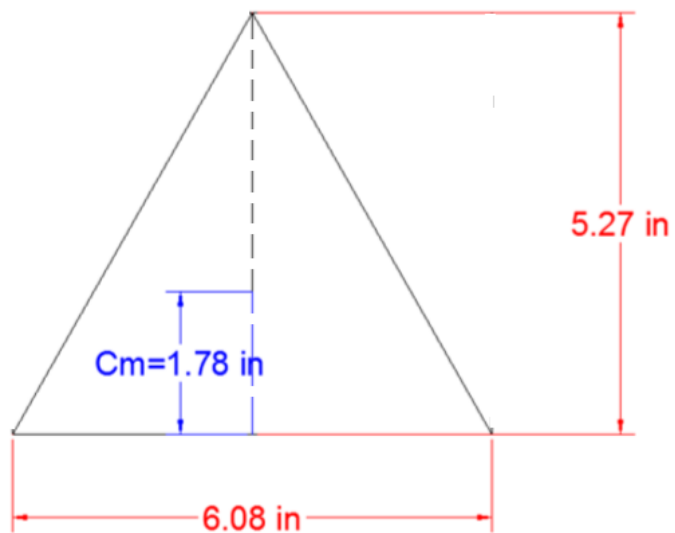
Figure A.3: Equilateral triangle bearing plate with fluke area of 16in^2
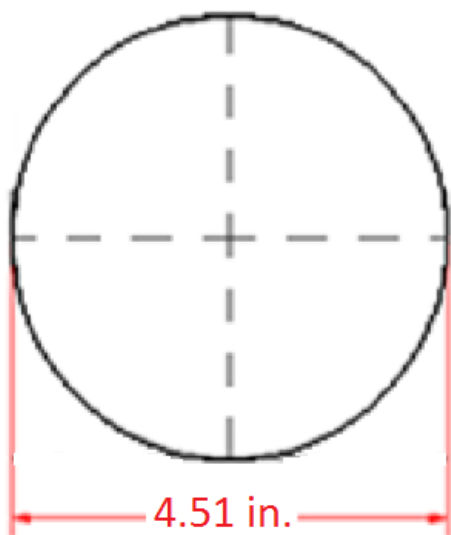
Figure A.4: Circle shaped bearing plate with fluke area of 16in^2
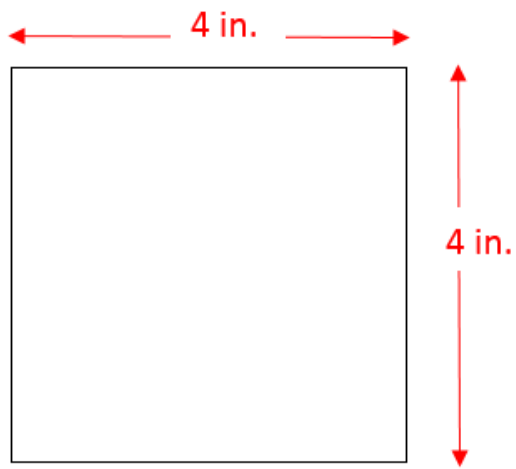
Figure A.5: Square shaped bearing plate with fluke area of 16in^2

A.2 DIMENSIONS OF SCALED MODEL FLYING WING ANCHORS®
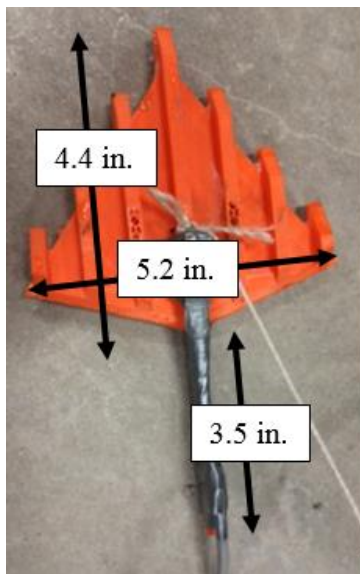
Figure A.6: Dimensions of the acrylic Diamond Flying Wing Anchor® with lower beam
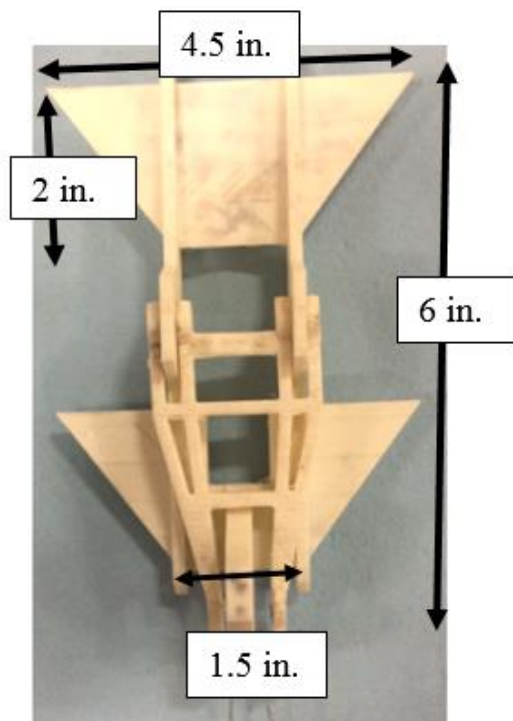
Figure A.7: Dimensions of the acrylic Paloma Flying Wing Anchor®
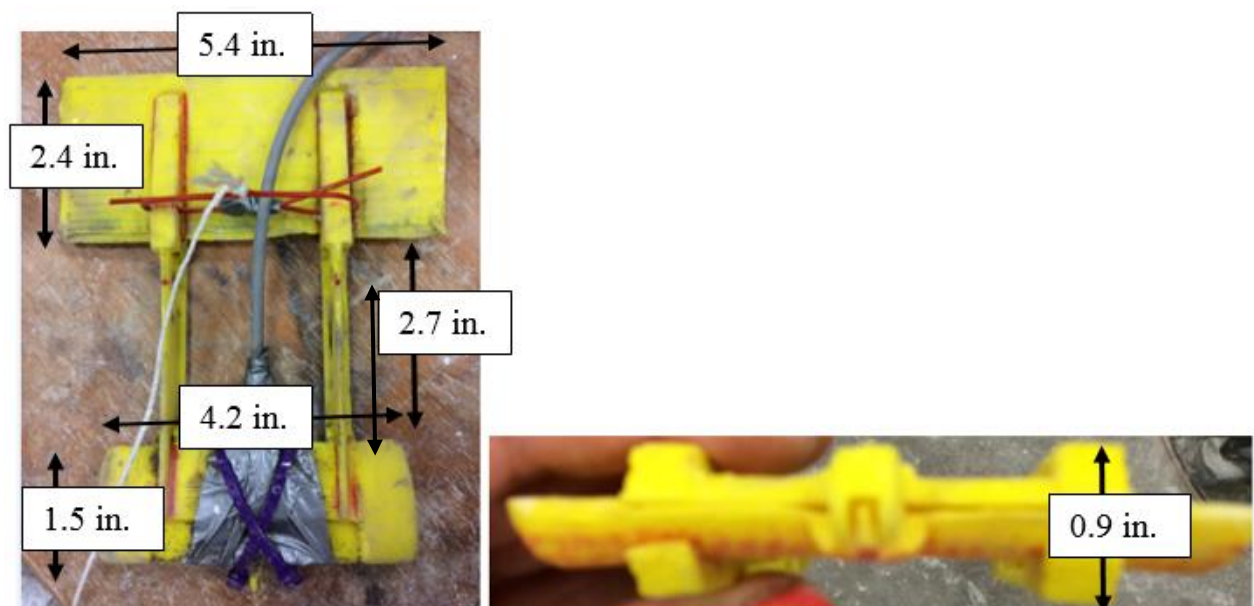
Figure A.8: Dimensions of the acrylic Speedy Flying Wing Anchor®

A.3 PURE LOADING YIELD THRESHOLD TESTS

This section includes the testing results of pure loading tests of bearing plates with simple geometries and the Flying Wing Anchor® concepts scaled models. The test information, the undrained shear strength profile of the soil test bed and the net anchor resistances measured during pure loading tests in that soil test bed are presented. Test information presents details about the bearing plate or the anchor model tested and the soil test bed. The testing dates are included to relate pure loading tests with the undrained shear strength profile of the soil test beds.

A.3.1 TESTS IN KAOLINITE SOIL TEST BEDS

Tests Performed on 04/01/2014 & 04/04/2014

- Pure Loading Tests, Diamond Shaped Anchor Model

- Plywood bearing plate, Fluke Area: 20 in^2

- Kaolinite, Gs: 2.58, LL= 54-58%, PI=20-26%, water content: 97%

- Saturated unit weight: 90 pcf

- Soil Depth: 15 in.
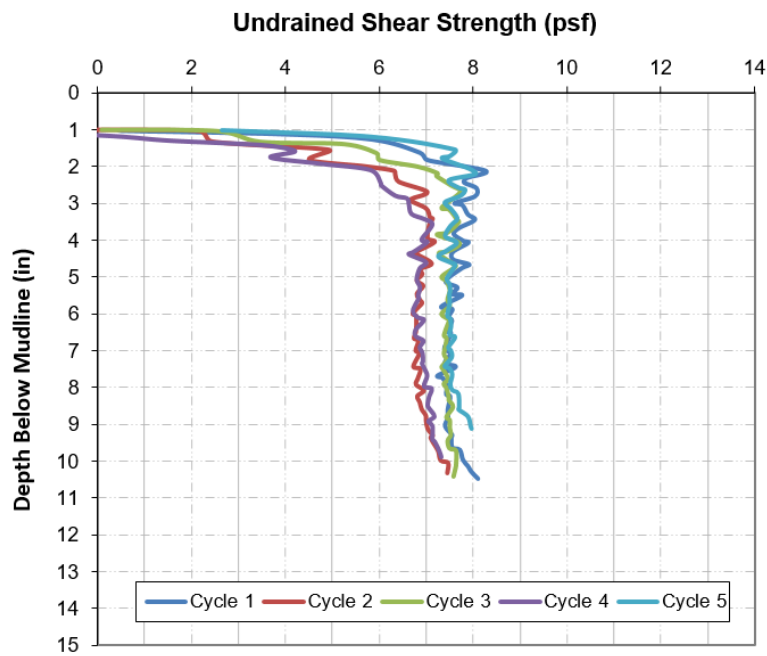
Figure A.9: Undrained shear strength profile of the test bed (4/1/2014)

St=1.0
A_f=20 in^2
04/01/2014
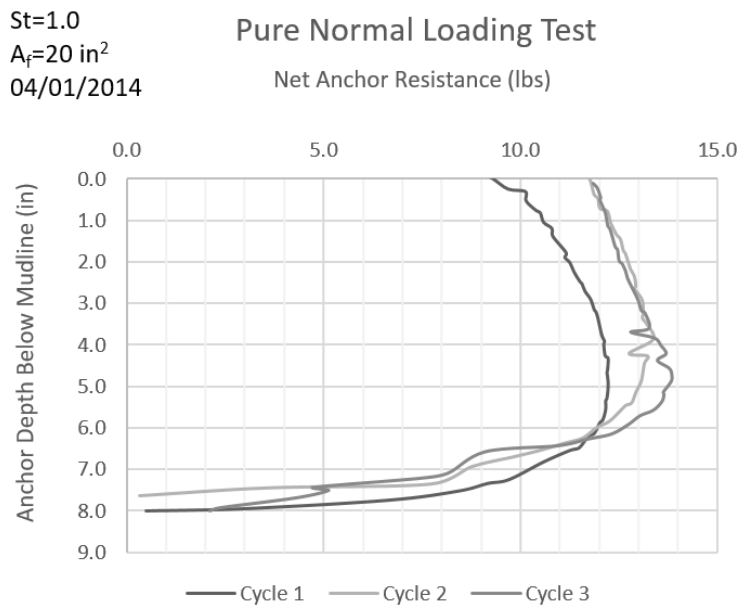
Figure A.10: Pure normal loading test results (04/01/2014)

St=1.0
A_f=20 in^2
04/01/2014

Pure In-Plane Shear Loading Test

Net Anchor Resistance (lbs)
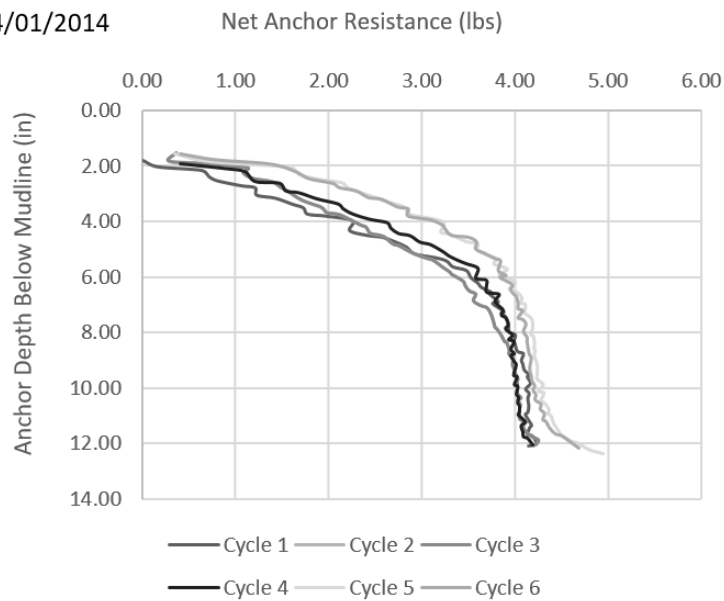
Figure A.11: Pure in-plane shear loading test results (04/01/2014)

St=1.0
A_f=20 in^2
04/01/2014

Pure Out-of-Plane Shear Loading Test

Net Anchor Resistance (lbs)
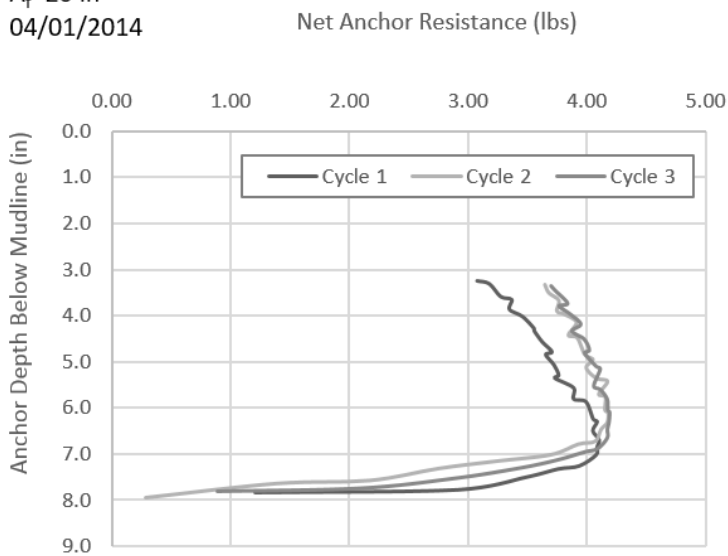
Figure A.12: Pure out-of-plane shear loading test results (04/01/2014)

238

St=1.0
A_f=20 in^2
04/01/2014
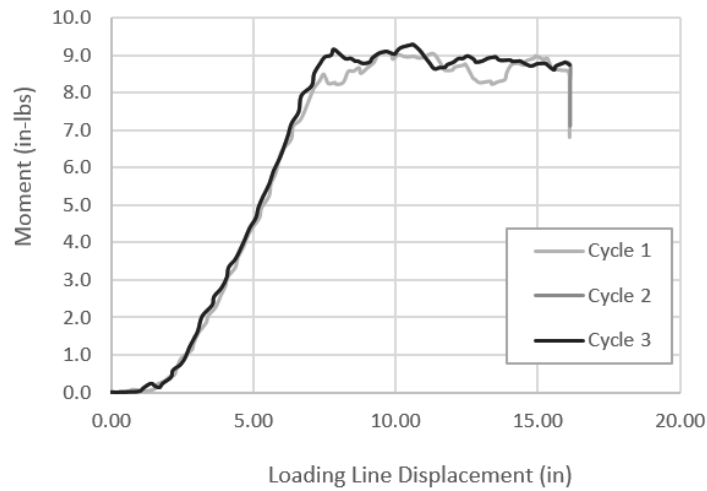
Figure A.13: Pure pitch loading test results (04/01/2014)
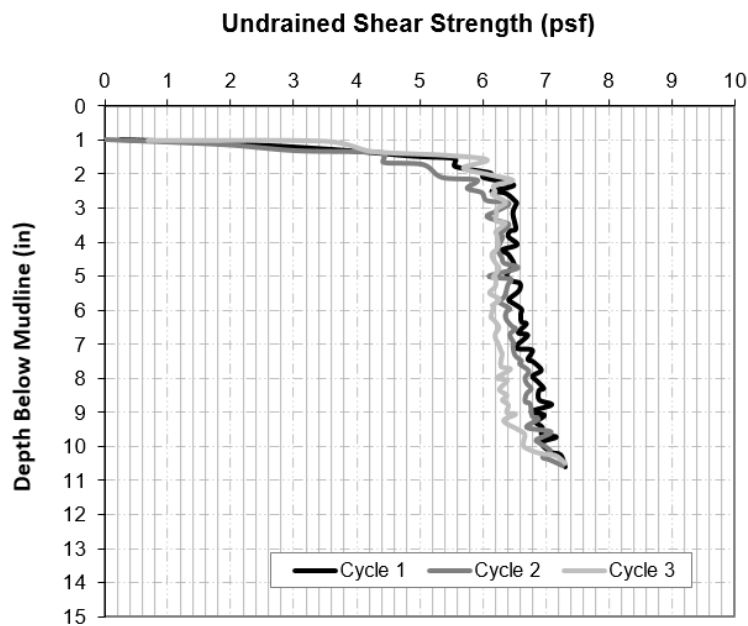
Figure A.14: Undrained shear strength profile of the test bed (4/4/2014)

239

St=1.0
A_f=20 in^2
04/04/2014

Pure Yaw Loading Tests
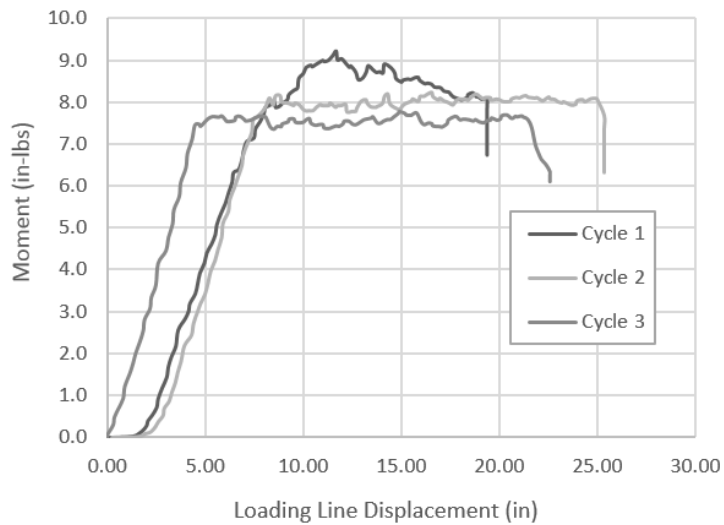
Figure A.15: Pure yaw loading test results (04/04/2014)

St=1.0
A_f=20 in^2
04/04/2014

Pure Roll Loading Tests
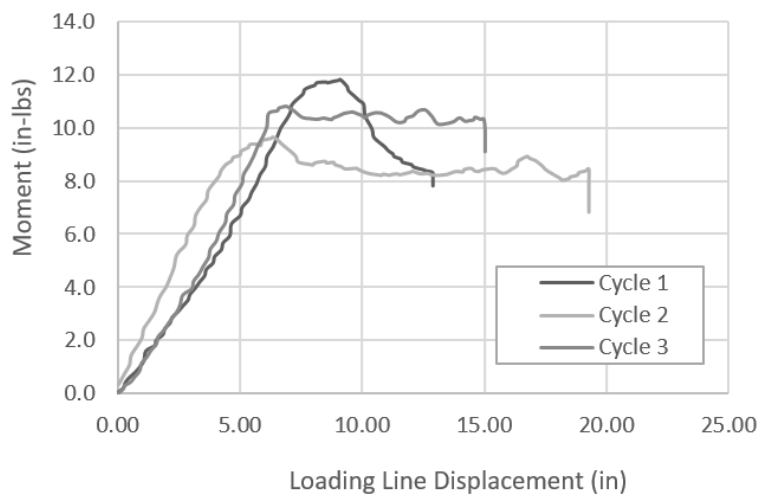
Figure A.16: Pure roll loading test results (04/04/2014)

240

Tests Performed on 05/25/2014

- Pure Loading Tests in Sensitivity> 1.0 soil, Diamond Shaped Anchor Model

- Rotational Loading Test at different loading rates

- Plywood Anchor Models, Fluke Area: 20 in^2

- Kaolinite, Gs: 2.58, LL= 54-58%, PI=20-26%, water content: 79-75%

- Saturated unit weight: 95pcf

- Soil Depth :20 in

- St= 1.7 and St=1.0
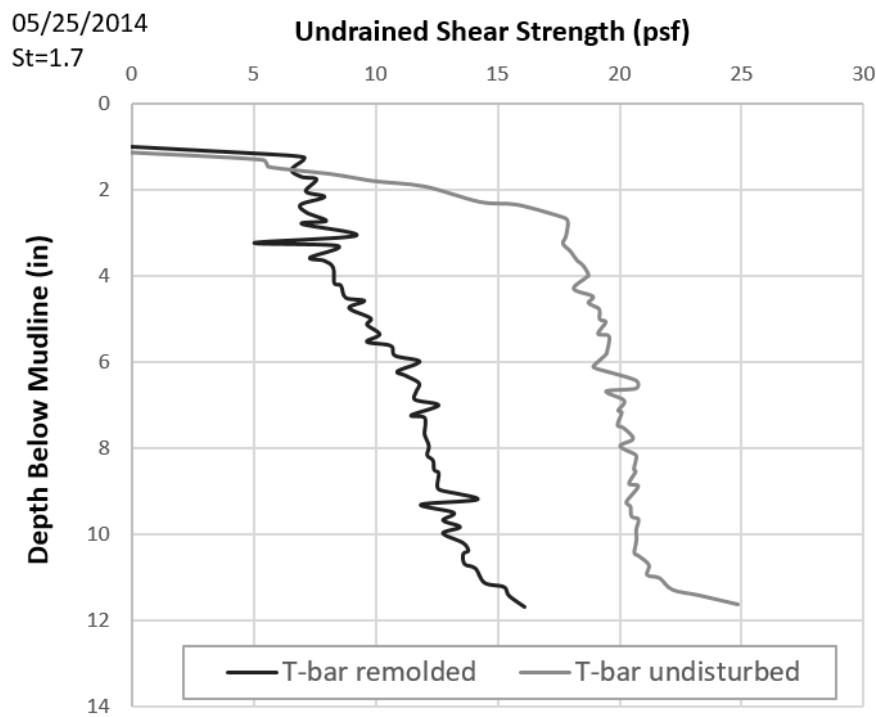
Figure A.17: Undrained shear strength profile of the test bed (5/25/214, St=1.7)
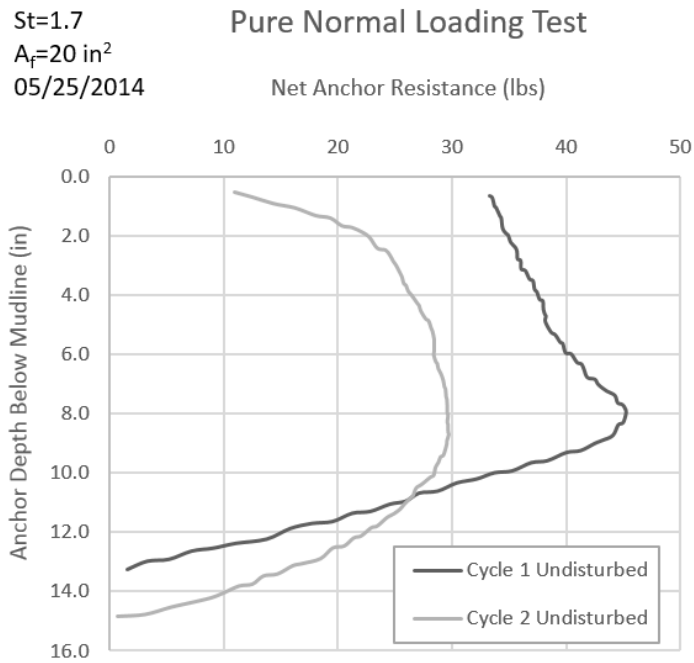
Figure A.18: Pure normal loading test results (5/25/214, St=1.7)
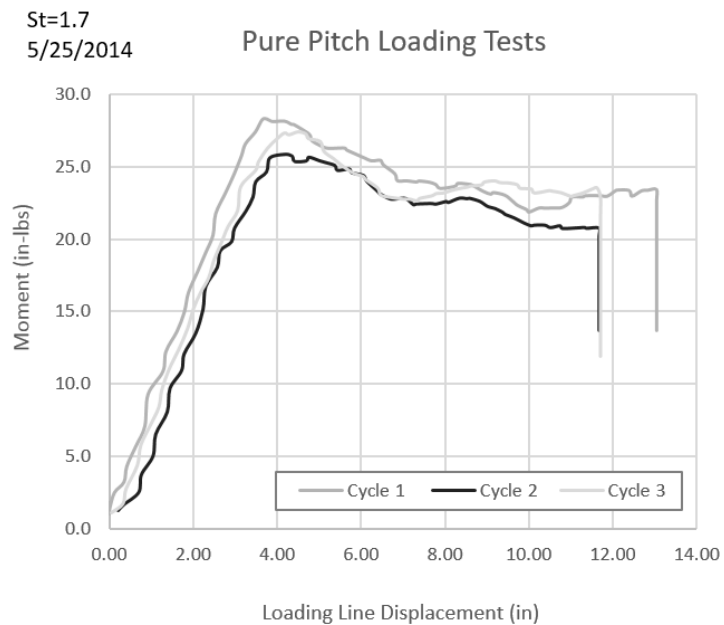
Figure A.19: Pure pitch loading test results (5/25/214, St=1.7)

242
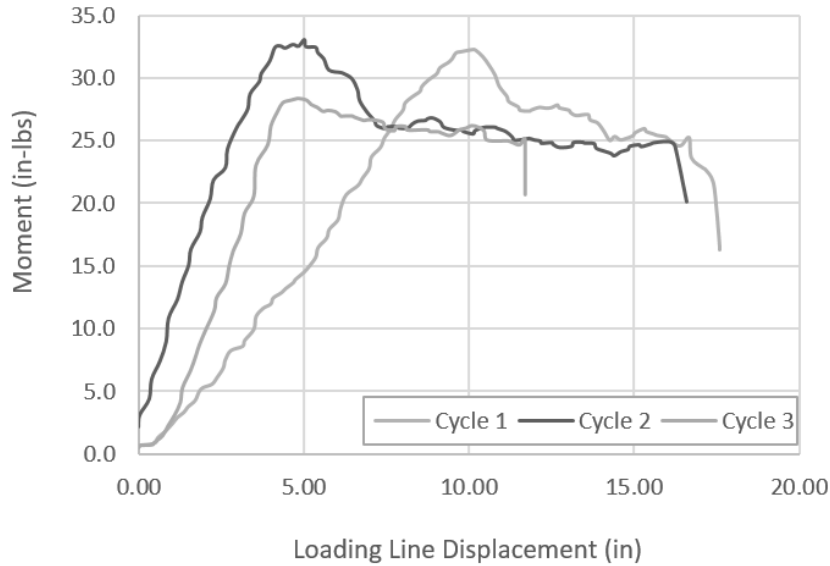
Figure A.20: Pure roll loading test results (5/25/214, St=1.7)
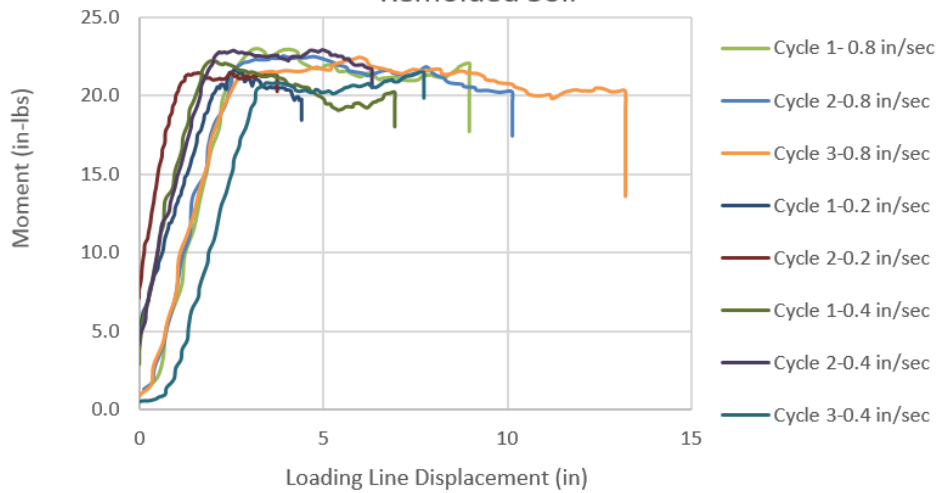
Figure A.21: Pure pitch loading test results (5/25/214, St=1.0)

243
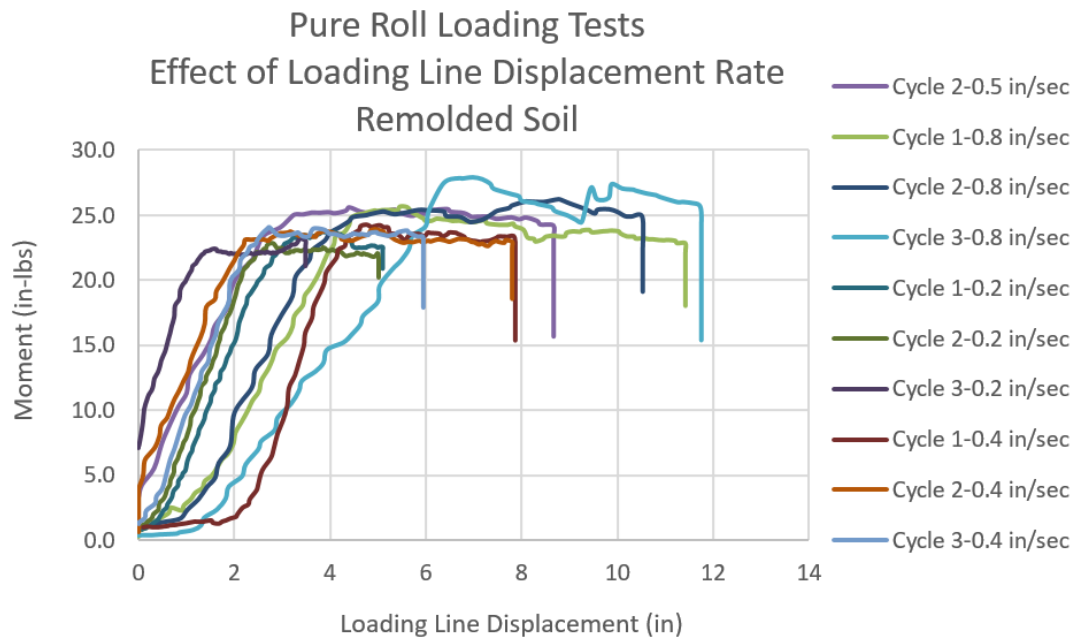
Figure A.22: Pure roll loading test results (5/25/214, St=1.0)
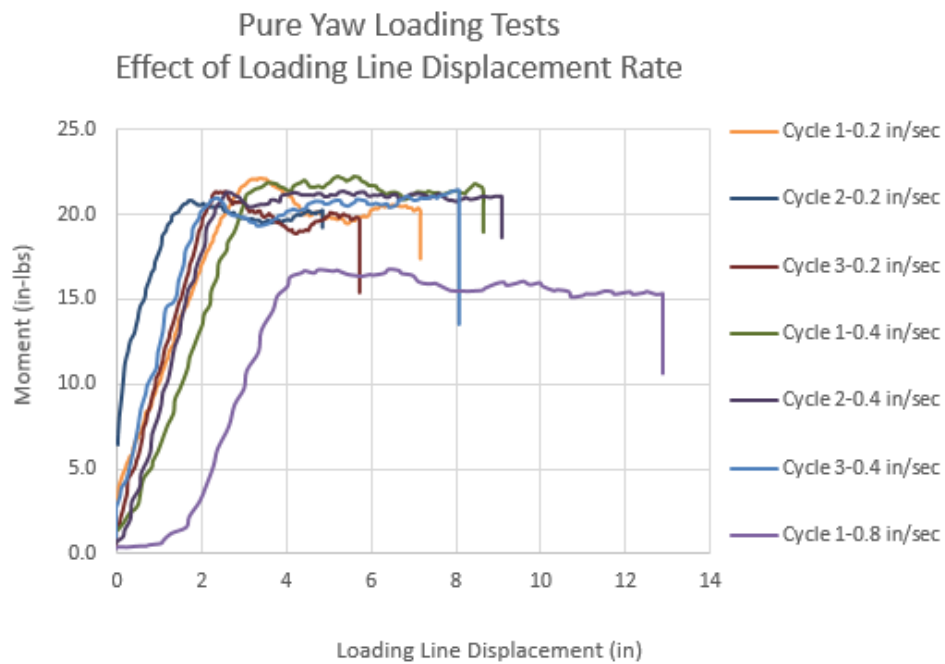
Figure A.23: Pure yaw loading test results (5/25/214, St=1.0)

244

Tests Performed on 06/18/2014, 06/25/2014 & 07/01/2014

- Shear Loading Tests in Remolded and Higher Sensitivity Soil

- Plywood Diamond Shaped Anchor Models, Fluke Area: 20 in^2

- Kaolinite, Gs: 2.58, LL= 54-58%, PI=20-26%, water content: 94-90% , saturated unit weight: 92pcf

- Soil Depth: 20 in.

- St=1.0-1.3-1.7

Tests Performed on 6/18/2015
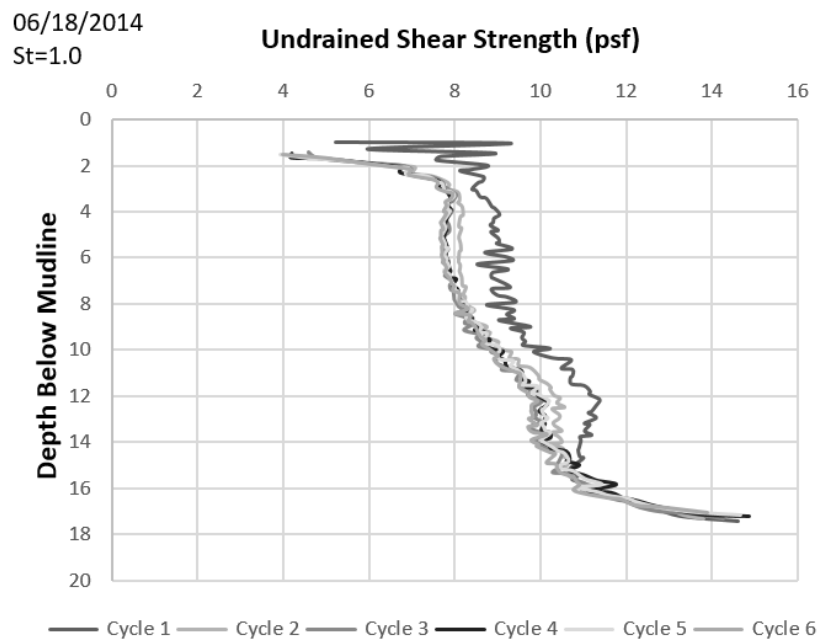
Figure A.24: Undrained shear strength profile of the test bed (6/18/2014)
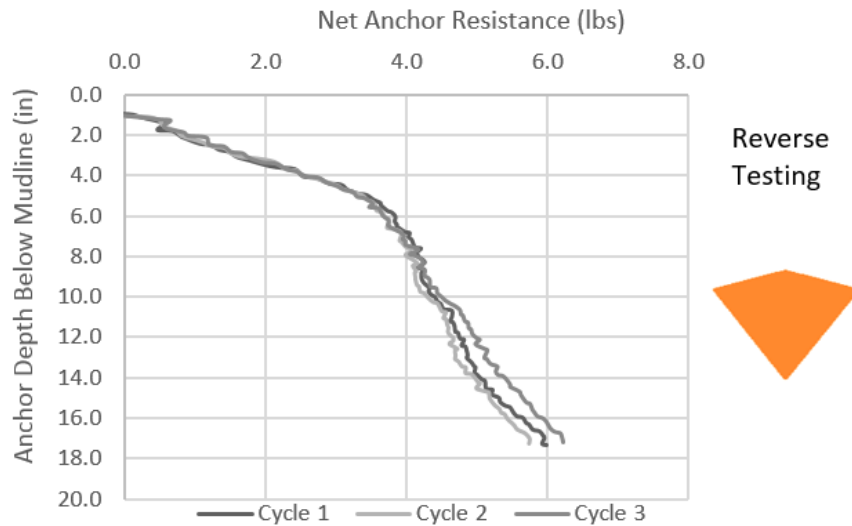
Figure A.25: Pure normal loading test results (6/18/214, St=1.0)
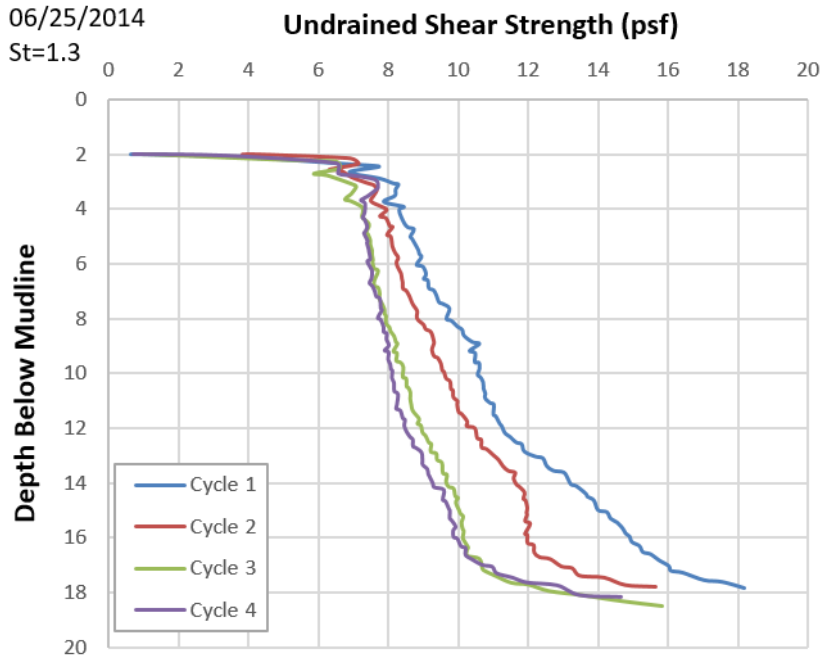
Figure A.26: Undrained shear strength profile of the test bed (6/25/2014, St=1.3)

246

St=1.3
A_f=20in^2
06/25/2014

Pure In-Plane Shear Loading Tests

Net Anchor Resistance (lbs)
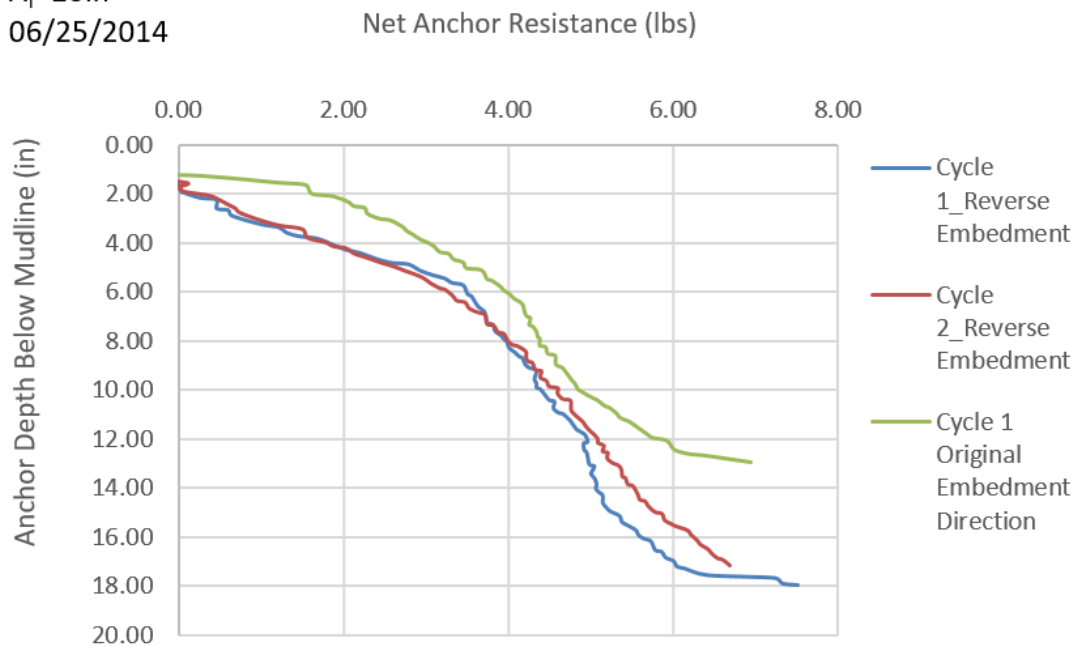
Figure A.27: Pure in-plane shear loading test results (6/25/214, St=1.3)

St=1.0

Undrained Shear Strength (psf)
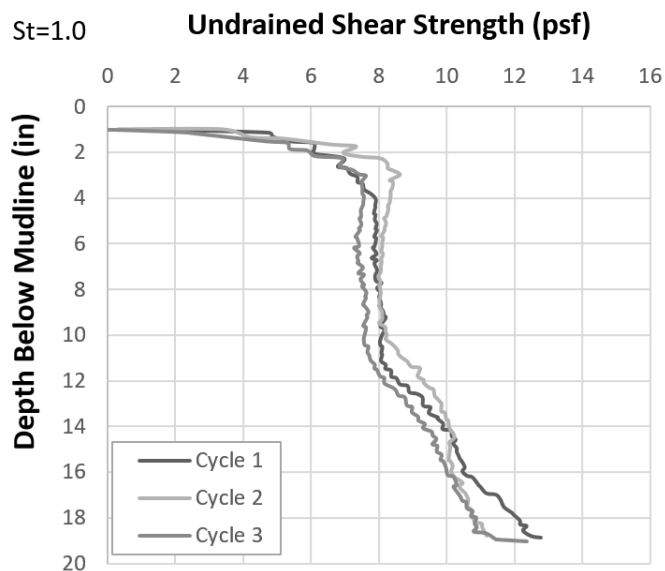
Figure A.28: Undrained shear strength profile of the test bed (7/1/2014, St=1)

247
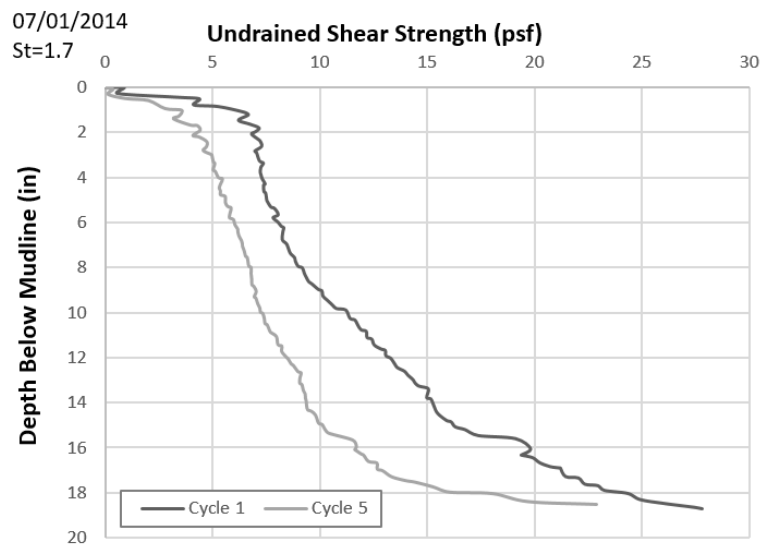
Figure A.29: Undrained shear strength profile of the test bed (7/1/2014. St=1.7)
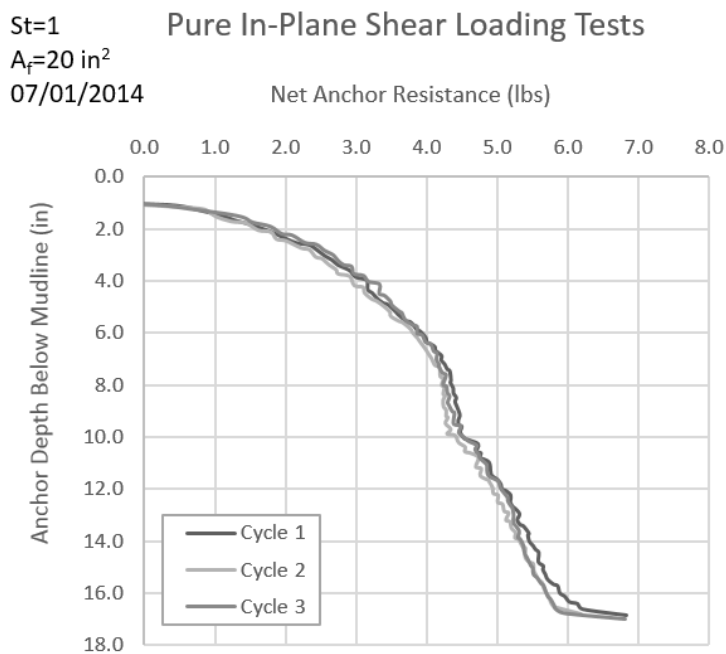
Figure A.30: Pure in-plane shear loading test results (07/01/2014, St=1.0)

248
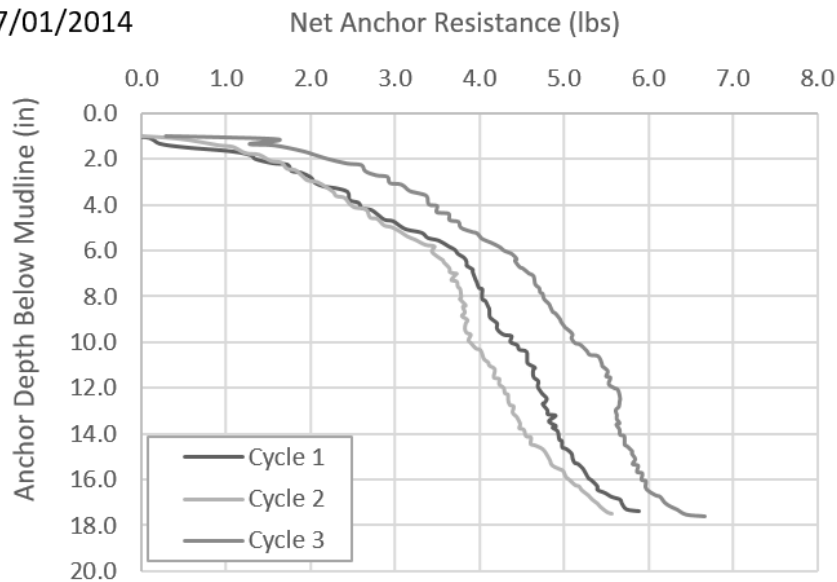
Figure A.31: Pure in-plane shear loading test results (07/01/2014, St=1.7)

Tests Performed on 7/17/2014, 7/18/2014, 7/22/2014, 7/24/2014

- Different anchor geometries, plywood models, $16in^2$ fluke areas

- Kaolinite, Gs: 2.58, LL= 54-58%, PI=20-26%, water content: 106%

- Saturated unit weight: 89pcf

- Remolded soil (St=1.0)

- Soil depth: 22 in.

- The out of Plane Shear Loading Direction and in-plane shear loading direction for circle is the same, only tested for one direction.

- Roll and Pitch loading directions for the circle anchor is the same, it is only tested for one loading direction.
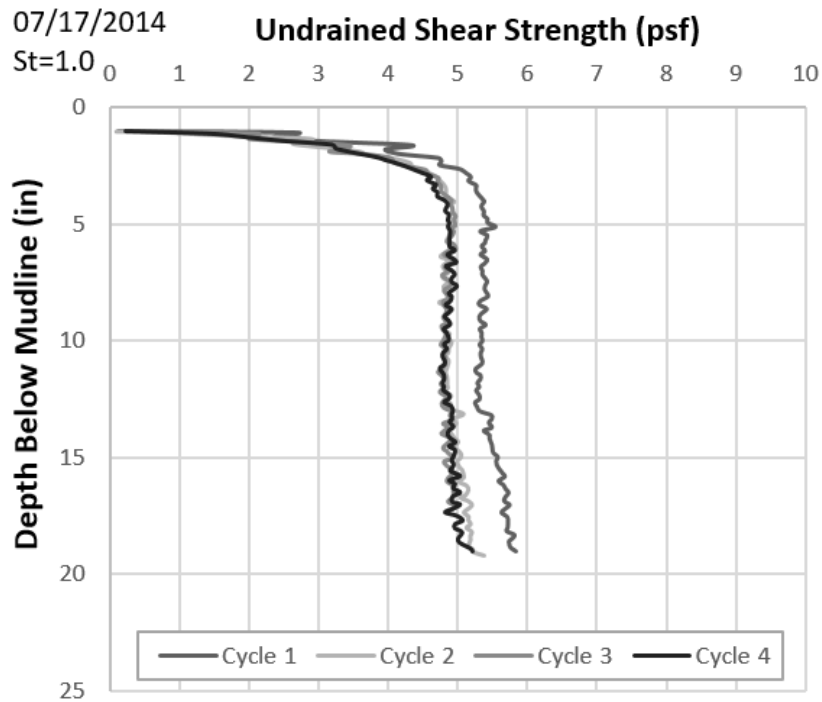
Figure A.32: Undrained shear strength profile of the test bed (7/17/2014)
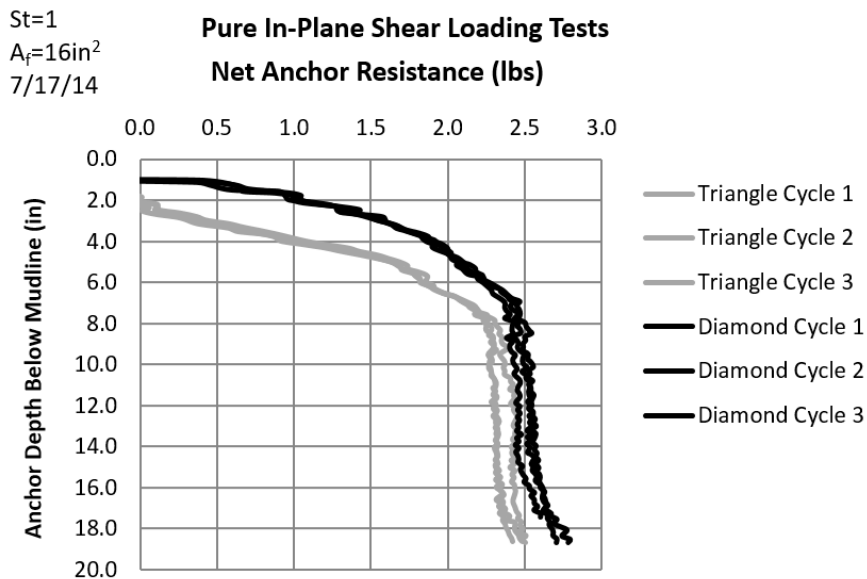
Figure A.33: Pure in-plane shear loading test results (07/17//214)

250
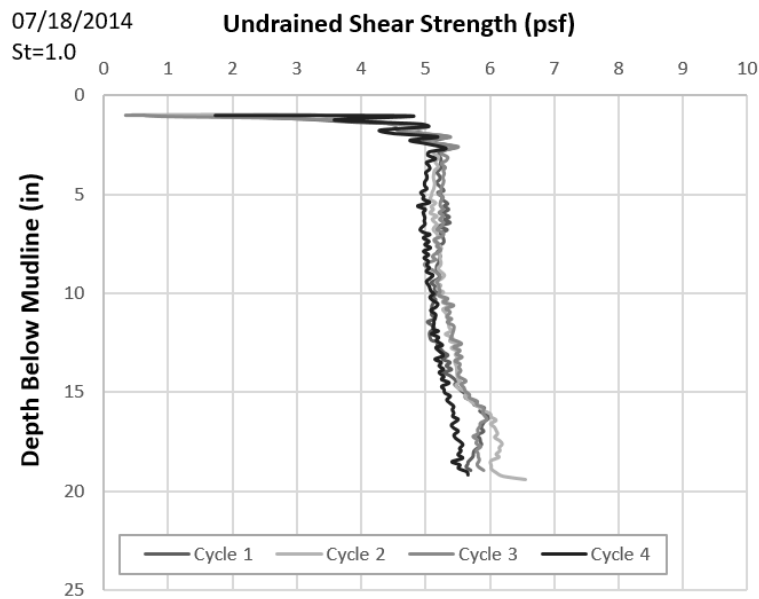
Figure A.34: Undrained shear strength profile of the test bed (7/18/2014)
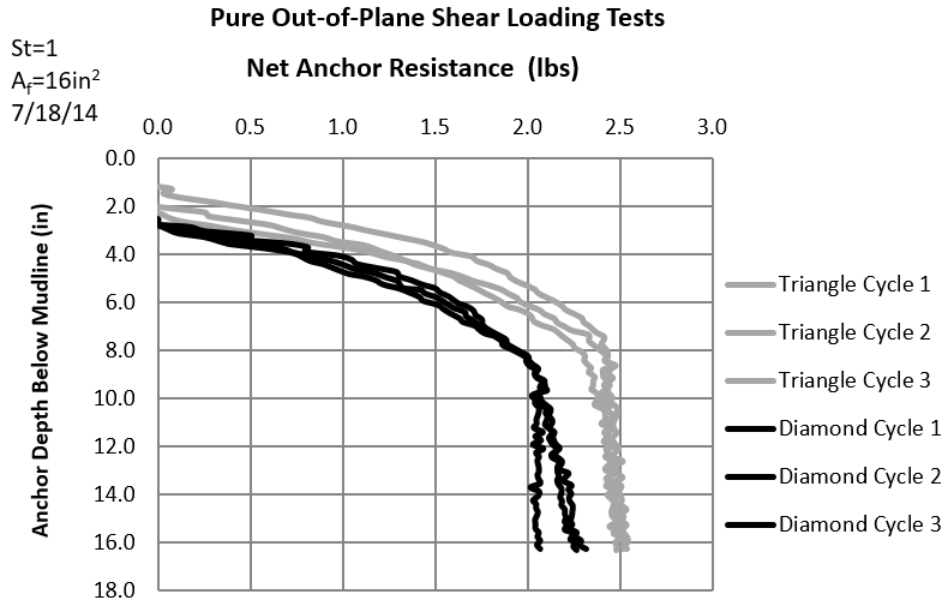
Figure A.35: Pure out-of-plane shear loading test results (07/18/214)
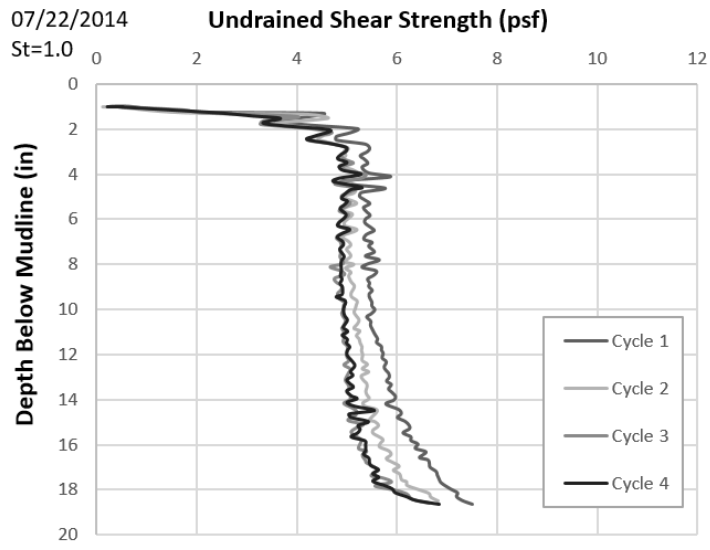
Figure A.36: Undrained shear strength profile of the test bed (7/22/2014)
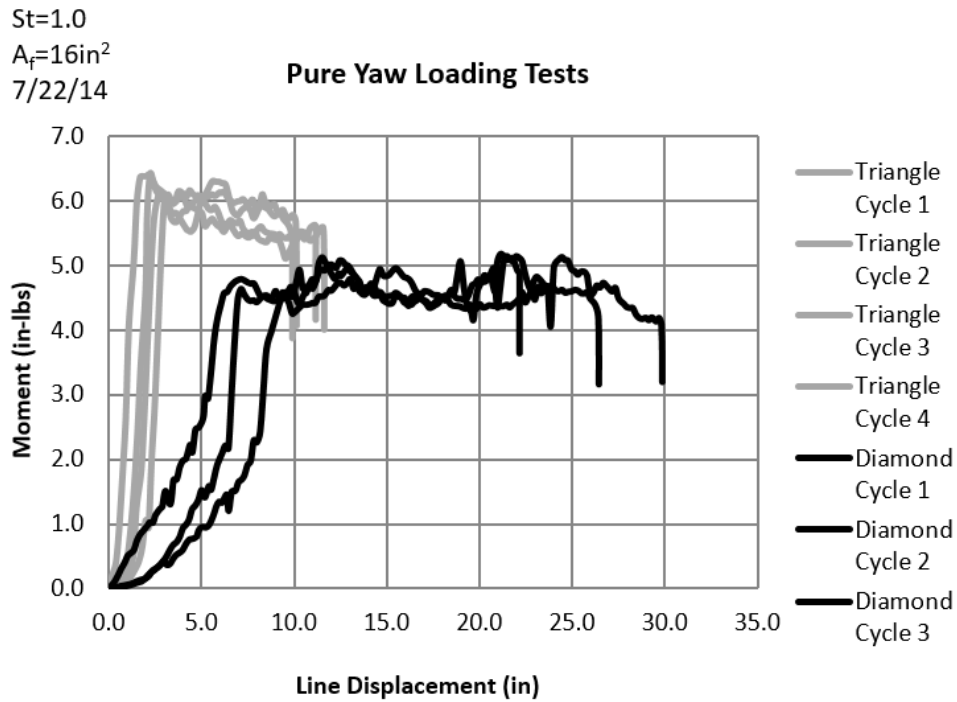
Figure A.37: Pure yaw loading test results (07/22/214)

252
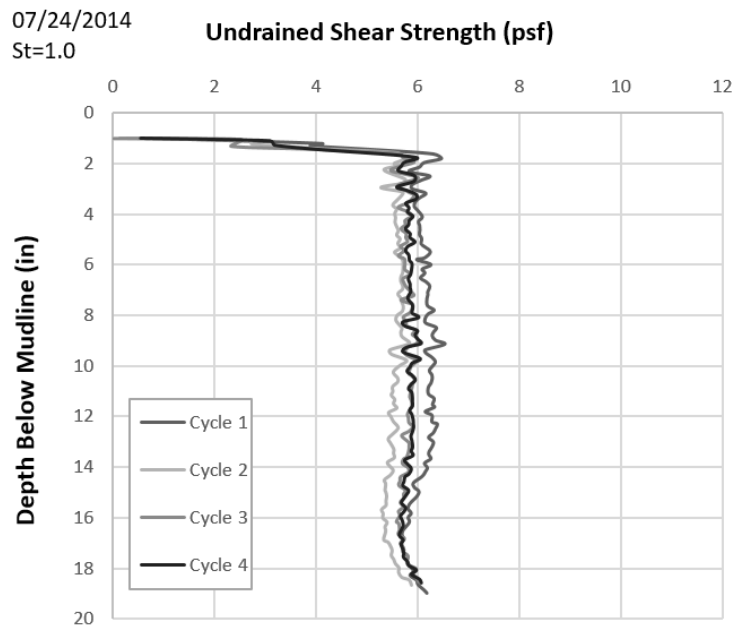
Figure A.38: Undrained shear strength profile of the test bed (7/24/2014)
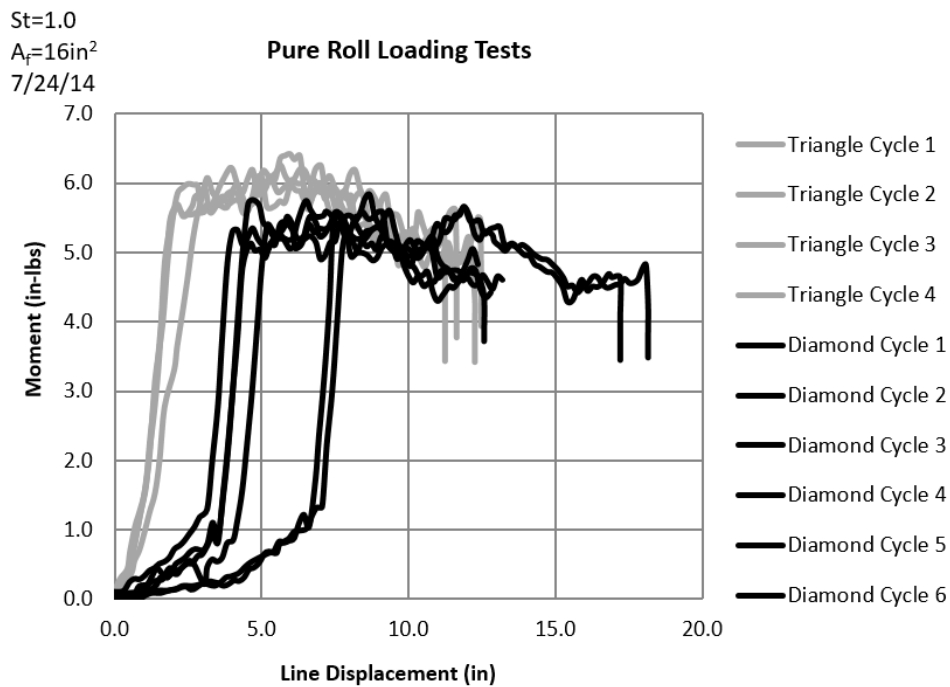
Figure A.39: Pure roll loading test results (07/24/214)

253

St=1.0
A$_f$=16in^2
7/24/2014
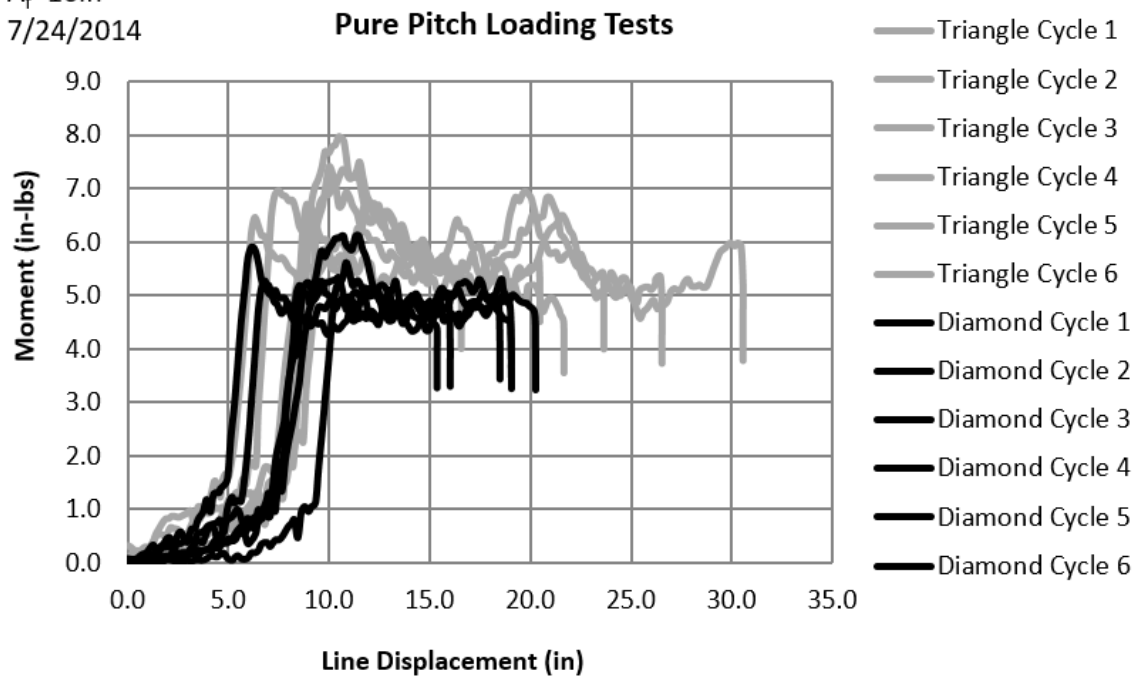
Figure A.40: Pure pitch loading test results (07/24/214)

Tests Performed on 8/13/2014

- Pure normal loading tests

- Different anchor geometries and fluke areas

- Kaolinite, Gs: 2.58, LL= 54-58%, PI=20-26%, water content: 103% ,

- Saturated unit weight: 89 pcf

- Remolded soil (St=1.0)

- Soil depth: 23 in.
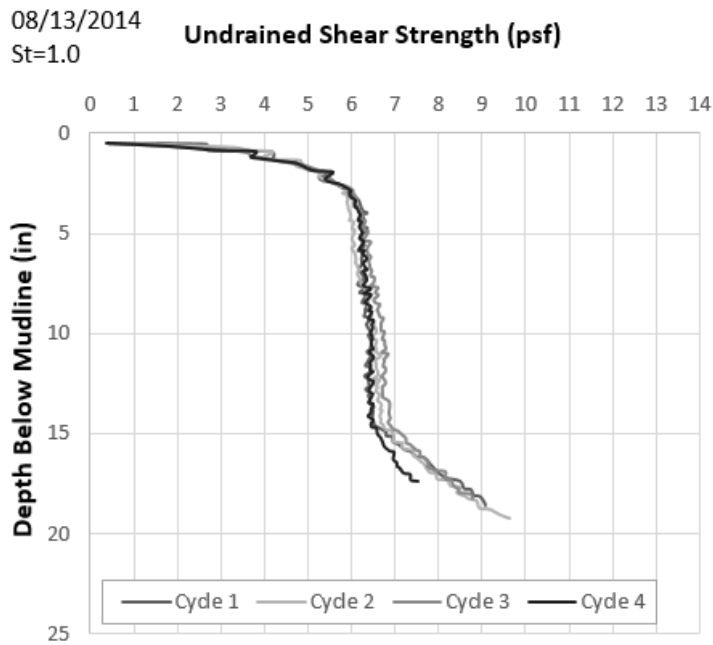
Figure A.41: Undrained shear strength profile of the test bed (8/13/2014)
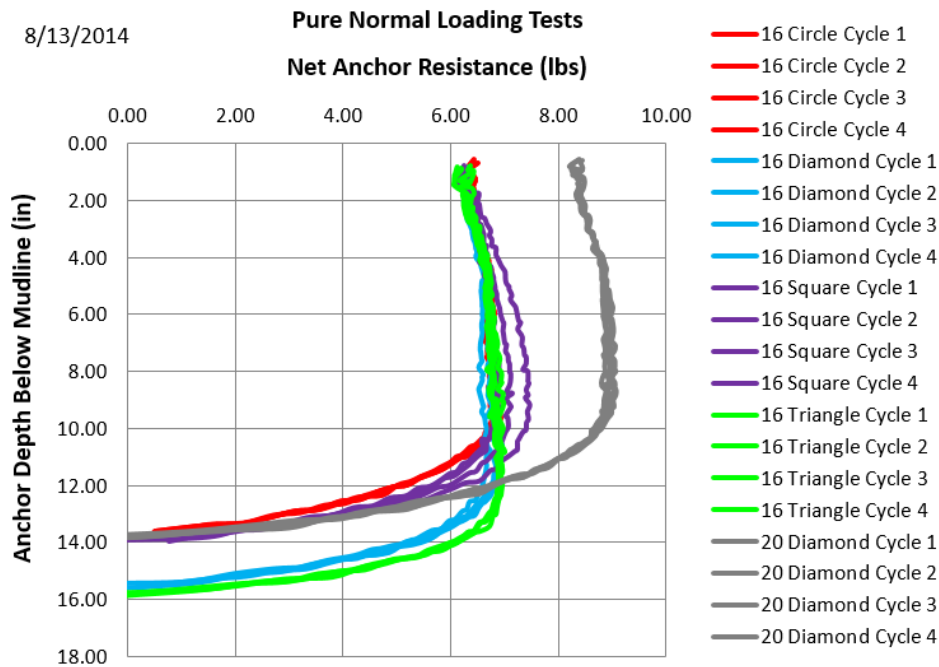
Figure A.42: Pure normal loading test results (08/13/214)

255

Tests Performed on 8/25/2014

- Normal Loading Tests

- Diamond anchor 16 in^2 fluke area, 0.5 in. fluke thickness

- Kaolinite, Gs: 2.58, LL= 54-58%, PI=20-26%, water content: 92%

- Saturated unit weight: 92pcf

- Remolded soil (St=1.0)

- Soil depth: 21 in.
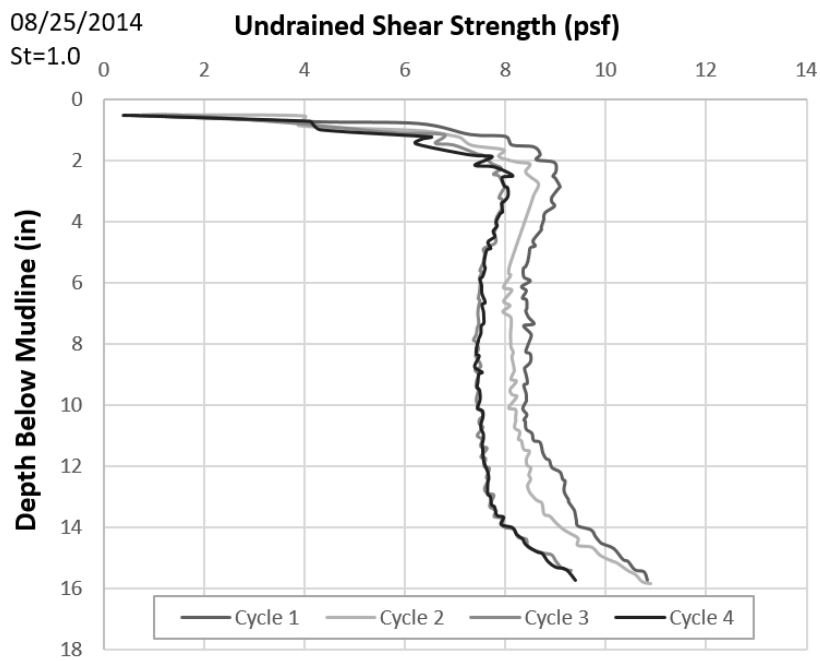
Figure A.43: Undrained shear strength profile of the test bed (8/25/2014)

Pure Normal Loading Tests
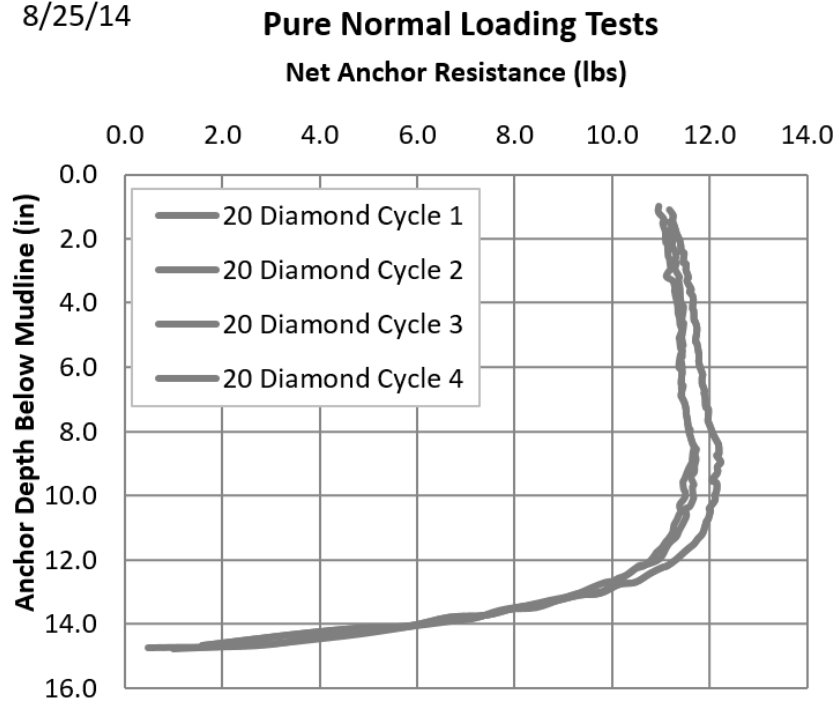
Figure A.44: Pure normal loading test results (08/25/214)

Tests Performed on 10/16/2014 & 10/17/2014

- Normal Loading Tests, pulling the anchor out of soil

- Different anchor geometries and fluke areas

- Kaolinite, Gs: 2.58, LL= 54-58%, PI=20-26%, water content: 70%

- Unit weight of soil: 97pcf

- Remolded soil (St=1.0)

- Soil depth: 20 in.
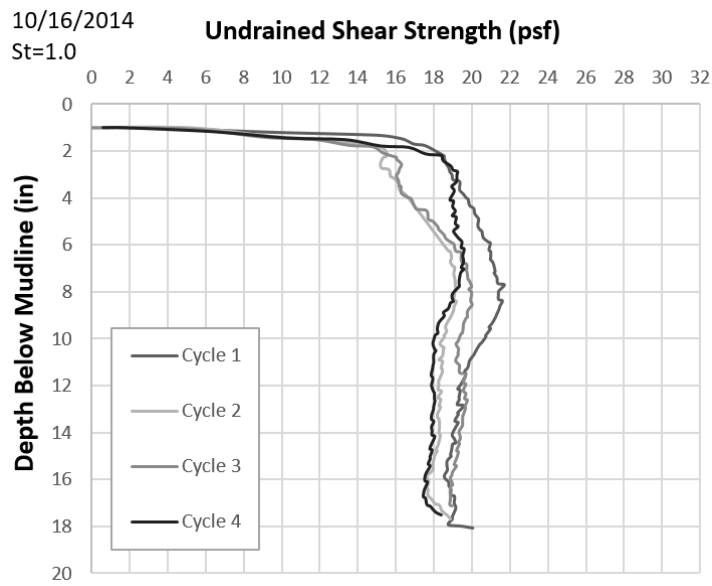
Figure A.45: Undrained shear strength profile of the test bed (10/16/2014)
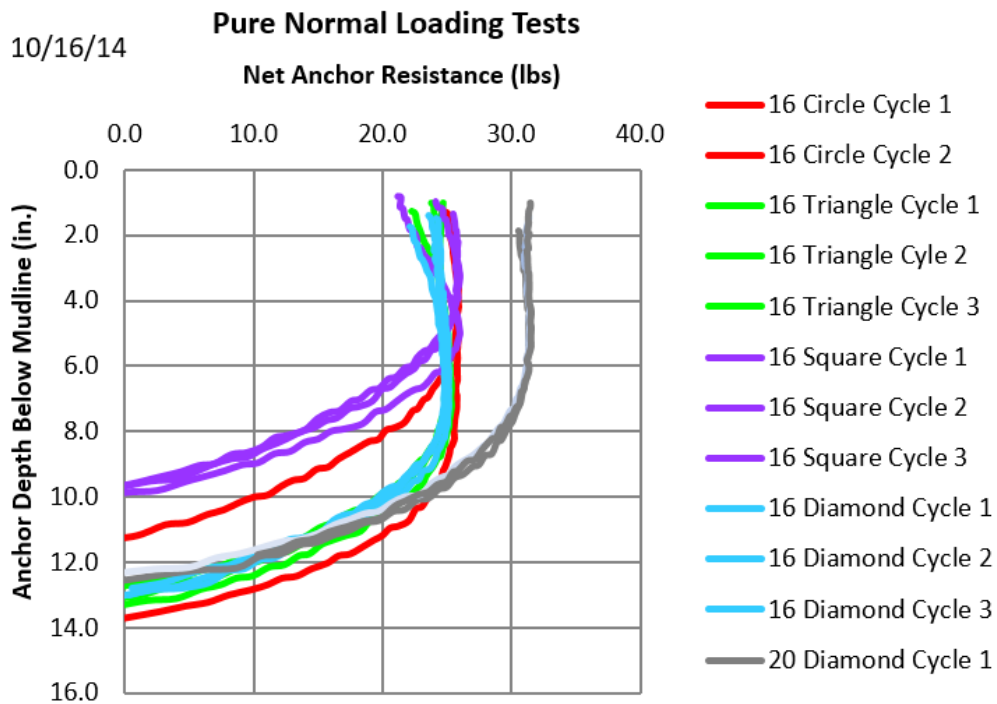
Figure A.46: Pure normal loading test results (10/16/214)
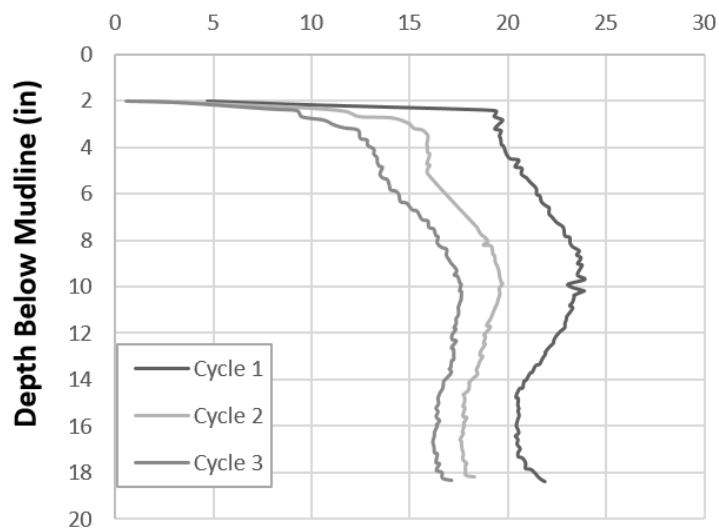
Figure A.47: Undrained shear strength profile of the test bed (10/17/2014)
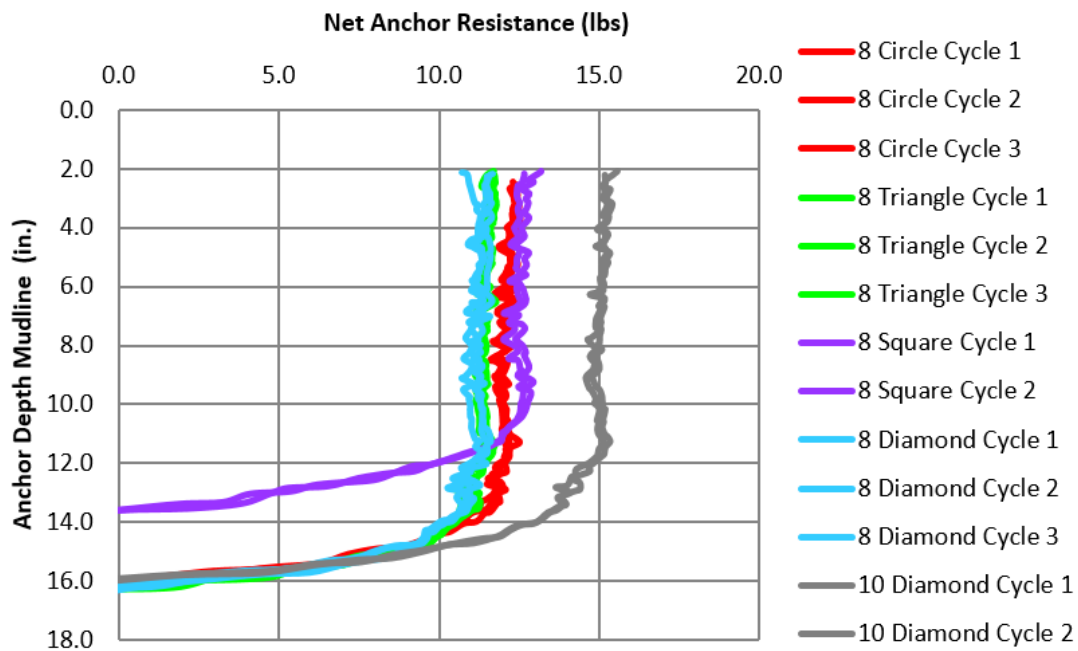
Figure A.48: Pure normal loading test results (10/17/214)

259

A.3.2 TESTS IN GULF OF MEXICO MARINE SOIL TEST BEDS

Tests Performed on 10/30/2014

- Normal Loading Tests

- Plywood Anchor Models

- Different anchor geometries

- Thickness 0.5 in.

- Gs: 2.75 water content: 100-95%

- Saturated unit weight: 95pcf

- Gulf of Mexico (GoM)clay is mixed with salty water (35ppt)

- Soil depth: 22 in.
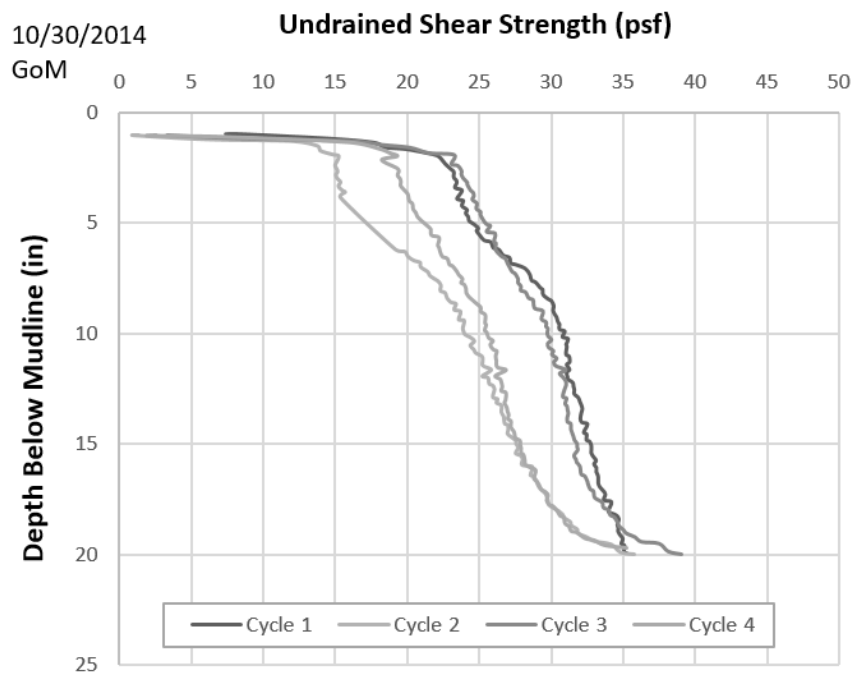
Figure A.49: Undrained shear strength profile of the test bed (10/30/2014)
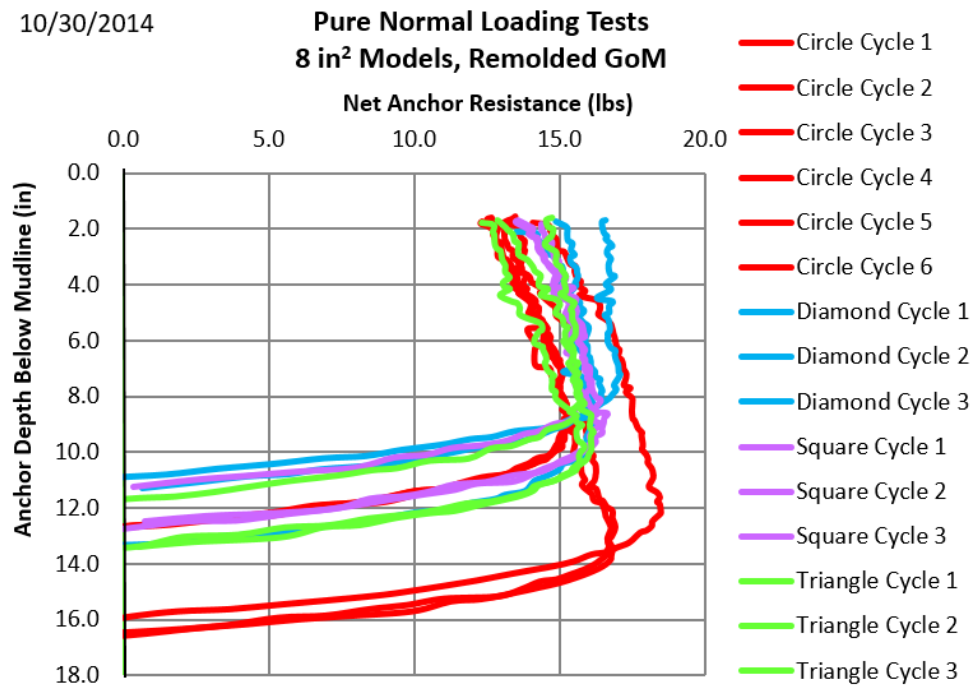
Figure A.50: Pure normal loading test results (10/30/214)

Test Performed on 02/10/2015 & 02/17/2015

- Aluminum anchor models, geometries: Square- Circle- Triangle- Diamond

- 6 degrees of freedom behavior (pitch and roll loading directions are same for square and circle models, only tested for one)

- Thickness: 0.5 in.

- Specific Gravity of Aluminum: 2.55-2.8

- Fluke Area: 16 in2

- Gs,Gulf of Mexico: 2.75 water content: 90 %

- Saturated unit weight: 94pcf

- Soil depth : 20 in.

- Anchor model weights: 0.80-0.83 lbs

261

Figure A.51: Undrained shear strength profile of the test bed (02/10/2015)

Figure A.52: Pure normal loading test results (2/10/2015)
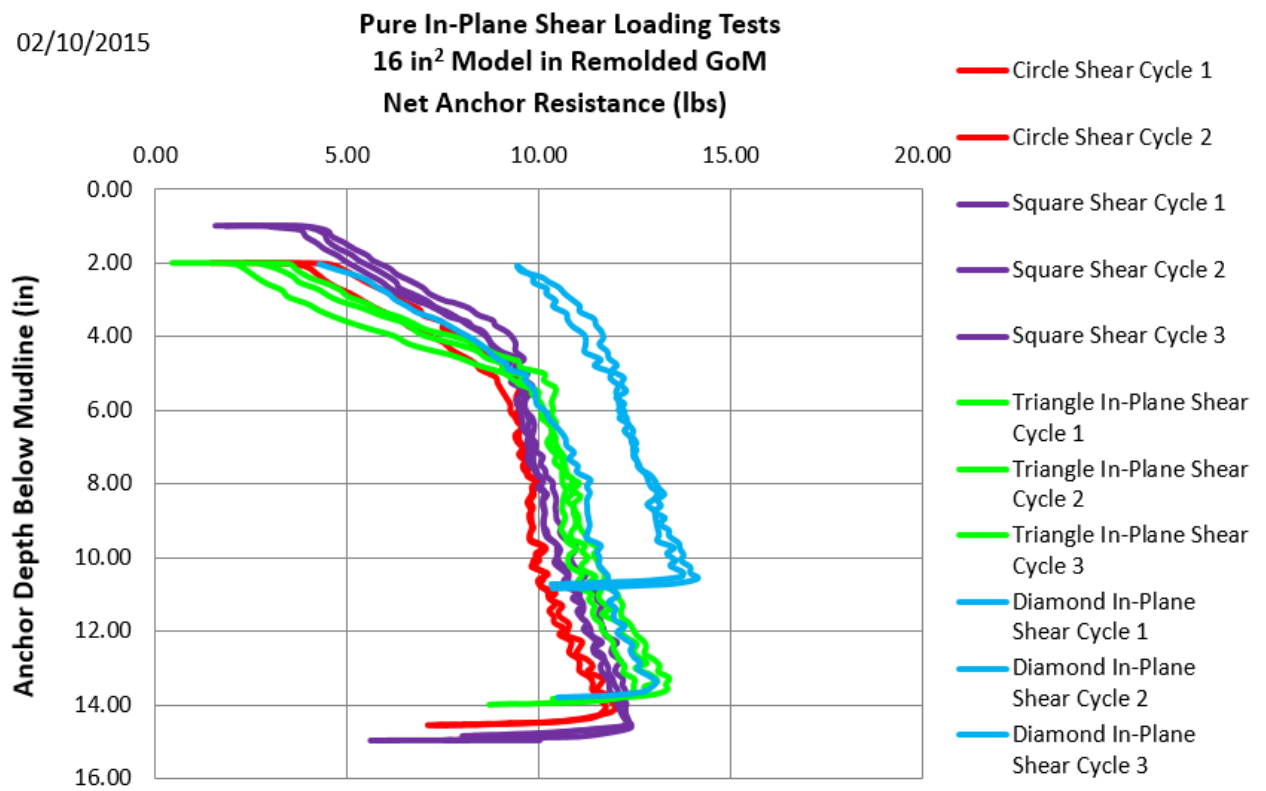
Figure A.53: Pure in-plane shear loading test results (02/10/2015)

Figure A.54: Pure out-of-plane shear loading test results (02/10/2015)

Pure Rotational Loading-Pitch and Roll Test
16 in² Model in Remolded GoM

Legend:
- Circle Pitch and Roll Cycle 1
- Circle Pitch and Roll Cycle 2
- Square Pitch and Roll Cycle 1
- Square Pitch and Roll Cycle 2
- Square Pitch and Roll Cycle 3
- Diamond Pitch Cycle 1
- Diamond Pitch Cycle 2
- Diamond Roll Cycle 1
- Triangle Pitch Cycle 1
- Triangle Pitch Cycle 2
- Triangle Roll Cycle 1
- Triangle Roll Cycle 2
- Triangle Roll Cycle 3

Y-axis: Moment (in-lbs)
X-axis: Loading Line Displacement (in)

Figure A.55: Pure pitch and roll loading test results (02/10/2015)

02/17/2015
St=1 GoM

Undrained Shear Strength (psf)

Y-axis: Depth Below Mudline (in)

Legend:
- Cycle 1
- Cycle 2
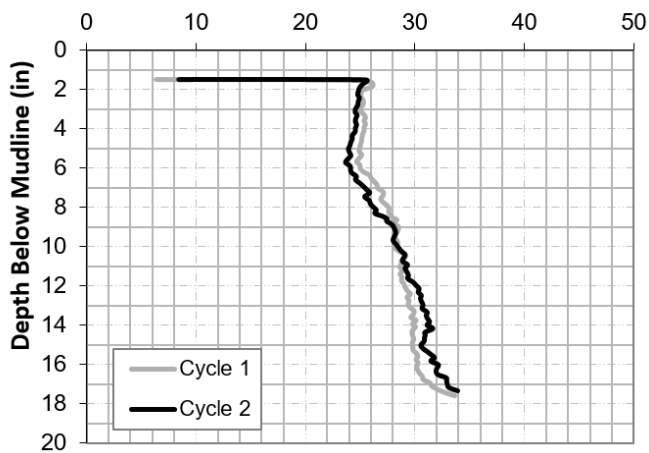
Figure A.56: Undrained shear strength profile of the test bed (2/17/2015)

02/17/2015

Pure Normal Loading Tests
16 in² Diamond, Remolded GoM

Net Anchor Resistance (lbs)
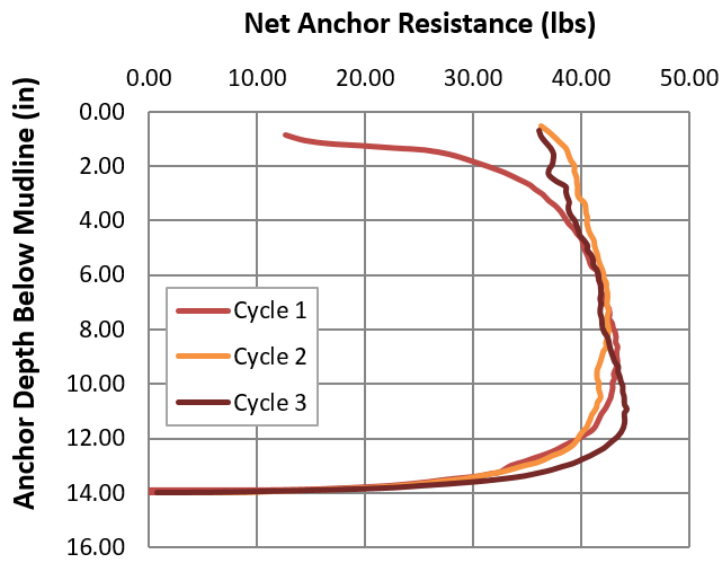
Figure A.57: Pure normal loading test results (02/17/2015)

02/17/2015

Pure In Plane Shear Loading Tests
16 in² Diamond in Remolded GoM

Net Anchor Resistance (lbs)
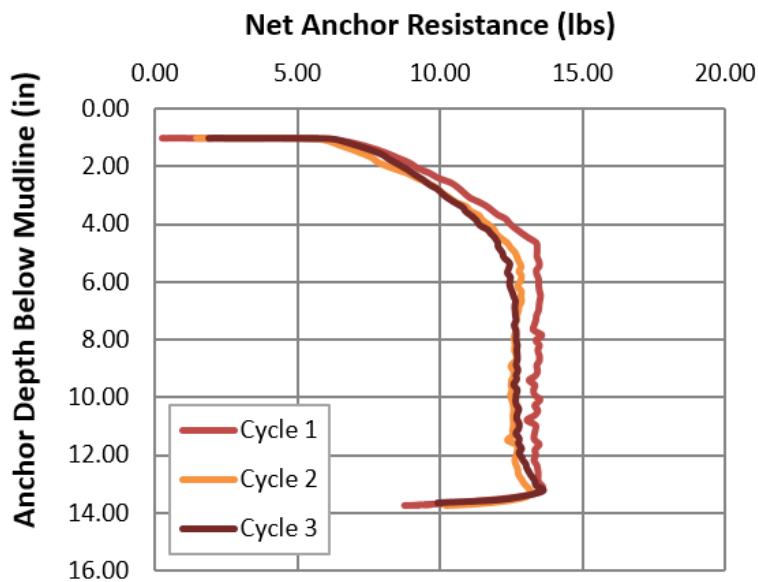
Figure A.58: Pure in-plane shear loading test results (02/17/2015)

266
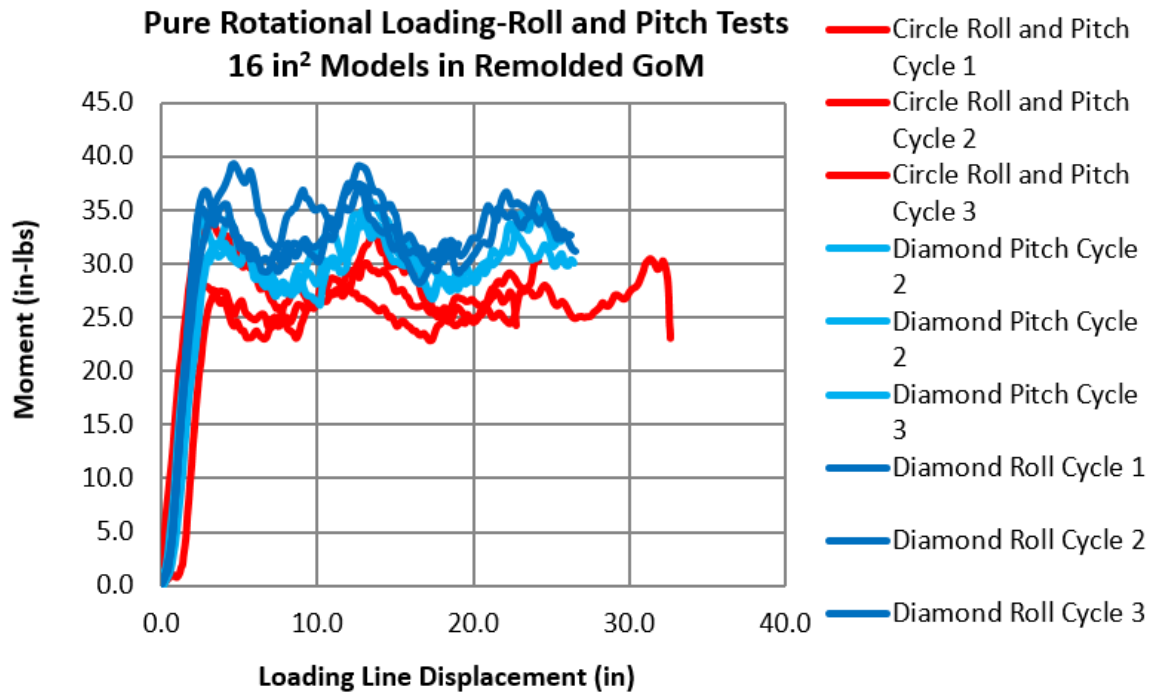
Figure A.59: Pure roll and pitch loading test results (02/17/2015)
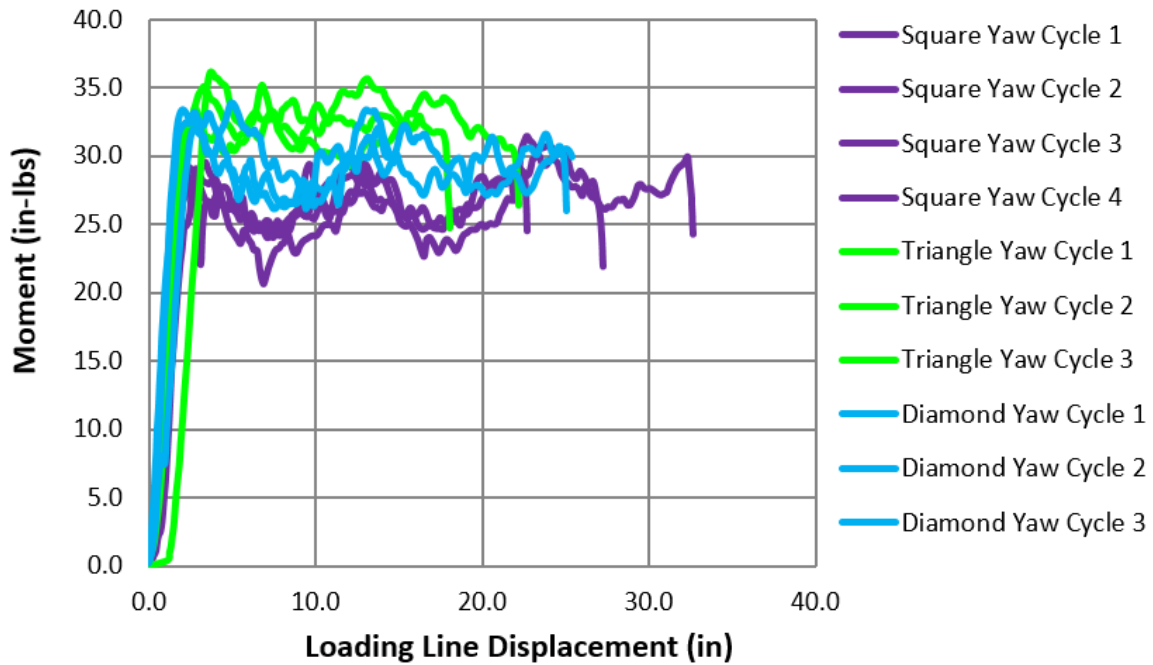
Figure A.60: Pure yaw loading test results (02/17/2015)

Test Performed on 07/22/2015

- Aluminum anchor models

- 6 degrees of freedom behavior

- Thickness: 0.5 in.

- Specific Gravity of Aluminum: 2.55-2.8

- Fluke Area: 16 in^2

- Gs, Gulf of Mexico: 2.75 water content: 92 % , saturated unit weight: 95 pcf

- Soil depth: 24 in.

- Anchor model weights: 0.80-0.83 lbs

- Geometries: Square- Circle- Triangle- Diamond
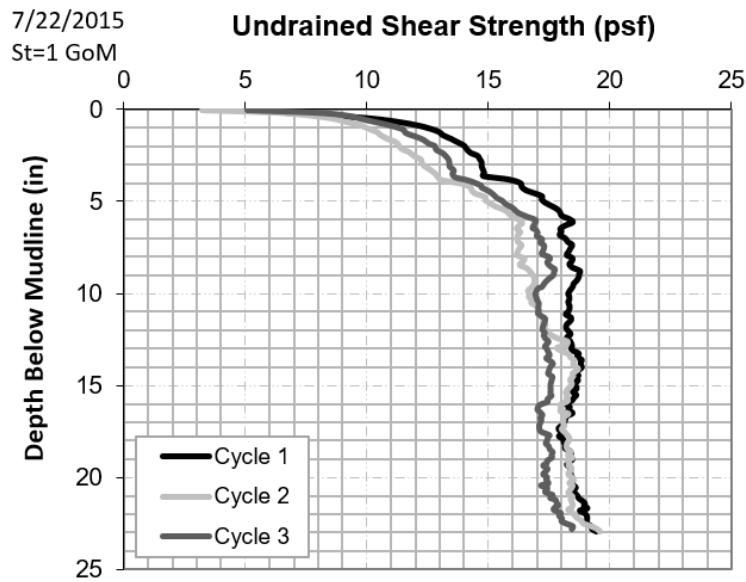
Figure A.61: Undrained shear strength profile of the test bed (7/22/2015)
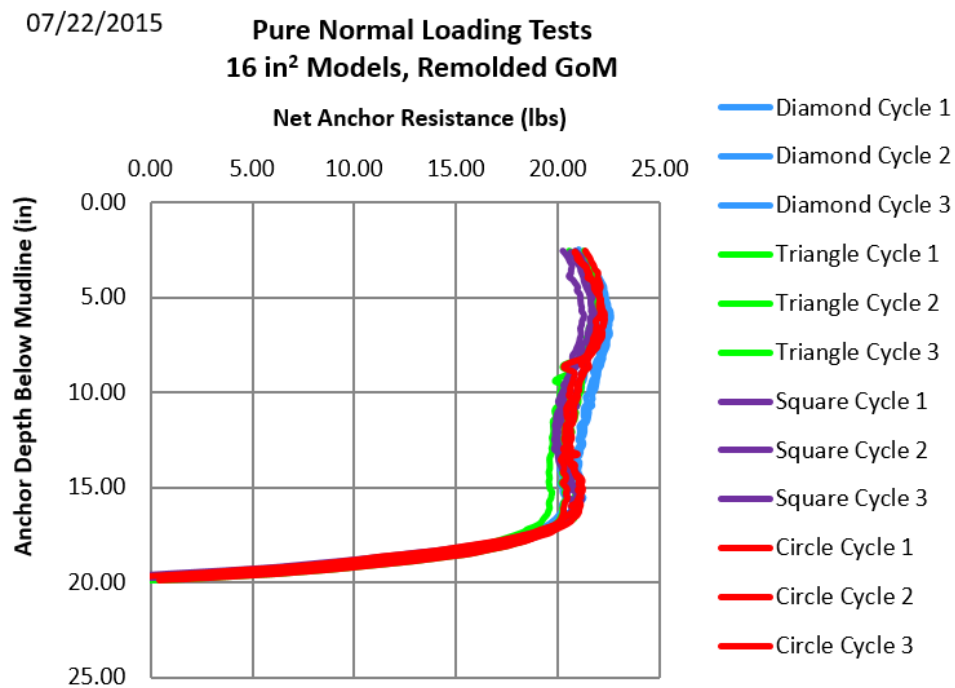
Figure A.62: Pure roll and pitch loading test results (07/22/2015)

269
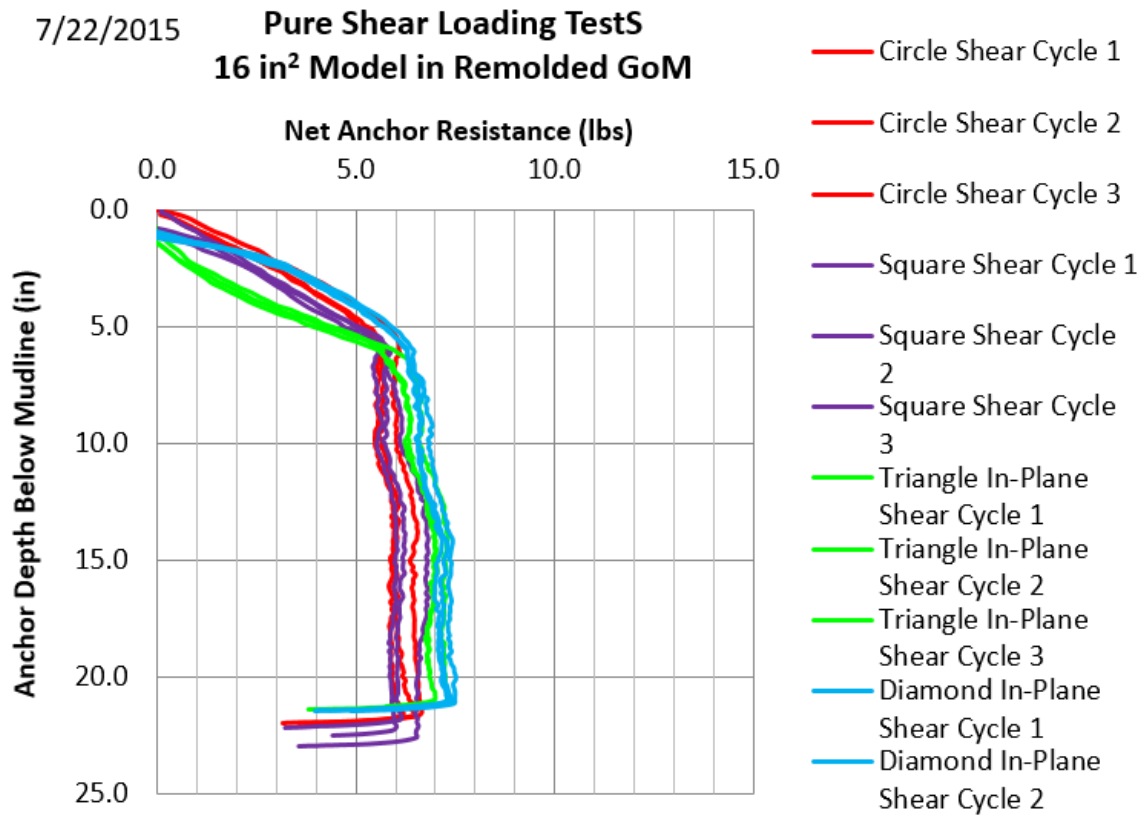
Figure A.63: Pure in-plane shear loading test results (07/22/2015)
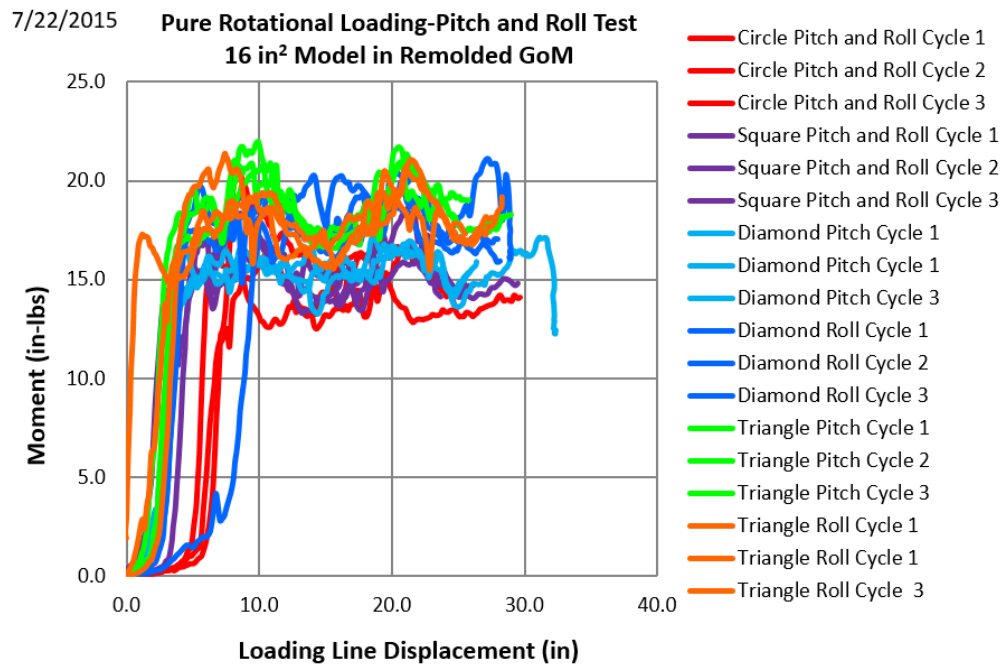
Figure A.64: Pure pitch and roll loading test results (07/22/2015)
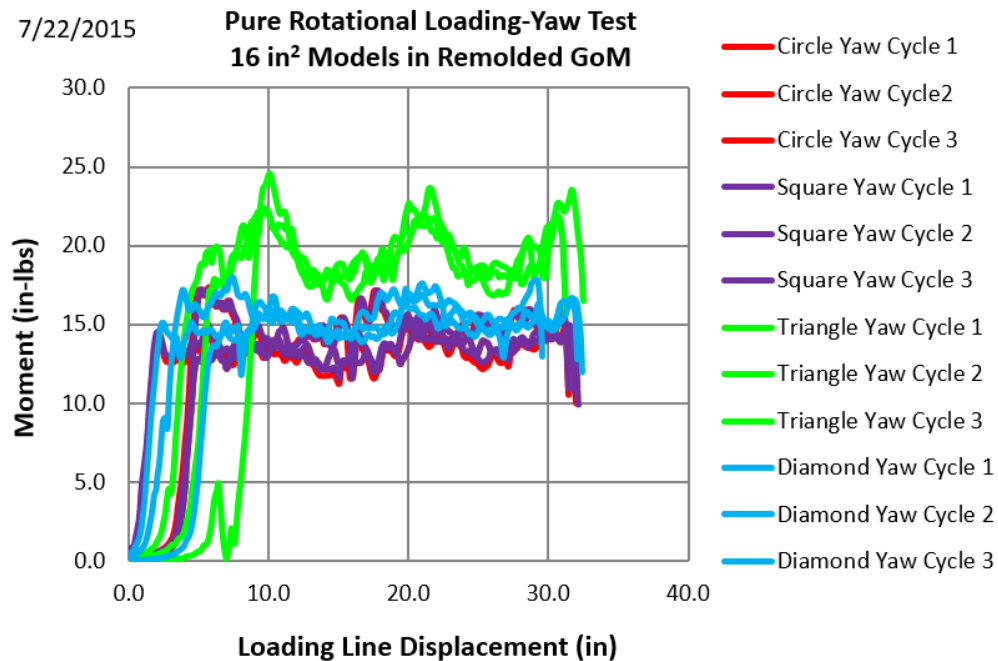
Figure A.65: Pure yaw loading test results (07/22/2015)

271

Pure Loading Yield Threshold Tests, Acrylic Diamond Anchor
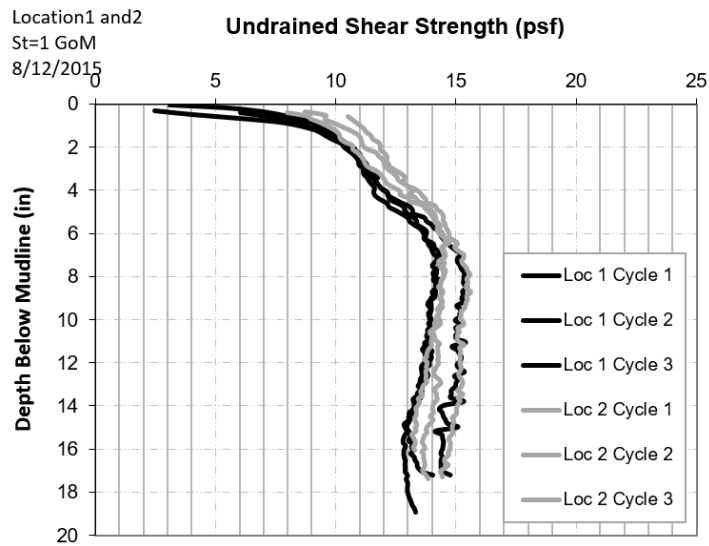
Figure A.66: Undrained shear strength profile of the test bed (8/12/2015)
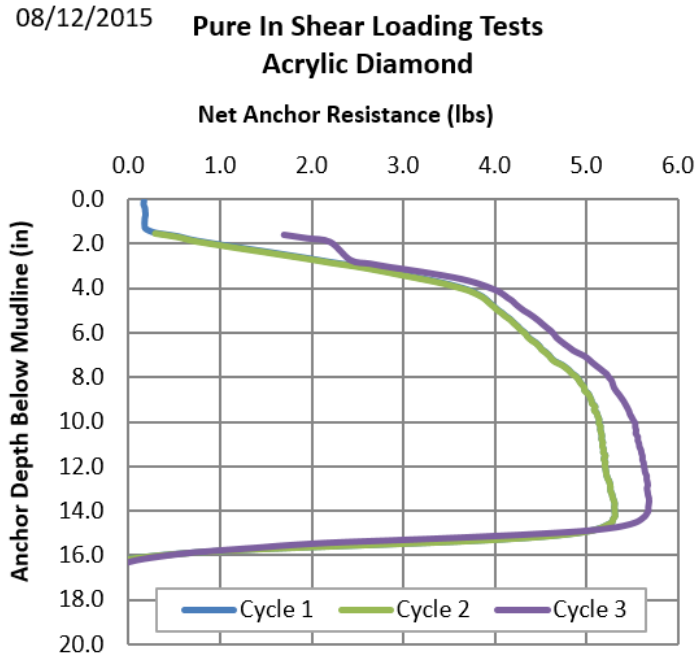
Figure A.67: Pure in-plane shear loading of Diamond Flying Wing Anchor®
(08/12/2015)
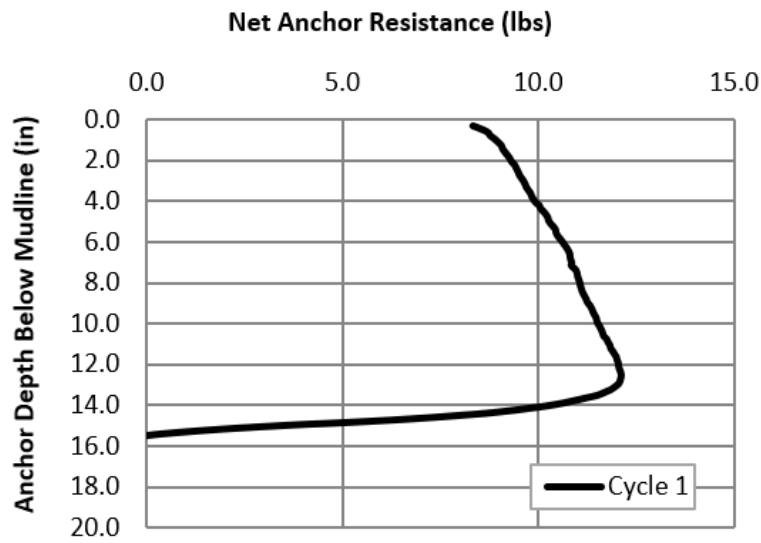
Figure A.68: Pure normal loading of Diamond Flying Wing Anchor® (08/12/2015)

Pure Loading Yield Threshold Tests, Paloma Anchor
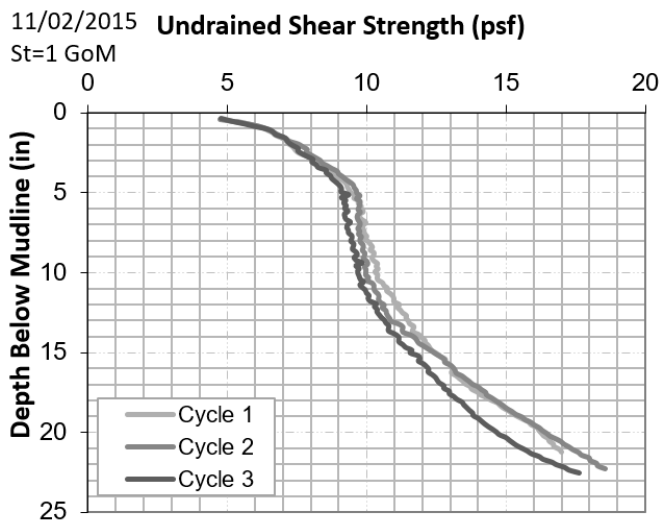
Figure A.69: Undrained shear strength profile of the test bed (11/02/2015)

273
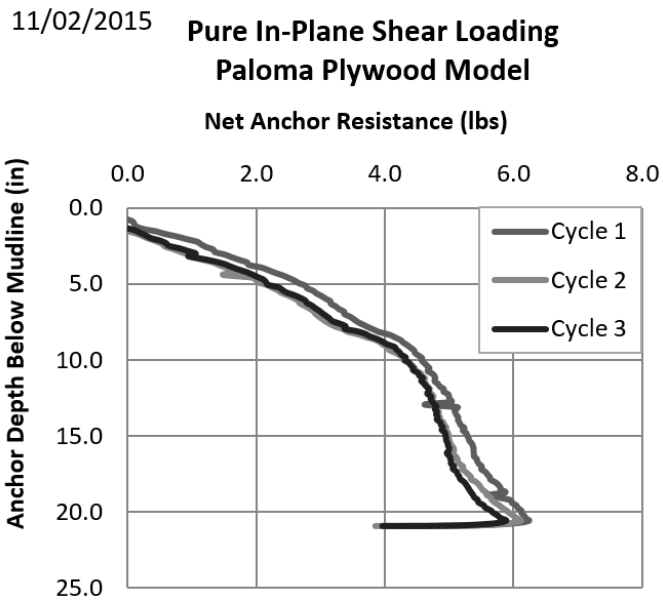
Figure A.70: Pure in-plane shear loading of Paloma Flying Wing Anchor®, plywood model (11/02/2015)
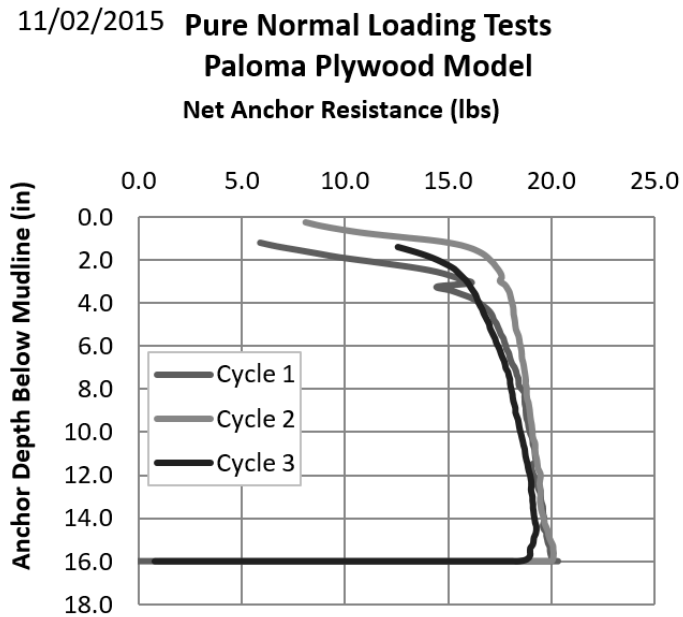
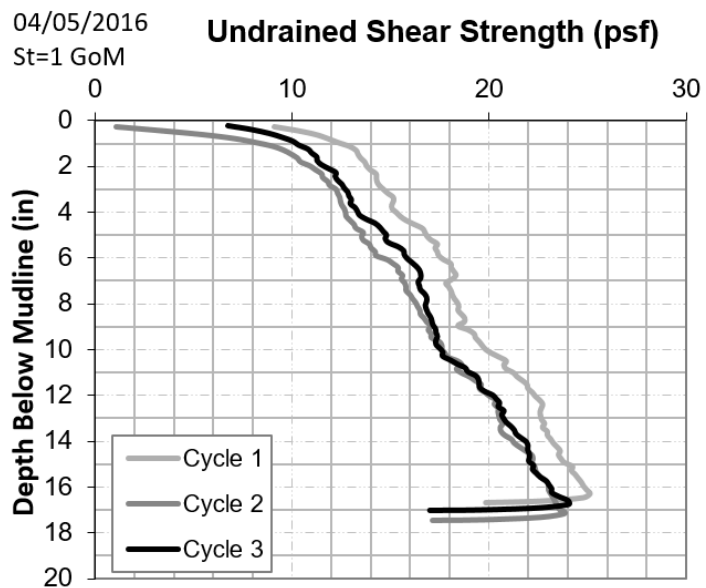Figure A.71: Pure normal loading of Paloma Flying Wing Anchor®, plywood model (11/02/2015)

274
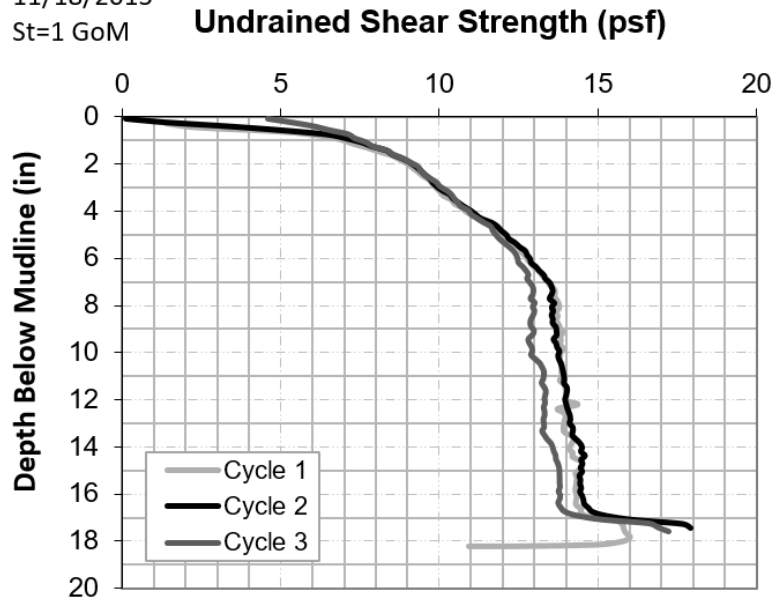
Figure A.72: Undrained shear strength profile of the test bed (11/18/2015)
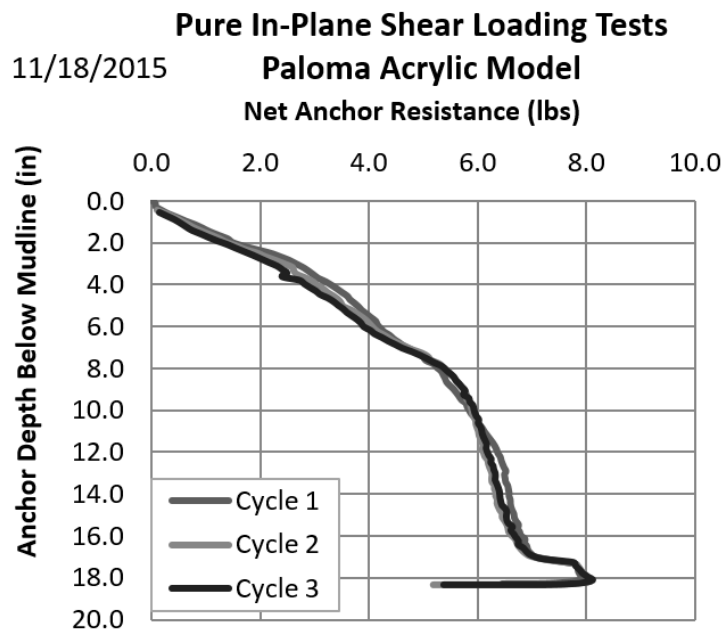
Figure A.73: Pure in-plane shear loading of Paloma Flying Wing Anchor®, acrylic model (11/18/2015)

Figure A.74: Pure normal loading of Paloma Flying Wing Anchor®, acrylic model (11/18/2015)
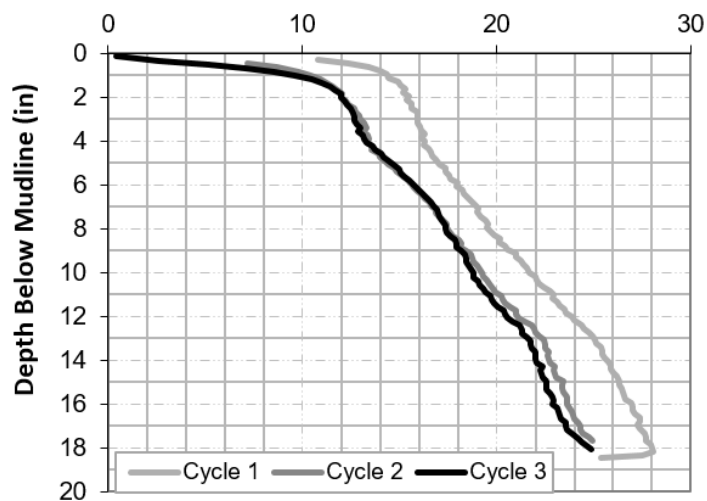
Figure A.75: Undrained shear strength profile of the test bed (01/26/2016)

276

Pure In-Plane Shear Loading Tests
Paloma Acrylic Model without Shank and Coupling Mechanism
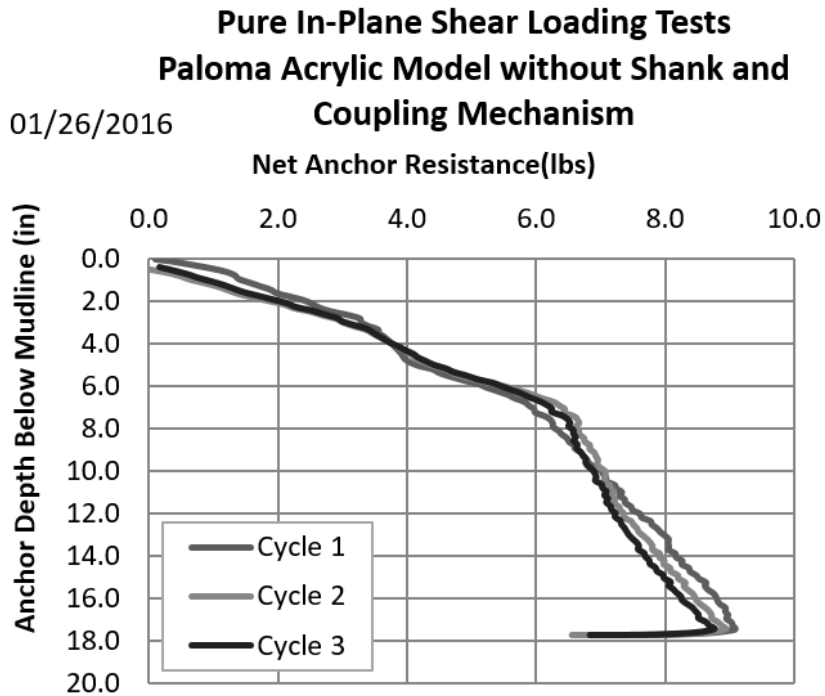
01/26/2016

Figure A.76: Pure in-plane shear loading of Paloma Flying Wing Anchor®, acrylic model without shank and coupling mechanism (01/26/2016)

Pure Loading Yield Threshold Tests, Speedy Anchor with Triangular and Elliptical Fins

Figure A.77: Speedy anchor model with triangular and elliptical fins

277
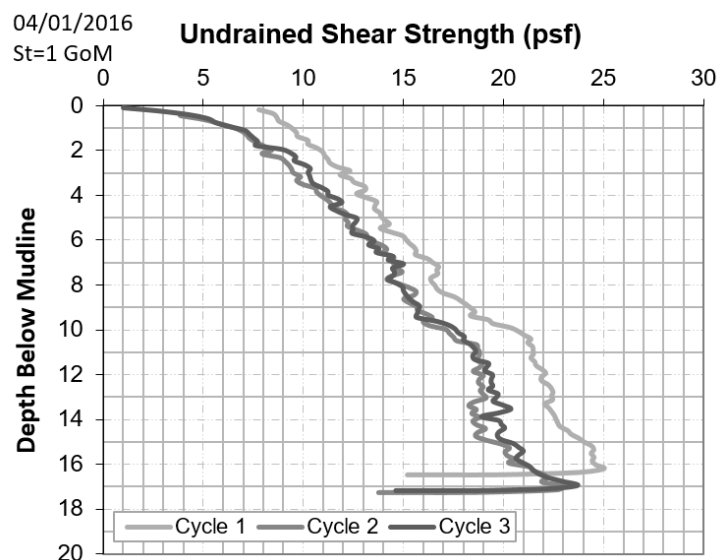
Figure A.78: Undrained shear strength profile of the test bed (4/1/2016)
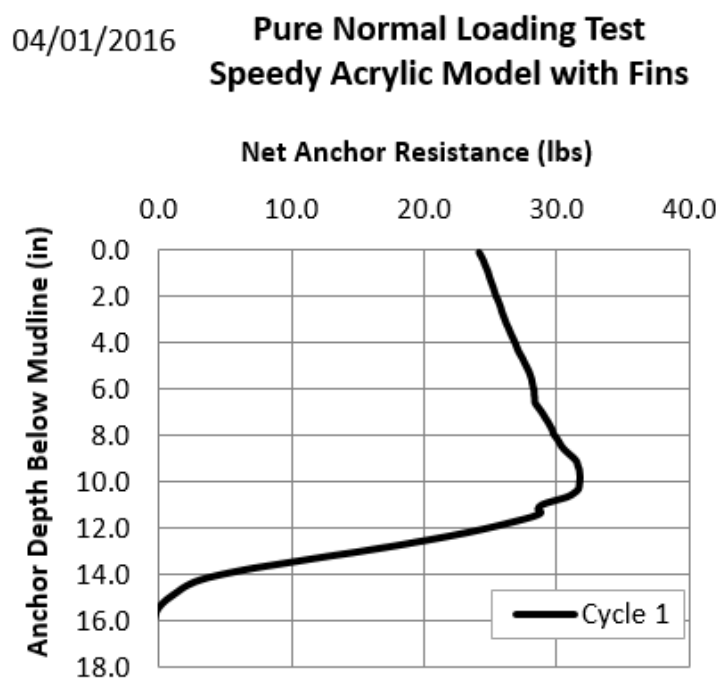
Figure A.79: Pure normal loading of Speedy Flying Wing Anchor®, acrylic model with fins (04/01/2016)
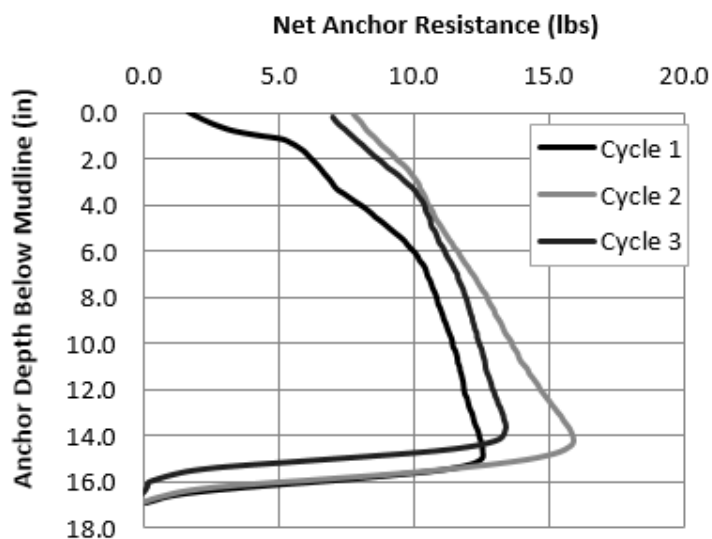
Figure A.80: Pure in-plane shear loading of Speedy Flying Wing Anchor®, acrylic model with fins (04/01/2016)

Pure Loading Yield Threshold Tests, Speedy Anchors with Fluke Separation Distance as Designed and Flukes Separated Further Apart
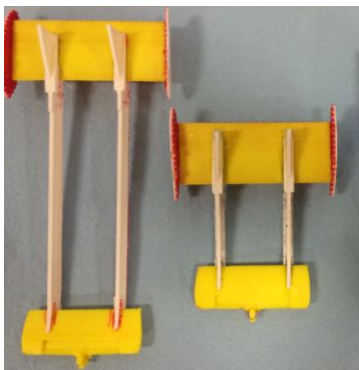
Figure A.81: Speedy anchor models with fluke separation distance as designed (right) and modified (left)

Figure A.82: Undrained shear strength profile of the test bed (4/5/2016)
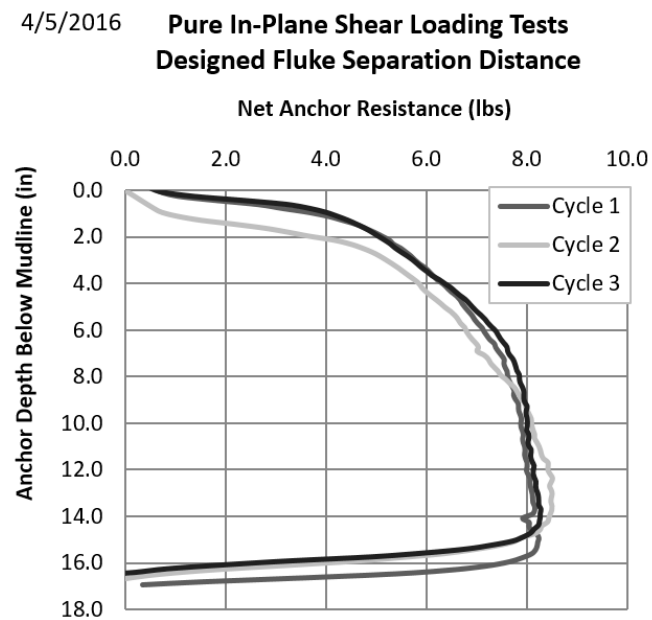
Figure A.83: Pure in-plane shear loading of Speedy Flying Wing Anchor®, fluke separation distance as designed (04/05/2016)

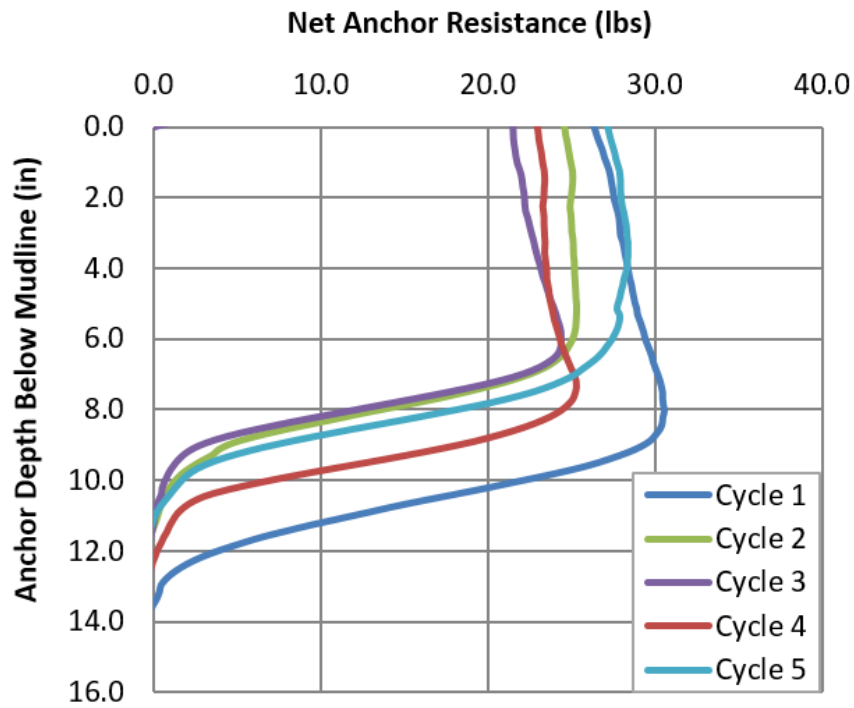**Pure Normal Loading Tests**
Designed Fluke Separation Distance

Net Anchor Resistance (lbs)
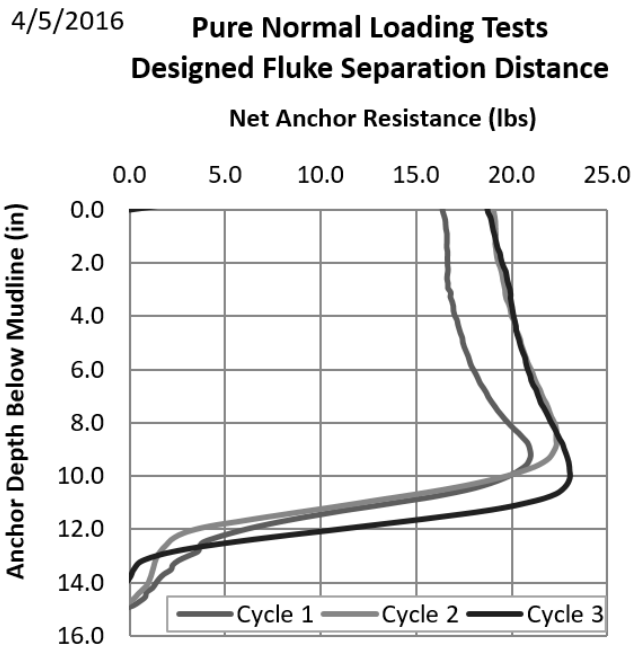
Figure A.84: Pure normal loading of Speedy Flying Wing Anchor®, fluke separation distance as designed (04/05/2016)

Pure In-Plane Shear Loading Tests
Modified Fluke Separation Distance

Net Anchor Resistance (lbs)
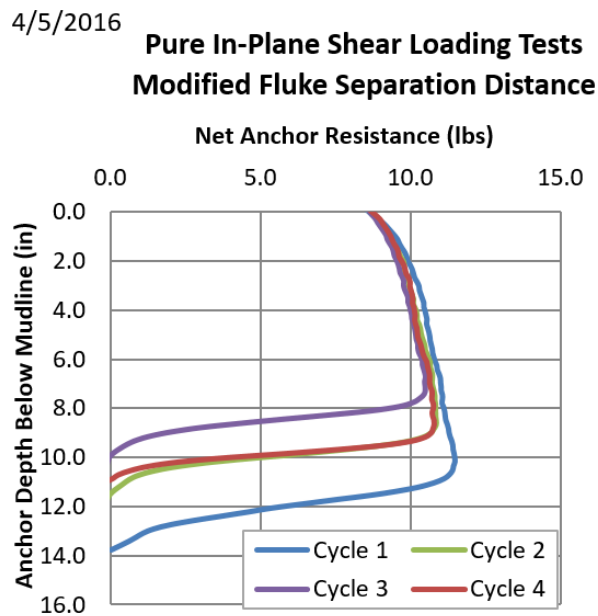
Figure A.85: Pure in-plane shear loading of Speedy Flying Wing Anchor®, fluke separation distance modified (04/05/2016)

Figure A.86: Pure normal loading of Speedy Flying Wing Anchor®, fluke separation distance modified (04/05/2016)

Pure Loading Yield Threshold Tests, Speedy Anchors without Fins
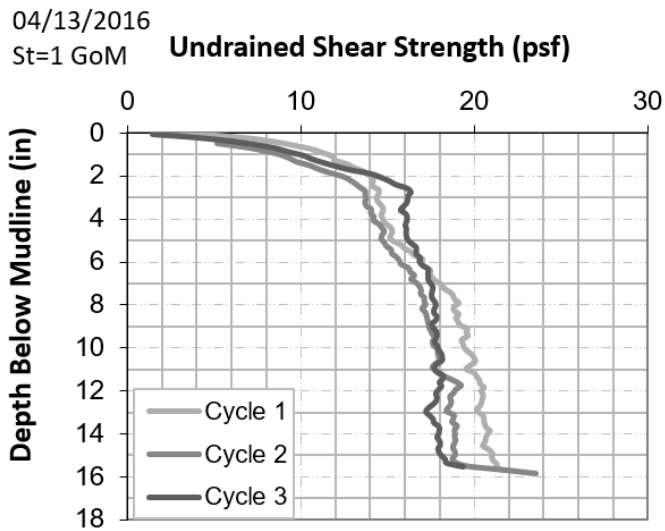
Figure A.87: Undrained shear strength profile of the test bed (4/13/2016)
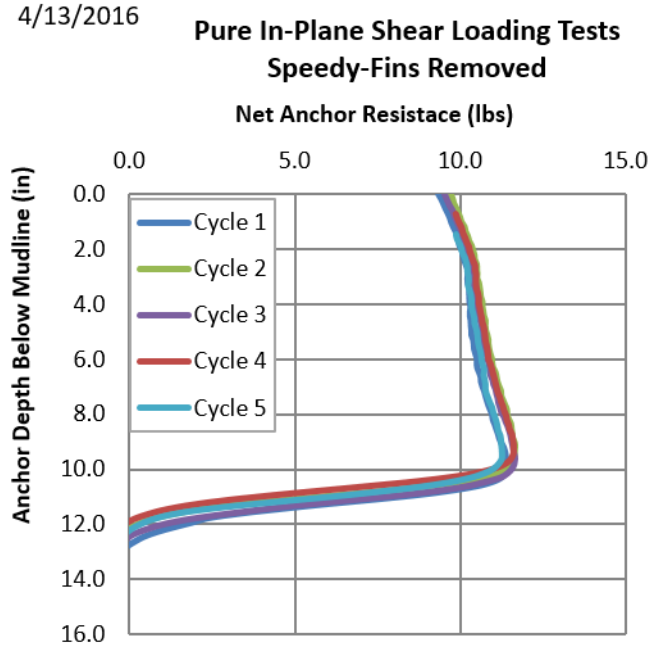
Figure A.88: Pure in-plane shear loading of Speedy Flying Wing Anchor®, without fins (04/13/2016)

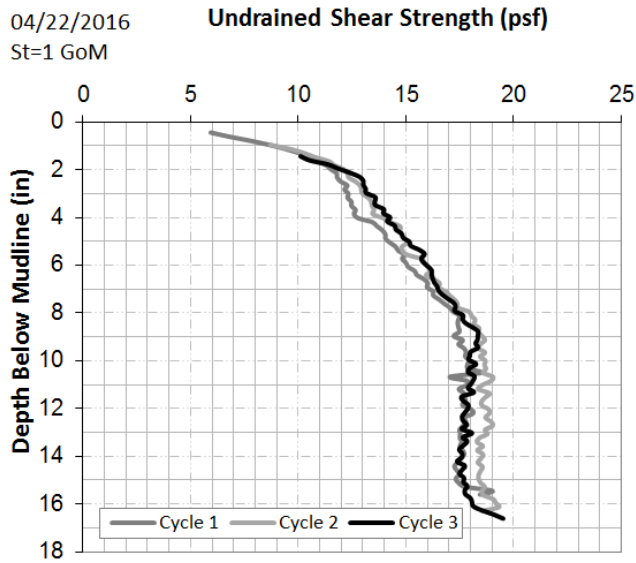*Pure Loading Yield Threshold Tests, Speedy Anchors with Modified Fins*

Figure A.89: Undrained shear strength profile of the test bed (4/22/2016)
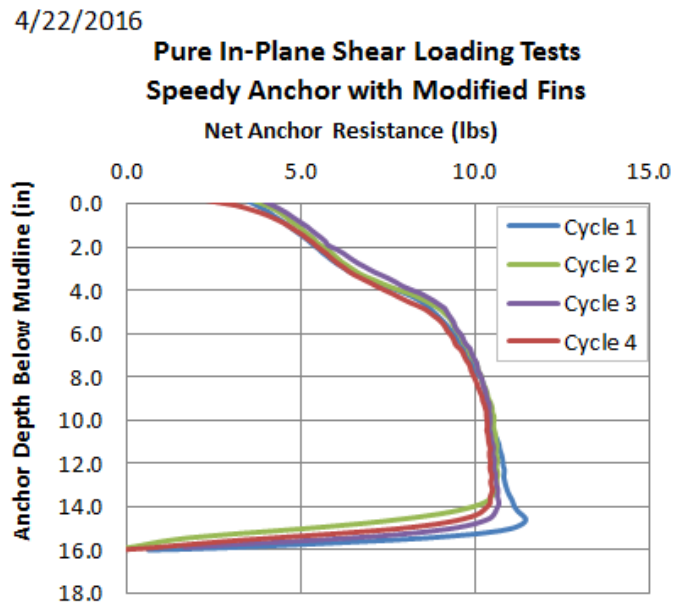

Figure A.90: Pure in-plane shear loading of Speedy Flying Wing Anchor®, with modified fins (04/22/2016)
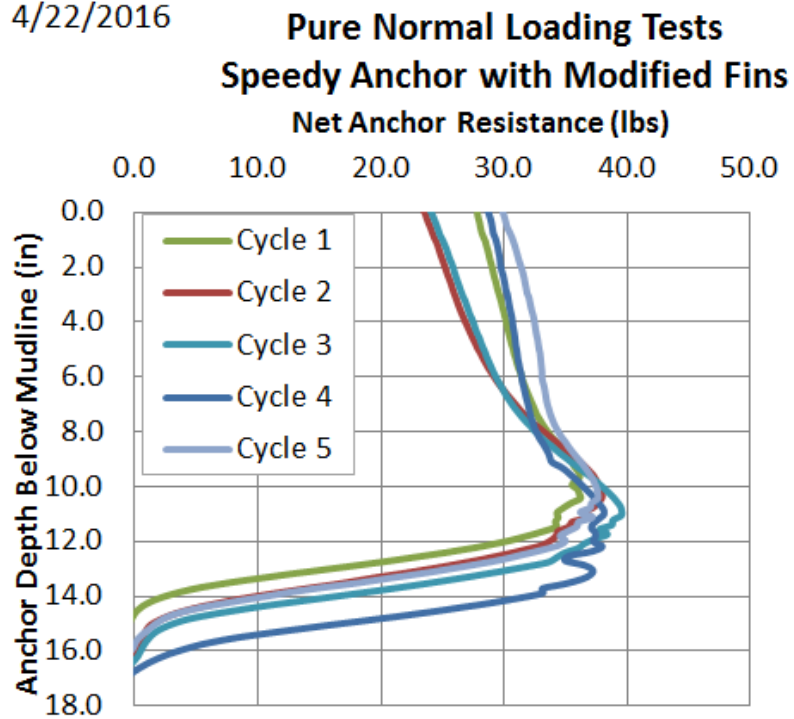
284

4/22/2016

Pure Normal Loading Tests
Speedy Anchor with Modified Fins

Figure A.91: Pure normal loading of Speedy Flying Wing Anchor®, with modified fins
(04/22/2016)

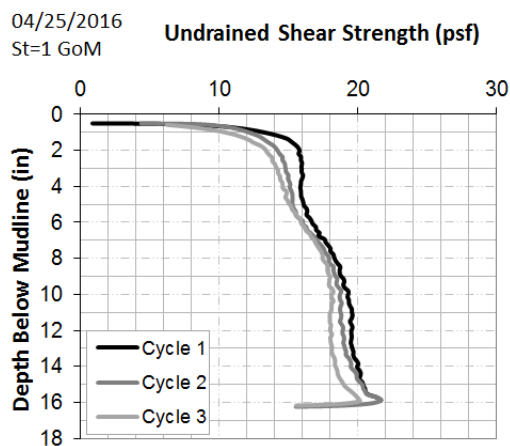*Pure Loading Yield Threshold Tests, Speedy Anchors with Smoothed Surface*

Figure A.92: Undrained shear strength profile of the test bed (4/25/2016)
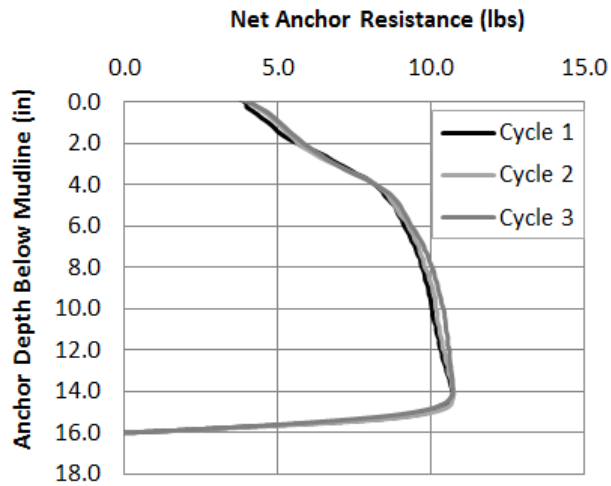
Figure A.93: Pure normal loading of Speedy Flying Wing Anchor®, with smoothed surface (04/25/2016)
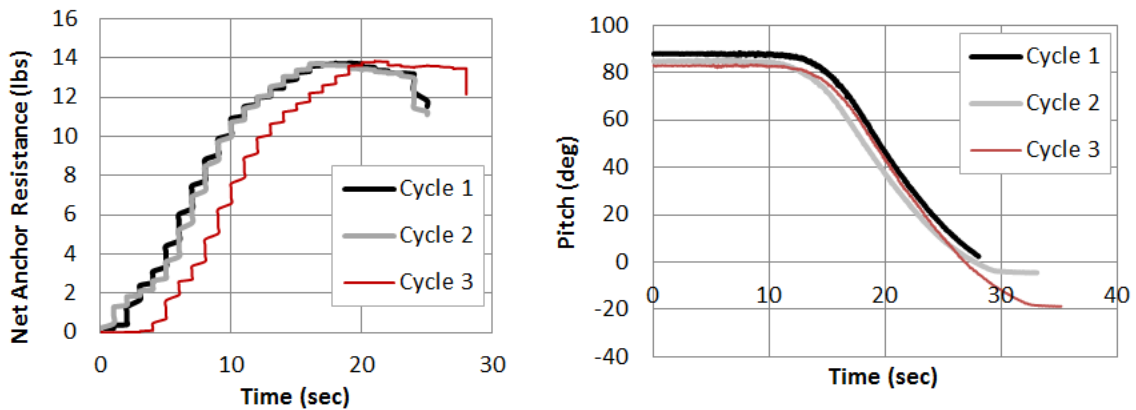

Figure A.94: Pure pitch loading of Speedy Flying Wing Anchor®, with smoothed surface (04/25/2016)

A.4 POST-YIELD MOVEMENT TESTS

This section presents the repeat tests that are performed in addition to the tests presented and discussed in the previous chapters. The undrained shear strength profile of the soil test bed, the magnetometer and load cell measurements are presented. The net anchor resistance is presented in terms of measured net resistance or the equivalent non-dimensional pure loading yield threshold (N_e). The magnetometer measurements are presented in terms of translational or rotational displacements in different directions.

A.4.1 PALOMA FLYING WING ANCHOR® POST-YIELD MOVEMENT TESTS

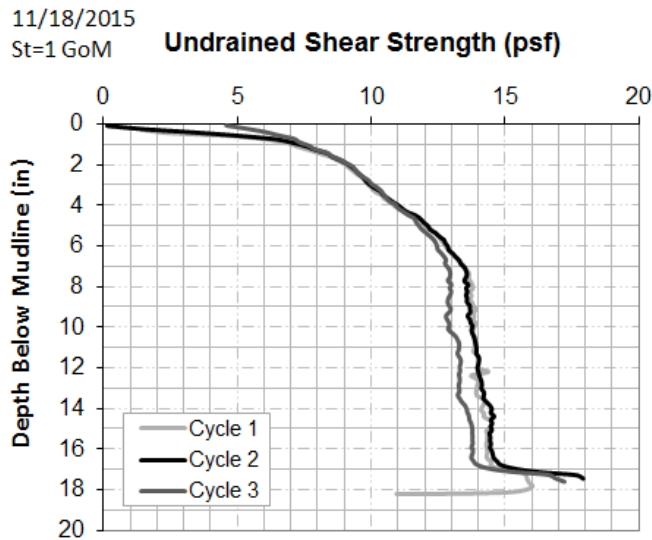*Acrylic Paloma Anchor Dive Trajectory Measurements*

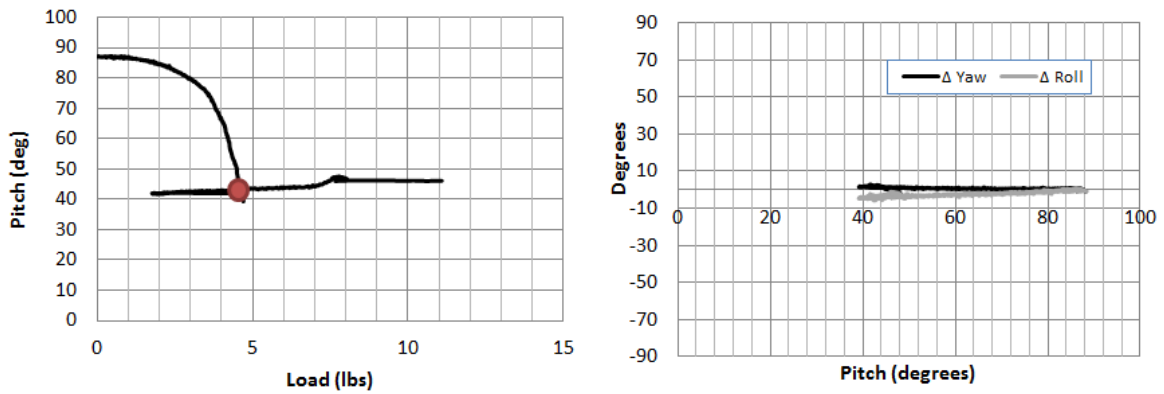Figure A.95: Undrained shear strength profile of the test bed (11/18/2015)

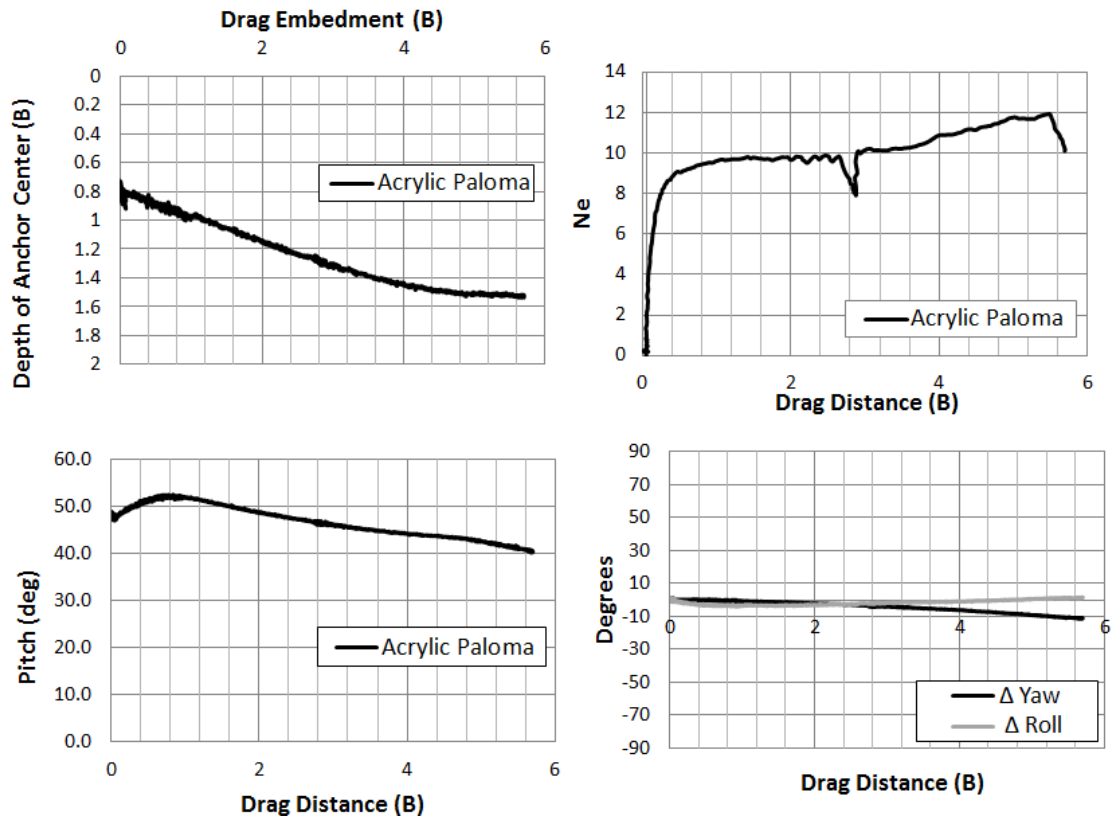Figure A.96: Acrylic Paloma anchor shank release tests (11/18/2015)

Figure A.97: Acrylic Paloma in-plane drag loading test (11/18/2015)
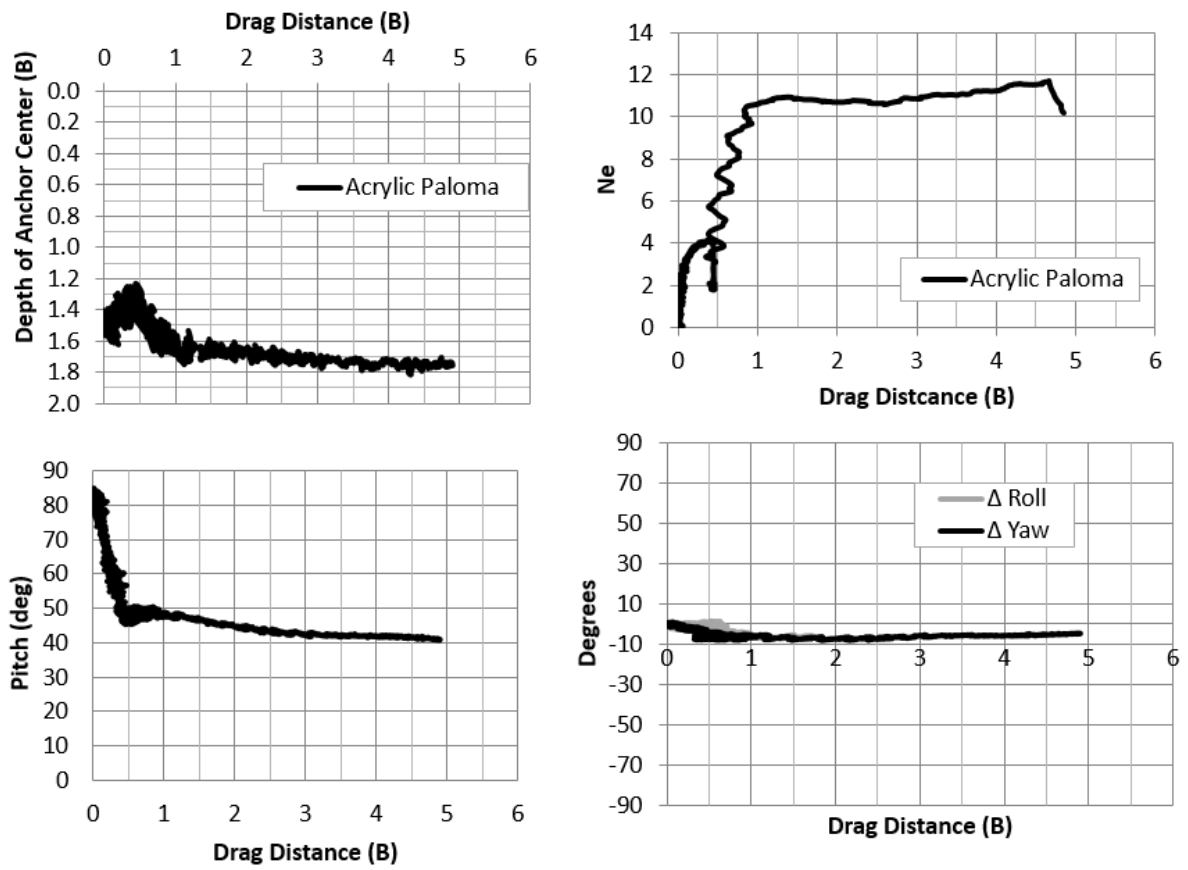
288

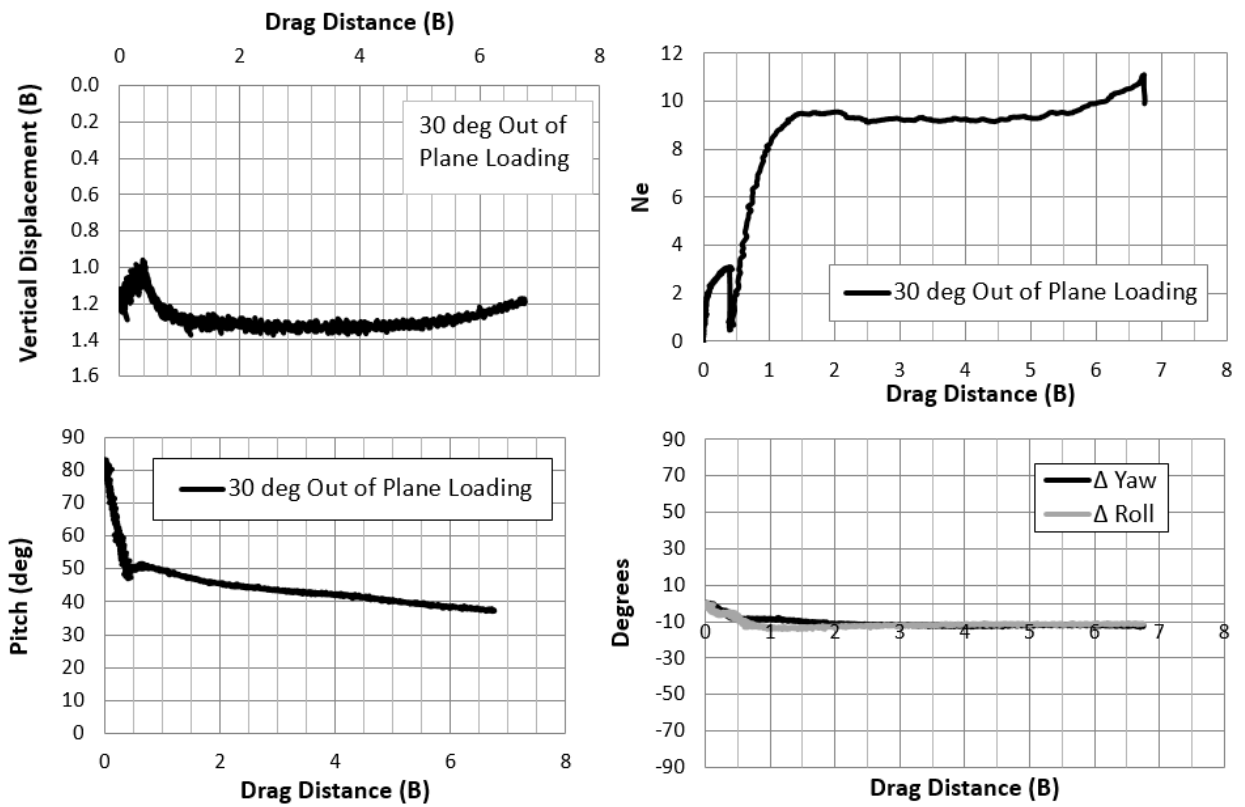Figure A.98: Acrylic Paloma in-plane drag loading repeat test (11/18/2015)

Figure A.99: Acrylic Paloma out-of-plane drag loading repeat tests (11/18/2015)

Acrylic Paloma Anchor Tests with Different Loading Rates
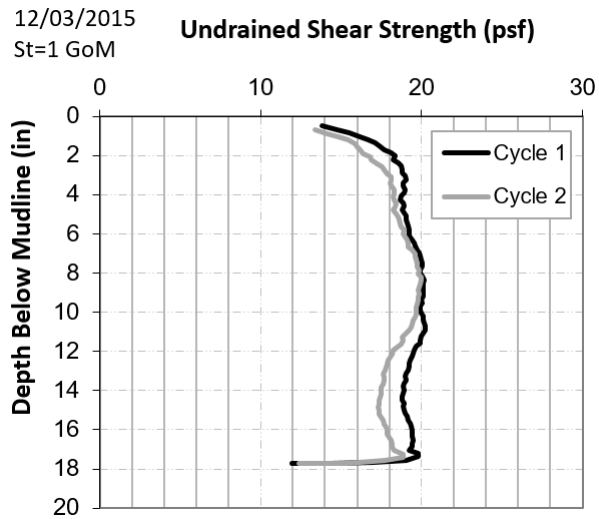
Figure A.100: Undrained shear strength profile of the test bed (12/03/2015)
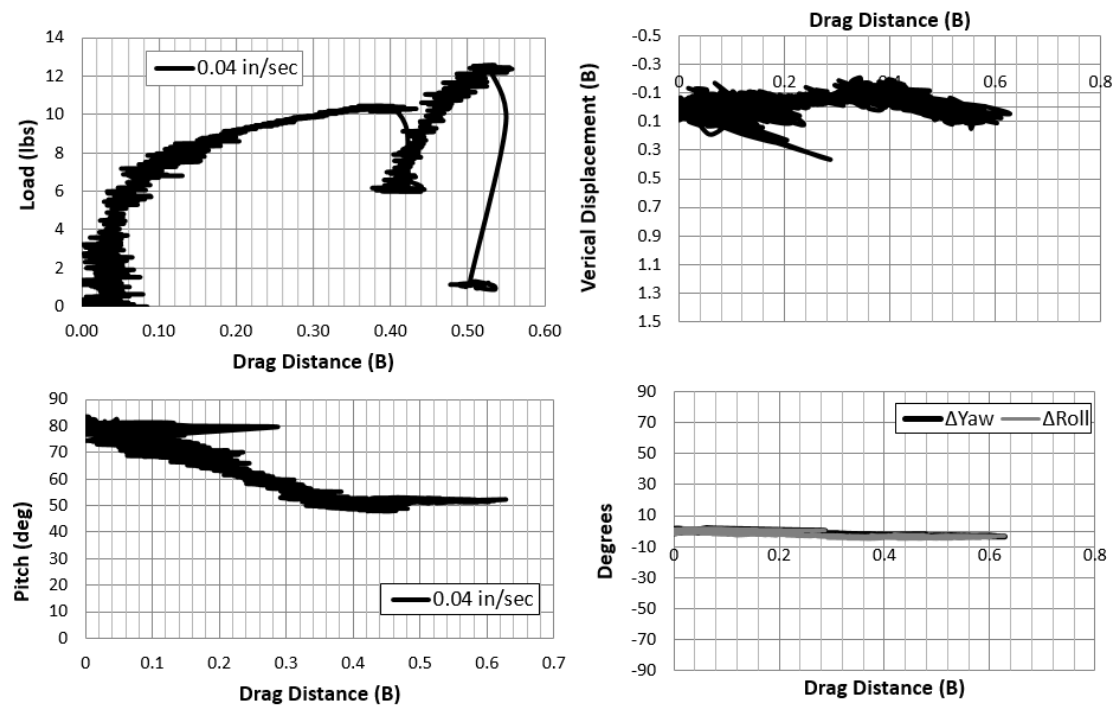
Figure A.101: continued next page.

Figure A.101: Acrylic Paloma, loading line displacement rate 0.04 in/sec test
(12/03/2015)

Figure A.102: Acrylic Paloma, loading line displacement rate 0.04 in/sec repeat test
(12/03/2015)
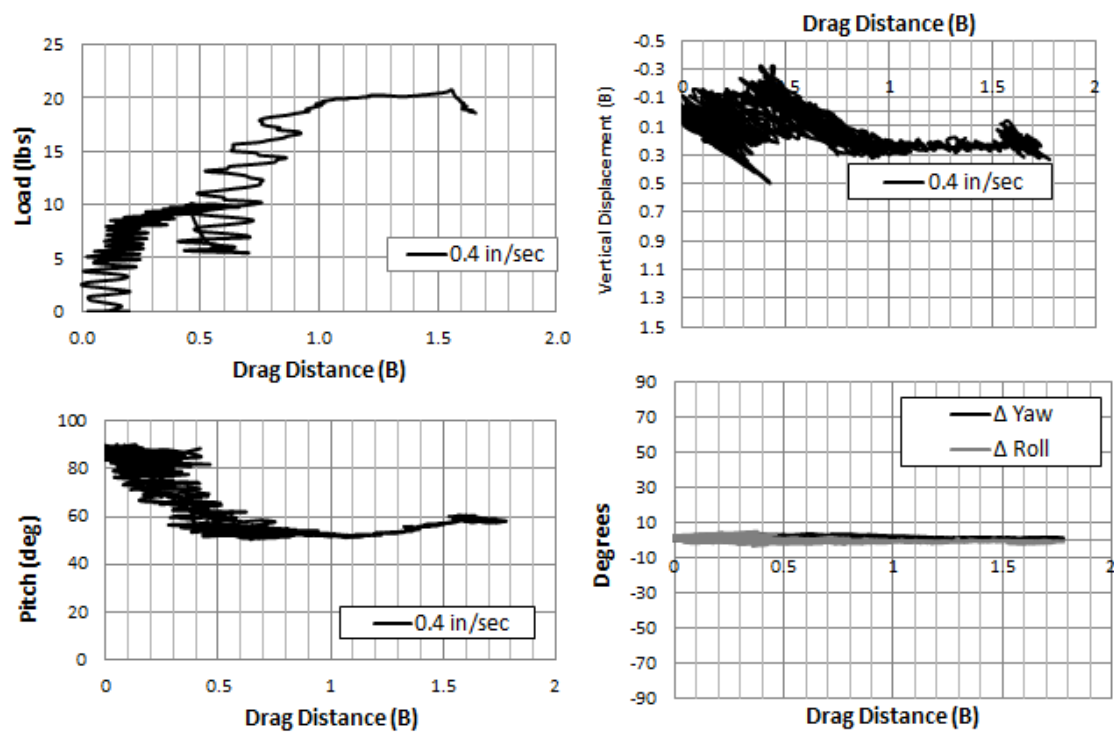
Figure A.103: Acrylic Paloma, loading line displacement rate 0.4 in/sec test (12/03/2015)
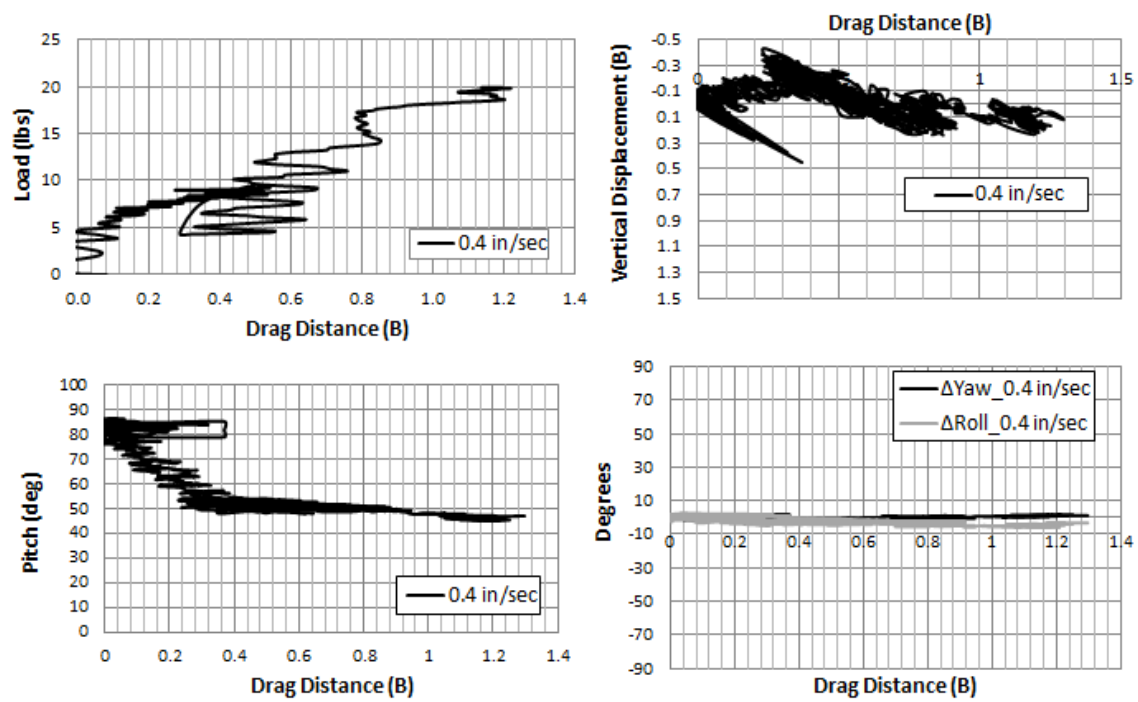
Figure A.104: Acrylic Paloma, loading line displacement rate 0.4 in/sec repeat test (12/03/2015)
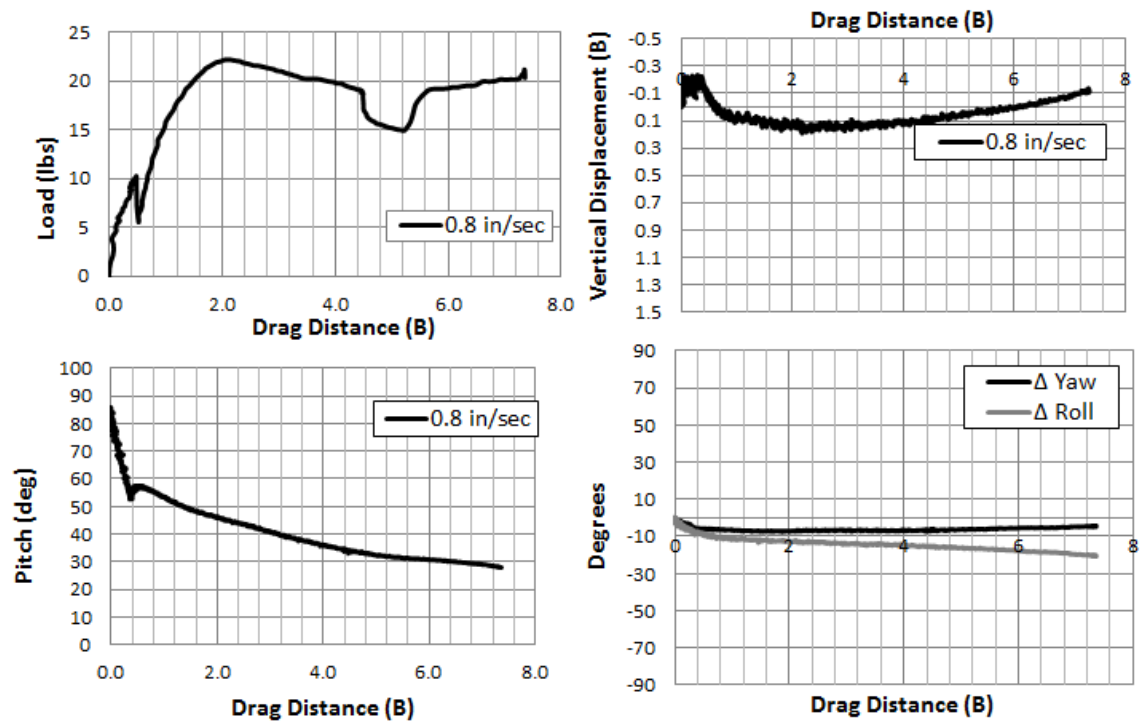
Figure A.105: Acrylic Paloma, loading line displacement rate 0.8 in/sec test (12/03/2015)
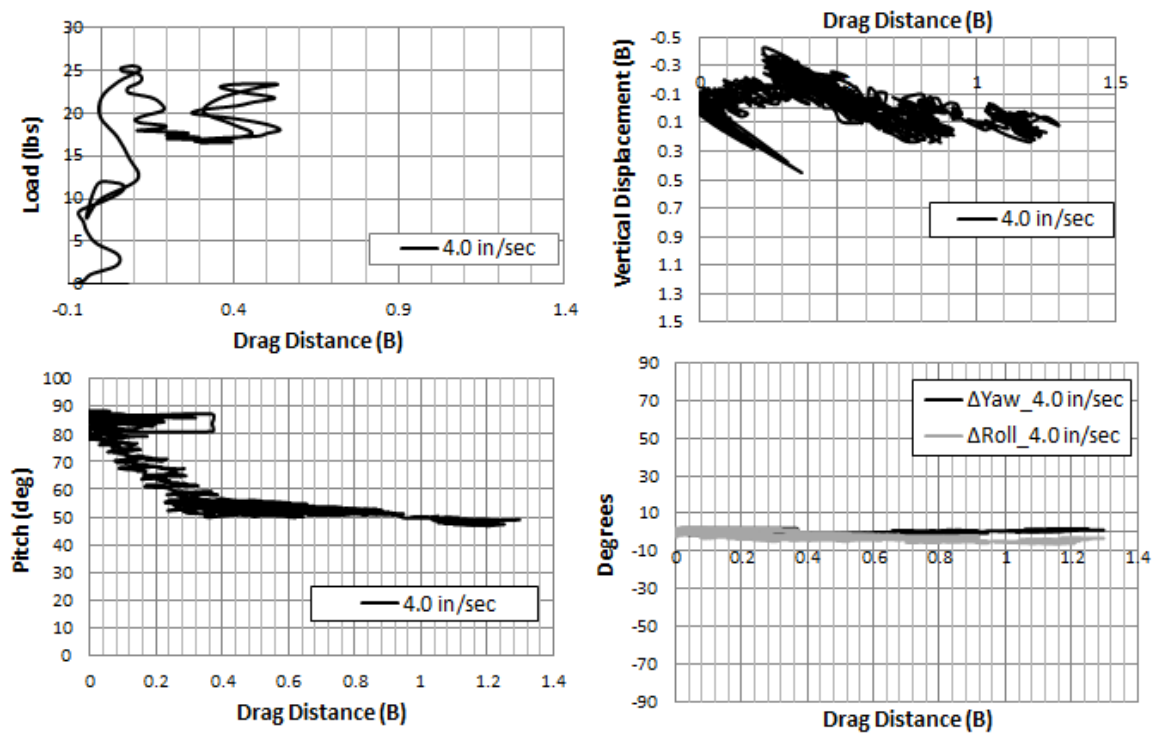
Figure A.106: Acrylic Paloma, loading line displacement rate 4.0 in/sec test (12/03/2015)
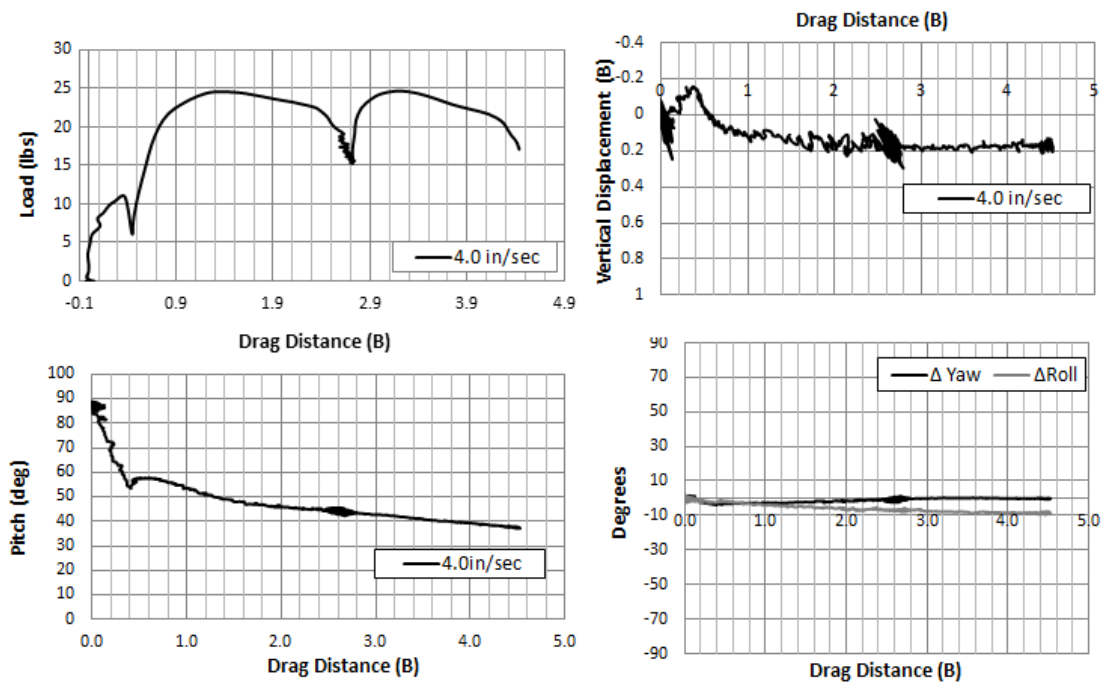
Figure A.107: Acrylic Paloma, loading line displacement rate 4.0 in/sec repeat test (12/03/2015)

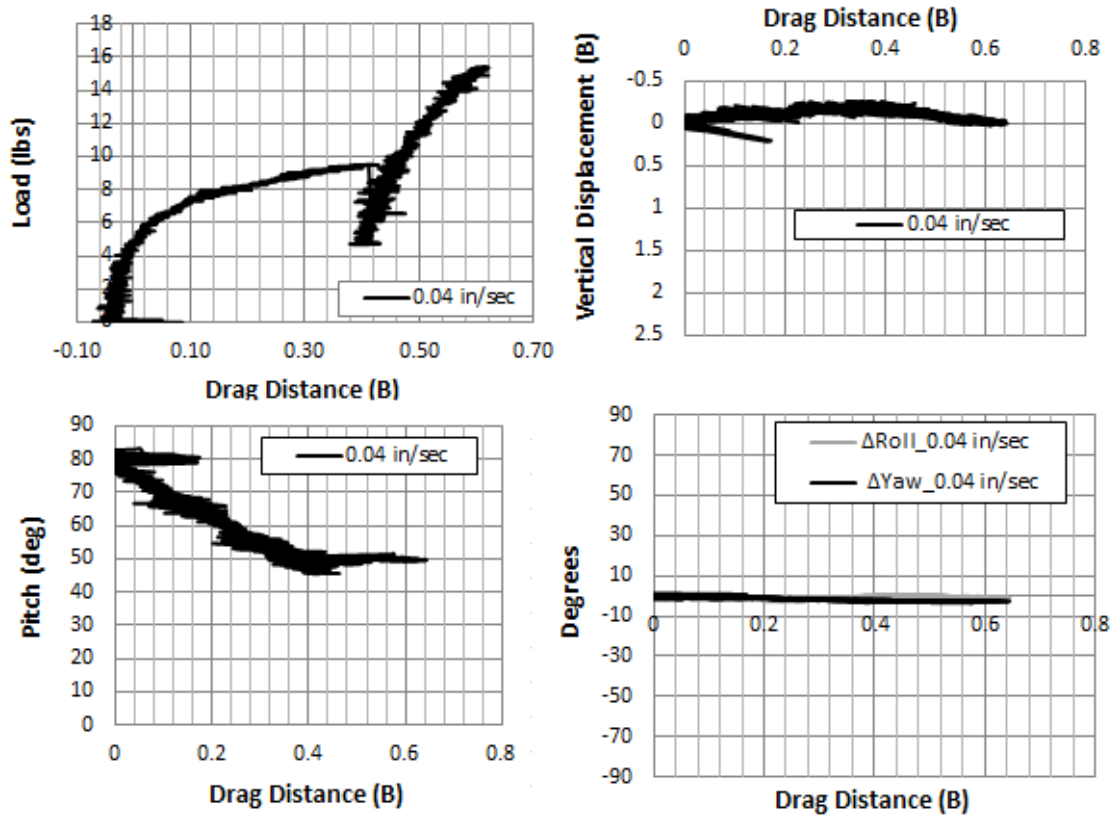## A.4.2 Speedy Flying Wing Anchor® Post-Yield Movement Tests

Acrylic Speedy Anchor Dive Trajectory Measurements
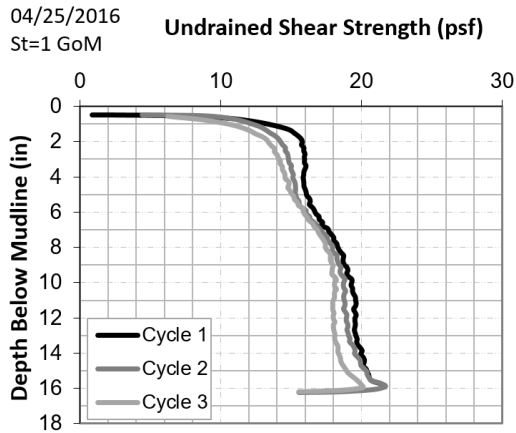
Figure A.108: Undrained shear strength profile of the test bed (4/25/2016)
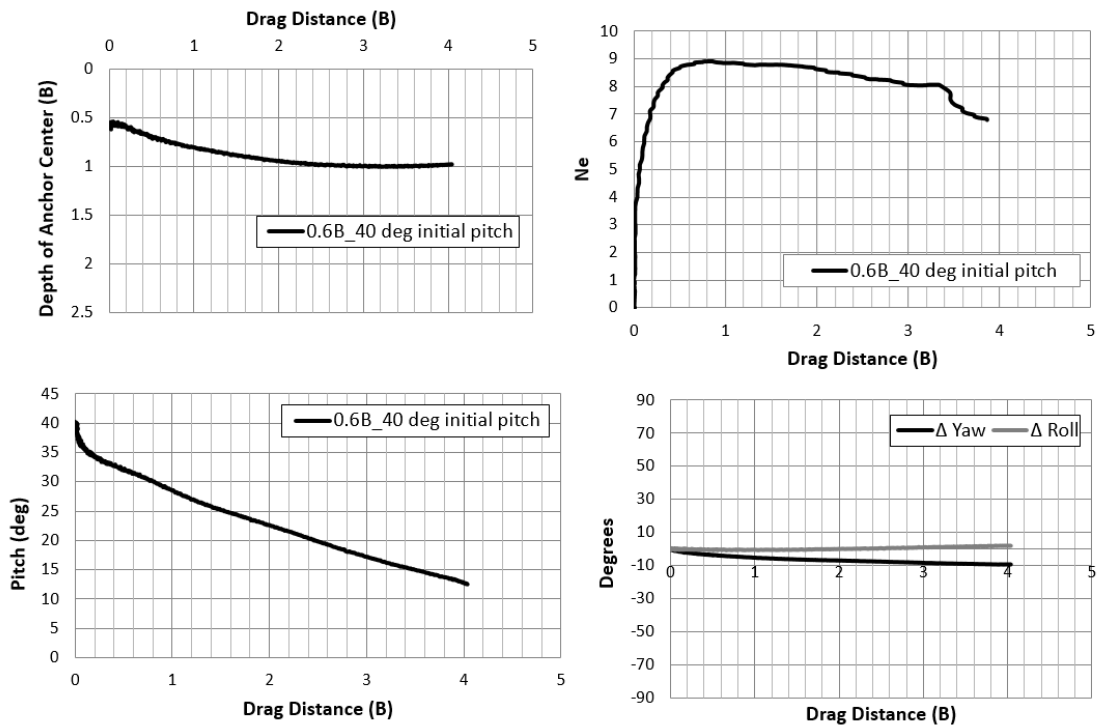
Figure A.109: Acrylic Speedy test, 0.6B initial embedment 40 deg initial pitch (4/25/16)
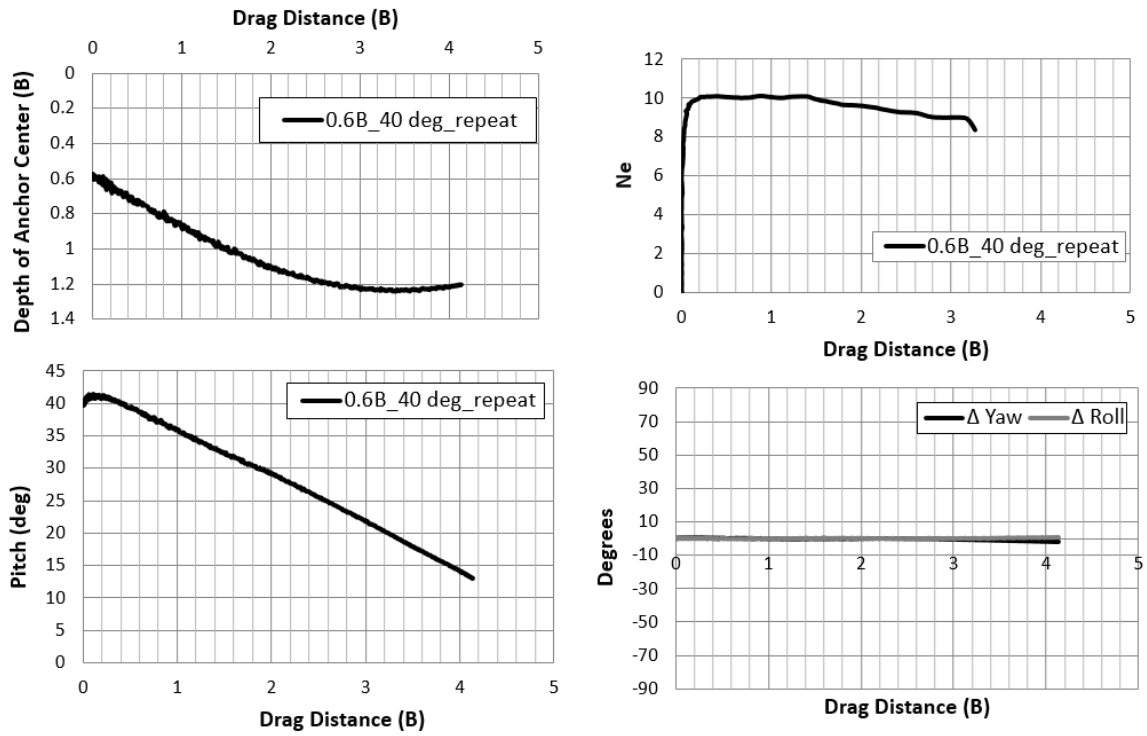
Figure A.110: Acrylic Speedy repeat test 0.6B initial embedment, 40-deg initial pitch (4/25/2016)
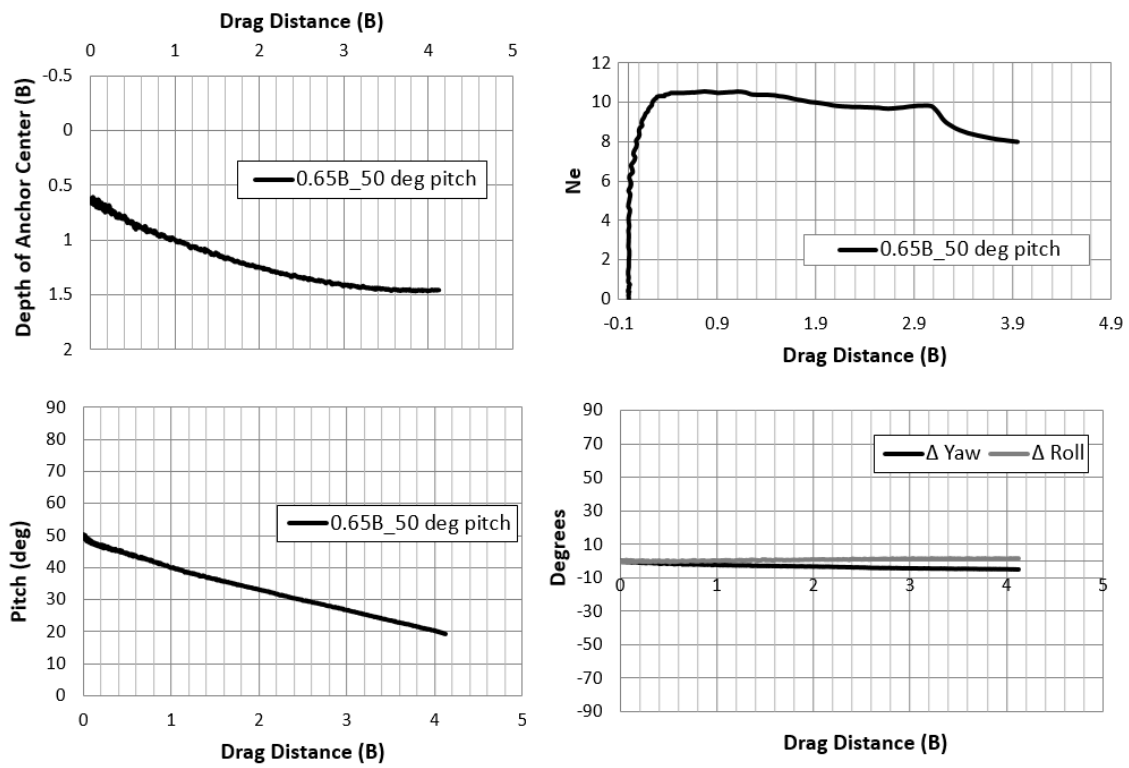
Figure A.111: Acrylic Speedy test 0.65B initial embedment, 50-deg initial pitch (4/25/2016)
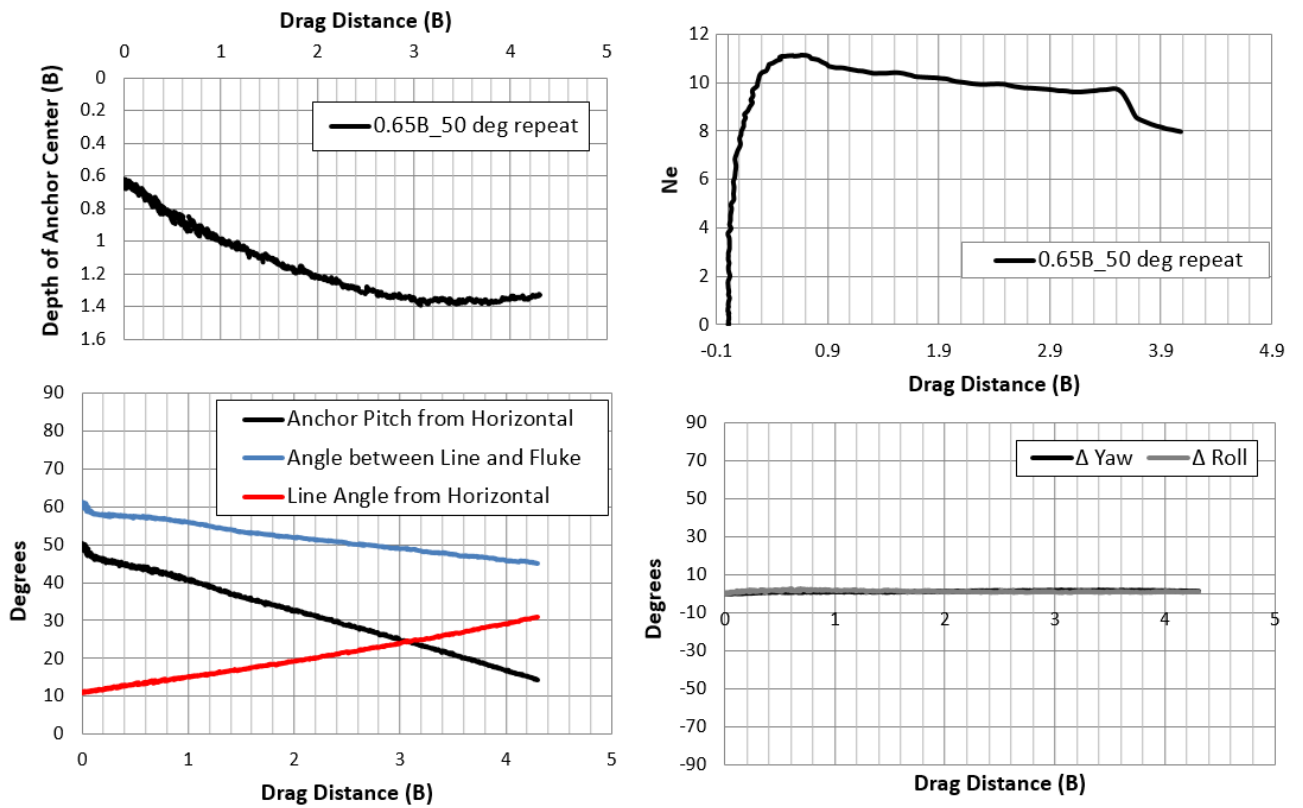
Figure A.112: Acrylic Speedy repeat test 0.65B initial embedment, 50-deg initial pitch
(4/25/2016)
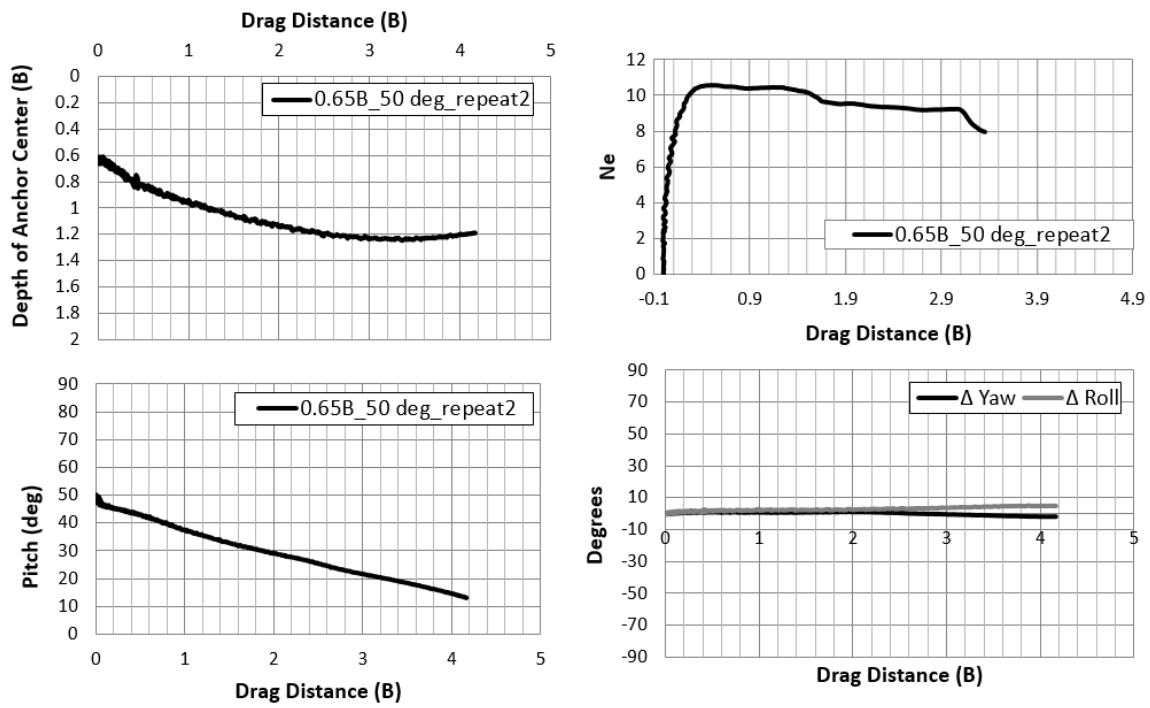
Figure A.113: Acrylic Speedy repeat 2 test 0.65B initial embedment, 50 deg- initial pitch (4/25/2016)

Figure A.114: Acrylic Speedy test 0.7B initial embedment, 60-deg initial pitch (4/25/2016)

Figure A.115: Undrained shear strength profile of the test bed (5/9/2015)

Figure A.116: Acrylic Speedy test with 1B initial embedment, 38-deg initial pitch (5/9/2016)

Figure A. 117: Acrylic Speedy test with 1.7 B initial embedment, 40-deg initial pitch (5/9/2016)

References

API 2GEO. (2011, April). *Geotechnical and Foundation Design Considerations*. ANSI/API Recommended Practice 2GEO American Petroleum Institute, First Edition.
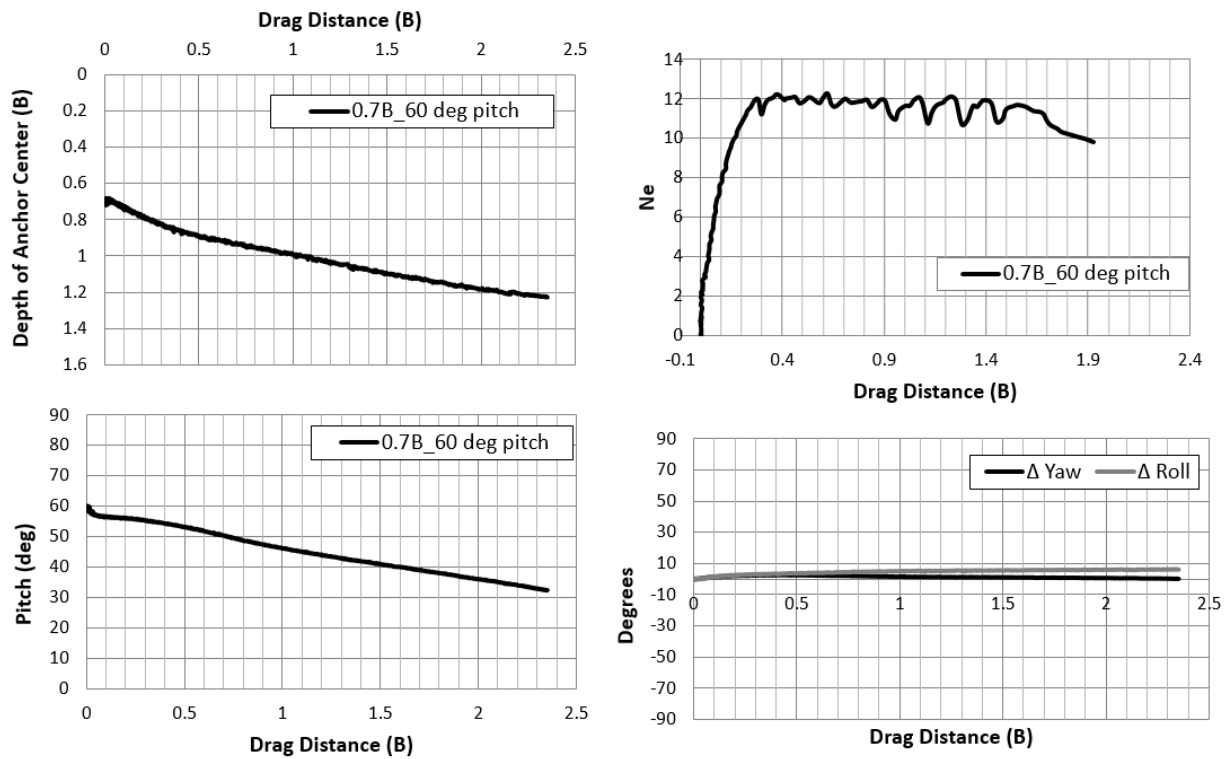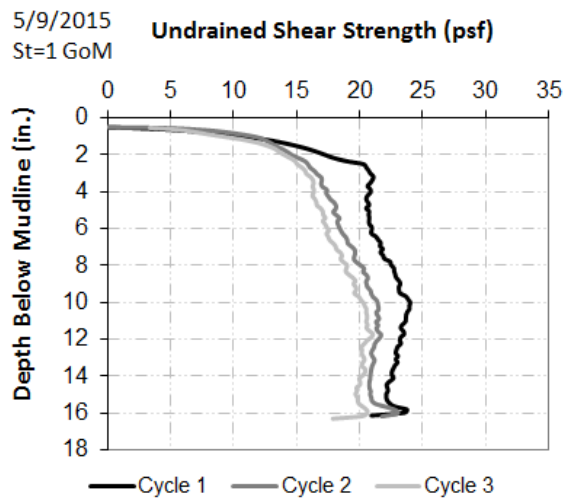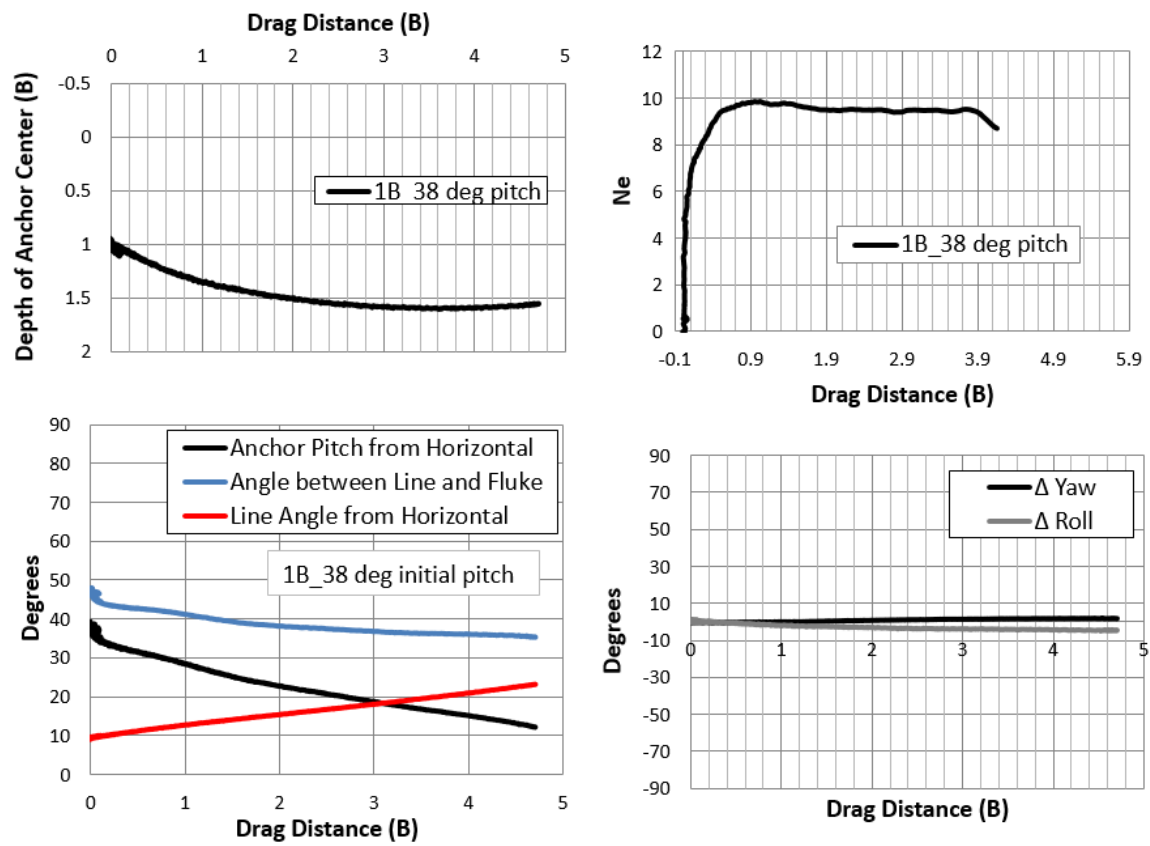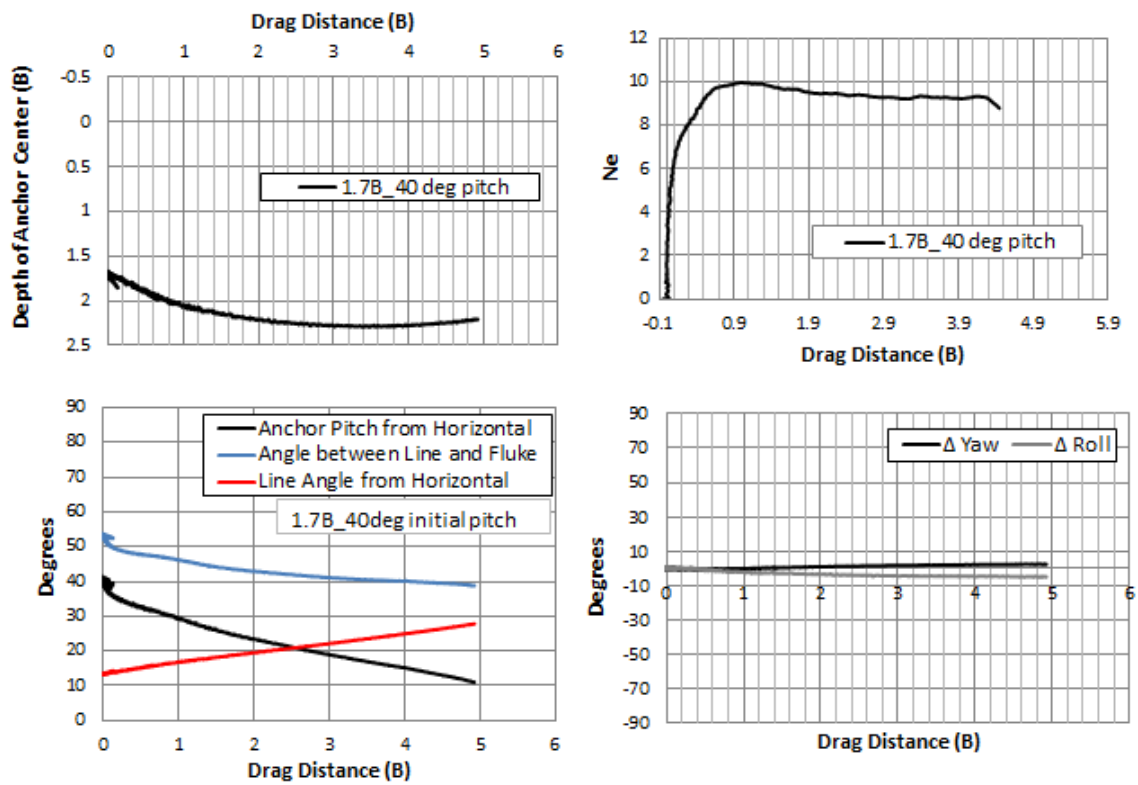
Araujo, J. B., Rogerio, D. M., & Medeiros Junior, C. J. (2004). High Holding Power Torpedo Pile- Results for the First Long Term Application. *23rd Int. Conf. on Offshore Mechanics and Arctic Engineering OMAE.* Vancouver. Canada.

Aubeny, C. P., & Chi, C. (2010). Mechanics of Drag Embedment Anchors in a Soft Seabed. *Journal of Geotechnical and Geoenvironmental Engineering*, Vol. 136, No. 1, pp. 57-68.

Aubeny, C. P., Gilbert, R. B., Randall, R., Zimmerman, E., McCarthy, K. B., Chen, C. -H., Drake, A., Yeh, P., Chi, C.-M., Beemer, R. (2011). *The Performance of Drag Embedment Anchors (DEA).* Contract Number M09PC00028, MMS Project Number 645, OTRC Project 32558-A6960, Minerals Management Service.

Aubeny, C., & Chi, C.-M. (2014). Analytical Model for Vertically Loaded Anchor Performance. *Journal of Geotechnical and Geoenvironmental Engineering*, 14-24.

Audibert, J. M., Morvant , M. N., Won, J.-Y., & Gilbert, R. B. (2006). Torpedo Piles: Laboratory and Field Research. *Proceedings of the Sixteenth International Offshore and Polar Engineering Conference* (pp. 462-468). San Francisco, California: The International Society of Offshore and Polar Engineers.

Bonfirm de Santos, A., & Henriques, C. C. (2004). Improvements Anchieved in the Project of FSPO P-50. *Offshore Technology Conference.* Houston, TX.

Bozorgmehrian, M., Terwad, M., & Peri, V. A. (2013, October). *www.offshore-mag.com.* Retrieved from www.offshore-mag.com: http://www.offshore-mag.com/content/dam/offshore/print-articles/Volume%2073/10/MOORING-092713-D9.pdf

Bradshaw, A. S. (2012). Framework for Scaling 1g Model Pile Tests for Offshore Wind Structures. *GeoCongress*, (pp. 336-345). Oakland, CA.

Bradshaw, A. S., Giampa, J., Dietrich, F., Gilbert, R. B., & Gerkus, H. (2015). Pullout Capacity of Plate Anchors in Sand for Floating Offshore Wind Turbines. *International Symposium of Frontiers in Offshore Geotechnics ISFOG.* Oslo, Norway.

Bransby, M. F., & O'Neill, M. (1999). Drag anchor fluke soil interaction in clays. *Proc. Int. Symp. on Numerical Models in Geomechanics* (pp. 489-494). Rotherdam, Netherlands: Balkema.

Chen, C.-H. (2013). Performance of Suction Caissons with a Small Aspect Ratio. *Ph.D. Dissertation*. The University of Texas at Austin.

Chen, W. F. (1975). *Limit analysis and soil plasticity.* N.Y.: Elsevier.

Cheon, J. Y. (2010). Analysis of Spatial Variability in Geotechnical Data. *Ph.D. Dissertation*. Austin, TX: The University of Texas at Austin.

Colliat, J.-L. (2002). Anchors for Deepwater to Ultradeepwater Moorings. *Offshore Technology Conference.* Houston, TX.

Craig, W. H. (1994). Size effects in anchor performance. *Canadian Geotechnical Journal*, 450-454.

Dahlberg, R. (1998). Design Procedures for Deepwater Anchors in Clay. *Offshore Technology Conference.* Houston, TX.

Davis, E. H., & Booker, J. R. (1973). The effect of increasing strength with depth on the bearing capacity of clays. *Geotechnique*, pp.551-563.

Degenkamp, G., & Dutta, A. (1989). Soil resistances to embedded anchor chains in soft clay. *Journal of the Geotechnical Engineering Division, ASCE*, Vol. 115, No. 10, 1420-1438.

DNV. (2002, December). Design and Installation of Plate Anchors in Clay. *Recommended Practice DNV-RP-E302*. Hovik, Norway: Det Norske Veritas.

Dunnavant, T. W., & Kwan, C.-T. T. (1993). Centrifuge modelling and parametric analyses of drag anchor behavior. *25th Annual Offshore Technology Conference*, (pp. pp.29-39). Houston, TX.

El-Gharbawy, S. L. (1998). The pullout capacity of suction caisson foundations. *Ph.D. Dissertation*. The University of Texas at Austin.

Elkhatib, S., & Randolph, M. F. (2005). The effect of interface friction on the performance of drag in-plate anchors. *Proc. Int. Symp. on Frontiers in Offshore Geotechnics (ISFOG)* (pp. 171-177). London, U.K.: Taylor & Francis.

Elkhatib, S., & Randolph, M. F. (2005). The effect of interface friction on the performance of drag-in plate anchors. *Proc. Int. Symp. on Frontiers in Offshore Geotechnics (ISFOG)* (pp. 171-177). London: Taylor&Francis.

El-Sherbiny, R. (2005). Performance of Suction Caisson Anchors in Normally Consolidated Clay . *Ph.D. Dissertation*. The University of Texas at Austin.

Gerkus, H., Giampa, J. R., Senanayake, A. I., Lai, Y., Huang, Y., Iturriaga Flores, J. E., Breithaupt, B., Sivarajah, S., Bradshaw, A., Gilbert, R. B. (2016). Preliminary Development of a New Concept to Improve Sustainability of Offshore Foundations. *Geo-Chicago 2016: Sustainability, Energy, and the Geoenvironment.* Chicago, IL.

Giampa, J. (2015). Personal Communication.

Gilbert, R. B., Aubeny, C. P., Chen, C.-H., McCarthy, K. B., & Vilkki, J. (2012). Experimental and Analytical Modeling for Drag Anchors. *Final Report Prepared for ABS Consulting, Project No. ABSC/1514096/DM-06 Offshore Technology Research Center Project 32558-B2930*.

Gilbert, R. B., Iturriaga Flores, J. E., & Gerkus, H. (2015). *United States of America Patent No. "Self-Installing Anchor", U.S. Provisional Patent Application No. 62/146,726*.

Gilbert, R. B., Lupulescu, C., Lee, C. H., Miller, J., Kroncke, M., Yang, M., Aubeny, C., Murff, J. D. (2009). Analytical and Experimental Modeling for Out-of-Plane Loading of Plate Anchors. *Offshore Technology Conference.* Houston, TX.

307

Gilbert, R. B., Morvant, M. N., & Audibert, J. (2008, March). Torpedo Piles Joint Industry Project- Model Torpedo Pile Tests in Kaolinite Test Beds. *Final Project Report prepared for Minerals Management Service MMS Project Number 575*. The University of Texas at Austin.

Gilbert, R. B., Morvant, M., & Audibert, J. (2009, March). Torpedo Piles Joint Industry Project- Model Torpedo Pile Tests in Kaolinite Test Beds. *Final Project Report Prepared for the Minerals Management Service MMS Project Number 575*. Offshore Technology Research Center.

Horan, A. J. (2012). The Mechanical Behavior of Normally Consolidated Soils as a Function of Pure Fluid Salinity. *M.Sc. Thesis*. Massaachusetss Institute of Technology.

Huang, Y. (2015). Designing a Laboratory Model Test Program for Developing a New Offshore Anchor. *Master's Thesis*. The University of Texas at Austin.

Iturriaga Flores, J. E. (2016, May). Risk-Informed Design of New Anchor Concept for Floating Energy Production Systems. *Ph.D. Dissertation*. The University of Texas at Austin.

Ladd, C., Foot, R., Ishihara, K., Schlosser, F., & Poulos, H. (1977, July 10-15). Stress-deformation and strength characeristics. *In Proceedings of the 9th International Conference on Soil Mechanics and Foundation Engineering, Vol.2 pp. 421-494*. Tokyo, Japan: Japanese Society of Soil Mechanics and Foundation Engineering.

Lee, C. H. (2008). Constructing Test Beds of Clay with a Specified Profile of Undrained Shear Strength versus Depth. *M.Sc. Thesis*. The University of Texas at Austin.

Liu, H., Zhang, W., Liu, C., & Hu, C. (2012). Movement direction of drag anchors in seabed soils. *Applied Ocean Researsh*, 78-95.

M., P. T. (2013, November). Patriot User Manual. Colchester, VA.

Mark, R., & Gourvenec, S. (2011). *Offshore Geotechnical Engineering.* New York, USA: Spon Press.

Martin, C. M. (1994). Physical and numerical modelling offshore fondations under combined loads. *Ph.D. Dissertation*. University of Oxford.

Martin, C. M., & Randolph, M. F. (2001). Applications of the lower and upper bound theorems of plasticity to collapse of circular foundations. *Proc.,10th Int. Conf., Vol 2* (pp. 1417-1428). Tucson, AZ: International Association of Computer Methods and Advances in Geomechanics.

Matha, D. (2009). *Model Development and Loads Analysis of an Offshore Wind Turbine on a Tension Leg Platform, with a Comparison to Other Floating Turbine Concepts.* National Renewable Energy Laboratory.

McCarthy, K. B. (2011). Experimental in-plane behavior of generic scale model drag embedment anchor in kaolinite test beds. *Master's Thesis*. The University of Texas at Austin.

Morrison, J. R., O'Brien, M. P., Johnson, J. W., & Schaaf, A. S. (1950). The force exerted by surface waves on piles. *Petroleum Transactions, American Institute of Mining and Metal Engineering*, Vol. 4, pp 11-22.

Murff, J. D. (1994). Limit analysis of multi-footing foundation systems. *Proc., 8th Int. Conf. on Computer Methods and Advances in Geomechanics* (pp. 233-244). Abington, U.K.: Vol. 1, Taylor & Francis.

Murff, J. D., Randolph, M. F., Elkhatib, S., Kolk, H. J., Ruinen, R., Strom, P. J., & Thorne , C. (2005). Vertically loaded plate anchors for deepwater applications. *Proc. Int. Symp. on Frontiers in Offshore Geotechnics ISFOG05* (pp. 31-48). Perth, Australia: Balkema.

Musial, W., & Butterfield, S. (2006). Energy from Offshore Wind. *Offshore Technology Conference.* Houston, TX.

Musial, W., & Ram, B. (2010). *Large-Scale Offshore Wind Power in the United States.* National Renewable Energy Laboratory.

NCEL. (1987). *Drag Embedment Anchors for Navy Moorings.* U.S. Navy, Port Hueneme, CA: Naval Civil Engineering Laboratory.

Neubecker, S. R., & Randolph, M. F. (1995). Performance of Embedded Anchor Chains and Consequences for Anchor Design. *Offshore Technology Conference*, (pp. 191-200). Houston, TX.

Neubecker, S. R., & Randolph, M. F. (1996). The Performance of Drag Anchors and Chain Systems in Cohesive Soils. *Marine Geosources & Ggeotechnology*, 77-96.

O'Beirne, C., O'Loughlin, C. D., Wang, D., & Gaudin, C. (2015). Capacity of dynamically installed anchors as asssed through field testing and three-dimensional large-deformation finite element analyses. *Canadian Geotechnical Journal*, 548-562.

O'Loughlin, C. D., Randolph, M. F., Randolph, M. F., & Richardson, M. (2004). Experimental and Theoretical Studies of Deep Penetrating Anchors. *Offshore Technology Conference.* Houston, TX.

O'Neill, M. P., Bransby, M. F., & Randolph, M. F. (2003). Drag anchor fluke-soil interaction in clays. *Canadian Geotechnical Journal*, 40: 78-94.

Patriot User Manual. (2008, February). Polhemus.

Polhemus T.M. (2013, November). Patriot User Manual. Colchester, VA.

Raie, M. S., & Tassoulas, J. L. (2009). Installation of Torpedo Anchors: Numerical Modeling. *Journal of Geotechnical and Geoenvironmental Engineering* , Vol. 135, No. 12 pp. 1805-1813.

Rankine, W. J. (1857). On Stability on Loose Earth. *Philosophic Transactions of Royal Society, London*, Part I, 9-27.

Richardson, G. E., Nixon, L. D., Kazanis, E. G., Montgomery, T. M., & Gravois, M. P. (2008). Deepwater Gulf of Mexico 2008: America's Offshore Energy Future. *Vols. 2008-013*. New Orleans, LA: U.S. Department of the Interior, Minerals Management Service, Gulf of Mexico OCS Region.

Ruinen, R., & Degenkamp, G. (2001). Anchor Selection and Installation for Shallow and Deepwater Mooring Systems. *Eleventh International Offshore and Polar Engineering Conference* . Stavanger, Norway : The International Society of Offshore and Polar Engineers.

Shelton, J. T. (2007). OMNI-Max Anchor Development and Technology. *Ocean Conference*. Vancouver, Canada.

Sincock, P., & Sondhi, N. (1993). *Drag Anchor for Floating Systems*. Berkshire, U.K.: Health and Safety Executive.

Stewart, D. P., & Randolph, M. F. (1994). T-Bar Penetration Testing in Soft Clay. *Journal of Geotechnical Engineering*, 2230-2235.

Vryhof B.V. (2015). *Anchoring Manual*. Global Maritime Vryhof.

Wong, P., Gaudin, C., Randolph, M. F., Cassidy, M. J., & Tian, Y. (2012). Performance of Suction Embedded Plate Anchors in Permanent Mooring Applications. *Proceedings of the Twenty-second International Offshore and Polar Engineering Conference* (pp. 640-645). Rhodes, Greece: International Society of Offshore and Polar Engineers (ISOPE).

Wu, X., Chow, Y. K., & Leung, C. F. (2016). Prediction of Drag Anchor Trajectory with Both Shallow and Deep Anchor Behavior. *Offshore Technology Conference Asia*. Kuala Lumpur, Malaysia.

www.bruceanchor.co.uk. (2016, June 6). Retrieved from Bruce Anchor: http://www.bruceanchor.co.uk/products/the-bruce-dennla/

www.deepseaanchors.com. (2016, February). Retrieved from Deep Sea Anchors: www.deepseaanchors.com

www.energy.gov. (2014, May 6). Retrieved from www.energy.gov: http://energy.gov/articles/top-10-things-you-didn-t-know-about-offshore-wind-energy

www.intermoor.com. (2016, June 7). Retrieved from Intermoor: www.intermoor.com

www.vryhof.com. (2016, June 6). Retrieved from Vryhof B.V.: www.vryhof.com

Yang, M., Aubeny, C. P., & Murff, J. D. (2011). Behavior of Suction Embedded Plate Anchors during Keying Process. *Journal of Geotechnical and Geoenvironmental Engineering*, Vol. 138, No. 2 pp. 174-183.

Yang, M., Murff, J. D., & Aubeny, C. P. (2008). *"Out of plane loading of plate anchors, analytical modeling" Phase II Rep. Prepared for the Offshore Technology Research Center*. College Station, TX: ABS Consulting.

Yang, M., Murff, J. D., & Aubeny, C. P. (2010). Undrained Capacity of Plate Anchor under General Loading. *Journal of Geotechnical and Geoenvironmental Engineering*, 1383-1393.

Zimmerman, E. H., Smith, M. W., & Shelton, J. T. (2009). Efficient Gravity Installed Anchor for Deepwater Mooring. *Offshore Technology Conference*. Houston, TX.

VITA

Hande Gerkus was born in Turkey in 1988. After graduating from FMV Isik High School, she enrolled in Istanbul Technical University. She received her B.Sc. degree in Civil Engineering in 2009 and her M.E. degree in Soil Mechanics and Geotechnical Engineering in 2011. She started to work on her Ph.D. in Geotechnical Engineering at The University of Texas at Austin in August 2011.

Email address: handegerkus@gmail.com

This dissertation was typed by the author.